



HAL
open science

**Title: Modern Mars' geomorphological activity, driven
by wind, frost, and gravity**

Serina Diniega, Ali M Bramson, Bonnie Buratti, Peter Buhler, Devon M Burr,
Matthew Chojnacki, Susan J. Conway, Colin M Dundas, Candice J Hansen,
Alfred S Mcewen, et al.

► **To cite this version:**

Serina Diniega, Ali M Bramson, Bonnie Buratti, Peter Buhler, Devon M Burr, et al.. Title: Modern Mars' geomorphological activity, driven by wind, frost, and gravity. *Geomorphology*, 2021, 380, pp.107627. 10.1016/j.geomorph.2021.107627 . hal-03186543

HAL Id: hal-03186543

<https://hal.science/hal-03186543>

Submitted on 31 Mar 2021

HAL is a multi-disciplinary open access archive for the deposit and dissemination of scientific research documents, whether they are published or not. The documents may come from teaching and research institutions in France or abroad, or from public or private research centers.

L'archive ouverte pluridisciplinaire **HAL**, est destinée au dépôt et à la diffusion de documents scientifiques de niveau recherche, publiés ou non, émanant des établissements d'enseignement et de recherche français ou étrangers, des laboratoires publics ou privés.

1 **Title: Modern Mars' geomorphological activity, driven by wind, frost, and gravity**

2
3 Authors: Serina Diniega^{1,*}, Ali M. Bramson², Bonnie Buratti¹, Peter Buhler³, Devon M. Burr⁴,
4 Matthew Chojnacki³, Susan J. Conway⁵, Colin M. Dundas⁶, Candice J. Hansen³, Alfred S.
5 McEwen⁷, Mathieu G. A. Lapôtre⁸, Joseph Levy⁹, Lauren Mc Keown¹⁰, Sylvain Piqueux¹,
6 Ganna Portyankina¹¹, Christy Swann¹², Timothy N. Titus⁶, Jacob M. Widmer

7
8 ¹Jet Propulsion Laboratory, California Institute of Technology, 4800 Oak Grove Dr., Pasadena,
9 CA 91009, USA

10 ²Department of Earth, Atmospheric, and Planetary Sciences, Purdue University, 550 Stadium
11 Mall Dr., West Lafayette, IN 47907, USA

12 ³Planetary Science Institute, 1700 East Fort Lowell, Suite 106, Tucson, AZ 85719, USA

13 ⁴Northern Arizona University, 537 S Beaver St, Flagstaff AZ 86011-6010, USA

14 ⁵CNRS UMR 6112 Laboratoire de Planétologie et Géodynamique, Université de Nantes, 44330
15 Nantes, France

16 ⁶U.S. Geological Survey, Astrogeology Science Center, 2255 N. Gemini Drive, Flagstaff, AZ
17 86001, USA

18 ⁷Lunar and Planetary Laboratory, University of Arizona, 1629 E University Blvd, Tucson, AZ
19 85721, USA

20 ⁸Department of Geological Sciences, Stanford University, 450 Jane Stanford Way, Stanford, CA
21 94305, USA

22 ⁹Colgate University, 13 Oak Dr., Hamilton, NY 13346, USA

23 ¹⁰National History Museum, Cromwell Rd, South Kensington, London SW7 5BD, United
24 Kingdom

25 ¹¹Laboratory for Atmospheric and Space Physics, University of Colorado – Boulder, 1234
26 Innovation Dr., Boulder, CO 80303, USA

27 ¹²U.S. Naval Research Laboratory, 4555 Overlook Ave. S.W., Washington, DC 20375, USA

28 *Correspondence author: serina.diniega@jpl.nasa.gov, +1 818-393-1487.

29
30 © 2020. All rights reserved.

31
32
33 **ABSTRACT**

34 Extensive evidence of landform-scale martian geomorphic changes has been acquired in the
35 last decade, and the number and range of examples of surface activity have increased as more
36 high-resolution imagery has been acquired. Within the present-day Mars climate, wind and
37 frost/ice are the dominant drivers, resulting in large avalanches of material down icy, rocky, or
38 sandy slopes; sediment transport leading to many scales of aeolian bedforms and erosion; pits of

39 various forms and patterned ground; and substrate material carved out from under subliming ice
40 slabs. Due to the ability to collect correlated observations of surface activity and new landforms
41 with relevant environmental conditions with spacecraft on or around Mars, studies of martian
42 geomorphologic activity are uniquely positioned to directly test surface-atmosphere interaction
43 and landform formation/evolution models outside of Earth. In this paper, we outline currently
44 observed and interpreted surface activity occurring within the modern Mars environment, and tie
45 this activity to wind, seasonal surface CO₂ frost/ice, sublimation of subsurface water ice, and/or
46 gravity drivers. Open questions regarding these processes are outlined, and then measurements
47 needed for answering these questions are identified. In the final sections, we discuss how many
48 of these martian processes and landforms may provide useful analogs for conditions and
49 processes active on other planetary surfaces, with an emphasis on those that stretch the bounds of
50 terrestrial-based models or that lack terrestrial analogs. In these ways, modern Mars presents a
51 natural and powerful comparative planetology base case for studies of Solar System surface
52 processes, beyond or instead of Earth.

53

54 KEY WORDS

55 Geomorphological activity; Mars; Comparative Planetology; Aeolian; Sublimation; Mass
56 wasting

57

58 HIGHLIGHTS

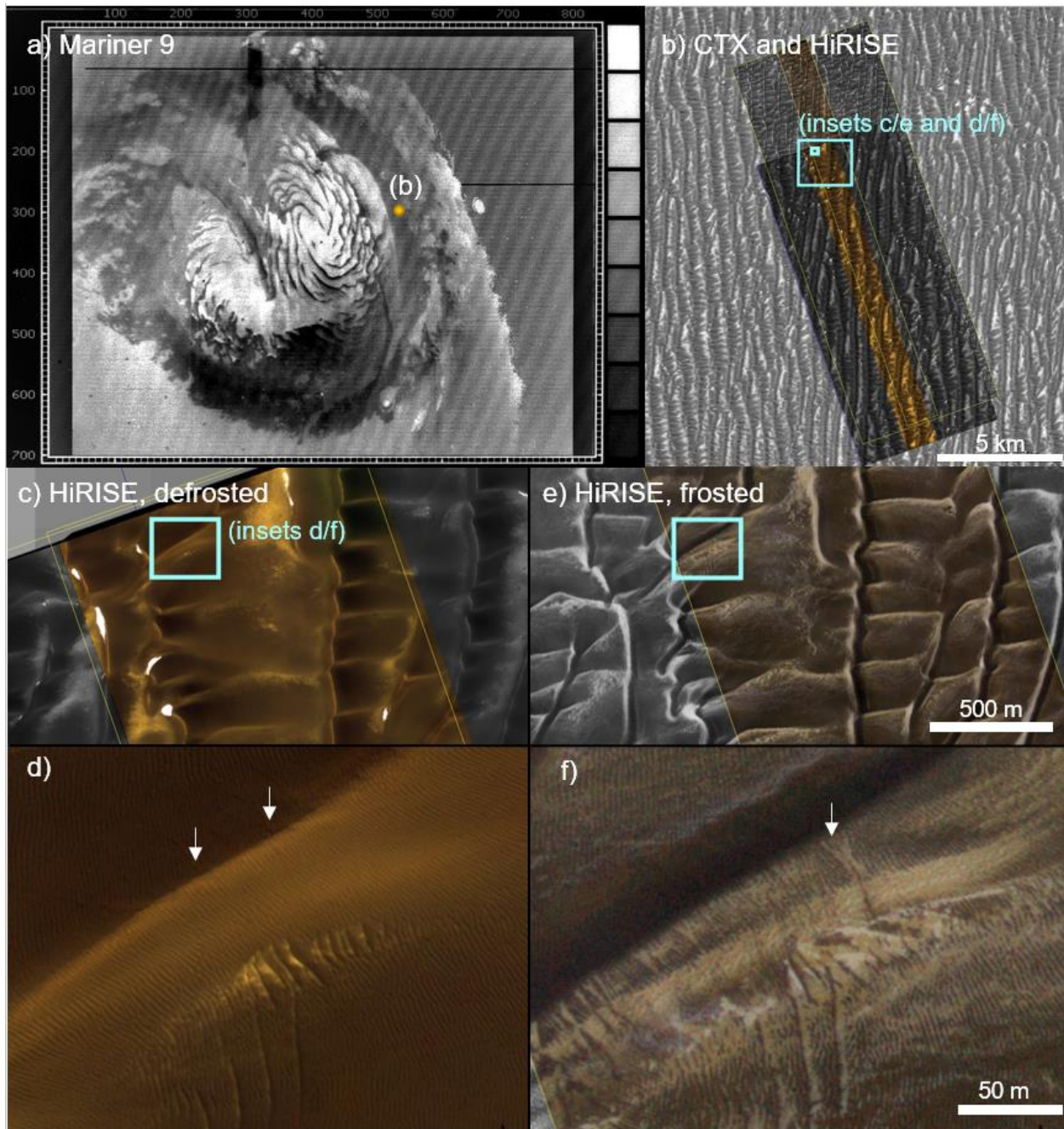
- 59 • Mars' surface is actively shaped in the present due to wind, frost/ice, and gravity.
- 60 • Overlapping, high-resolution images from orbit are key for detection of activity.
- 61 • In situ and orbital data are needed to fully characterize the active Mars processes.
- 62 • Mars studies provide critical information about activity beyond that seen on Earth.

63		
64	1	Introduction..... 5
65	1.1	Why focus on wind and sublimation as drivers for surface activity? 9
66	1.1.1	Other known present-day surface changes Erreur ! Signet non défini.
67	1.1.2	Other potential/hypothesized causes of recent surface changes Erreur ! Signet non
68		défini.
69	1.2	Sources of seminal data..... 11
70	2	Wind-formed landforms..... 15
71	2.1	Depositional and Erosional Aeolian Landscapes: Materials and Landforms 17
72	2.1.1	Wind-transported sediment grain properties..... 17
73	2.1.2	Wind-transported sediment composition 18
74	2.1.3	Bedforms: Types and Morphologies..... 20
75	2.2	Aeolian Transport, Fluxes, and Erosion Rates 24
76	2.2.1	Thresholds of motion and transport hysteresis 25
77	2.2.2	Bedform migration and evolution..... 29
78	2.2.3	Erosion Rates 32
79	2.3	Open questions for martian aeolian landforms and sediment history 33
80	2.4	Open questions for the physics of aeolian processes 34
81	3	Seasonal Frost/Ice-formed Landforms..... 35
82	3.1	Currently-formed surface frost/ice types on Mars 36
83	3.2	Seasonal sublimation triggered mass-wasting landforms 38
84	3.2.1	Gullies..... 38
85	3.2.2	Dune alcoves..... 41
86	3.3	Basal sublimation formed landforms 42
87	3.3.1	Linear gullies 42
88	3.3.2	Araneiforms 43
89	3.4	Open questions for seasonal frost/ice and related landforms 45
90	4	Long-term sublimation of ices 46
91	4.1	Polar surface landforms..... 47
92	4.1.1	South Polar Residual Cap 47
93	4.1.2	Massive CO ₂ Ice Deposit and its capping H ₂ O ice layer 50
94	4.1.3	North Polar Residual Cap H ₂ O ice surface 50
95	4.2	Present/recent subsurface water ice..... 52
96	4.2.1	Present-day water ice stability 52
97	4.2.2	Present-day water ice distribution..... 53
98	4.3	Sublimation thermokarst 55
99	4.4	Patterned Ground..... 56
100	4.5	Open questions for long-term sublimation of ice..... 59
101	5	Mass-wasting aided landforms 61
102	5.1	Recurring Slope Lineae (RSL)..... 61
103	5.2	Avalanches/rock falls from rocky and icy slopes..... 64
104	5.3	Open questions for these mass-wasting aided landforms..... 65
105	6	Summary of the measurements needed to answer these questions..... 66
106	7	Mars as a “natural laboratory” for comparative planetology studies..... 71
107	7.1	Aeolian surface processes and meteorological dynamics 72
108	7.2	Sublimation-driven geomorphic dynamics 76

109	7.3	Planetary bodies with variable-density atmospheres	81
110	8	Lessons learned from planetary geomorphological studies	84
111	9	Acknowledgements	85
112		References	86
113			
114			
115			

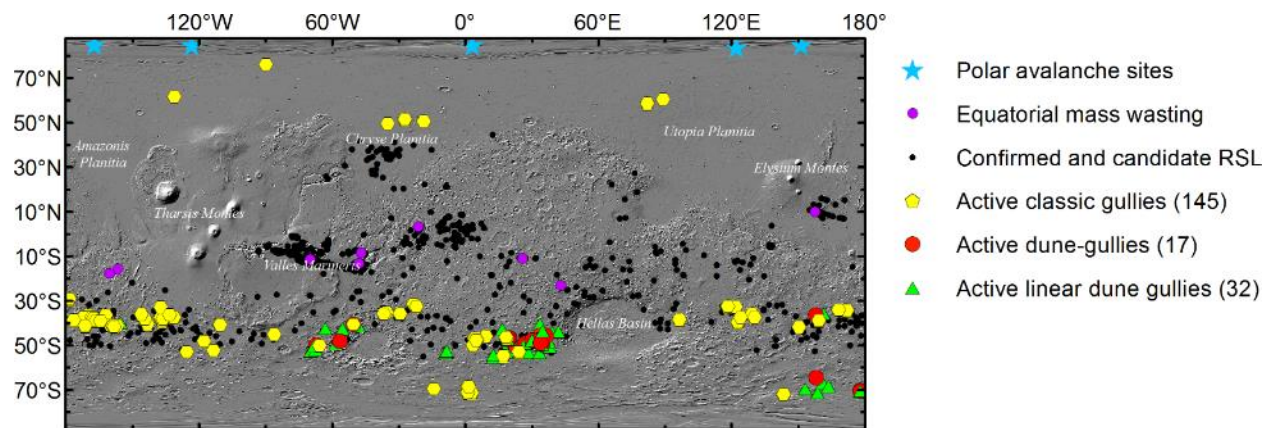
116 **1 Introduction**

117 Numerous studies since the early Mars missions have documented evidence of surface
118 activity on Mars (e.g., Figure 1), but it was only with the advent of high-resolution and repeat
119 imaging over multiple martian years that the full scope of present-day martian surface activity,
120 including topographic changes, has been appreciated. Direct observations of geomorphological
121 activity, over all areas of Mars (Figure 2), has enabled testing of hypotheses about the driving
122 conditions and processes causing observed changes. In particular, many of the types of
123 landforms hypothesized to be recently formed have been shown to form or be modified in the
124 present day, with observations and models tying activity rates and timing to frost(s), wind, and
125 gravity (i.e., movement down slopes).
126



127
 128 Figure 1. Example images of early and recent images of martian polar dunes, and the details that
 129 become apparent in zoomed-in images. (a) Mariner 9 image of the north polar cap and polar erg,
 130 acquired 1972-10-12 (= Mars Year (MY) 10 L_s 95°, see §1.2 for date nomenclature), ~3 km/px
 131 (MTVS 4297-47). (b) Basemap is from CTX images (~5 m/px) and shown are 2 pairs of
 132 monochromatic and false color HiRISE images (50 cm/px): ESP_027012_2610, acquired 2012-
 133 05-01 (MY 31 L_s 104°) and ESP_058950_2610, acquired 2019-02-22 (MY 34 L_s 345°). At L_s
 134 104° (early summer), the seasonal frost layer is subliming, with only a few small patches of ice
 135 remaining (i.e., the bright spots). The large ripples are clearly visible on the dunes (§2.1.3), along
 136 with a few new dune furrows (arrows; §3.3.2). At L_s 354° (end of winter), the surface is
 137 completely covered in CO₂ frost, so is more uniform in color and brighter. Some underlying

138 ripples are visible beneath the frost, as is a new dune alcove (arrow; §3.2.2). The false color
139 scheme is based on an automatic contrast enhancement algorithm with further manual tweaks to
140 increase visibility of small features. The dunes are dark in color because they are made of basalt
141 and the interdune substrate is lighter, with frost/ice brightest. North is up and illumination is
142 from the left in all HiRISE images. Scale bars are approximate as images are not orthorectified.
143



144 Figure 2. Map showing observations of activity for features where global surveys have been
145 completed; note that this map is incomplete due to the patchy spatial coverage of repeat imaging:
146 monitoring locations for polar avalanches (Becerra et al., 2020) and presumed to occur at all
147 steep scarps, equatorial mass-wasting (M.F. Thomas et al., 2020), RSL (Stillman et al., 2020),
148 classic gullies (Dundas et al., 2019a), dune gullies (Dundas et al., 2019a; Diniega et al., 2010),
149 and linear dune gullies (Dundas et al., 2019a; Pasquon et al., 2016).
150

151
152 Studies of present-day geomorphological activity, especially if tied to correlated observations
153 of activity and the relevant environment, are uniquely positioned to directly test surface-
154 atmosphere interaction and landform formation/evolution models. Such studies are of great
155 importance for understanding Mars' environmental and geologic history because landforms can
156 serve as proxy records of specific processes and environmental conditions, such as surface
157 thermo/mechanical properties, grain size(s), and wind velocities and variability. Studies of
158 present-day activity on Mars are also uniquely enabling for studies of processes active on other
159 planetary bodies because these either provide a matchless detailed planetary data point outside of
160 Earth's gravity, atmosphere, and other conditions for comparison to terrestrial studies and
161 derived models, or provide a detailed look into a process that has no terrestrial analog.

162 This review is on martian landforms that can be robustly connected to specific surface
163 environmental conditions and processes. We focus on martian surface activity that (1) is
164 observed or hypothesized to be happening in the present climate (albeit, in some cases,
165 potentially at very slow, not yet directly observable rate), and (2) creates a specific and

166 interpretable change to the martian rocky or icy surface's shape that can be detected for >1
167 martian year.

168 Throughout this paper, we discuss the “modern Mars” environment, and in particular on the
169 present martian climate, which has been observed at high frequency and resolution over the last
170 few decades via spacecraft. However, modern Mars also includes the “recent” climate—a term
171 generally used to refer to the time since the last major obliquity excursion (around 500 kyr,
172 *Laskar et al.*, 2004), as this is the time period for the most recent significant sculpting of the
173 currently observable landscape. This time period is important as it is the only period where direct
174 characterization of the environment, based on present-day measurements, can be paired with
175 specific surface changes and thus hypothesized landform formation and evolution models can be
176 robustly tested with observations. Additionally, the climate conditions during the present and
177 recent past are thought to be representative of the martian climate over the last few billion years.
178 Throughout this period, called the Amazonian, Mars is thought to have been dry and cool, with
179 very low surface pressures and little liquid water. (Recent studies and our present understanding
180 about the Amazonian climate are summarized in *Diniaga and Smith*, 2020.) Thus, while this
181 review focuses on activity that has been observed in or hypothesized to be occurring in the
182 present day, what we learn about surface-altering processes and driving environmental
183 conditions is likely to be relevant through a few billion years of Mars' geological and
184 climatological history—and so interpretations of even relict landscapes should take into account
185 the presently observed surface-altering processes.

186 In this review, we will outline observed and interpreted surface activity occurring within the
187 modern Mars environment. This activity, when tied to specific environmental drivers, has been
188 shown to be primarily caused by wind- and frost-related processes, although in many cases the
189 exact mechanism driving the geomorphological change has not yet been determined. The frost or
190 ice involved in present-day landform evolution is of two broad classes: the atmosphere-sourced
191 CO₂ and H₂O frost that accumulates each winter on the martian surface, and the previously
192 buried/preserved ice deposits beneath the martian surface or within the polar cap that now are
193 undergoing long-term loss (although for the cap, short-term loss occurs in some areas but it is
194 unclear if there is total net long-term loss or gain). Three sections describe landforms with
195 formation mechanisms associated with wind (i.e., aeolian features) and these two classes of frost.
196 Gravity also plays a role as many of these landforms involve material moving downslope (i.e.,

197 mass-wasting features). In a separate section, we describe a few landforms where the initiation of
198 or additional environmental control on such downslope movement has not yet been determined.

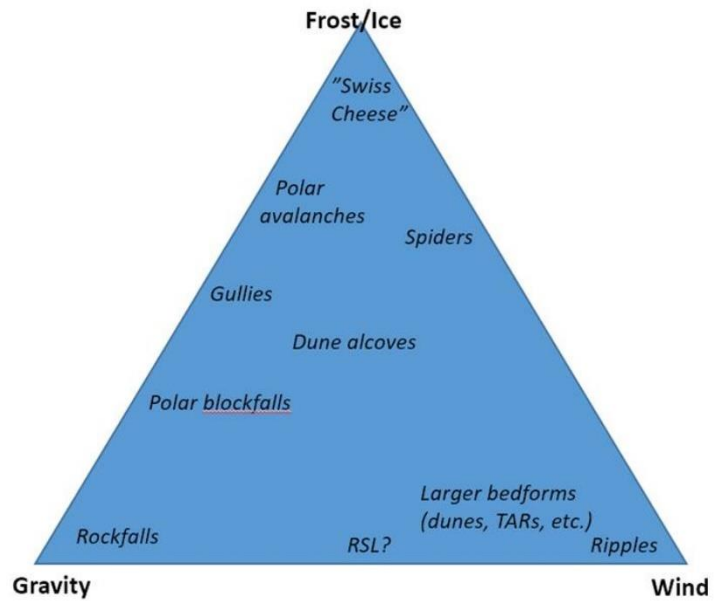
199 In each of these sections, after outlining what is known, we outline open questions about the
200 exact processes and environmental thresholds/controls. We also summarize current big questions
201 about the martian surface and atmosphere environment in the present and through the
202 Amazonian that could be addressed through continued study of these specific surface changes
203 and landforms. Additionally, we identify the measurements needed to answer these questions.
204 Finally, we discuss how many of these environmental conditions and processes may provide
205 useful analogs for conditions and processes active on other planetary surfaces, with an emphasis
206 on those that lack terrestrial analogs and for which Mars is a more natural comparative
207 planetology base case.

208

209 **1.1 Why focus on wind and sublimation as drivers for surface activity?**

210 Some of the earliest Mars investigations via Earth-based telescopes or spacecraft observed
211 Mars' atmosphere and seasonal frost (e.g., *Johnson*, 1965; *Lowell*, 1895). Orbital observations
212 have enabled tracking of seasonal frost caps (§3.1) and movement of dust and sand (§2), as
213 reflected in bedform movement and regional albedo changes. In situ indications of wind and at
214 least trace amounts of seasonal frost (H₂O and/or CO₂) have been observed by all Mars landers
215 that have survived through a martian winter (missions listed in Table 2, references listed in §3.1).
216 The northernmost lander (*Phoenix*) even had one of its solar panels crushed due to accumulation
217 of a thick layer of frozen CO₂
218 (https://www.nasa.gov/mission_pages/phoenix/news/phx20100524.html). Evidence that both
219 wind and seasonal frost affect landform evolution has built up over the last two decades as the
220 martian surface environment and morphology, and changes in the surface morphology, have
221 been observed and characterized globally at sub-landform-scales and in places at sub-meter-scale
222 resolution (§2–3, 5). As shown in Figure 3, many of the examples of observed present-day
223 surface changes appear to be explained through some combination of wind, annual frost/ice
224 formation or sublimation, and gravity (i.e., mass wasting). Close study of these
225 landforms/surface changes along with concurrent measurement of their environment enables
226 testing and refinement of quantitative models of the underlying processes, under Mars
227 conditions.

228 In addition, there are martian landforms that have not yet been directly observed to form and
 229 change, but which are interpreted to be forming in the present climate due to long-term (i.e.,
 230 multi-annual) sublimation or
 231 modification of surface or
 232 subsurface water ice reservoirs (§4).
 233 Such landforms are also important to
 234 study, again with concurrent detailed
 235 measurement of their present
 236 environments, because they provide
 237 a bridge to a recent past climate
 238 when that ice was deposited.



239 **Figure 3. A ternary diagram**
 240 **illustrating the proposed relative**
 241 **controls by frost/ice, wind, and**
 242 **gravity on many of the landforms discussed in this review (§2–3, 5). (Not included here are the**
 243 **landforms created through long-term subsurface ice processes, §4, and landforms not discussed**
 244 **within this paper.)**

245
 246
 247 Beyond wind and frost, a few other known or hypothesized present-day surface processes are
 248 widespread and can move large amounts of material over the martian surface. However, for
 249 reasons described here, these processes and landforms are not discussed further within this paper.

- 250 • Rocky landforms and textures that appear similar to terrestrial features formed through wind
 251 erosion, such as ventifacts (*Laity and Bridges, 2009*) and yardangs (*Liu et al., 2020; Ward,*
 252 *1979*) have been identified on Mars. Such erosion is likely occurring in the present martian
 253 climate but would be occurring at very slow rates; terrestrial sand abrasion occurs at tens to
 254 thousands of microns per year (discussed in *Laity and Bridges, 2009*) and bulk Mars surface
 255 aeolian erosion rates are at the low end of that range (§2.2.3). Thus, we are not yet able to
 256 draw quantitative connections to specific environmental conditions, including roughly when
 257 these environmental conditions existed, and constrained modeling of the formation process
 258 is difficult. Hence, we do not discuss such landforms in this review.
- 259 • Impact cratering is also actively changing the shape of the martian surface in the present
 260 climate (e.g., *Daubar et al., 2013; 2019*), but the dominant controls for that process are

261 characteristics of the impactor and the impacted surface structure, not the environment at the
262 time of impact. Thus, impactor-related processes are not a focus of this review.

263 • We will not discuss processes that generally change the appearance of the surface by
264 moving around only a surficial layer, such as insolation-driven dust lifting or dust devils
265 (*Balme and Greeley, 2006*) or thin slope streaks (*Chuang et al., 2007*), although slope
266 streaks do occasionally transport greater thicknesses (*Dundas, 2020b*). Such processes do
267 not yield a significant change in the shape of the landscape and/or a clear geomorphic
268 change retained for >1 martian year, and so are considered beyond the scope of this study.
269 One exception is recurring slope lineae (RSL, discussed in §5.1), which is a landform of
270 recent high interest.

271 Other drivers, such as volcanism or liquid water, have been proposed to explain observed
272 geomorphologies and, in a few cases, observed surface activity. Some studies have suggested
273 that these other drivers may be important and influential for shaping martian geology during the
274 Amazonian and into the present. However, as outlined above, we focus this review on
275 geomorphic processes known or generally thought to be active in the present day, and processes
276 where existing observations of the martian environment are (so far) at least qualitatively
277 consistent with the models we describe. For example, we note that this review does not include
278 discussion of liquid water-driven geomorphic activity because, although many studies have
279 proposed recent or present-day water-driven activity to explain observed geomorphologies (e.g.,
280 *Chevrier and Rivera-Valentin, 2012; Malin et al., 2006*), no studies have yet been able to explain
281 a water source that is consistent with all environmental observations or with behaviors/timing of
282 activity that is consistent with observations of changes. In addition to liquid water-driven
283 processes, volcanism, tectonics, glacial flow, rainfall, and biological activity will not be
284 discussed within this review.

285 286 **1.2 Sources of seminal data**

287 The primary data that have led to studies of present-day surface geomorphological changes
288 have been high-resolution visible images that allow for identification of smaller surface features
289 and changes. For the latter, a key enabler were visible images of the same site, repeated over
290 time—between the high resolution of these images (down to 0.25 cm/px by the Mars
291 Reconnaissance Orbiter (MRO) High Resolution Imaging Science Experiment (HiRISE)) and a
292 longer temporal baseline (currently at seven martian years for the highest-resolution images;

293 longer for comparisons to coarser resolution data: Table 1), many more examples of surface
294 changes have been identified. An example of such repeat images is shown in Figure 4;
295 comparisons of such images need to consider different resolutions and illumination conditions
296 (i.e., time of day).

297 In discussions of the timing of observed activity, we use the common Mars Year (MY – note
298 the difference from million years = Myr) and solar longitude (L_s) nomenclature. Enumeration of
299 Mars Years and seasons is described in detail by *Piqueux et al.* (2015a), but a brief description is
300 as follows:

- 301 • A Mars year is nearly twice as long as an Earth year (~687 Earth days).
- 302 • The solar longitude denotes the position of Mars in its orbit, running from L_s 0° to 360° .
303 (Due to Mars' orbital eccentricity, a degree of L_s spans 1.5-2.2 martian days or 'sols'.)
- 304 • A Mars Year starts at L_s 0° = northern spring equinox, and proceeds to L_s 90° = northern
305 summer solstice, L_s 180° = northern autumnal equinox, and L_s 270° = northern winter
306 solstice.
- 307 • MY 1, L_s 0° started on April 11, 1955.

308 After a surface change has been clearly identified, science investigations of that present-day
309 activity generally aim to identify the driving environmental conditions and relevant processes.
310 With visible imagery, a temporal survey can be done over a sequence of overlapping images to
311 determine when the change occurs, or a spatial survey can be used to constrain where this
312 landform exists (as well as where it doesn't exist). With other observational datasets,
313 environmental information can be gathered—for example:

- 314 • spectral data can yield constraints for the surface composition;
- 315 • atmospheric observations and modeling can yield information about wind patterns and
316 surface pressure variations; and
- 317 • topographic data, measurements of shadows, or photogrammetry analysis can yield
318 estimates of heights and slopes.

319 Such environmental information can be gathered from orbit or in situ. Table 2 contains a listing
320 of the Mars rovers and landers often referenced in studies of present-day activity and
321 surface/atmosphere environmental conditions.

322

323 Table 1. Primary instruments used to acquire orbital visible imagery used in studies of present-day surface activity, in reverse
 324 chronological order of start of operations. To definitively measure a feature or surface change in an image, at least three pixels are
 325 generally needed. The date of last contact is used to denote the end of operations.

Instrument	Spacecraft	Period of Operation	Nadir Pixel Scale	Field of View	Global Coverage (as of July 2020)
Colour and Stereo Surface Imaging System (CaSSIS: <i>N. Thomas et al., 2017</i>)	ESA's ExoMars Trace Gas Orbiter (TGO)	2016-11-22 to present	~5 m/px	>8 km-wide swath in 3-colors or >6 km-wide swath in 4 colors; typical length of 50 km	Total area of images is 2.3%, but <1.6% after removing overlap
High Resolution Imaging Science Experiment (HiRISE: <i>McEwen et al., 2007</i>)	NASA's Mars Reconnaissance Orbiter (MRO)	2006-03-24 to present	~0.3 m/px for most images (from 300 km altitude)	6 km-wide swath in grayscale, with nested 1.2 km wide swath in 3-colors; typical length of 10 km	Total area of images is 3.6%, but <2.5% after removing overlap
Context (CTX) Camera (<i>Malin et al., 2007</i>)	(MRO)	2006-04-13 to present	~6 m/px (from 300 km altitude)	30 km-wide swath in grayscale; typical length of 90 km	~100%, and a global mosaic has been created (<i>Dickson et al., 2018</i>)
High Resolution Stereo Camera (HRSC: <i>Neukum et al., 2004a</i>)	ESA's Mars Express (MEx)	2004-01-14 to present	~10 m/px for nadir channel (from 250 km altitude)	53 km-wide swath in 4-colors with length at least 300 km for regular images	~75% with resolution 10-20 m/px; 100% with resolution >100 m/px (<i>Gwinner et al., 2019</i>)
Mars Orbital Camera (MOC: <i>Malin et al., 1992</i>)	NASA's Mars Global Surveyor (MGS)	1997-09-15 to 2006-11-02	1.4–12 m/px for narrow angle; 225–7500 m/px for wide angle (from 378 km altitude)	3 km-wide swath in grayscale for narrow angle; 115 km-wide swath in 2-colors for wide angle; typical length of 30 km	0.5% at better than 3 m/px; 5.45% at better than 12 m/px (<i>Malin et al., 2010</i>); 100% for wide angle

326

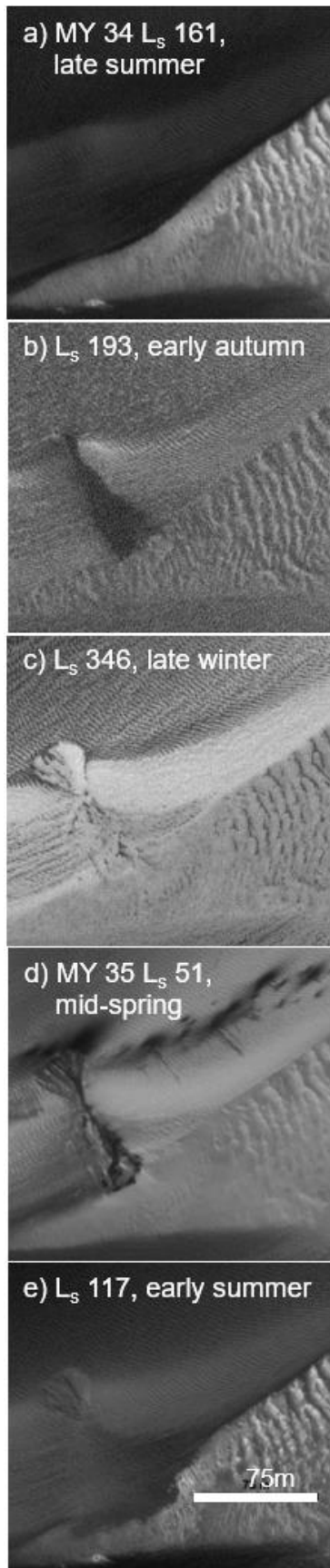


Figure 4. An example of how repeat imagery enables identification of activity, with timing constraints. In this chronological sequence of images, the polar dune slope (Tleilax dune field, 83.5°N, 118.5°E) becomes covered with frost and a new dune alcove forms (*b*) during L_s 161–193° (and likely during L_s 180–189°, intervening images are shown in SOM1). The alcove has formed by L_s 346° (*c*) and is clearly present under the seasonal frost layer. Sublimation begins in spring, with spots appearing preferentially along the dune brink and within the alcove and apron (*d*). Sublimation completes L_s 51–117°. HiRISE images are (*a*) ESP_054971_2635, (*b*) ESP_055683_2635, (*c*) ESP_058967_2635, (*d*) ESP_060734_2635, and (*e*) ESP_062633_2635. A scale bar is shown in the last image (75 m), but absolute distances are approximate as images are not orthorectified. North is up and illumination is from the left.

343 Table 2. Successful Mars rovers and landers are often referenced in studies of present-day
 344 activity and surface/atmosphere environmental conditions, as these provide critical in situ data.
 345 These are listed here, in reverse chronological order of start of operations. For missions that have
 346 ended, the date of last contact is given to denote the end of operations.

Mission/Spacecraft	Landing site	Period of Operation
NASA's <i>InSight</i> lander	4.5°N, 135.9°E Elysium Planitia	2018-11-26 to present
NASA's Mars Science Laboratory (MSL) rover, <i>Curiosity</i>	4.6°S, 137.4°E Gale crater	2012-08-06 to present
NASA's <i>Phoenix</i> lander	68.2°N, 234.3°E Vastitas Borealis	2008-05-05 to 2008-11-02
NASA's Mars Exploration Rover (MER)-B, <i>Opportunity</i>	1.9°S, 354.5°E Meridiani Planum	2004-01-25 to 2018-06-10
NASA's Mars Exploration Rover (MER)-A, <i>Spirit</i>	14.6°S, 175.5°E Gusev crater	2004-01-04 to 2010-03-22
NASA's Mars Pathfinder <i>Sojourner</i> rover	19.1°N, 326.7°E Ares Vallis	1997-07-04 to 1997-09-27
NASA's <i>Viking 2</i> lander	47.64°N, 134.3°E Utopia Planitia	1976-09-03 to 1980-04-12
NASA's <i>Viking 1</i> lander	22.27°N, 312.1°E Chryse Planitia	1976-07-20 to 1982-11-11

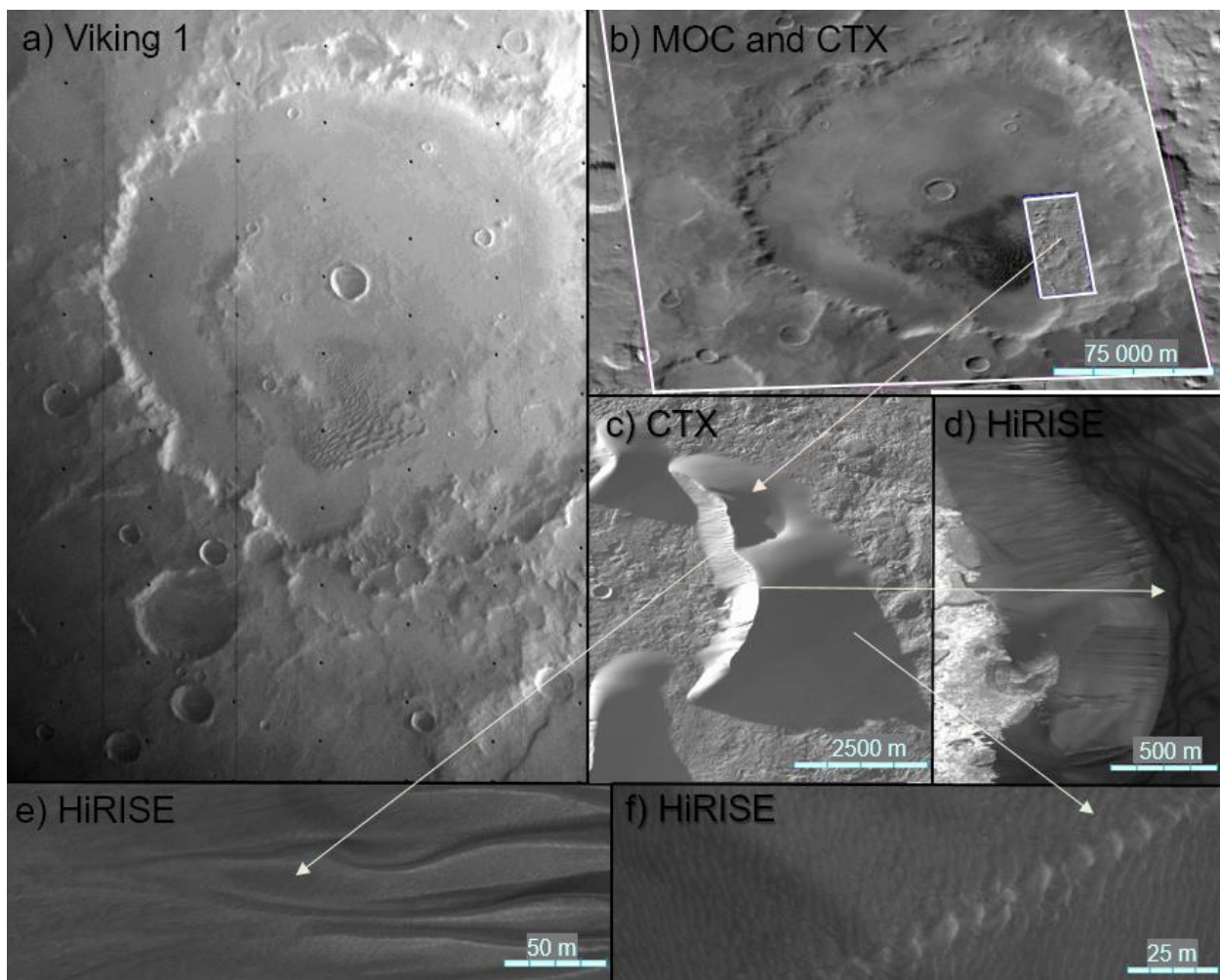
347
 348 **2 Wind-formed landforms**

349 Although the martian atmosphere is very thin compared to the Earth's (~0.1–1% surface
 350 pressure; e.g., *Banfield et al.*, 2020; *Harri et al.*, 2014; *Hess et al.*, 1976; *Taylor et al.*, 2010;
 351 *Withers and Smith*, 2006), wind-driven sediment transport has been observed (e.g., *Baker et al.*,
 352 2018a; 2018b; *Bridges et al.*, 2012a; 2012b; 2017) and aeolian bedforms analogous to terrestrial
 353 features have been found over all scales. These include decimeter- and decameter-scale
 354 windblown ripples (e.g., *Lapôtre et al.*, 2018; *Silvestro et al.*, 2010), migrating barchan dunes
 355 (e.g., *Chojnacki et al.*, 2015; 2018; 2019), and megadunes (e.g., Figure 5; *Silvestro et al.*, 2012).
 356 In many cases, higher-resolution images show that multiple scales of bedforms are superimposed
 357 over each other (Figures 5, 6), reflecting the dominant local wind conditions over different
 358 spatial and temporal scales and potentially different types of surface-atmosphere interaction
 359 dynamic regimes (e.g., see §2.2). Studies of these bedforms have yielded much insight into
 360 atmospheric characteristics, wind directions and speeds (and variability), surface grain
 361 characteristics and availability, and sediment fluxes (as summarized for a range of planetary
 362 bodies in *Diniaga et al.*, 2017). Environmental and geologic history, as inferred from these
 363 bedforms and the grains that compose them, are the focus of much of this section. Additionally,

364 we briefly describe some of the fundamental models used to relate atmospheric and grain
365 characteristics to sediment fluxes (§2.2).

366 Sediment flux rates can also be estimated based on the appearance of denuded surfaces and
367 degraded crater forms, where the amount of removed sediment and absolute age of the present
368 surface can be estimated (§2.2.3). Wind-driven erosion can also be inferred from features such as
369 yardangs and ventifacts which are common on the martian surface; however, rates of erosion or
370 sediment flux are difficult to estimate from studies of these features, so we do not discuss them
371 in this review.

372



373
374 Figure 5. Images of Kaiser crater (47.4°S, 18.8°E) and its dunes, acquired over the last 50 years.
375 (a) This Viking 1 image (094A42) was acquired 1976-09-22 (MY 12 L_s 126°) and has a
376 resolution of 259 m/px. The identification of a dune field in a nearby crater in a Mariner 9 image
377 was the first indication that sufficient sediment transport for bedform development was occurring
378 in the thin martian atmosphere (Sagan *et al.*, 1972 -- see Figure 11, image ID MTVS 4264:16).
379 However, >20 years later, the MOC camera on the Mars Global Surveyor orbiter reimaged

380 Kaiser crater (the large image in (b): MOC M0101026, was acquired MY 24 L_s 137° or 1999-05-
381 11). While some MOC images had resolution ~5 m/px, the image shown in (b) is of resolution
382 233 m/px – but in all cases, no signs of dune shape change or migration were identified. It wasn't
383 until MRO arrived that clear signs of present-day activity were identified: (b/c) this CTX image
384 (P21_009193_1329_XI_47S339W, acquired MY 29 L_s 97° or 2008-07-12) with resolution <4
385 m/px showed mass-wasting features in the barchan megadune. HiRISE images of that same dune
386 yielded clear information about surface activity, including: dust devil tracks (the dark curvy lines
387 along the upwind/right slope of the dune in (d)), large-scale mass-wasting in the dune gullies
388 along the southern side of the downwind slope of the dune in (d) (first reported in *Diniega et al.*,
389 2010), (e) small-scale downslope sediment avalanching is evident in surface roughness changes
390 over the ripple patterns, and (f) several scales of ripples migrating up the stoss dune slope. The
391 HiRISE image shown in (d-f) is ESP_058972_1330_RED (acquired 2019-02-24 or MY 34 L_s
392 346°, resolution 0.25 m/px). The arrows extending from (b) to (c) and from (c) to (d-f) are to
393 show the locations of the zoom-in views. The megadune that is the main landform within (c,d) is
394 ~750 m tall—the largest known barchan dune in the Solar System. In all images, north is up. In
395 the Viking image illumination is from the bottom right; in the MOC image illumination is from
396 the upper left; in the CTX and HiRISE images illumination is from the upper left. Contrast has
397 been tweaked to bring out details for each view.
398

399 **2.1 Depositional and Erosional Aeolian Landscapes: Materials and Landforms**

400 **2.1.1 Wind-transported sediment grain properties**

401 In situ observations of bedforms and transported grains by MER showed that a variety of
402 grain sizes, from dust (<62 µm diameter) to sand (up to 2 mm) to granules (> 2 mm) (*Greeley et al.*
403 *et al.*, 2006; *Sullivan et al.*, 2008), are transported via present-day aeolian processes. *Curiosity*
404 visited the Bagnold dune field and confirmed that martian dune sand was unimodally distributed
405 in the very-fine-to-fine sand range, with median grain size of 100–150 µm (*Ehlmann et al.*, 2017;
406 *Ewing et al.*, 2017; *Lapôtre et al.*, 2016; *Sullivan and Kok*, 2017; *Weitz et al.*, 2018). This
407 countered early hypotheses, based on coarse resolution (2–30 km/px) orbital thermal
408 measurements, that martian dune sand was composed of coarse sand grains with diameter ~500
409 µm (*Edgett and Christensen*, 1991; *Pelkey and Jakosky*, 2002); *Edwards et al.* (2018) suggested
410 that some of these previous estimates may have overestimated grain size due to subpixel mixing
411 of sandy and rocky materials. Much of the dune sands actively transported on Mars today are
412 likely to be similar in size to the grains found in the Bagnold dunes because this size is thought
413 to be most easily mobilized by winds (§2.2.1).

414 Coarser grains have been observed by *Curiosity* along the crest of large ripples along the
415 trailing edge of the Bagnold dune field (median ~ 350 µm; *Weitz et al.*, 2018), where coarse
416 grains are expected to concentrate based on analogy with terrestrial dune fields (*Ewing et al.*,
417 2017; *Lapôtre et al.*, 2016), as well as along the crests of isolated ripples (e.g., *Day and Kocurek*,

418 2016), in a sand shadow (*Minitti et al.*, 2013), and in ripple fields outside of the Bagnold dunes
419 (median ~300–500 μm with $<\sim 1\%$ grains >1 mm; *Weitz et al.*, 2018). Some of these coarser-
420 grained ripples were covered in dust (*Lapôtre et al.*, 2018; *Weitz et al.*, 2018), similar to
421 observations by the *Spirit* rover at El Dorado (*Sullivan et al.*, 2008). On bedrock surfaces,
422 coarser sediments (~1–3 mm) appear to be mobilized by aeolian processes (*Baker et al.*, 2018a).

423 Other observations of contiguous dune fields near their putative sand sources show
424 decreasing thermal inertia downwind, suggesting some grain size variability (*Chojnacki et al.*,
425 2014). Alternatively, in situ investigations have shown surface crusts composed of dust,
426 including on bedforms, that have been suggested to form from slow chemical weathering and/or
427 salt formation as duricrusts (*Ewing et al.*, 2017; *McSween et al.*, 2004; *Moore et al.*, 1999;
428 *Sullivan et al.*, 2008). This apparent induration of dusty bedform surfaces may play a role in the
429 occurrences of lithified dune fields found with largely intact morphologies (*Chojnacki et al.*,
430 2020; *Edgett and Malin*, 2000; *Milliken et al.*, 2014).

431 In situ observations of grains generally find them to be subangular with high circularity (e.g.,
432 *Ehlmann et al.*, 2017; *Weitz et al.*, 2018), which is consistent with the observed properties of
433 many smaller grains in desert aeolian systems on Earth (e.g., *Goudie and Watson*, 1981). Slip
434 faces of dunes and large ripples at Gale crater have Earth-like $\sim 30^\circ$ angle of repose, with a few
435 steeper outliers, possibly indicating local cohesion but otherwise largely loose sand (*Atwood-*
436 *Stone and McEwen*, 2013; *Ewing et al.*, 2017). Their results are consistent with MER in situ
437 observations of grains that suggest low-to-no cohesion in non-dusty aeolian materials (*Sullivan et*
438 *al.*, 2008).

439

440 **2.1.2 Wind-transported sediment composition**

441 One important control in aeolian processes is the source of wind-transported sediment
442 because the source region influences the availability of sediment and physical properties of the
443 grains. (Here we discuss primarily the ‘latest’ erosion-source of the sediment, which is not
444 necessarily the original source because grains presently eroding out of a crater or icy wall may be
445 exhumed from sedimentary deposits formed during past aeolian transport (e.g., *Chojnacki et al.*,
446 2014b; *Fenton*, 2005; *Tirsch et al.*, 2011).) In some areas the sources of sediment are easy to
447 identify in visible images, such as in the north polar erg where sand is clearly seen to be eroding
448 from within the north polar basal unit (*Byrne and Murray*, 2002; *Massé et al.*, 2012; *Tsoar et al.*,
449 1979; SOM 2). In other areas, it is likely that aeolian sands have been transported long distances

450 (up to hundreds of kilometers) and may then be mixed with several sources within sediment
451 “sinks,” such as topographic lows (*Dorn and Day, 2020*).

452 However, in most cases, visible imagery is insufficient to definitively locate sediment
453 sources for specific observed bedforms. In conjunction with visible imagery, orbital and in situ
454 compositional data can be used to attempt to constrain the source regions of saltating sand. Such
455 studies consistently find that martian dune sand is primarily basaltic (pyroxene-rich and olivine-
456 bearing sands), consistent with the bulk composition of the martian surface, with some broad
457 concentrations of gypsum and other sulfates primarily within the north polar erg (e.g., *Achilles et*
458 *al., 2017; Chojnacki et al., 2014b; Ehlmann et al., 2017; Fenton et al., 2019; Gendrin et al.,*
459 *2005; Johnson et al., 2017; 2018; Rampe et al., 2018; Rogers and Aharonson, 2008; Sullivan et*
460 *al., 2008*). This broad similarity in martian dune sand composition makes it difficult to link
461 aeolian sediments to their potential source, although a few studies have attempted to do this.
462 Based on orbital data, candidate sources for intracrater fields were identified in nearby mafic
463 layers outcropping in crater or valley walls (e.g., *Chojnacki et al., 2014b; Fenton, 2005; Lapôtre*
464 *et al., 2017; Stockstill-Cahill et al., 2008; Tirsch et al., 2011*) based on the presence of a few
465 minor phases. (Although, in the study by *Fenton (2005)*, the grain composition was also traced to
466 other, widespread rocky units in the region, suggesting that sand-bearing layers may have first
467 accumulated through region-wide deposition(s), with numerous local exposures being now
468 exhumed and recycled.) However, both orbital and in situ data have also shown compositional
469 variation within a dune field (e.g., *Chojnacki et al., 2014a; Lapôtre et al., 2017; Pan and Rogers,*
470 *2017; Seelos et al., 2014*), suggesting that winds may sort grains by mineralogy, potentially due
471 to correlations between grain composition and phenocryst size, grain density, and shape
472 (*Baratoux et al., 2011; Fedo et al., 2015; Lapôtre et al., 2017; Mangold et al., 2011*). For
473 example, observations from the *Spirit* rover found that mafic minerals were concentrated in the
474 coarse-grained targets in Gusev crater (e.g., *Morris et al., 2006; Ming et al., 2008; Sullivan et al.,*
475 *2008*), and observations from *Curiosity* found Mg, Fe, Ni, and Mn to be enriched in coarser
476 samples (*O’Connell-Cooper et al., 2017; 2018*) and more crystalline and amorphous ferric
477 materials in finer-grained targets (*Johnson et al., 2017; 2018*). Such sorting would affect bulk
478 mineral composition measurements and cause significant variation from that of the parent rock
479 after aeolian transport.

480 Grain composition can also yield information about the general history of sediment on a
481 planetary body and provide clues for a grain's original source region. For example, both orbital
482 and in situ measurements of the dune sand within Gale crater showed that a small (<10%)
483 fraction of sand was composed of X-ray amorphous materials, indicating the presence of
484 weathered silicates and nanophase Fe oxides and sulfates (*Achilles et al.*, 2017; *Ehlmann et al.*,
485 2017; *Lane and Christensen*, 2013; *Rampe et al.*, 2018). Such materials suggest the grains were
486 weathered through contact with water (*Ehlmann et al.*, 2017). However, without clear knowledge
487 of the source region of the grains, it is difficult to tie their history to the geologic history of a
488 specific site. Additionally, this amorphous component may come from martian dust, which is
489 well mixed globally, reflecting regular global circulation of fine particles (*Berger et al.*, 2015;
490 *Lasue et al.*, 2018). In situ measurements of martian airfall dust by multiple rovers have shown
491 that it is very consistent over the martian surface and is reflective of the global Mars soil unit and
492 its general basaltic crust, but is elevated in S and Cl relative to martian rocks and sand (*Berger et al.*
493 *et al.*, 2015; *Ehlmann et al.*, 2017; *Lasue et al.*, 2018; *Yen et al.*, 2005).

494 495 **2.1.3 Bedforms: Types and Morphologies**

496 From orbiter images, aeolian bedforms of meter-wavelength ripples (i.e., just visible at the
497 highest image resolution: Table 1) to kilometers-scale megadunes have been mapped and
498 measured around the globe (e.g., *Bridges et al.*, 2007; *Brothers and Kocurek*, 2018; *Hayward et al.*
499 *et al.*, 2007; 2014). Rovers have driven through a few centimeters-high to meter-high ripples (e.g.,
500 *Curiosity* drove through Dingo gap (*Arvidson et al.*, 2017)) and around the meters-high dunes in
501 Bagnold dune field (*Bridges and Ehlmann*, 2017; *Lapôtre and Rampe*, 2018). In this section, and
502 again when discussing bedform migration (§2.2.2), we discuss five classes of bedforms (their
503 names are underlined) because these are presently proposed to reflect different regimes of
504 aeolian bedform dynamics; however, questions remain about how distinct these bedforms may
505 be.

506 Sand ripples with decimeter wavelength have been observed by all Mars rovers (Table 2), but
507 are below the image resolution limit of orbital data. (Larger ripples observed by these rovers
508 were recognizable in orbital images, see below.) The *Spirit* rover observed dark decimeter-scale
509 ripples within the El Dorado ripple field (*Sullivan et al.*, 2008), which were some of the first
510 documented to migrate (*Sullivan et al.*, 2008), demonstrating that these were active aeolian
511 bedforms (discussed further in §2.2.2). Within Gale crater, similar ripples with wavelengths of

512 ~5–12 cm, straight crests, and subdued sub-centimeter topography were observed in fine sand
513 (*Ewing et al.*, 2017; *Lapôtre et al.*, 2016; 2018). On Earth, ripples of similar size and
514 morphology (i.e., with straight crests and relatively subdued profiles) are called impact ripples
515 and are created through grain splash (*Bagnold*, 1941; *Rubin*, 2012; *Sharp*, 1963; *Werner et al.*,
516 1986; *Wilson*, 1972). By analogy, decimeter-scale ripples on Mars have been interpreted as
517 impact ripples—an interpretation also consistent with numerical (*Yizhaq et al.*, 2014) and
518 theoretical modeling (*Andreotti et al.*, 2006; *Duran Vinent et al.*, 2019), predicting impact ripples
519 should have decimeter-scale wavelengths on Mars.

520 Larger (i.e., meter- to decameter-wavelength) ripples were originally grouped together within
521 the polygenetic class of “mega-ripples,” similar to how aeolian ripples on Earth were originally
522 designated by scale and grain size population as smaller unimodal impact ripples and larger
523 bimodal “mega-ripples” (*Bagnold*, 1941; *Sharp*, 1963). However, the martian megaripple class
524 has since been divided into three groups based on observed activity, morphology, albedo, and
525 consistency of grain size within the features. Dark meter-scale ripples are visible in orbital
526 imagery of dune fields and sand sheets, which shows them to be ubiquitous and to migrate over
527 seasonal timescales (§2.2.2) (*Bridges et al.*, 2012a; SOM 3). In addition to being larger than
528 martian impact ripples, these features differ in morphology. For example, their crestline
529 geometry and orientation is highly variable, with dark meter-scale ripples on the gentle stoss of
530 dunes tending to be transverse-to-oblique and highly sinuous, whereas those on steeper slopes
531 have straight linear crests (*Ewing et al.*, 2017; *Lapôtre et al.*, 2016; 2018). Their downwind
532 profiles also vary, from transverse large ripples with asymmetric profiles, gentle stoss slopes, and
533 near-angle of repose lee faces (*Ewing et al.*, 2017; *Lapôtre et al.*, 2016; 2018; *Sullivan et al.*,
534 2008) to longitudinal large ripples with symmetric profiles (*Lapôtre et al.*, 2018). Furthermore,
535 grainfall and grainflow deposits are observed on the lee of transverse large ripples (*Ewing et al.*,
536 2017; *Lapôtre et al.*, 2016; 2018), and decimeter-scale impact ripples form concurrently and
537 migrate on the stoss of large ripples (*Ewing et al.*, 2017; *Lapôtre et al.*, 2016; 2018; *Sullivan et*
538 *al.*, 2008). These bedform wavelengths were found to correlate negatively with elevation on the
539 planet (*Lapôtre et al.*, 2016; *Lorenz et al.*, 2014) (discussed again in §7.3).

540 Two additional classes of meter-scale (and larger) ripples are observed on Mars with coarser
541 grains inferred to occur along the crest and limited observed activity: coarse-grained ripples and
542 transverse aeolian ridges. As with terrestrial mega-ripples, the coarser fraction along the crest has

543 implications for both the morphology and activity of these bedforms. As coarser elements
544 accumulate near the crests, mega-ripple dimensions (spacing and heights) gradually increase
545 (*Andreotti et al.*, 2002). Mega-ripples on Earth migrate and respond to changes in winds
546 relatively slowly as typical wind stresses are below the threshold to initiate and sustain surface
547 creep of coarser sand (*Bagnold*, 1941; *Lämmel et al.*, 2018). Critically, mega-ripples may need
548 ample saltating sand driven by a formative, preferentially uni-directional wind regime to migrate
549 (e.g., during infrequent storms).

550 Meter-scale, bimodal coarse-grained ripples (descriptive term employed here without
551 implication of specific modes of transport) were identified during MER traverses at Gusev crater
552 (*Sullivan et al.*, 2008) and Meridiani Planum (*Jerolmack et al.*, 2006; *Sullivan et al.*, 2005). For
553 example, with the active decimeter ripples, ~3 m wavelength and ~30 cm tall dark ripples were
554 observed in the El Dorado ripple field. This location contained both fine- and coarse-grained
555 ripples, and both appeared to be static based on the grain size distribution and lack of sediment
556 mobility, except for dust removal (*Sullivan et al.*, 2008). Coarse-grained ripples have also been
557 observed by the *Curiosity* rover in Gale crater along the trailing edge of Bagnold dune field and
558 outside of the active dune field in isolated sand sheets (Figure 6), with variable crest grain sizes
559 and amount of dust cover (*Lapôtre et al.*, 2018; *Weitz et al.*, 2018). More recently martian
560 “mega-ripples” were interpreted using orbital data due to their greater dimensions (5–20 m
561 spacing, ~1–5 m tall) and brighter crests than typical dark decameter ripples, where the latter was
562 inferred as a coarser grain size component (*Silvestro et al.*, 2020). These intermediate-scale
563 bedforms are typically trailing the stoss side of or flanking dunes, dominantly transverse in
564 morphology, and some were recently reported to be migrating (*Chojnacki et al.*, 2019; *Silvestro*
565 *et al.*, 2020; SOM 4).

566 Larger, martian bedforms (10–200 m wavelength, 1–14 m tall) termed transverse aeolian
567 ridges (TARs) were first noted and debated following their discovery in early high-resolution
568 image data (*Bourke et al.*, 2003). TARs tend to have longer, more widely distributed
569 wavelengths and are brighter than the large ripples (*Lapôtre et al.*, 2016), and tend to have more
570 symmetric profiles than most bedforms (*Zimelman*, 2010). These enigmatic bedforms are
571 concentrated in the martian tropics, appearing in isolated or expansive fields across plains, within
572 craters or canyons, or in association with large dark dunes (*Balme et al.*, 2008; *Berman et al.*,
573 2011; 2018; *Bourke et al.*, 2003; *Geissler*, 2014; *Geissler and Wilgus*, 2017; *Hugenholtz et al.*,

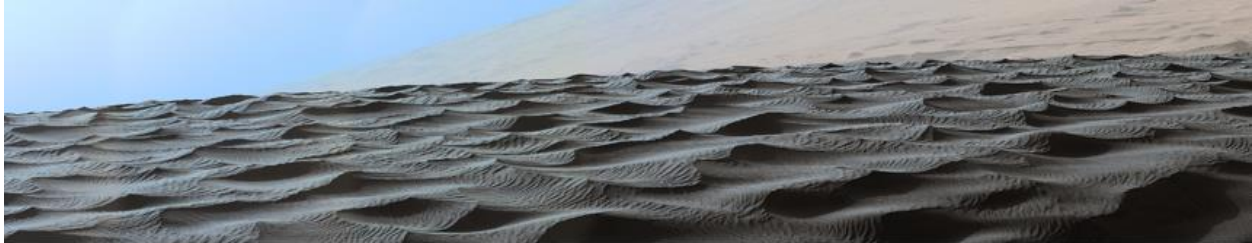
574 2017; *Wilson and Zimbelman, 2004; Zimbelman, 2010; 2019*). TARs are generally thought to
575 form from surface creep of coarse-grained particles (e.g., *Bourke et al., 2003; Hugenholtz et al.,*
576 *2017; Zimbelman, 2010*) or the deposition, induration, and erosion of dominantly dust-sized
577 particles (*Geissler, 2014*). Although initially without a good terrestrial analog, moderate-scale
578 aeolian bedforms (2–250 m wavelength, 1–4 m tall) were recently identified in deserts of Iran
579 and Libya (*Foroutan and Zimbelman, 2016; Foroutan et al., 2019*). It was also recently proposed
580 that *Curiosity* traversed a TAR in Gale crater (*Zimbelman and Foroutan, 2020*).

581 As on the Earth, the largest aeolian bedform class are sand dunes. These features were seen
582 in some of the earliest imagery (*Greeley et al., 1992; Masursky, 1973; Sagan et al., 1972; 1973*)
583 and have been mapped globally (*Hayward et al., 2007; 2010; 2012; 2014; Fenton, 2020*). The
584 most extensive coverage of dune sand occurs within the northern circum-polar basins as nearly
585 continuous sand seas (e.g., Olympia Undae) (*Hayward et al., 2014; Lancaster and Greeley,*
586 *1990*). Impact craters are the most wide-spread locale for dune fields because these serve as a
587 natural sediment sink (*Dorn and Day, 2020; Greeley et al., 1992; Hayward et al., 2007; 2014;*
588 *Roback et al., 2020*). Other common settings for dune fields are topographic depressions such as
589 troughs, valleys, and chaotic terrain, including the great structural rift system of Valles Marineris
590 (*Chojnacki et al., 2014a*). Less commonly, extra-crater plains may host dispersed clusters of
591 dunes (*Chojnacki et al., 2018; Fenton, 2005; Hayward et al., 2007*).

592 Specific dune morphologies could be properly classified following the advent of high-
593 resolution image data (*Malin et al., 1992; 2007; McEwen et al., 2007*) and are sorted using
594 classic terrestrial classifications as defined by *McKee (1979)* (SOM 5). The vast majority of
595 martian dune morphologies occur as crescent-shaped dunes (i.e., barchan, barchanoid) where
596 horns overall point in the downwind direction (e.g., Figures 4, 5), although the occurrence of
597 asymmetric barchans and linear dunes growing through a fingering instability (*Courrech du Pont*
598 *et al., 2014*) has been recognized on Mars (e.g., *Ewing et al., 2017; Silvestro et al., 2016*). Other
599 not-uncommon dune types include linear, transverse (e.g., Figure 1), star, sand sheet, and dome
600 dunes (*Davis et al., 2020; Fenton et al., 2013; Hayward et al., 2007*). Overlapping dunes
601 (compound) and/or combinations of dune morphologies (complex) are also very commonly
602 observed in large dune fields or ergs (*Brothers and Kocurek, 2018; Chojnacki et al., 2014a;*
603 *Fenton et al., 2013*). Less common classes of topographically related dunes may be found on
604 crater or canyon walls as falling or climbing dunes (*Bourke et al., 2004; Chojnacki et al., 2010*).

605 Additional occurrences of dunes possessing unusual morphologies that were not readily
606 classified using terrestrial types were also found (*Hayward et al.*, 2007). For example, “bullseye”
607 dune fields, based on their concentric ring patterns, only occur in high-southern latitude craters
608 and are unreported on Earth (*Fenton and Hayward*, 2010; *Hayward et al.*, 2014). More broadly,
609 sand dune morphology of the high southern latitudes (poleward of 50°S) show well-rounded
610 crests and lee-sides below the angle of repose, likely due to limited aeolian activity and the
611 prominence of ground ice (*Banks et al.*, 2018; *Fenton and Hayward*, 2010). Ultimately, these
612 different dune morphologies form in response to the numerous extraneous environmental factors
613 of Mars (e.g., wind direction and variability, transport capacity, sand supply, topography,
614 seasonal frost/ice) (e.g., *Courrech du Pont et al.*, 2014; *Ewing and Kocurek*, 2010; *Gao et al.*,
615 2015; *Kocurek and Lancaster*, 1999, *Rubin and Hunter*, 1987). The only ground observations of
616 martian dunes to-date come from *Curiosity*’s investigation of the Bagnold dune field, where
617 barchans migrate along the field’s trailing edge, transitioning into barchanoidal ridges and into
618 linear oblique dunes further south towards Aeolis Mons (informally known as Mount Sharp)
619 (*Bridges and Ehlmann*, 2017; *Lapôtre and Rampe*, 2018).

620



621
622 [Figure 6. MSL Mastcam image showing two sizes of ripples over the stoss slope of Namib dune,](#)
623 [Bagnold dune field. The large ripples have ~2-m wavelength, and the smaller ones have ~10-cm](#)
624 [wavelength. Image is NASA photojournal PIA20755, acquired 2015-12-13 on *Curiosity*’s 1192nd](#)
625 [sol.](#)

626

627 **2.2 Aeolian Transport, Fluxes, and Erosion Rates**

628 Knowledge of the minimum wind speed capable of inducing aeolian transport is central in
629 predicting bedform migration rates, resurfacing rates, and dust emissions in ancient and
630 contemporary martian climates (e.g., *Bagnold*, 1941; *Greeley and Iversen*, 1985; *Kok et al.*,
631 2012; *Sullivan and Kok*, 2017). Winds below the threshold, or minimum wind speed for motion,
632 are not sufficient to mobilize material; thus, determining the minimum wind speed required to
633 initiate motion on the surface of Mars can unlock clues regarding Mars’ past climate and weather
634 phenomena. For example, aeolian sedimentary strata reveal the sizes of grains transported under

635 past climates and directional changes in transport. Such strata are found throughout Mars’
636 landscape giving us hard evidence for how the wind has interacted with the surface, especially
637 when having speeds greater or equal to the threshold for grain motion (e.g., *Banham et al.*, 2018;
638 *Chojnacki et al.*, 2020; *Day et al.*, 2019; *Grotzinger et al.*, 2005; *Milliken et al.*, 2014). By
639 understanding how the threshold of wind-driven grain motion has changed over time as the
640 climate shifted, we can begin mapping aeolian processes throughout Mars’ history using the
641 process-based evidence solidified in martian sedimentary strata. We can also use these thresholds
642 to predict contemporary activity on Mars—in particular to forecast surface dust emission rates,
643 which is critical for landed robotic and human exploration.

644 **2.2.1 Thresholds of motion and transport hysteresis**

645 The fluid threshold for wind-blown sand is the minimum shear velocity required to initiate
646 grain movement by the force of the wind alone and was developed to predict dust emission and
647 landform change in sandy environments on Earth (*Bagnold*, 1936; 1937). The Shields-type
648 function is central to most modern threshold equations for Mars and uses shear velocity, a height
649 independent variable that represents the momentum transfer from the boundary layer to the
650 surface, $u_* = \sqrt{\frac{\tau}{\rho}}$ (in m/s; where τ is stress in Pa, ρ is density in kg/m³), to predict the onset of
651 motion:

$$652 \quad u_{*t} = A \sqrt{\left(\frac{\rho_s - \rho}{\rho}\right) g d} \quad (\text{Eqn 1})$$

653 where u_{*t} is the threshold shear velocity (m/s), ρ_s and ρ are sediment and fluid densities (kg/m³),
654 g is gravitational acceleration (m/s²), d is grain size (m), and A is an empirically derived
655 constant (equal to square root of the Shields criterion) that includes a dependence on particle
656 Reynolds number at threshold conditions, $Re_{pt} = \frac{u_* d}{\nu}$, where $\nu = \frac{\mu}{\rho}$ is the kinematic viscosity of
657 the winds (m²/s), with μ as their dynamic viscosity (Pa·s). The first threshold models for Mars
658 resolved estimates of the A parameter based on wind tunnel experiments in the Planetary Aeolian
659 Laboratory’s MARTIAN SURFACE WIND TUNNEL (MARSWIT) at NASA’s Ames Research Center
660 (*Greeley et al.*, 1976; 1980; *Iversen and White*, 1982): the threshold was reached when
661 “...saltation (along the entire wind tunnel) test bed was initiated (following *Bagnold* (1941))”
662 (*Greeley et al.*, 1976, p. 418). Observations of u_{*t} were used to back out detailed models for
663 estimating the A parameter using Re_{pt} , resulting in three conditional models:
664

665
$$A = 0.2 \sqrt{\frac{\left(1 + \frac{0.006}{\rho_s g d^{2.5}}\right)}{1 + 2.5 Re_{pt}}} \text{ for } 0.03 \leq Re_{pt} \leq 0.3 \quad (\text{Eqn 2})$$

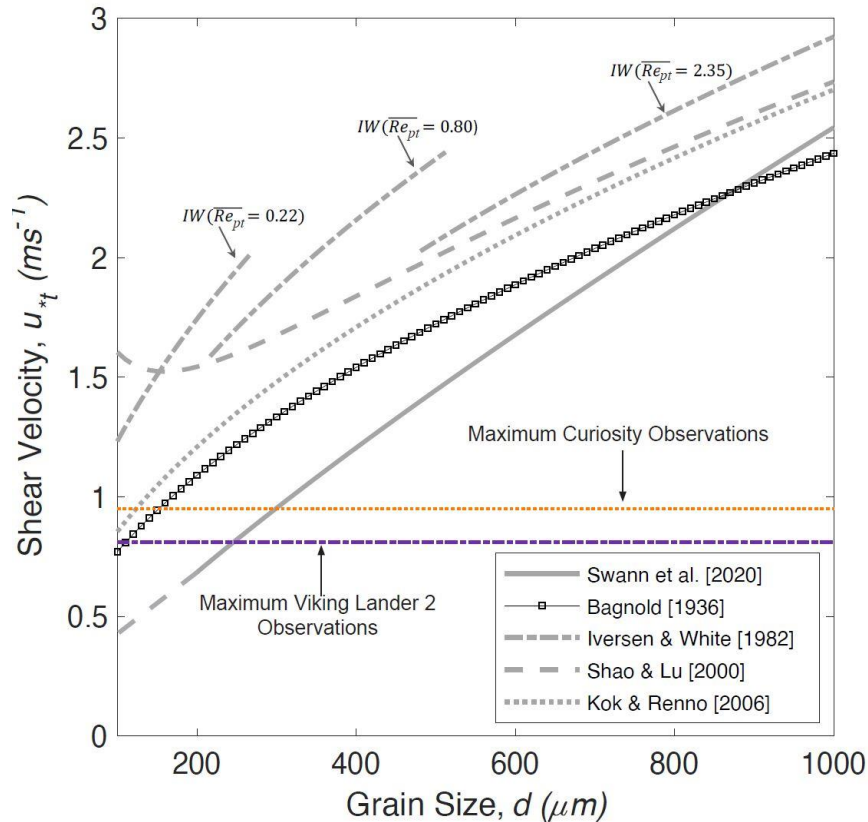
666
$$A = 0.129 \sqrt{\frac{\left(1 + \frac{0.006}{\rho_s g d^{2.5}}\right)}{1.928 Re_{pt}^{0.092} - 1}} \text{ for } 0.3 \leq Re_{pt} \leq 10 \quad (\text{Eqn 3})$$

667
$$A = 0.120 \sqrt{\left(1 + \frac{0.006}{\rho_s g d^{2.5}}\right)} \{1 - 0.0858 \exp[-0.0671(Re_{pt} - 10)]\} \text{ for } Re_{pt} \geq$$

 668 10 (Eqn 4).

669 These original models predicted the minimum shear velocity required to mobilize sand as well as
 670 the optimum grain size for windblown transport over a range of atmospheric densities (Figure 7).
 671 Yet, these equations predict threshold winds speeds higher than those modelled or measured at
 672 the surface of on Mars (e.g., *Gomez-Elvira et al.*, 2014; *Lorenz*, 1996; *Newman et al.*, 2017) and
 673 leading to a discrepancy between lower than threshold martian wind speeds and active sediment
 674 transport observed from orbital imagery and landers on Mars.

675



676
 677 Figure 7. Plot showing different Martian threshold models for sediment transport, along with
 678 estimated shear velocities from *Curiosity* and Viking Lander 2. ‘IW’ refers to the Iversen and
 679 White (1982) model, estimated using specified values of Re_{pt} .
 680

681 Two reasons for this discrepancy are (1) the experimental criterion used to define the
 682 threshold and (2) the absence of a complete dimensional transformation of their empirical data
 683 (Swann *et al.*, 2020). Defining the threshold as the onset of continuous motion over the test bed,
 684 a common practice on Earth, disregards intermittent sporadic motion that occurs at slower shear
 685 velocities. In particular, this definition disregards the ability for a small burst of sand grains to
 686 induce equilibrium transport downwind through impact cascades (Bauer *et al.*, 2009; Sullivan
 687 and Kok, 2017). Through a set of numerical experiments, Sullivan and Kok (2017) determined
 688 that, on Mars, cascading saltation can lead to continuous saltation but over distances much longer
 689 than available in laboratories. This finding is highly significant for martian aeolian processes.
 690 High-frequency turbulent fluctuations that momentarily exceed the threshold for motion can
 691 induce transport of a small patch of grains that, downwind, can become equilibrium transport.
 692 The concept is hinged on a lower, impact threshold, u_{*it} . The impact threshold occurs at slower
 693 shear velocities because the momentum transferred to particles at rest is a function of the wind
 694 and the impact of saltating grains. Thus, the momentum from the wind does not need to be as

695 great in order to sustain motion because the impact of saltating grains dislodges particles at rest.
696 On Earth, the impact threshold is approximately 80% of the fluid threshold, but on Mars it is
697 predicted to be as low as 10–20% of the fluid threshold due to the much lower atmospheric
698 density (*Kok, 2010*). Thus, once particles are mobilized, wind speed has to drop significantly in
699 order for particle motion to cease.

700 In light of these findings, new experimental observations were recently conducted in the
701 MARSWIT to resolve the threshold at the onset of cascading saltation of sand-sized particles
702 (*Burr et al., 2020: 150–1000 μm; Swann et al., 2020: 200–800 μm*). Incrementally increasing the
703 speed over a bed of particles at rest, these studies dimensionally transformed wind tunnel
704 observations from a set of vertically stacked pitot tubes to calculate shear velocities
705 corresponding to discontinuous, sporadic motion; here, we report primarily on the results from
706 *Swann et al. (2020)*. These shear velocities were used to resolve Bagnold’s *A* parameter for
707 cascading motion from Equation (1):

$$708 \quad A_{Fluid} = 0.0502 D_*^{0.3157} \quad (\text{Eqn 5})$$

$$709 \quad A_{General} = 0.0646 D_*^{0.2426} \quad (\text{Eqn 6})$$

710 where

$$711 \quad D_* = d \left(\frac{\rho(\rho_s - \rho)}{\mu^2} \right)^{\frac{1}{3}} \quad (\text{Eqn 7}).$$

712 The new model predicts threshold shear velocities that are slower than previous models by a
713 factor of 1.6 to 2.5. In their model, for a surface with an average grain size of 200 μm, the
714 minimum shear velocity required to initiate cascading motion ranges from 0.63 to 0.81 m/s at
715 atmospheric densities between 0.013 to 0.025 kg/m³, reconciling theory with measured wind
716 speeds (Figure 7). However, their model is only valid for particles ranging from 200 to 800 μm,
717 excluding values for finer particles where interparticle cohesion increases the threshold for
718 motion (*Bagnold, 1937; Iversen and White, 1982; Shao and Lu, 2000*). The transition from
719 cohesion-dominated to gravity-dominated threshold is represented by a marked upturn, or
720 inflection, in threshold curves where forces required to initiate motion increase due to an
721 increase in interparticle attractive forces between finer particles (Figure 7). Predicting the
722 inflection point in the threshold curve determines the optimum grain size (i.e. the easiest particles
723 to move by the force of the wind) and represents the most commonly mobilized particles. Early
724 workers estimated that this inflection point should lie between 100 and 200 μm (*Bagnold, 1937;*

725 *Iversen and White, 1982; Shao and Lu, 2000*); this prediction is consistent with *Curiosity's*
726 observations of well sorted, unimodally distributed 100–150 μm sand in the active Bagnold dune
727 field (e.g., *Weitz et al., 2020*).

728

729 **2.2.2 Bedform migration and evolution**

730 Bedforms, from small impact ripples up through mature dunes, have been observed to
731 migrate in a range of locations on Mars. These migration rates and the scale of the bedforms
732 indicate variable sediment flux rates, which are typically an order of magnitude lower than
733 terrestrial rates (*Bridges et al., 2012b; Chojnacki et al., 2019*).

734 Small ripples with decimeter wavelength have been observed to migrate short distances over
735 a few sols around Mars rovers during windy seasons (i.e., southern summer (*Ayoub et al., 2014;*
736 *Baker et al., 2018b*)). For example, poorly sorted <300- μm sand at El Dorado were observed to
737 migrate about 2 cm over 5 sols (*Sullivan et al., 2008*), and small ripples in fine sand were
738 observed to migrate by up to 2.8 cm/sol in sand patches at Gale crater (*Baker et al., 2018b*).
739 Assuming activity during half of the martian year, extrapolated migration rates range from 10 cm
740 to 10 m per martian year (*Baker et al., 2018b*).

741 Migration of dark meter-scale ripples, ubiquitous in association with dark dunes (*Bridges et*
742 *al., 2007*), has been observed in high-resolution repeat orbital images (e.g., SOM 3). In these
743 images, ripple displacements can be measured manually or in aggregate for larger areas using the
744 Co-registration of Optically Sensed Images and Correlation (COSI-Corr) methodology (*Bridges*
745 *et al., 2013; Leprince et al., 2007*). The first unambiguous meter-scale modification of ripples
746 and dune edges was documented in Nili Patera (*Silvestro et al., 2010*), where superposed
747 decimeter-tall ripples (*Ewing et al., 2017; Lapôtre et al., 2018*) may migrate up to several meters
748 per year, but average ~ 0.5 m/yr from larger sampling (*Ayoub et al., 2014; Bridges et al., 2012a;*
749 *Chojnacki et al., 2018; Preston and Chojnacki, 2019; Runyon et al., 2017; Silvestro et al., 2013*).
750 Ripples are swiftest mid-way up a dune's stoss slope through the dune crest: ~ 5 x faster than
751 ripples at the base of the stoss or in the lee or flanks areas (*Bridges et al., 2012a; Preston and*
752 *Chojnacki, 2019; Roback et al., 2019; Runyon et al., 2017*). In general a linear relationship
753 between ripple migration rate and ripple elevation on the dune has been demonstrated (*Bridges et*
754 *al., 2012a; Runyon et al., 2017*), likely due to streamline compression from dune topography as
755 winds are pushed upslope. Isolated ripple patches not associated with a dune field have the
756 lowest migration rates; such rates are detected using image pairs spanning two or more martian

757 years. These measurements reflect sand flux rates between $0.1\text{--}2.3\text{ m}^3\text{ m}^{-1}\text{ yr}^{-1}$, which are
758 typically several factors less than the saltation rate suggested by the migration rate of
759 neighboring dunes (Ayoub *et al.*, 2014; Bridges *et al.*, 2012b; Roback *et al.*, 2019; Runyon *et al.*,
760 2017; Silvestro *et al.*, 2013). Saltation rates also appear higher during the northern hemisphere
761 autumn/winter, which is also when driving winds are likely greatest (Ayoub *et al.*, 2014; Roback
762 *et al.*, 2019).

763 The first clear observation of bedform change from orbital data was the gradual
764 disappearance of two small ($\sim 1000\text{ m}^2$) north polar dome dunes and $\sim 85\%$ deflation of a third
765 over a five-year time span (1999–2004) in MOC images (Bourke *et al.*, 2008). Since then,
766 several studies have used various combinations of HiRISE pairs and topography to estimate
767 migration rates and sand fluxes for dunes (Ayoub *et al.*, 2014; Bridges *et al.*, 2012a; 2012b;
768 Cardinale *et al.*, 2020; Chojnacki *et al.*, 2015; 2017; 2018; Hansen *et al.*, 2011; Runyon *et al.*,
769 2017; Silvestro *et al.*, 2013; Figure 8; SOM 2–4, 6). Reported average migration rates are
770 consistently $\sim 0.5\text{ m/yr}$ ($\pm 0.4\text{ m/yr}$, 1σ) for dunes that are $\sim 2\text{--}120\text{-m}$ tall (average height 19 ± 14
771 m) (Chojnacki *et al.*, 2019). These reported rates are typically for barchan or barchanoid dune
772 morphologies in uni-directional wind regimes (e.g., SOM 6), but include some instances of
773 linear, dome, and falling dunes. Average crest flux measurements for dune fields ranged between
774 $1\text{--}18\text{ m}^3\text{ m}^{-1}\text{ yr}^{-1}$ (average across $q_{\text{crest}} = 7.8\pm 6.4$ (1σ) $\text{m}^3\text{ m}^{-1}\text{ yr}^{-1}$), where the maximum flux for an
775 individual dune was $35\text{ m}^3\text{ m}^{-1}\text{ yr}^{-1}$ (Chojnacki *et al.*, 2019). These rates and fluxes are relatively
776 variable in terms of geography and timing. For example, the highest sand fluxes documented to
777 date appear to concentrate in three regions: Syrtis Major, Hellespontus Montes, and the north
778 polar erg (Chojnacki *et al.*, 2019). Poleward of 45° S , dunes sites show limited bedform
779 mobility, and southward of 57° S only ripple migration has been detected (i.e., no bulk dune
780 movement) (Banks *et al.*, 2018). Dunes surrounding the north polar layered deposits and residual
781 cap display the greatest migration rates and fluxes: $\sim 50\%$ greater than on average for Mars (11.4
782 vs. $7.8\text{ m}^3\text{ m}^{-1}\text{ yr}^{-1}$) (Chojnacki *et al.*, 2019). These higher values are found in the polar regions
783 despite the limited sediment state caused by autumn/winter $\text{CO}_2/\text{H}_2\text{O}$ ice accumulation that
784 reduces surface interactions with the wind (Diniaga *et al.*, 2019a; Hansen *et al.*, 2011; 2015).

785

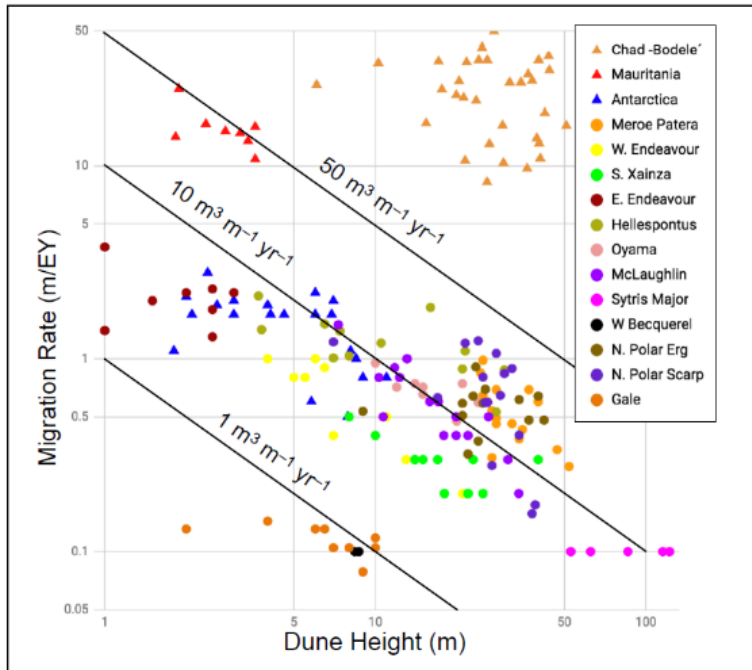


Figure 8. Log-log plot of dune migration rates vs. dune heights for select martian and terrestrial dune fields. Dune rates are averages per site using the longest-baseline HiRISE orthoimages available. Migration rate confidence intervals are typically ± 0.1 – 0.3 m/yr and account for orthoimage registration offsets and human error in manual measurements. The "terrestrial" estimates are from dune field data collected in Chad, Mauritania, and Antarctica (Bourke *et al.*, 2009; Ould Ahmedou *et al.*, 2007; Vermeesch and Drake, 2008). Mars dune flux estimates are from earlier work by Chojnacki *et al.* (2017; 2018; 2019).

805 Aside from many ripples within the southern dune fields, many smaller martian bedforms
 806 show no sign of present-day migration; such features may also have superposed craters, debris,
 807 and fracturing that indicate a long-term lack of migration and renewal. In particular, with a few
 808 newly identified exceptions (Silvestro *et al.*, 2020), TARs appear to be inactive based on
 809 morphology and context (Berman *et al.*, 2018). For example, crater age dating indicates certain
 810 TAR fields in Schiaparelli crater have been inactive for the last ~ 100 kyr to ~ 2 Myr, suggesting
 811 that they are relict deposits (Berman *et al.*, 2018). Numerous authors investigating dark ripples or
 812 dunes via comparison of HiRISE image pairs have reported on the lack of apparent motion for
 813 nearby TARs. However, efforts just may not have used sufficiently long temporal baselines; for
 814 example, these investigations typically used images spanning 2–3 martian years for a survey of
 815 low sand flux regions (e.g., Valles Marineris, Meridiani) or dune migration (Banks *et al.*, 2015;
 816 Berman *et al.*, 2018; Bridges *et al.*, 2012a; Chojnacki *et al.*, 2014a; 2017; Geissler *et al.*, 2012).
 817 Using longer baseline images (>4 martian years) and targeting known high flux dunes within
 818 McLaughlin crater, several bright-toned TAR-like bedforms showed unambiguous crest
 819 displacements (Silvestro *et al.*, 2020). It may be that certain TAR populations within high flux
 820 sand corridors are subjected to enough repeated saltation to dislodge their presumably coarser-
 821 grained crest areas. Preliminary results suggest mega-ripple and TARs that are migrating today

822 are doing so with rates and fluxes an order of magnitude lower than those estimated for adjacent
823 sand dunes (*Silvestro et al.*, 2020; SOM 4).

824 825 **2.2.3 Erosion Rates**

826 We focus here on bulk surface erosion rates that are likely to be primarily driven by aeolian
827 erosion (versus mass wasting, which is discussed in §3, 5), predominantly via sand abrasion
828 (*Laity and Bridges*, 2009). Bulk surface erosion rates have generally been estimated based on the
829 existence, age, and geomorphology of various crater populations along with geologic setting. For
830 example, locations in Gusev crater showed in situ and orbital estimates of 10^{-3} – 10^{-5} m/Myr (note
831 that m/Myr is equivalent to $\mu\text{m/yr}$) (*Golombek et al.*, 2006) and rates of 10^{-2} – 10^{-3} m/Myr were
832 estimated for Elysium Planitia based on crater depth degradation and rim erosion (*Sweeney et al.*,
833 2018). Based on deviations in small-crater counts from expected isochrones, the crater
834 obliteration rate for light-toned sedimentary rocks suggests an average erosion rate of 10^{-1}
835 m/Myr (*Kite and Mayer*, 2017). Younger terrain in Meridiani Planum yielded higher rates 1–10
836 m/Myr (*Golombek et al.*, 2014), which may be more similar to wind-driven scarp retreat in Gale
837 crater, as suggested by radiogenic and cosmogenic dating of exposed sediments within Aeolis
838 Mons (*Farley et al.*, 2014). (As noted in those studies, terrestrial continental denudation rates for
839 arid regions are still a few (2–5) orders of magnitude higher.)

840 To quantitatively connect surface abrasion rates to aeolian sand flux rates, the total sand flux
841 (i.e., saltation plus reptation) is needed. This can be estimated from the dune crest fluxes and
842 making some assumptions about the mass loss from impacting sand on the target material. For
843 basalt sand grains hitting basaltic rocks at the impact threshold for Mars, this value of abrasion
844 susceptibility is $\sim 2 \times 10^{-6}$, based on laboratory measurements (*Greeley et al.*, 1982) and
845 accounting for the energetics of martian saltation and reptation (*Bridges et al.*, 2012b). Taking
846 the estimated saltation and reptation trajectories for Mars of 0.1–0.5 m (*Kok*, 2010) and interdune
847 sand fluxes, abrasion rates for a range of sloping surfaces (i.e., flat ground to a vertical rock face)
848 can be approximated (a detailed methodology for doing this is explained in *Bridges et al.*
849 (2012b)). Abrasion rates for several sites have been reported (e.g., Nili Patera, Gale crater,
850 Mawrth Vallis, Jezero crater) and range 0.01–1.3 m/Myr for flat ground and 0.3–47 m/Myr for
851 vertical rock faces (*Bridges et al.*, 2012b; *Chojnacki et al.*, 2018; *Farley et al.*, 2014).

852

853 **2.3 Open questions for martian aeolian landforms and sediment history**

854 Major questions remain open about the age, sources, and amounts of dust and sand on Mars.
855 The few areas where dune sand is traced back to a source involve eroding crater walls or polar
856 layered deposits, where sand appears to be recycled from sandstone or an ancient erg,
857 respectively (e.g., *Chojnacki et al.*, 2014b; *Tirsch et al.*, 2011). On Earth, most sand grains form
858 from chemical and physical erosion of quartz down to a stable grain size (*Krinsley and Smalley*,
859 1972); Mars instead is predominantly basaltic (*Ehlmann et al.*, 2017; *Greeley and Iverson*, 1985;
860 *Minitti et al.*, 2013; *Yen et al.*, 2005). Models predict that sand-sized grains could be created
861 through explosive volcanic processes (*Edgett and Lancaster*, 1993; *Wilson and Head*, 1994), but
862 the most recent volcanism occurred 2–10 Mya (e.g., *Neukum et al.*, 2004b). Others have
863 proposed that sand grains may form by fragmentation driven by impact and aeolian processes
864 (*Golombek et al.*, 2018; *McGlynn et al.*, 2011). Some have proposed that the general generation
865 and flux of granular material on Mars has declined over time, with the impact, volcanic and
866 chemical weathering processes on an ancient, wet Mars generating the majority of sediment
867 (*Grotzinger and Milliken*, 2012; *McLennan et al.*, 2019). However, it is not currently known if
868 most martian sand has been recycled or if a significant amount is actively forming in the present
869 climate.

870 Similar questions can be asked about dust. The global dust budget and surface reservoir
871 distribution, as well as the dust lofting rate, present important controls on climate models. It is
872 important to understand not only the present state, but also how dust availability and distribution
873 may have changed through climate cycles (i.e., thousands to millions of years) and climate
874 epochs (i.e., to billions of years).

875 Observations of a few dune fields suggest that sand is size and compositionally sorted (e.g.,
876 *Chojnacki et al.*, 2014b; *Lapôtre et al.*, 2017; *Pan and Rogers*, 2017; *Seelos et al.*, 2014) as it
877 progresses through a transport pathway and aeolian bedforms. Such observations present an
878 interesting feedback question, as grain size can influence evolution/mobility of the bedforms and
879 further grain transport. This also suggests that additional complexity may be needed in models
880 connecting landform morphology to formation history.

881 Although hypotheses for the growth-limiting mechanism of meter-scale ripples are
882 converging towards an aerodynamic process (e.g., *Duran Vinent et al.*, 2019; *Lapôtre et al.*,
883 2016; 2021; *Sullivan et al.*, 2020) the nature of their inception mechanism is still being debated

884 (*Duran Vinent et al.*, 2019; *Sullivan et al.*, 2020). Questions about present-day activity rates (if
885 nonzero) and formative history of such features, and why this diversity of bedforms is found,
886 remain an open area of study. While these questions are about the evolution of landforms, such
887 models are built from sediment flux and saltation layer models, which in turn depend on models
888 of how individual grains are moved along the surface (e.g., the fractional contributions of
889 saltation versus reptation to a wind-driven sand flux)—discussed more in §2.4.

890

891 **2.4 Open questions for the physics of aeolian processes**

892 Regarding the fundamental physics of aeolian grain transport, terrestrial and laboratory
893 studies form the basis of the majority of information known about the influence of different
894 parameters (summarized in *Pahtz et al.*, 2020). In application of these models towards the
895 martian environment, current threshold models predict minimum wind speeds that align with
896 observed wind speeds on Mars (*Burr et al.*, 2020; *Kok et al.*, 2012; *Swann et al.*, 2020).
897 However, a number of uncertainties in the application of thresholds to natural boundary layers
898 acting over spatially heterogeneous surfaces and bedforms on Mars remain, including: (1) the use
899 of idealized surface conditions for threshold model derivation, (2) the difficulty in obtaining
900 necessary parameters such as grain size, shape and density on Mars, and (3) potential errors in
901 estimating shear velocity from single-height wind speed observations.

902 Empirical coefficients in Martian threshold models are derived for idealized surface
903 conditions, saltating particles moving over flat beds of cohesionless grains with uniform size
904 distributions. These do not represent the more complex surfaces and bedforms found on Mars,
905 e.g., stoss slopes of dunes, mixed grain size surfaces and bedforms, and coarse-lag deposits.
906 Surfaces and bedforms with mixed grain size distributions, sediment consolidation levels, or
907 coarse lag deposits can act to increase the minimum wind speed required to initiate saltation or
908 become active by a different mode of transport (e.g., saltation vs. rolling particles or reptation).

909 Uncertainty in threshold predictions also arises from the difficulty in determining grain size,
910 shape, and density comprising aeolian bedforms on Mars. In situ observations from landers and
911 rovers have been successful at determining these characteristics. For example, *Curiosity's* Mars
912 Hand Lens Imager (MAHLI) determined particle sizes and shapes within ripples throughout Gale
913 crater (*Weitz et al.*, 2018). However, these observations are geographically limited and remote
914 sensing techniques do not have the resolution required to determine grain size and density that
915 are required to predict the threshold for motion.

916 Finally, there is uncertainty in estimating shear stress, or shear velocity, on the surface of
917 Mars. Shear velocity, a surrogate for bed shear stress, can be estimated from single-height wind
918 speed observations using either the covariance of 2D or 3D velocity components or von
919 Karman's Law of the Wall. However, local thermal convection at the surface on Mars induces a
920 dynamically unstable boundary layer (*Fenton and Michaels, 2010*). The instability in the
921 boundary layer, represented by deviations from typical logarithmically distributed velocity
922 fluctuations, is difficult to predict. At present, wind speeds on Mars are observed at a single
923 height (typically ~1.5 m above the surface) and sampled at low frequencies. Thus, we have yet to
924 measure how the boundary layer responds to variations in local convection, or estimate the error
925 associated in low-frequency sampling that can alias shear velocity calculations, in particular
926 when using the covariance derivation. In situ measurements of vertical velocity gradients within
927 unstable boundary layers at the surface of Mars are necessary to reduce error in shear velocity
928 estimation.

929 Unfortunately, testing different sediment transport processes further is not possible with
930 existing rover payloads or from orbit. Additionally, it is difficult to mimic martian conditions,
931 especially over sufficient distances to allow full formation of the saltation layer, within present
932 terrestrial laboratories. As will be discussed in §6, in situ investigations are needed to acquire the
933 high-frequency, high-resolution measurements that can correlate driving environmental
934 conditions (such as wind velocities, including gusts, and surface pressure) with the sediment
935 movement.

936

937 **3 Seasonal Frost/Ice-formed Landforms**

938 The martian atmosphere is ~95% CO₂ and contains trace amounts of water vapor (e.g., on the
939 order of a few tens of precipitable microns). Under typical present-day martian surface
940 conditions, CO₂ and H₂O condenses near ~145 K and ~198 K, respectively (*Ingersoll, 1970*;
941 *James et al., 1992*). Frost condensation temperatures are reached at virtually all latitudes
942 (*Piqueux et al., 2016*), although, as on Earth, the exact duration of the period when the
943 environment is sufficiently cold for frost or ice to accumulate (e.g., seconds, to seasons, to
944 astronomical cycles) depends on latitude and local surface and subsurface conditions (e.g., grain
945 size and composition, subsurface water ice content and depth) that influence the local thermal
946 inertia, shadowing due to topography, and atmospheric conditions such as dust opacity (*Putzig
947 and Mellon, 2007*).

948 In this section, we describe the frost and ice types that currently form on the martian surface
949 (§3.1). Sublimation of this diurnal (i.e., only overnight) or seasonal frost/ice is highly energetic
950 and is thought to cause erosion by inducing and enhancing mass wasting (§3.2) or by
951 digging/scouring out material from the surface directly under a subliming ice slab (§3.3).

952

953 **3.1 Currently formed surface frost/ice types on Mars**

954 Present-day CO₂ and H₂O deposition can be in the form of diurnal frosts, seasonal frosts, or
955 snowfall. As the amount of precipitable water is so limited in the tenuous martian atmosphere,
956 water frost/ice condensation will depend on the local partial pressure of water vapor. In contrast,
957 CO₂ ice requires significantly lower temperatures to condense out of the atmosphere, but it is
958 more abundant than water and thus is not limited by diffusion through the lower atmosphere.
959 Tens to hundreds of micrometer thick diurnal CO₂ frost layers form overnight over a significant
960 fraction of the planet (*Piqueux et al.*, 2016). During current martian winters, as much as a third
961 of atmospheric CO₂ can be deposited onto the surface (*James et al.*, 1992; *Leighton and Murray*,
962 1966) dramatically redistributing CO₂ and decreasing surface pressures. Accumulated decimeters
963 or thicker depth layers of seasonal CO₂ frost will sinter, forming polycrystalline CO₂ slab ice(s)
964 (*Matsuo and Heki*, 2009) with optical and thermal properties very different from terrestrial water
965 frost and ice. In particular, CO₂ ice is transparent to visible wavelengths but opaque to thermal
966 infrared (*Matsuo and Heki*, 2009). As the surface warms moving towards spring, the
967 accumulated CO₂ and H₂O frost/ice will sublime, but not uniformly. Visible solar radiation can
968 penetrate the CO₂ ice layer and, via a process known as the solid state greenhouse effect (*Matson*
969 *and Brown*, 1989) because it is analogous to the greenhouse effect in planetary atmospheres but
970 happens in a transparent solid body instead of a gaseous atmosphere, lead to the springtime
971 insolation-induced basal sublimation of the translucent, impermeable slab ice (*Kieffer et al.*,
972 2006). Defrosting marks will appear first, readily visible in high-resolution images, such as
973 sublimation spots, fans, and dark linear ‘flow’ features (*Gardin et al.*, 2010; *Kaufmann and*
974 *Hagermann*, 2017; *Kieffer*, 2007; *Malin and Edgett*, 2001; *Pilorget et al.*, 2011; 2013) and
975 polygonal fracturing of the ice slab (*Piqueux and Christensen*, 2008; *Portyankina et al.*, 2012).
976 In general, sublimation can be very energetic and is thought to be a key driver for the formation
977 of many landforms (as described below). Seasonal frosts and snowfall events have some
978 interannual variability in terms of location and duration, which have begun to be documented in

979 a systematic manner as more complete records of the present-day climate and weather are
980 acquired (*Calvin et al.*, 2015; *Hayne et al.*, 2016; *Piqueux et al.*, 2015b; *Widmer et al.*, 2020).

981 To date, the majority of present-day surface activity connected to surface frost/ice has been
982 hypothesized to be controlled primarily by the deposition and/or sublimation of seasonal CO₂
983 frost/ice. The seasonal frost cap begins to form early in the martian fall, reaches maximal extent
984 (i.e., equatorward reach) at the end of the fall, and sublimates between the end of the winter and
985 into the spring (*Piqueux et al.*, 2015b). CO₂ snowfall is observed to contribute to the seasonal
986 frost accumulation (*Gary-Bicas et al.*, 2020; *Hayne et al.*, 2012; 2014). Seasonal ice sheets reach
987 up to ~2 m in thickness near the poles (*D.E. Smith et al.*, 2001) and fractured ice layers and
988 detached ice blocks have been observed in the mid-latitudes (e.g., *Dundas et al.*, 2012). From
989 orbital observations, patchy seasonal surface deposits of CO₂ frost have been observed as far
990 equatorward as ~42° N (*Widmer et al.*, 2020) and 33° S (*Schorghofer and Edgett*, 2006;
991 *Vincendon et al.*, 2010a). In the north, which is the hemisphere with more water in its polar cap
992 (*Ojha et al.*, 2019) and atmosphere (*M.D. Smith*, 2002), a ring of water ice is annually observed
993 equatorward of the CO₂ seasonal frost cap (*Appéré et al.*, 2011; *Langevin et al.*, 2005; 2007;
994 *Wagstaff et al.*, 2008). H₂O frost has been detected from orbit as far equatorward as 32° N and
995 13° S (*Vincendon et al.*, 2010b), while in situ observations suggest H₂O frost at 48° N with the
996 *Viking 2* lander (*Hart and Jakosky*, 1986; *Svitek and Murray*, 1990; *Wall*, 1981), at 2° S with the
997 *MER Opportunity* (*Landis*, 2007), and at 5° S with *Curiosity* at Gale crater (*Martinez et al.*,
998 2017).

999 Although not yet well characterized through observations or models, it is likely that H₂O and
1000 CO₂ frost/ices do not form and evolve independently of each other and that their interplay, and
1001 interaction with incorporated atmospheric dust, constitutes an additional control on
1002 geomorphological activity that is not yet well understood. For example, CO₂ ice can serve as a
1003 sink for water vapor (*Houben*, 1997; *Houben et al.*, 1997), and H₂O deposits affect basal
1004 sublimation of CO₂ (*Titus et al.*, 2020). In addition to influencing accumulation and sublimation
1005 timing and rates, mechanical interactions between different types of frost/ice may create another
1006 control on some geomorphological activity. For example, differences in grain sizes between a
1007 surface condensed frost layer and snowfall may enhance wintertime mass-wasting activity
1008 (*Hansen et al.*, 2018; §3.2.2).

1009 Over recent Mars history, Mars' obliquity shifts have also affected the spatial distribution
1010 and stability of accumulated seasonal frost/ice. Past multi-annual (up to tens of thousands of
1011 years) accumulation of CO₂ ice has formed up to ~1 km thick units within the polar regions
1012 (*Phillips et al.*, 2011); similarly, over long periods of time, fluxes of water through the
1013 atmosphere can result in the formation of large reservoirs at the poles (*Bierson et al.*, 2016;
1014 *Buhler et al.*, 2020; *Manning et al.*, 2019), as well as within middle and equatorial latitudes
1015 (*Jakosky et al.*, 2005; *Mellon et al.*, 2004; *Mellon and Jakosky*, 1993; 1995; *Mellon et al.*, 1997).
1016 As the orbital parameters change, these water ice reservoirs can become unstable. Landforms
1017 created through present-day or recent sublimation of such ice reservoirs are discussed in §4, and
1018 study of these units, coupled with studies of present-day frost/ice driven surface activity, is
1019 necessary to extend models to past climatic periods and interpret relict landforms (§7.3).
1020 (However, discussion of the past formation and preservation of such perennial ices is outside the
1021 scope of this review.)

1022

1023 **3.2 Seasonal sublimation triggered mass-wasting landforms**

1024 **3.2.1 Gullies**

1025 Based on morphological similarity to terrestrial gullies (i.e., comprising alcove, channel, and
1026 apron features), martian gullies were initially hypothesized to be formed through liquid water
1027 flow, perhaps through groundwater seepage (*Malin and Edgett*, 2000), but a source for the water
1028 was not apparent. Early MOC observations showed signs of defrosting activity in south polar
1029 gullies (*Bridges et al.*, 2001; *Hoffman*, 2002) but did not document any significant changes to the
1030 frost-free surface. *Malin et al.* (2006) provided the first detailed description of contemporary
1031 gully activity, reporting two new digitate light-toned deposits in southern-hemisphere craters.
1032 Both deposits were associated with poorly developed gullies and were relatively superficial.
1033 *Malin et al.* (2006) suggested that these flows indicated discharge of shallow groundwater, but
1034 *Pelletier et al.* (2008) modeled one of the deposits in detail and found that it could be explained
1035 by dry granular flow. *Kolb et al.* (2010) carried out similar modeling of additional light-toned
1036 deposits without constrained formation ages and found that they too could be reproduced by dry
1037 flows.

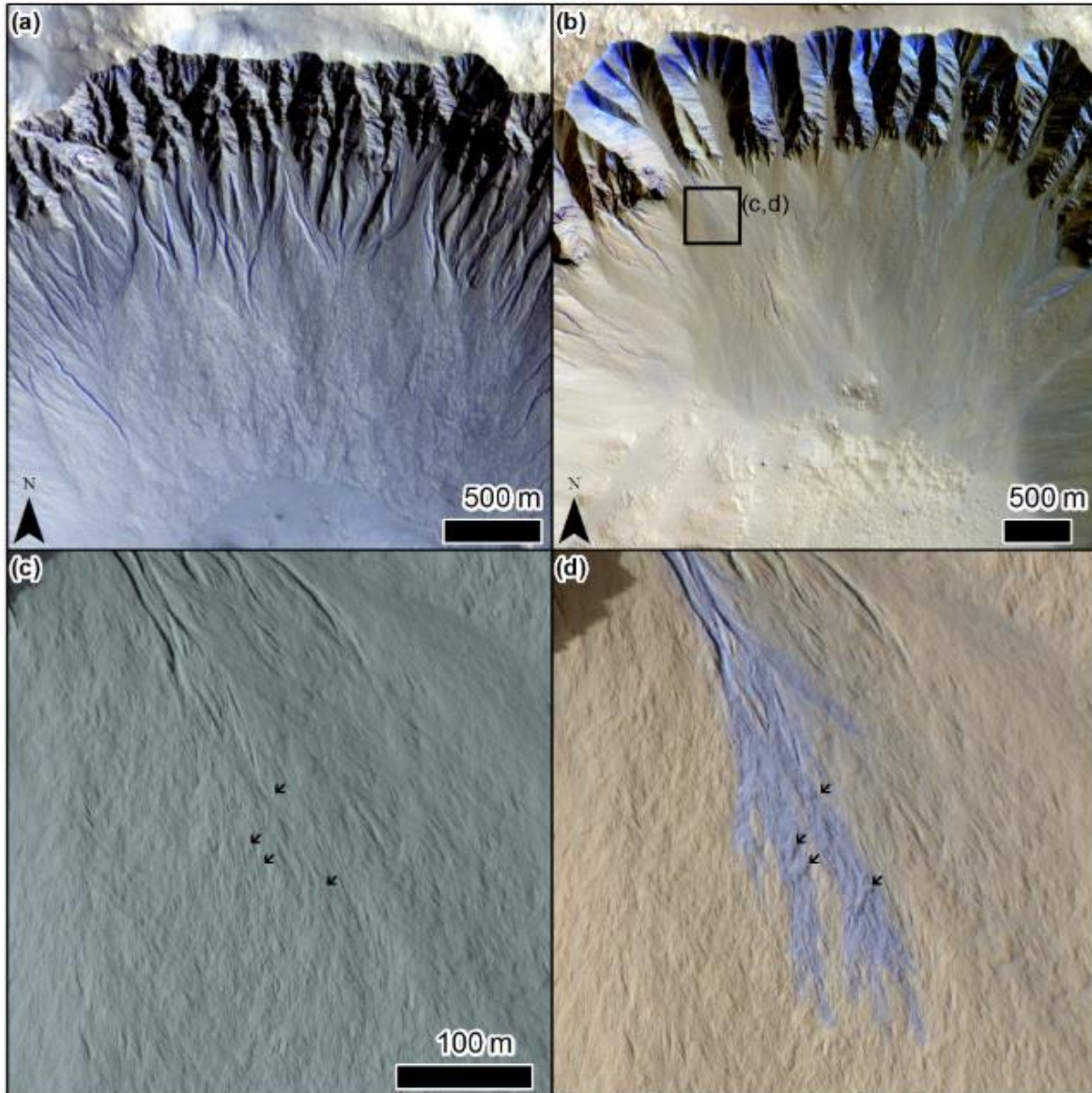
1038 Subsequent detections of more active flows in gullies along both crater walls and dune slopes
1039 (e.g., Figures 4, 9) have led to better constraints on the processes causing activity. *Harrison et al.*
1040 (2009), *Diniega et al.* (2010), and *Dundas et al.* (2010) all examined active gullies and reported

1041 weak seasonal constraints favoring cold-season activity for gullies on both sand dunes and other
1042 surfaces. *Harrison et al.* (2009) favored seasonal occurrence of liquid water based on
1043 geomorphological similarities to terrestrial debris flows, while *Diniega et al.* (2010) and *Dundas*
1044 *et al.* (2010) proposed that winter CO₂ frost was driving activity in some fashion. The latter
1045 option was strongly supported when *Dundas et al.* (2012) reported active flows with much
1046 tighter timing constraints that correlated well with observed CO₂ frost, including observations of
1047 creeping flows slowly advancing down frosted channels over a period of weeks, as well as one-
1048 off events producing larger morphologic changes. Expanded observations with more locations
1049 are consistent with these behaviors (*Dundas et al.*, 2015a; 2019a), as is a detailed study of gullies
1050 in a pit near the south pole (*Raack et al.*, 2015; 2020). Morphological changes in gullies can be
1051 extensive (*Dundas et al.*, 2012; 2015a; 2019a).

1052 Gullies located on sand dunes with classic alcove-channel-apron morphology appear to be
1053 more active and have even larger morphological changes, possibly because of the loose substrate
1054 (*Diniega et al.*, 2010; *Dundas et al.*, 2012; 2015a; 2019a). These features have been found on
1055 sand dunes through the southern mid-latitudes, many with extensive annual activity (*Dundas et*
1056 *al.*, 2019a). *Pasquon et al.* (2019a; 2019b) documented several styles of CO₂-frost driven activity
1057 that drove changes in channel sinuosity, noting an initial alcove-collapse stage followed by
1058 transport into the lower parts of the gullies.

1059 The details of the processes by which CO₂ frost causes gully activity on rocky or sandy
1060 slopes are not yet well understood. Starting shortly after the discovery of gullies, several frost-
1061 driven processes were proposed. *Hoffman* (2002) suggested gas-lubricated flows initially
1062 triggered by basal sublimation of translucent CO₂ frost and further mobilized by additional
1063 sublimation during transport. *Ishii and Sasaki* (2004) proposed that avalanches of CO₂ frost
1064 could occur, while *Hugenholtz* (2008) suggested that frosted granular flow could operate in
1065 gullies. In the latter process, coatings of frost help to lubricate flow. *Cedillo-Flores et al.* (2011)
1066 showed that sublimating CO₂ frost could effectively fluidize overlying granular material but did
1067 not provide a mechanism for how such frost would be emplaced under regolith. *Pilorget and*
1068 *Forget* (2016) demonstrated that basal sublimation would be effective at generating gas eruptions
1069 in some gullies, and also that CO₂ ice could condense in the regolith pore space under some
1070 conditions, but did not explain the formation of channel morphologies (that study specifically
1071 focused on new channels forming amongst linear gullies (§3.3.1)). *Dundas et al.* (2019a) carried

1072 out calculations that showed the available energy budget was sufficient to generate gas from
1073 entrained CO₂ frost during the flow, providing fluidization, and *de Haas et al.* (2019) provided a
1074 more detailed description of the relevant physics.
1075



1076
1077 Figure 9. (a) Gullies in Galap crater in CaSSIS image MY34_005744_220_1. (b) Gullies in Gasa crater
1078 in CaSSIS image MY34_005684_218_1, with black box showing the location of detailed panels (c, d). (c)
1079 Image of a gully fan prior to a depositional event, HiRISE image ESP_012024_1440. (d) Image of a gully
1080 fan after a depositional event, HiRISE image ESP_020661_1440. Arrows point to lobate deposits not
1081 visible in previous image. Incidence angles for (c) and (d) are 57.4 and 57.9°, respectively, so these
1082 changes are not an illumination effect; see *Dundas et al.* (2012) for an animation that provides a blink
1083 comparison. Scale is the same as in (c).
1084

1085 **3.2.2 Dune alcoves**

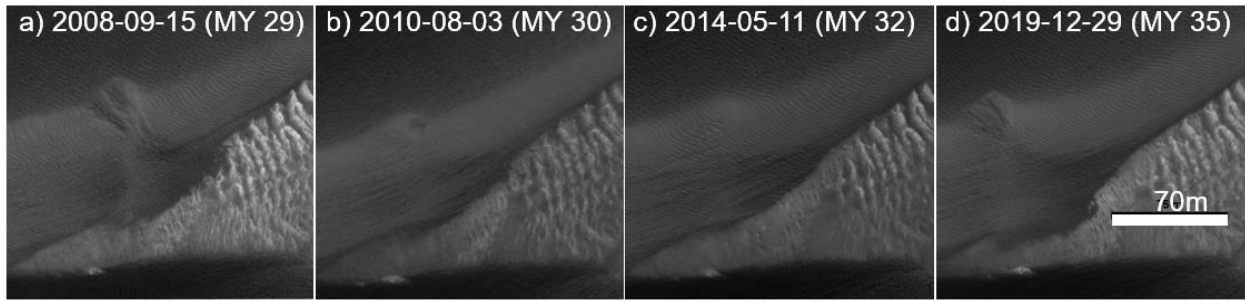
1086 New 5–40 m wide erosional alcoves are actively forming on dune lee-side slopes in the north
1087 polar erg, often connected to a depositional apron (Figure 10); these features are called “dune
1088 alcoves” rather than “dune gullies” (§3.2.1), as they generally lack a channel. Newly formed
1089 alcove-apron features in the north polar erg were first reported on by *Hansen et al.* (2011), who
1090 noted that these features formed annually and were found on ~40% of the dune slopes. In that
1091 study, the alcove-aprons were correlated with springtime sublimation activities, such as the
1092 appearance of dark spots and flows (*Gardin et al.* (2010); this timing and morphological
1093 similarity to dune gullies in the southern mid-latitudes led to the hypothesis that these features
1094 were formed through a seasonal-frost driven process— and specifically that springtime
1095 sublimation was leading to the alcove formation activity (*Hansen et al.*, 2011). Later studies
1096 demonstrated that new alcoves were visible under winter frosts (*Horgan and Bell*, 2012), but
1097 were likely forming after the first autumnal frosts, thus moving the timing of alcove formation
1098 activity to early autumn (*Diniega et al.*, 2019a; *Hansen et al.*, 2015). This led to a new
1099 hypothesis that sublimation of diurnal frosts or interactions between early autumnal surface
1100 frosts and snowfalls may initiate this mass wasting (*Diniega et al.*, 2019a; *Hansen et al.*, 2018).

1101 Due to this difference in timing of activity as well as dune alcoves not being reactivated in
1102 subsequent Mars years (i.e., once the alcove forms, it fills in due to aeolian sand transport
1103 (Figure 10), but does not widen or lengthen during subsequent winters, as many gullies are
1104 observed to do), these features appear to be different from gullies, including dune gullies
1105 (§3.2.1). The morphologies are also different, as few dune alcoves have a channel connecting
1106 them to their depositional aprons (potential exceptions discussed in *Grigsby and Diniega*
1107 (2018)).

1108 Subsequent studies have documented that dune alcoves are found within some mid-latitude
1109 dune fields (*Diniega et al.*, 2019b). Although a much lower number of overlapping images
1110 means timing of formation of these mid-latitude dune alcoves cannot yet be well constrained,
1111 these features are all found in dune fields that experience seasonal frost and snowfalls, thus
1112 remaining consistent with the polar erg-based hypotheses. However, improved constraints on the
1113 environments where dune alcoves form, versus environments where they do not form, remain
1114 under study and a formation mechanism model has not yet been developed.

1115

1116



1117

1118

1119

1120

1121

1122

1123

1124

1125

1126

1127

Figure 10. Example dune alcoves forming on a polar dune slope (Teilax dune field, 83.5°N, 118.5°E). The slope fills in due to aeolian sand transport (*c,d*) and then a new nearby dune alcove forms (*d*). This is the same location as shown in Figure 4; here, all images were acquired at about the same mid-summer period (L_s 127–129°), so illumination conditions are consistent. HiRISE images are (*a*) PSP_010019_2635, (*b*) ESP_018839_2635, (*c*) ESP_036510_2635, and (*d*) ESP_062923_2635. A scale bar is shown in the last image, but absolute distances are approximate as images are not orthorectified. The bright ripples in the interdune region appear immobile over this timescale and can be used to determine relative location. North is up and illumination is from the left.

1128

3.3 Basal sublimation formed landforms

1129

3.3.1 Linear gullies

1130

1131

1132

1133

1134

1135

1136

1137

1138

1139

Martian “linear gullies” were first identified within Russell crater (*Mangold et al.*, 2003) and these decameters to kilometers-long, meters-wide troughs have since been found on a range of sandy slopes (e.g., *Dundas et al.*, 2012; *Pasquon et al.*, 2016; Figure 11). Based on their resemblance to terrestrial rills, these features were originally likened to terrestrial debris flows and proposed to be formed by surface water flow due to meltwater following a period of high obliquity (e.g., *Jouannic et al.*, 2012; *Mangold et al.*, 2003; 2010; *Miyamoto et al.*, 2004) or present-day atmospheric condensates (*Vincendon et al.*, 2010b). However, their terminal morphology (i.e., lack of debris aprons and instead ending abruptly or with pits) and the observation that some linear gully troughs and pits were forming in the present day (*Dundas et al.*, 2012; *Reiss et al.*, 2010) did not support this model.

1140

1141

1142

1143

1144

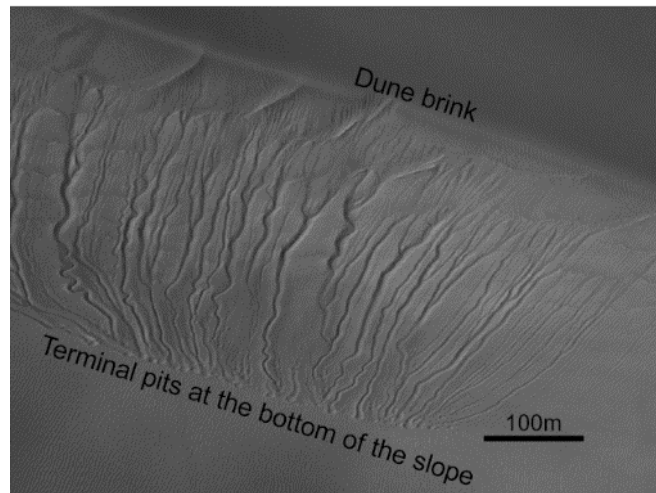
1145

1146

Diniaga et al. (2013) proposed a dry model, with the idea that these features may be similar to boulder-tracks—although lacking a boulder. According to this model, the trough forms due to a block of CO₂ ice rolling or sliding downslope, carving out its path on a sandy surface. Such ice forms within the seasonal frost layer that is observed to be deposited across these mid-latitude slopes each martian winter. As the frost on the dune slopes sublimates, ice remains cold trapped in shaded dune alcoves at the top of the dunes, but eventually may become dislodged, falling onto relatively warm, exposed dark sand. Sublimation at the base of this dry ice block lifts the block

1147 slightly from the sandy surface (in a manner similar to the Leidenfrost effect), allowing it to
1148 freely roll or slide down the sandy slope, unencumbered by friction and carving out a trough.
1149 Upon stopping, the dry ice block would continue to sublime in situ, digging out a pit that then
1150 would be the remaining record after the block disappears. Field experiments with dry ice slabs
1151 slid down terrestrial desert dune slopes (*Bourke et al.*, 2016a; 2016b; *Diniega et al.*, 2013) and
1152 laboratory experiments that examine interactions between sublimating dry ice blocks and a
1153 granular substrate (*McKeown et al.*, 2017) have shown that it is feasible for the “hovercrafting
1154 dry ice block” model to broadly produce many of the observed linear gully morphologies. CO₂
1155 ice blocks, up to ~3-m diameter, have also been observed to form and migrate downslope within
1156 martian features (e.g., *Dundas et al.*, 2012), and further modeling of interactions between CO₂
1157 ice and sediment support development of this process in the present martian climate (e.g.,
1158 *Pilorget and Forget*, 2016). However, a refined model of block transport and quantitative
1159 understanding of how linear gully morphological characteristics, such as width and sinuosity,
1160 relates to formation history has not yet been developed, limiting interpretation of these features.
1161 In particular, it is not yet known if the ~10 m-wide troughs seen in Russell crater formed under a
1162 past climate when significantly larger blocks of CO₂ may have formed, or if these have widened
1163 (albeit slowly) in the present climate due to ice blocks sliding down over many martian winters,
1164 with blocks similar to those forming new ~meter-wide troughs (*Dundas et al.*, 2012; *Jouannic et*
1165 *al.*, 2019; *Reiss et al.*, 2010).

1166
1167 **Figure 11.** Example of a linear gully cluster
1168 on a climbing dune slope (50.2°S, 292.1°E),
1169 along the inside of the rim of an unnamed
1170 crater. Note the range of sinuosities, trough
1171 widths (1-10 m including levees), and pits
1172 (2-5 m) even in this one cluster. Image ID:
1173 HiRISE ESP_030624_1295, north is up and
1174 illumination is from the left.



1175 **3.3.2 Araneiforms**

1176 Araneiforms (also known as “spiders”)
1177
1178 are unique surface features that have no Earth analogs. Located primarily on the south polar
1179 layered deposits and surroundings (*Piqueux et al.*, 2003; *Schwamb et al.*, 2018), these features
1180 are characterized by dendritic, tortuous troughs several meters wide and deep which extend from
1181 a central pit and range from <50 m to 1 km in diameter (Figure 12d). Their specific morphology

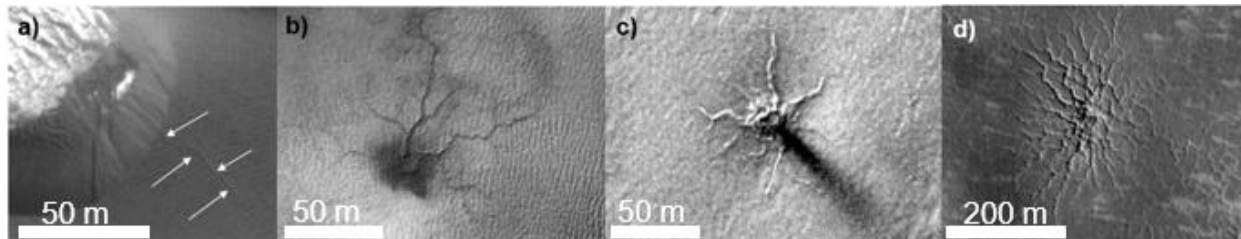
1182 types range from 'fat' to 'starburst' (*Hansen et al.*, 2010) and these sub-types tend to cluster non-
1183 randomly (*Hao et al.*, 2020).

1184 These features are widely accepted to form via basal sublimation of CO₂ slab ice due to the
1185 solid state greenhouse effect (*Matson and Brown*, 1989) (see §3.1 for a longer description). As a
1186 consequence of this phenomenon, informally called the “Kieffer model,” sublimation at the base
1187 of the CO₂ ice leads to a buildup of gas pressure beneath the ice overburden. Eventually this gas
1188 pressure exceeds the strength of the ice, causing it to crack or rupture at a weak spot. Pressurized
1189 gas rushes towards the vent, emerging as a plume and depositing the entrained material as fans
1190 and spots (Figure 12c). The escaping gas entrains particulates from the substrate, gradually
1191 eroding troughs (*Kieffer*, 2007; *Kieffer et al.*, 2006; *Piqueux et al.*, 2003).

1192 Repeated venting episodes are believed to build the full extent of araneiforms over thousands
1193 of martian years (*Hansen et al.*, 2010; *Piqueux and Christensen*, 2008; *Portyankina et al.*, 2010;
1194 *N. Thomas et al.*, 2010). Most araneiform terrains show annual repeating sublimation activity: in
1195 spring, dark fans and blotches drape over troughs of araneiforms indicating CO₂ jet activity. As
1196 the ice layer continues to sublime, the bright frost is removed and so the dark deposits fade or
1197 even completely disappear, and the cycle repeats again in the next spring. However, despite
1198 continuous monitoring of araneiform terrains by high-resolution remote sensing, no detection of
1199 changes in the topography of large, well-developed araneiforms has been reported over the last 6
1200 martian years. This leads to the question about whether the large araneiforms are currently
1201 evolving with a slow erosive process by the sub-ice CO₂ gas flow that modifies the substrate at a
1202 rate below current detection limits, or are dormant remnants of some past climate. It also
1203 highlights uncertainty in existing estimates of araneiform ages: *Piqueux and Christensen* (2003)
1204 estimated that they are at least 10⁴ martian years old based on an erosion-rate estimate of ~1
1205 m³/yr, but *Portyankina et al.* (2017) observed erosion rates of ~8 m³/yr.

1206 Away from old(er) araneiform terrains, newly forming dendritic troughs have been recently
1207 detected with HiRISE (*Portyankina et al.*, 2017). These troughs form in the vicinity of sand
1208 dunes and have been observed to grow interannually (Figure 12b). Dendritic troughs are
1209 proposed to represent the early stages of araneiform formation (*Portyankina et al.*, 2017). Even
1210 smaller-scale (~tens of meters long) dendritic features known as sand furrows annually scour
1211 northern hemisphere dune slopes, but these are erased in summer (*Bourke and Cranford*, 2011;
1212 *Diniega et al.*, 2019a; Figure 12a). While laboratory experiments have replicated dendritic

1213 patterns on granular substrate via CO₂ sublimation (*Mc Keown et al.*, 2021), the factors that
1214 distinguish the apparent disparity in activity, scale, latitudinal distribution and morphology
1215 between sand furrows, dendritic troughs and araneiforms have not yet been delineated.
1216



1217
1218 Figure 12. Examples of dendritic troughs, increasing towards right in network-complexity. The
1219 first 2 show annually active features: (a) dune furrows (extending towards bottom right corner
1220 from the dune brink, between arrows) and (b) the dendritic features described in *Portyankina et al.*
1221 *et al.* (2017). The furrows disappear before the following year, while the dendritic trough has
1222 grown through multiple martian years. The two on the right (c, d) are araneiforms, which have
1223 not yet been observed to change. HiRISE images are from (a) *Diniega et al.* [2018] and (b-d)
1224 *Portyankina et al.* [2017]: ESP_017895_2650, ESP_011842_0980, ESP_023600_1095, and
1225 ESP_032009_0985, respectively. (NASA/JPL/UA).

1226

1227 3.4 Open questions for seasonal frost/ice and related landforms

1228 For many of the landforms discussed above, observations for the timing and locations of
1229 activity implicate some form of seasonal frost/ice as a driver, and it is generally thought that the
1230 energy generated through frost/ice sublimation are a key control. However, models of frost
1231 formation and sublimation have not yet been quantitatively connected to sediment fluxes or
1232 erosion rates, and thus it is not known exactly what form(s) and amount of frost/ice may be
1233 needed to induce landform creation, evolution, or modification. Terrestrial analog studies are
1234 often used to provide a starting model (with an analog chosen based on similar geomorphology),
1235 but recent studies demonstrating that CO₂ frost/ice is a major geomorphic agent suggests that
1236 there are limits in how far Earth-based (often liquid water controlled) models can be applied. The
1237 sublimation-dominant dynamics of CO₂ frost and ice, and even H₂O when exposed under Mars
1238 pressure conditions (e.g., *Herny et al.*, 2019; *Massé et al.*, 2016; *Raack et al.*, 2017), have no
1239 terrestrial analog.

1240 Generation of landform evolution models are hampered by lack of knowledge about the
1241 behavior and properties of the martian seasonal frost/ice layer, including how this layer evolves
1242 through the winter. Passively sensing orbital instruments generally cannot observe during the
1243 period of interest due to polar night; additionally, as the surface first reaches CO₂ condensation

1244 temperatures in the autumn, an atmospheric haze (i.e., the polar hood) obscures visible images.
1245 No in situ measurements of the seasonal CO₂ frost layer have yet been collected due to technical
1246 challenges in having a spacecraft survive through the winter (*ICE-SAG*, 2019). Laboratory
1247 experiments have begun to look at CO₂ frost/ice formation (e.g., *Portyankina et al.*, 2019), as
1248 well as at how both H₂O and CO₂ sublimation may interact with granular materials (e.g.,
1249 *Chinnery et al.*, 2018; *Herny et al.*, 2019; *Kaufmann and Hagermann*, 2017; *Massé et al.*, 2016;
1250 *Mc Keown et al.*, 2017; 2021; *Pommerol et al.*, 2019; *Portyankina et al.*, 2019; *Raack et al.*,
1251 2017; *Sylvest et al.*, 2016; 2019; *Yoldi et al.*, 2021). By necessity due to present lab capabilities,
1252 such experiments are small-scale and simplified in terms of the variables incorporated.
1253 Eventually such experiments will also need to consider the interactions between varying amounts
1254 of different types of frost (e.g., fine-grained CO₂ snowfall over or under a layer of surface frost,
1255 or how H₂O and CO₂ surface frost may interlayer and affect optical and mechanical properties of
1256 the full frost layer). Models are also needed to scale laboratory results to natural martian
1257 conditions and to extrapolate to past environmental conditions, as well as observation of present
1258 Mars surface and atmospheric conditions to constrain and refine such models.

1259 Finally, martian landforms with similar morphologies are often studied in aggregate, with
1260 active examples treated as analogs for similar-appearing landforms not (yet) observed to be
1261 active. In such studies, a common question is if much larger and/or more complex features that
1262 have not yet been observed to be active are active at very slow rates or if they are instead records
1263 of a past, more intense frost environment. Older records may evolve, possibly via a process
1264 continuing through shifting climate conditions, or via process(es) different from that involved in
1265 initial formation. Additionally, just as in application of comparative geomorphology between the
1266 Earth and Mars, it is possible that similar appearing morphologies on Mars may form through
1267 different processes (i.e., the principle of equifinality).

1268

1269 **4 Long-term sublimation of ices**

1270 In the present martian climate, water ice is found in the polar caps (§4.1) and in the
1271 subsurface (§4.2–4). For all of this ice, connection to the atmosphere allows sublimation of the
1272 ice and specific geomorphologies have been tied to this volatile transport (§4.1, 4.3–4). If the
1273 rate of sublimation can be determined from the observed activity or geomorphology, the absolute
1274 ages and stability of the ice deposits can be estimated—yielding environmental constraints on
1275 recent past climates, including variations in ice formation and stability under different obliquities

1276 (see §4.2.1). Alternatively, if the ages and sizes of past ice reservoirs can be estimated, this can
1277 yield bounds on the rate at which water ice is subliming and escaping through the regolith.

1278 Interpreting the geological and climatological history reflected in subsurface water ice
1279 deposits requires comparison between two types of analysis: model predictions of water ice
1280 stability (as a function of depth, latitude, and subsurface thermophysical properties: §4.2.1) and
1281 observational evidence of where water ice is or was present (§4.2.2, 4.3–4). When these two
1282 lines of investigation are consistent, this provides credence to the applied models and
1283 environmental parameters. When these two lines of investigation differ, this leads to either
1284 focused questions about the models and/or assumed environmental parameters or constraints on
1285 the age of geomorphic features and preservation mechanisms (i.e., if ice may have been present
1286 in the past, but no longer exists).

1287

1288 **4.1 Polar surface landforms**

1289 **4.1.1 South Polar Residual Cap**

1290 The South Polar Residual Cap (SPRC) is a <10-m-thick layer of CO₂ ice overlying a layer of
1291 H₂O ice (*Bibring et al.*, 2004; *Byrne and Ingersoll*, 2003b; *Titus et al.*, 2003) that covers $7.9 \times$
1292 10^9 m² (*P.C. Thomas et al.*, 2016) offset slightly west from the south pole, potentially due to
1293 broad-scale topography modulation of south polar circulation (*Colaprete et al.*, 2005). The CO₂
1294 ice is incised into discrete mesas by ubiquitous sublimation pits that annually enlarge in diameter
1295 by meters per year (dubbed “swiss cheese terrain”: *Byrne and Ingersoll*, 2003b; *Malin et al.*,
1296 2001; *P.C. Thomas et al.*, 2005) and manifests in a spectacular variety of planform shapes
1297 (Figure 13; *P.C. Thomas et al.*, 2016). This annual pit enlargement led to the initial hypothesis
1298 that the SPRC is only a few hundred years old, perhaps indicating that its existence is evidence
1299 of recent climate change (*Byrne and Ingersoll*, 2003a; *Malin et al.*, 2001).

1300 Continued cataloguing and documentation of the SPRC’s diverse landforms (*P.C. Thomas et*
1301 *al.*, 2005; 2009; 2013) culminated in a comprehensive map of its morphology and refined
1302 estimates of its mass balance (*P.C. Thomas et al.*, 2016), including the revelation that some
1303 regions show evidence of net local and regional accumulation over the recent past (*Buhler et al.*,
1304 2017; *P.C. Thomas et al.*, 2016). Importantly, observations indicate that widespread net annual
1305 vertical accumulation may offset local horizontal pit wall ablation, leading to net mass
1306 equilibrium with a complete turnover in material every ~100 martian years (*P.C. Thomas et al.*,
1307 2016). Mass equilibrium is consistent with the observation that Mars’ mean annual pressure is

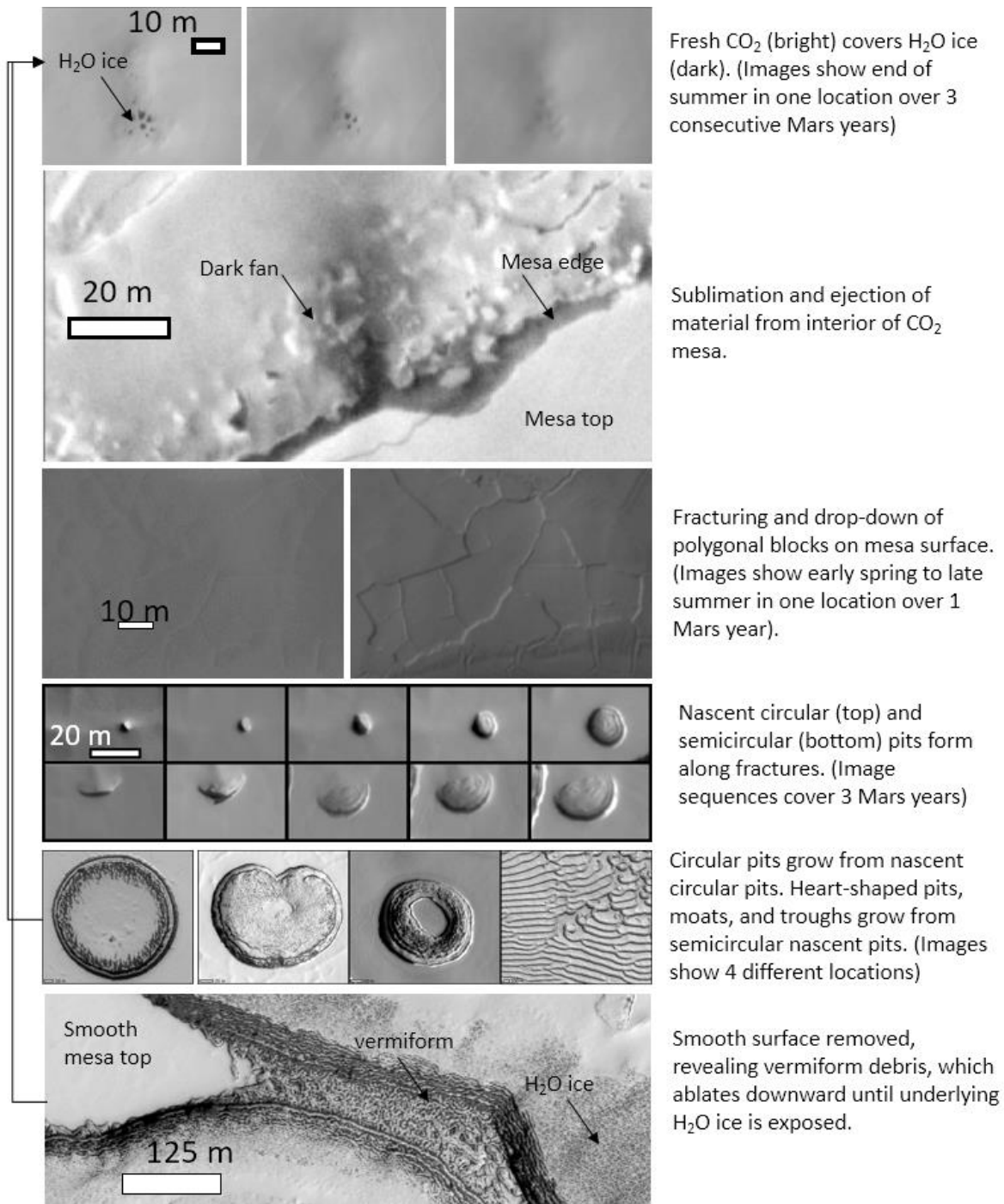
1308 the same to within ~10 Pa between *Viking* lander measurements and the present day (*Haberle et*
1309 *al.*, 2014) and SPRC landform modeling (*Byrne et al.*, 2015). Further refinement of the SPRC's
1310 annual mass balance will require observations with higher vertical accuracy and a longer
1311 baseline (*Buhler et al.*, 2018; *P.C. Thomas et al.*, 2016).

1312 There are four broad categories of SPRC pit morphologies: circular and heart-shaped pits,
1313 linear troughs, and moats (Figure 13; *P.C. Thomas et al.*, 2016). Thus far, quantitative numerical
1314 morphological modeling can only produce circular pits (*Byrne et al.*, 2015). However, a
1315 conceptual model based upon observation indicates that all four main types of morphologies
1316 develop via the interplay of wintertime accumulation and summertime ablation (*Buhler et al.*,
1317 2017). Aeolian reworking (*P.C. Thomas et al.*, 2020) and dust storms (*Becerra et al.*, 2015;
1318 *Buhler et al.*, 2017) may also influence morphologic development and mass balance. Future
1319 maturation of numerical landform models will be essential for quantifying the mass balance of
1320 the SPRC under orbital (i.e., polar insolation) conditions different from the modern day.

1321 In the conceptual model of morphologic development (Figure 13; *Buhler et al.*, 2017),
1322 summertime sunlight causes internal sublimation of the SPRC, leading to the collapse of its
1323 surface, creating fractures. The roughness caused by fracturing leads to enhanced local
1324 sublimation, forming nascent pits. Two types of nascent pits form: circular, where a fracture
1325 widens uniformly at a point, and semicircular, where one side of the fracture falls lower, forming
1326 a steep scarp and a smooth ramp. The circular pits grow larger and stay circular. The
1327 semicircular pits grow into either heart-shaped pits or linear troughs with scrolled edges. The
1328 intersection of growing scarps and slopes can create geometries where moats form.

1329 Ablating pit walls typically leave behind an extended debris ramp of blocky, vermiform
1330 material with a lower albedo relative to the smooth-topped CO₂ mesas (*P.C. Thomas et al.*,
1331 2020). In some regions where the surface of the CO₂ ice reaches a critical roughness, the
1332 morphology degrades into extensive (>1 km diameter) vermiform debris fields that ablate over
1333 the course of typically tens of years until the underlying H₂O ice is exposed (*P.C. Thomas et al.*,
1334 2020). Within a few years, fresh seasonal CO₂ ice survives the summer where the H₂O ice was
1335 exposed, restarting the growth of a new, smooth-topped perennial CO₂ ice mesa.

1336



1337
 1338 **Figure 13. Cycle of CO₂ deposition and ablation in the South Polar Residual Cap (SPRC).**
 1339 **Seasonal CO₂ deposits on exposed H₂O ice, survives summer, accumulates year-over-year to**
 1340 **become perennial SPRC CO₂. Sunlight penetrates and heats CO₂ within mesa, causing material**
 1341 **loss and fracturing of the mesa surface. Nascent pits form along fractures. Pits that are initially**
 1342 **circular in shape grow into larger circular pits. Pits that are initially semicircular in shape**
 1343 **develop into heart-shaped pits, moats, or troughs, depending on local sublimation and**
 1344 **accumulation conditions. Horizontal pit ablation exposes underlying H₂O ice. Where the mesa**
 1345 **surface is sufficiently damaged, vermiform terrain develops, which ablates downward until H₂O**
 1346 **ice is exposed. Then the cycle repeats. Adapted from *Buhler et al. (2017)*.**

1347

1348 **4.1.2 Massive CO₂ Ice Deposit and its capping H₂O ice layer**

1349 Exposed beneath the SPRC and covering the recently discovered Massive CO₂ Ice Deposit
1350 (MCID; *Phillips et al.*, 2011; *Putzig et al.*, 2018) is a <20-m-thick layer of H₂O ice (Figure 14c).
1351 This H₂O ice layer hosts 1- to 100-km-scale circular, scalloped, and trough depressions with
1352 depths up to ~100 m, which likely form due to sublimation and collapse of the underlying MCID
1353 (Figure 14; *Phillips et al.*, 2011). Viscous flow of the MCID likely also shapes the topography of
1354 the H₂O ice layer (*Cross et al.*, 2020; *I.B. Smith et al.*, 2016).

1355 The H₂O ice layer is heavily fractured, which may derive from volumetric collapse due to
1356 sublimation of the underlying MCID (Figure 14; *Buhler et al.*, 2020; *Phillips et al.*, 2011) or
1357 thermal expansion (*Bierson et al.*, 2016). Material exchange between the MCID and the
1358 atmosphere through this H₂O ice layer likely keeps the SPRC in mass balance over obliquity
1359 cycles (*Buhler et al.*, 2020). Based on models, the morphology of the H₂O ice layer may be
1360 changing at ~1 mm/yr rates (*Buhler et al.*, 2020; *Jakosky et al.*, 1990) and hold important clues
1361 to whether this H₂O ice layer is permeable to CO₂ gas. Because the permeability of the H₂O ice
1362 layer is debated (*Manning et al.*, 2019), continued study of the morphology and thermal behavior
1363 of this H₂O ice layer is important for understanding the long-term (>10⁴ yr) behavior of Mars'
1364 global atmospheric pressure and climate.

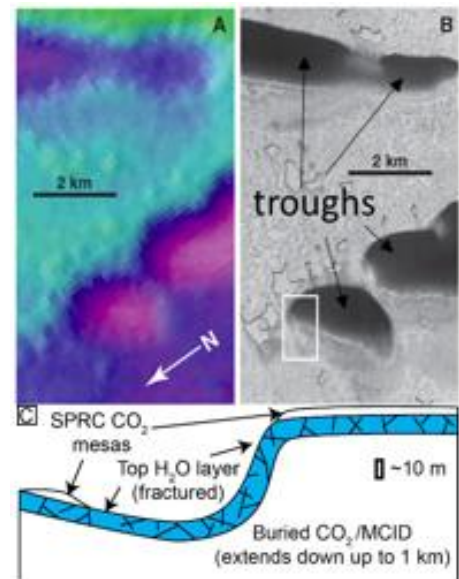
1365

1366 Figure 14. Depressions in the H₂O ice layer beneath the
1367 SPRC near 87° S, 268° E. (A) MOLA topography, ~75 m
1368 elevation range from pink (low) to green (high). (B)
1369 Context Camera image of the same location. H₂O ice
1370 (dark) is exposed in the troughs through windows in SPRC
1371 CO₂ ice mesas (bright). (C) Schematic cross section of
1372 SPRC, H₂O ice layer, and the MCID, illustrating proposed
1373 layering. A and B modified from *Phillips et al.* (2011).

1374

1375 **4.1.3 North Polar hummocky H₂O ice surface**

1376 The surface of the perennial North Polar Residual Cap
1377 (NPRC) is primarily H₂O ice, as opposed to the CO₂ ice
1378 deposits in the south (*P.C. Thomas et al.*, 2000). The H₂O
1379 ice has a rough, hummocky texture of ~10 m-scale semi-regular depressions and mounds
1380 (*Nguyen et al.*, 2020; *Parra et al.*, 2017; *Russell et al.*, 2019). Although observations of changes
1381 within the polar region indicates there are seasonal and interannual periods and locations of both



1382 net deposition and ablation (e.g., *Brown et al.*, 2016; *Calvin et al.*, 2015), other observations
1383 have been proposed to indicate that the current NPRC surface is underdoing net, long-term
1384 ablation. For example, large-grained ice dominates the NPRC at the end of northern summer,
1385 possibly implying exhumation of older, sintered ice (*Langevin et al.*, 2005); however, the ice also
1386 has a low dust content, indicating a lack of the dust lag that might be expected if the ice were
1387 ablating (*Langevin et al.*, 2005). Another example is that *Milkovich et al.* (2012) observed that
1388 the wavelength of the hummocky texture has a positive correlation with elevation and latitude,
1389 which they interpreted as indicating the formation of the hummocky texture via ablation.
1390 However, modeling by *Wilcoski and Hayne* (2020) indicates that hummocks would form in both
1391 ablational and depositional settings and, further, that hummock wavelength correlates primarily
1392 with age regardless of net ablation or deposition; they find that the typically observed ~10 m
1393 hummock wavelengths are reached after ~1 kyr. This timescale is consistent with ~1.5 kyr ages
1394 derived from cratering statistics (*Landis et al.*, 2016). Ablation and deposition of H₂O ice also
1395 modify craters on the NPRC, with the current crater population being estimated to have
1396 accumulated within the last ~20 kyr and ice accumulation rates within craters of ~3–4 mm/yr
1397 (*Banks et al.*, 2010).

1398 Wind is also likely a driver for evolving geomorphology of icy features on the NPRC
1399 because it can influence volatile fluxes at the surface, vapor transport, and distribution of both
1400 CO₂ and H₂O ice. However, most of these processes driven by both wind and sublimation are not
1401 directly observable due to very slow rates. Large-scale features like the chasmae/spiral troughs in
1402 the NPRC are thought to have formed into their present state over millions of years of erosion by
1403 katabatic winds and asymmetric insolation/sublimation (e.g., *Bramson et al.*, 2019; *Howard*,
1404 2000; *Smith and Holt*, 2010). Smaller-scale periodicities in the landscape may be related to
1405 sublimation dynamics of perennial ice layers interacting with the winds over thousands of years
1406 (e.g., *Bordiec et al.*, 2020; *Herny et al.*, 2014; *Howard*, 2000; *Nguyen et al.*, 2020).

1407 Because the NPRC is the uppermost layer of the NPLD (*Tanaka et al.*, 2005), further study of
1408 NPRC surface morphology evolution will be important for understanding how layers
1409 accumulated in the NPLD, as well as how structure of the layers may record aeolian and
1410 sublimation interactions when that layer of material was exposed on the surface, and how to
1411 interpret the climate under which those layers formed (*I.B. Smith et al.*, 2020). The layers within
1412 the NPLD (and in the Southern Polar Layered Deposits (SPLD)) are of high interest for Mars

1413 polar and climate studies because they are thought to be analogous to the layers found within
1414 terrestrial ice cores and thus record martian climate cycling (*I.B. Smith et al.*, 2020).

1415 1416 **4.2 Present/recent subsurface water ice**

1417 **4.2.1 Present-day water ice stability**

1418 The fundamental principles controlling subsurface H₂O ice stability have been understood for
1419 some time (e.g., *Smoluchowski*, 1968). Given some water vapor content in the atmosphere, ice
1420 will be deposited in locations that are below the frost point temperature and will sublime at
1421 locations that are warmer. Integrated over the course of a martian year, ice is stable at locations
1422 where the average water vapor pressure over ice is less than or equal to that in the atmosphere;
1423 these locations will also experience net deposition. At equatorial latitudes under current
1424 conditions, temperatures are too warm for ice to be stable, and ice does not accumulate. At
1425 middle to high latitudes, peak surface temperatures may still be high, but annual and seasonal
1426 variations are damped in the subsurface. The equilibrium water vapor pressure is nonlinearly
1427 dependent on temperature, which allows ice to become stable in the shallow subsurface, at a
1428 depth that becomes shallower with increasing latitude.

1429 The development of increasingly sophisticated maps of the distribution of stable ice, based
1430 on the above framework, is summarized by *Mellon et al.* (2004). Recent ice stability maps have
1431 also been produced by *Chamberlain and Boynton* (2007), *Schorghofer and Aharonson* (2005),
1432 and *Steele et al.* (2017). Broadly, these all place the present-day stability boundary near 45–60°
1433 latitude, and show similar longitudinal variations correlated with surface albedo and thermal
1434 inertia. Differences in ice stability predictions are largely due to assumptions of near-surface
1435 atmospheric water vapor content and past atmospheric conditions.

1436 Mars' orbit varies over time, leading to H₂O ice sublimation and deposition as the global ice
1437 stability field evolves in response. *Dundas et al.* (2014) found that ice newly exposed by fresh
1438 impact craters persisted for longer than expected, given the currently measured atmospheric
1439 water vapor column. Their observations indicated that either the lowest-latitude ice has not
1440 equilibrated with the current climate or that the ice is stabilized by local factors, such as
1441 enhanced near-surface water vapor concentration. Remnant out-of-equilibrium ice that was
1442 deposited recently (within ~1 Ma) provides one possible explanation for the low-latitude icy
1443 craters (*Schorghofer and Forget*, 2012). Similar modeling by *Bramson et al.* (2017) concluded
1444 that such ice could be considerably older (>10s Ma) than estimated by *Schorghofer and Forget*

1445 (2012) if the ice started sufficiently thick and has also been protected by thick lag deposits built
1446 up by dust and lithic debris released from the sublimating ice.

1447 The current solutions for Mars' orbital variations (*Laskar et al.*, 2004) indicate that ~4 Ma,
1448 Mars entered a low obliquity epoch in which mid-latitude ice has generally been less stable and
1449 polar ice has been more stable. Correspondingly, modeling and observations indicate net
1450 transport of ice from the middle latitudes to the poles over this timeframe (e.g., *Levrard et al.*,
1451 2007; *I.B. Smith et al.*, 2016). However, higher frequency (~50 to 100s of kyr) periodicities in
1452 Mars' orbital parameters (particularly obliquity) likely generate many excursions away from the
1453 long-term average conditions. Therefore, the spatial distribution of ice deposition and
1454 sublimation has likely been very dynamic over ~50 to 100 kyr timescales. Understanding this
1455 dynamic movement of ice is essential to deciphering the evolution of icy terrains. The modeling
1456 described above shows that the current distribution and stability state of mid-latitude ice could
1457 place important constraints on Mars' recent past climate. Such model predictions can be coupled
1458 with observations of landforms (such as sublimation thermokarst, patterned ground, and viscous
1459 flow features) to improve interpretation of such landforms or to test the climate condition
1460 assumptions.

1461

1462 **4.2.2 Present-day water ice distribution**

1463 Presently, exposed water ice is only stable on the surface at the poles; it is stable at lower
1464 latitudes when buried in the subsurface under an insulating, desiccated coating of dust and/or
1465 regolith. Data from the Mars Odyssey Neutron Spectrometer show the near subsurface (within
1466 the upper meter) at middle and high latitudes to be hydrogen rich, which has been attributed to
1467 the presence of water ice (*Boynton et al.*, 2002; *Pathare et al.*, 2018). As discussed in §4.3–4.4,
1468 numerous geomorphological features, including glacial and viscous flow features, thermal
1469 contraction polygons, and ice-loss (also referred to as thermokarstic) terrains, suggest a recent
1470 and/or present-day ice-rich subsurface across most of the mid-latitude plains. Thermal analysis
1471 indicates widespread water ice at latitudes as low as 35°N/45°S, with high lateral ice depth
1472 variability—sometimes buried only a few centimeters below sand-like material—and correlated
1473 with putatively periglacial features (*Piqueux et al.*, 2019).

1474 Due to warm temperatures at the equator, in general, the ice must be buried at greater depth
1475 for increasingly-equatorward locations (e.g., *Fanale et al.*, 1986; *Leighton and Murray*, 1966;

1476 *Paige*, 1992). For example, the Phoenix lander excavated nearly pure water ice in the upper
1477 centimeters of the surface at 68°N (*P.H. Smith et al.*, 2009). Recently-discovered scarps near
1478 ~55° latitude in both the northern and the southern hemispheres expose thick, massive ice that
1479 appears to extend to within a meter of the surface in high-resolution images (*Dundas et al.*,
1480 2018). These slopes can be several kilometers long and over 100 m tall. Bare ice at these
1481 locations likely are actively subliming; *Dundas et al.* (2018) observed boulders falling from one
1482 scarp and estimated that the sublimation rate was on the order of millimeters per year.
1483 Additionally, H₂O ice spectral features at a second scarp weakened over the course of the
1484 summer, suggesting the gradual accumulation of a thin sublimation lag of dust. This ice loss
1485 results in ongoing slope retreat and the growth of depressions, which are morphologically
1486 distinct from the thermokarst features discussed below (§4.3), likely because a bare ice surface is
1487 maintained in these landforms (*Dundas et al.*, 2018).

1488 Recent (<15 years old) impact craters have exposed and excavated nearly-pure water ice
1489 (likely >90% ice by volume) within a meter of the surface as close to the equator as 39°N (*Byrne*
1490 *et al.*, 2009; *Dundas et al.*, 2014). The appearance of these exposures slowly fades over time as
1491 the exposed ice sublimates (*Dundas and Byrne*, 2010). Some of the ice remains distinctive in color
1492 for several martian years (*Dundas et al.*, 2014), indicating clean ice (>90% water ice by volume)
1493 with a low lithic content.

1494 Ice is not expected to be stable near the equator at any depth, though the most equatorward
1495 boundary of subsurface mid-latitude ice is still an outstanding question and unstable, sublimating
1496 ice may exist. Recent efforts have focused on integrating numerous datasets and techniques to
1497 constrain the distribution of mid-latitude ice, especially from the perspective of its utilization as
1498 an in situ resource for crewed missions, and include studies across swaths of the northern plains
1499 regions (*Orgel et al.*, 2019; *Ramsdale et al.*, 2019; *Sejourne et al.*, 2019) as well The Mars
1500 SWIM (Subsurface Water Ice Mapping) Project (swim.psi.edu). So far, the areas found to be
1501 most consistent with abundant water ice occur poleward of ~40°N, in the northern plains region
1502 of Arcadia Planitia, where widespread ground ice was previously inferred in radar sounding and
1503 geomorphic crater studies (*Bramson et al.*, 2015; *Viola et al.*, 2015), and within an extensive
1504 network of debris-covered glaciers in the Deuteronilus Mensae region (*Petersen et al.*, 2018).
1505 This is generally more poleward than the regions focused on by human exploration planners, due
1506 to other constraints on human access and operations (e.g., *ICE-WG*, 2015).

1507
1508
1509
1510
1511
1512
1513
1514
1515
1516
1517
1518
1519
1520
1521
1522
1523
1524
1525
1526
1527
1528
1529
1530
1531
1532
1533
1534
1535
1536
1537
1538

4.3 Sublimation thermokarst

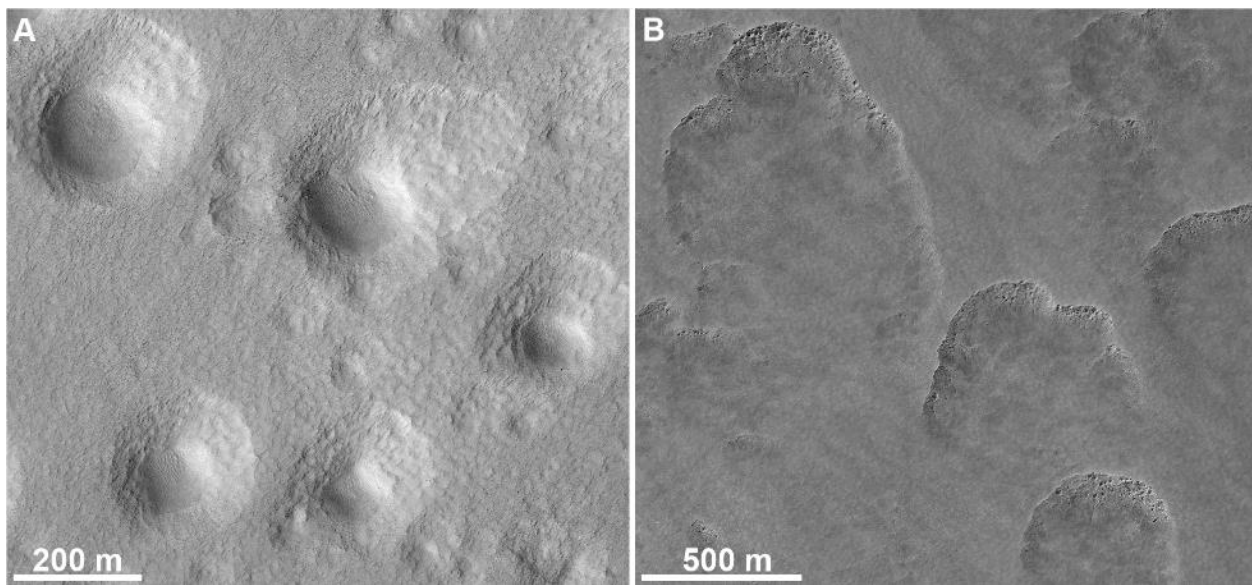
Candidate thermokarstic landscapes were identified in images dating back to the Mariner and Viking missions (*Anderson et al.*, 1973; *Costard and Kargel*, 1995; *Sharp*, 1973). These landforms result from surface collapse following loss of subsurface ice, leading to rimless depressions that are often hundreds of meters in size, and meters to tens of meters deep. Scalloped features (e.g., *Dundas et al.*, 2015b; *Lefort et al.*, 2009; 2010; *Morgenstern et al.*, 2007; *Séjourné et al.*, 2011; 2012; *Soare et al.*, 2007; 2008; 2011; *Ulrich et al.*, 2010; *Zanetti et al.*, 2010) and expanded craters (e.g., *Dundas et al.*, 2015b; *Viola et al.*, 2015; *Viola and McEwen*, 2018) are considered to be some of the most iconic examples of ice loss features (Figure 15). Initial interpretations included formation via melting akin to terrestrial thermokarst and alases (*Soare et al.*, 2007; 2008; 2011), but the present general consensus is that these are formed via sublimation.

Given the importance of temperature on ice stability, evolution of the terrain often proceeds through enhanced retreat of the warmer slopes. Under the present obliquity those are equator-facing. This leads to asymmetric landforms, with scalloped terrains often being elongated in the direction of retreat and exhibiting shallower slopes on the equatorward-facing slopes. It has been debated whether the scalloped depressions form primarily via retreat of the pole-facing slope at high obliquity (*Séjourné et al.*, 2011; *Ulrich et al.*, 2010) or retreat of the equator-facing slope under conditions similar to the present (*Lefort et al.*, 2009; *Morgenstern et al.*, 2007; *Zanetti et al.*, 2010). More complicated landscapes can form through the merging of the features, and the intervening terrain between collapse features is generally thought to retain the ice-rich subsurface unit.

Numerical landscape evolution modeling (*Dundas*, 2017; *Dundas et al.*, 2015b) shows that standard martian ice-stability theory (§4.1) can produce both scalloped-depression and expanded-crater morphologies via sublimation. The model is driven by surface topography and a high subsurface ice content, which produce uneven sublimation and an evolving landform. In the model, retreat of both pole- and equator-facing slopes occur, although the latter appears to be most important. The subsurface ice loss is triggered by some local disturbance (such as an impact, in the case of expanded craters). Modeling of the process suggests that these landforms may take 10^4 – 10^5 years or more to form, though the development of a sublimation lag will eventually help preserve these landforms from additional ice loss (*Dundas et al.*, 2015b).

1539 These landforms likely develop gradually over tens to hundreds of thousands of years
1540 (*Dundas, 2017; Dundas et al., 2015b*) since the surface debris slows sublimation and protects the
1541 ice from high peak temperatures. As such, landform evolution is unlikely to be occurring at
1542 scales that are observable from orbit, unless slow ice loss occasionally triggers larger mass
1543 wasting events. However, given the likelihood of out-of-equilibrium ice (§4.1), it is likely that at
1544 least some of these sublimation-thermokarst features are evolving at present. It is even possible
1545 that this could occur in ice that is generally in equilibrium, since the process will work on any
1546 slope that is locally out of equilibrium.

1547



1548 Figure 15. (A) Expanded secondary craters on the northern plains. Note funnel shape suggesting
1549 widening and shallowing of the rim. HiRISE image ESP_045303_2320. (B) Scalloped
1550 depressions south of the Hellas basin (58.1° S, 74.0° E). Note the steep pole-facing slopes.
1551 HiRISE image ESP_049581_1215. In both images, illumination is from the left and north is up.
1552
1553

1554 4.4 Patterned Ground

1555 Polygonally patterned ground, containing polygons with a wide large range of diameters
1556 (meters to tens of kilometers), is one of the most common and, based on superposition, youngest
1557 landforms on Mars. Polygonally patterned ground is either sorted (with surface patterns defined
1558 by rock fragments) or unsorted landforms (with surface patterns defined by thermal contraction
1559 cracks without sediment motion) (*French, 2007*). On Earth, sorted patterned ground is most
1560 commonly found in fine-grained sediments overlain by coarser rock fragments because these are
1561 the most susceptible to frost heave and sorting as a function of grain size during freeze-thaw
1562 cycling (*Kessler and Werner, 2003*). In addition to the polygons, stripes, piles, and other

1563 morphologies found on Earth are also found on Mars, and with transitions between them
1564 occurring in the same way as on Earth, lending support for the “convection” model that is freeze-
1565 thaw sorting (e.g., *Gallagher and Balme, 2011; Gallagher et al., 2011; Soare et al., 2016*),
1566 although such processes can also occur on Earth without freeze-thaw (e.g., *Sletten et al., 2003*).
1567 The limit of HiRISE resolution (Table 1) necessitates that all clasts used to define sorted
1568 patterned ground consists of boulder-sized or larger sediments. *Soare et al. (2019)* also used
1569 locality with potential pingos in such feature identification.

1570 Non-sorted polygonally patterned ground (thermal contraction crack polygons) are
1571 widespread on Mars and dominate surfaces poleward of ~30-40° latitude (*Levy et al., 2009b*;
1572 *Mangold, 2005*) where ground ice is abundant (*Boynton et al., 2002*) and where thawed active
1573 layers (portions of the soil column that seasonally freeze and thaw) have been rare to absent on
1574 flat-lying surfaces over at least the past ~5 Ma (*Kreslavsky et al., 2008*). Thermal contraction
1575 crack polygons on Mars are overwhelmingly high-centered features with low bounding troughs,
1576 although examples of low-centered polygons with elevated shoulders occur in a few locations
1577 (Figure 16) (*Soare et al., 2014; 2018*). The more common high-centered morphology indicates
1578 that either excess ground ice has escaped via sublimation along the fracture traces, and/or that
1579 infilling of fractures by fines is slow compared to subsurface ice loss. Alternatively, the center
1580 might be deformed upwards by pressures created by aggrading sand wedges (e.g., *Sletten et al.,*
1581 *2003*).

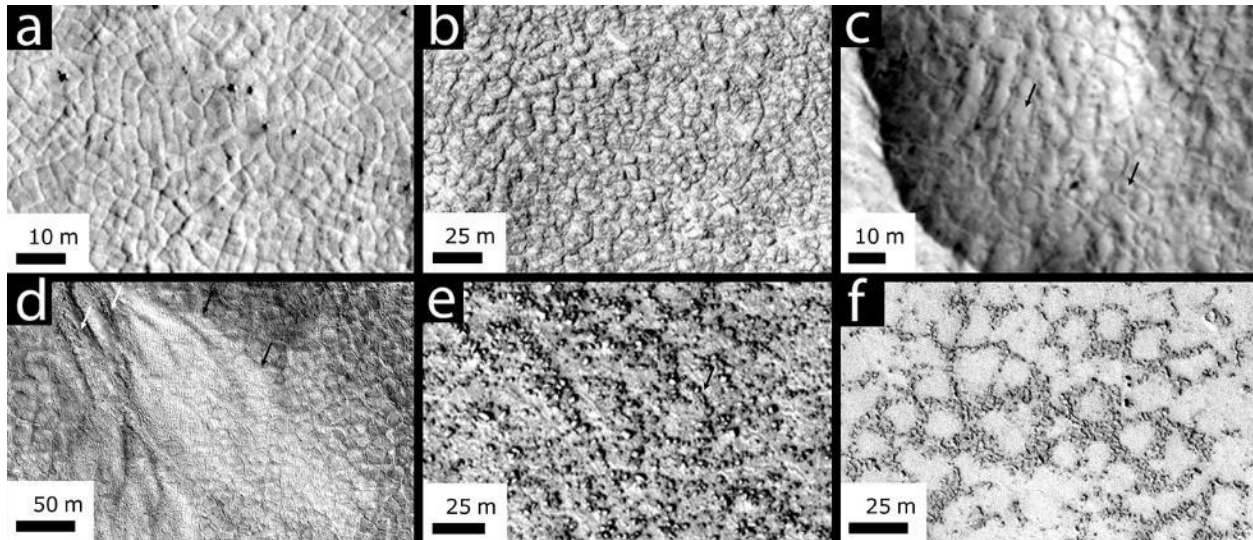
1582 Thermal contraction cracks can form under modern martian climate conditions (*Mellon,*
1583 *1997*), suggesting that polygons are actively forming and expanding locations where ice-rich
1584 permafrost and/or buried ice is present (*Mellon et al., 2008*). Continued formation and growth of
1585 thermal contraction crack polygons is consistent with observations that polygon fracture
1586 networks crosscut many young deposits on Mars, including gully fans (*Levy et al., 2010*) (Figure
1587 16). In many locations, ice-rich mantling deposits (e.g., *Head et al., 2003*) are extensively
1588 fractured, with polygon troughs cross-cutting almost all but the most recent impact craters (*Byrne*
1589 *et al., 2009; Levy et al., 2010*), suggesting that mantling units may have crater retention ages of
1590 10-100 kyr.

1591 While there is little debate about the origin and current activity of unsorted patterned ground
1592 on Mars, the widespread existence and mechanism of formation for sorted patterned ground are
1593 both topics of considerable debate, particularly as to whether freeze-thaw is necessary for its

1594 formation. Potential sorted patterned ground consists of three main groups: high-latitude
1595 boulders concentrated in thermal contraction crack troughs (*Levy et al.*, 2009b; *Mellon et al.*,
1596 2008; *Orloff et al.*, 2011), clasts arranged in boulder halos (*Barrett et al.*, 2017; *Levy et al.*,
1597 2018), and low-latitude albedo networks (*Balme et al.*, 2009). Boulders may be sorted into
1598 polygon troughs at high latitude via slumping of over-steepened trough shoulders (*Levy et al.*,
1599 2010; *Mellon et al.*, 2008), seasonal frost-related locking and sliding mechanisms (*Orloff et al.*,
1600 2013), or differential inflation of soil profiles at polygon troughs vs. centers (*Levy et al.*, 2018).
1601 At middle latitudes where boulders are present in rock rings called boulder halos, boulders
1602 commonly cluster in beaded networks (Figure 16), some of which are confined to polygon
1603 troughs and some of which are not, leading (*Barrett et al.*, 2017) to interpret these sites as
1604 possible evidence of freeze-thaw-driven sorting under near-recent climate conditions. Finally,
1605 equatorial examples of potential clastic networks have been identified near Cerberus Fossae
1606 (*Balme et al.*, 2009). These occur in the absence of thermal contraction crack polygons and have
1607 been interpreted as evidence of relict freeze-thaw heaving mechanisms. A lack of meter-scale or
1608 larger boulders in these deposits (Figure 16) makes these deposits less comparable to the sorted
1609 clasts observed in the other two examples, and their proximity to volcanic deposits associated
1610 with Cerberus Fossae outflow raises the possibility that they are features of volcanic origin.

1611 On Earth, sorted patterned ground can form on timescales of years to millennia (*Hallet*,
1612 2013), while unsorted patterned ground typically matures over millennial to million-year
1613 timescales (*Levy et al.*, 2006; *Marchant et al.*, 2002; *Sletten et al.*, 2003). Rates of thermal
1614 contraction crack wedge expansion typically are on the order of millimeters per year, challenging
1615 efforts to detect change in martian patterned ground. However, it is likely that patterned ground
1616 formation and evolution—especially thermal contraction crack fracturing and wedge growth are
1617 occurring on modern Mars and are actively working to resurface middle- and high-latitude
1618 landscapes.

1619



1620 Figure 16. Polygonally patterned ground on Mars. (a) High-centered, unsorted patterned ground.
 1621 Portion of HiRISE image PSP_001474_2520. (b) High-centered, unsorted patterned ground.
 1622 Portion of HiRISE image PSP_003217_1355. (c) Example of low-center / raised-rim unsorted
 1623 patterned ground. Arrows point to low-centered polygons. Portion of HiRISE image
 1624 PSP_002175_2210. (d) Bright gully fan material (black arrows) emerging from a gully channel
 1625 (white arrows) that has been crosscut by underlying thermal contraction cracks. Portion of
 1626 HiRISE image PSP_001846_2390. (e) Candidate sorted patterned ground. Portion of HiRISE
 1627 image ESP_017580_2460. (f) Candidate low-latitude, sorted patterned ground. Portion of
 1628 HiRISE image PSP_004072_1845.
 1629

1630

1631 4.5 Open questions for long-term sublimation of ice

1632 A primary goal of Mars polar science investigations is to unlock the climate history stored in
 1633 Mars' polar deposits (*I.B. Smith et al.*, 2020). Improved estimates of the modern annual polar
 1634 CO₂ and H₂O ice and nonvolatile mass balance, coupled with a better understanding of the
 1635 annual reworking of the SPRC and NPRC surface, will be essential to interpreting the climatic
 1636 conditions encoded in layers of the NPLD and SPLD. Improved observational resolution,
 1637 cadence, and baseline of observations as well as development of physics-based numerical
 1638 simulations that are capable of reproducing morphologic observations of polar landforms will
 1639 both be critical to this endeavor. Additionally, the net annual mass flux of polar material remains
 1640 poorly constrained. Improved measurement of atmospheric transport of volatiles and dust as well
 1641 as observation and modeling of surface morphology (including its evolution), seasonal frost layer
 1642 evolution (§3.4), and thermal cycles of the surfaces of the SPRC and NPRC will greatly enhance
 1643 our understanding of the current net annual polar mass balance.

1644 Outside of the polar region, a global map of where ice is presently found in the subsurface
 1645 (and at what depth) along with the structure, volume, and purity of that ice is needed. This is of

1646 particular interest for understanding where ice is currently aggrading or sublimating. Improved
1647 knowledge of the near-surface water vapor concentration is also needed to understand the
1648 equilibrium distribution of ice (i.e., where it “should” be). Phoenix measurements suggest a
1649 stronger atmosphere-regolith interchange in the martian arctic than at lower latitudes (*Fischer et*
1650 *al.*, 2019) and orbital column measurements are challenged by possible near-surface
1651 concentration of vapor (*Tamppari and Lemmon, 2020; Tamppari et al., 2010*). Also needed is
1652 characterization of the surface materials over this ice—especially its depth and bulk
1653 thermoconductive properties. More refined information about the structure of the lag (and
1654 variations in its thermoconductive properties) would provide additional constraints for
1655 development and testing of models related to the preservation of ice (Figure 17). In particular, an
1656 understanding of the impact of the dust component of lags would contribute to estimates of dust
1657 accumulation through recent martian history, feeding new constraints into studies of present and
1658 past climates, how dust can influence ice layer evolution and accumulation, and sediment
1659 transport pathways and reservoir amounts.

1660 Generally, improved measurements of the thermoconductive, mechanical, and compositional
1661 properties of regolith where discussed geomorphologies and/or ground ice are found would
1662 enable improved modeling and laboratory investigations of the processes discussed here.
1663 Improved process models would in turn enable improved interpretation of these landforms,
1664 regarding their formative environments and ages. In general, global identification of these
1665 geomorphological features is complete (or can be completed) down to the decameters-scale
1666 within global CTX imagery; higher resolution images are needed to map polygons and other
1667 smaller morphologies.

1668 Addressing these open science questions would also contribute towards high-priority human
1669 exploration questions regarding in situ resource utilization (ISRU). Water ice deposits within a
1670 few meters of the surface are of high interest for human and fuel needs, and regolith (including
1671 sublimation lag deposits) properties would feed into mining and operations designs.

1672

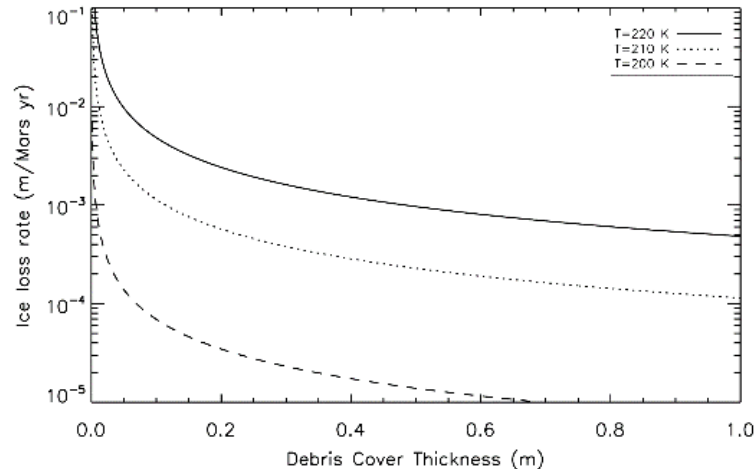


Figure 17. Retreat rate of ice under lags of varying thickness at T=200, 210, and 220 K, assuming background atmospheric water vapor with a frost point of 198.5 K. Calculation follows *Hudson et al. (2007)*.

1686

1687 **5 Mass-wasting aided landforms**

1688 In addition to the wind- and frost-driven features discussed above that involve mass wasting
 1689 (§3.2: gullies, dune alcoves) and gravity-driven transport (§3.3: linear gullies), here we discuss
 1690 two additional examples of observed downslope movement of materials. For these two cases, a
 1691 suite of processes may be involved in initiation and enhancement of the transport; gravity is the
 1692 only well-established driver. Recurring slope lineae (§5.1) were originally proposed to be driven
 1693 by liquid water, but, as is discussed, the initiation mechanism for the formation of these features
 1694 is not yet conclusively established and current observations may be more consistent with a dry
 1695 mass-wasting mechanism. Avalanches and rockfalls (§5.2) both obviously occur due to gravity,
 1696 with initiation mechanisms potentially related to thermal stresses and, from at least icy slopes,
 1697 sublimation.

1698

1699 **5.1 Recurring Slope Lineae (RSL)**

1700 Recurring slope lineae (RSL; Figure 18; SOM 7) are relatively dark linear markings on steep
 1701 slopes with low albedos (indicating relatively little coverage by bright dust), typically originating
 1702 at bedrock outcrops (*McEwen et al., 2011; 2014*). Individual lineae are up to a few meters wide
 1703 and up to 1.5 km long. The lineae grow incrementally or gradually over several months, usually
 1704 during the warmest time of year, then fade (and typically disappear) when inactive. RSL recur in
 1705 multiple martian years (by definition) over the same slopes, but not necessarily every year and
 1706 not necessarily at the exact same locations. RSL often follow pristine small gullies or channels.
 1707 Hundreds of individual lineae may be present over a local slope, and thousands are captured in
 1708 single HiRISE images in some cases. A confirmed site (each HiRISE image sequence is
 1709 considered a site) is where repeat images show incremental growth and fading, repeated over

1710 multiple martian years. A candidate site has similar-looking features in the same settings and
1711 seasons as typical RSL, but repeat imaging of the site is insufficient to document growth, fading,
1712 and recurrence. There were at least 98 confirmed and 650 candidate sites prior to MY34
1713 (*Stillman, 2018*) (Figure 2).

1714 RSL are common in (1) the southern middle latitudes (-60° to -30° latitude) where they are
1715 most active in southern summer on generally equator-facing (including east- and west-facing)
1716 slopes; (2) the equatorial regions where activity is usually coincident with the local slope
1717 receiving peak insolation; and (3) in Acidalia/Chryse Planitia and other northern middle latitudes
1718 with activity in northern spring and summer (*McEwen et al., 2011; 2014; Stillman, 2018;*
1719 *Stillman and Grimm, 2018; Stillman et al., 2014; 2016; 2017*). However, exceptions to these
1720 timing patterns do occur (*Dundas, 2020a; Ojha et al., 2014*).



1721

Figure 18. Hundreds of RSL present on the northwest-facing slope of a 935 m diameter simple impact crater, imaged at L_s 313° (southern summer) of MY34, located at 47.3° S, 1.3° E. Black arrows point at the lowermost tips of a few lineae, which begin near the crater rim. The full HiRISE image shows hundreds of

1738

1739 dust devil tracks, indicating fresh dust deposition during the MY34 planet-encircling dust event
1740 (PEDE) in southern spring. Color composed of infrared, red, and blue-green bandpasses,
1741 stretched to increase contrast. North is up and illumination is from the northwest (upper left).
1742 [ESP_058208_1325](#).

1743
1744 Many publications have favored wet models for RSL activity (e.g., *Chevrier and Rivera-*
1745 *Valentin, 2012; Grimm et al., 2014; Huber et al., 2020; Levy, 2012; McEwen et al., 2011; 2014;*
1746 *Ojha et al., 2013; 2014; 2015; Stillman, 2018; Stillman and Grimm, 2018; Stillman et al., 2014;*
1747 *2016; 2017; Wang et al., 2019*). The darkening and gradual growth resembles seeping water, and
1748 the fading could be explained by drying. RSL appearance and temporal behavior are similar to

1749 that of water tracks in Antarctica (*Dickson et al.*, 2013; *Levy*, 2012). The surface temperatures
1750 corresponding to RSL activity are above the freezing points for salty solutions, which can be as
1751 low as nearly 200 K (e.g., *Möhlmann and Thomsen*, 2011). However, explaining the source of
1752 sufficient water for seepage is extremely difficult in the present-day martian environment (e.g.,
1753 *Dundas et al.*, 2017, and references therein). Evidence for water playing some role in RSL from
1754 detection of rare hydrated salts (*Ojha et al.*, 2015) now appears to be a data processing artefact
1755 (*Leask et al.*, 2018; *Vincendon et al.*, 2019). Deep groundwater may persist in Mars and might
1756 occasionally reach the surface (*Abotalib and Heggy*, 2019; *Stillman et al.*, 2016), but RSL are
1757 found over a wide range of elevations and settings not consistent with natural groundwater
1758 discharge, including the tops of isolated peaks and ridges (*Chojnacki et al.*, 2016). Highly
1759 deliquescent salts are known to exist on Mars and may temporarily trap atmospheric water in
1760 extremely small quantities, perhaps sufficient to darken the surface (*Heinz et al.*, 2016), but not
1761 sufficient for seepage down slopes (*Gough et al.*, 2019a; 2019b). Some workers have speculated
1762 that small quantities of water could trigger granular flows (*Dundas et al.*, 2017; *McEwen*, 2018;
1763 *Wang et al.*, 2019). Relatively small quantities of boiling water may trigger granular flows
1764 (*Herny et al.*, 2019; *Massé et al.*, 2016; *Raack et al.*, 2017), but these quantities are far more than
1765 can be supplied by the martian atmosphere with a typical water column abundance of 10
1766 precipitable microns (*M.D. Smith*, 2008). Other hypotheses are that mass wasting may occur
1767 when damp surface materials dehydrate (*Schorghofer et al.*, 2002) or from migration of
1768 subsurface brines (*Bishop et al.*, 2020). Surface frost (CO₂ and H₂O) forms in only some RSL
1769 source regions and will sublime before RSL typically become active (*Schorghofer et al.*, 2019).

1770 Some recent papers have favored dry RSL models. *Edwards and Piqueux* (2016) found that
1771 the thermal signature of RSL-bearing slopes at Garni crater was consistent with <3% water,
1772 although *Stillman et al.* (2017) pointed out that none of the thermal observations were
1773 synchronous with observations of sufficient coverage by lineae to enable thermal detection.
1774 *Schmidt et al.* (2017) suggested that RSL could operate via granular flows driven by a Knudsen-
1775 pump gas-flow mechanism enhanced by distinct shadowing. *Dundas et al.* (2017) found that
1776 RSL terminate on slopes matching the dynamic angle of repose for dry sand. *Tebolt et al.* (2020)
1777 reported RSL that terminate on lower slopes, but *Dundas* (2020a) noted that some of their
1778 reported locations do not correspond to RSL. *Stillman et al.* (2020) concluded that the slopes in
1779 Garni crater were consistent with granular flows within slope errors; *Munaretto et al.* (2020)

1780 reached the same conclusion about RSL in Hale crater. *Schaefer et al.* (2019) reported evidence,
1781 including relative albedo analysis that RSL in Tivat crater fade similarly to boulder and dust
1782 devil tracks, potentially due to dust removal from the larger region, and proposed that RSL are
1783 dry features that mobilize dust. *Vincendon et al.* (2019) also proposed that RSL are due to dust
1784 removal based on relationships between RSL and aeolian activity. *Dundas* (2020a) proposed that
1785 RSL are grainflows where sand is seasonally replenished by the uphill migration of ripples, most
1786 of which are smaller than the 25-30 cm/pixel scale of HiRISE. Following the MY34 planet-
1787 encircling dust event (PEDE) in 2018, there was a pronounced increase in RSL activity (>5x the
1788 activity in other years), showing a close connection to recent atmospheric deposition of dust
1789 (*McEwen et al.*, 2019; 2021). Dust lifting activity (also forming dust devils) may directly cause
1790 RSL formation on steep slopes, and/or dust storms may correlate with some other factor, such as
1791 sand transport, that facilitates later RSL activity (*Dundas*, 2020a).

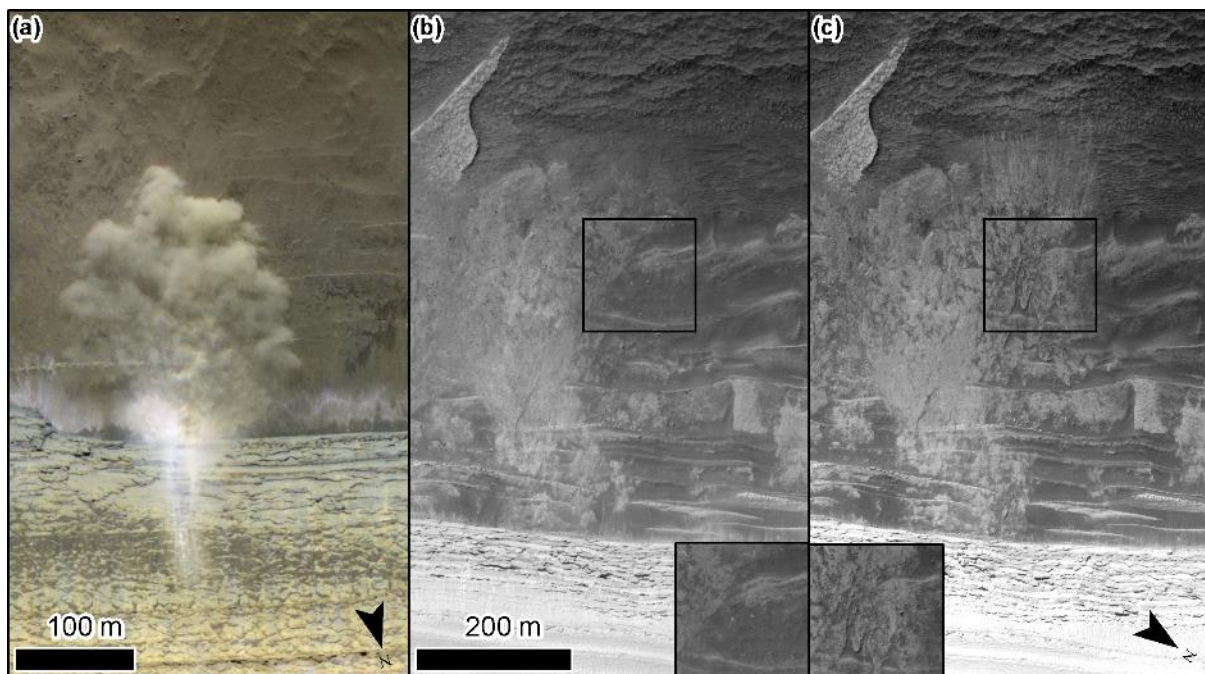
1792

1793 **5.2 Avalanches/block falls from rocky and icy slopes**

1794 Both individual fragments and clouds of material have been mobilized down steep slopes and
1795 cliffs of both rock and ice on Mars. Rocks tumbling down hillslopes leave bounce and roll-marks
1796 in their wake, whose distribution around impact craters has been used to infer that thermal stress
1797 is a necessary pre-conditioning factor for their release (*Tesson et al.*, 2020). Other studies have
1798 used the presence of these rockfall tracks as evidence of seismic activity on Mars (*Roberts et al.*,
1799 2012; *Brown and Roberts*, 2019; *Senthil Kumar et al.*, 2019). Rocks have also been observed to
1800 move downslope without leaving a visible track on the surface, in a manner that suggests an
1801 independent rock-transport process (*Dundas et al.*, 2019b; *Raack et al.*, 2020). Precise timing
1802 data are often lacking and sometimes contradictory, therefore further work is needed to
1803 investigate connections between rock breakdown and frost accumulation/sublimation or other
1804 seasonal effects.

1805 Avalanches and blocks (Figure 19) have been observed to descend from the steep scarps of
1806 the northern polar ice cap of Mars (*Fanara et al.*, 2020a; 2020b; *Herkenhoff et al.*, 2007; *Russell*
1807 *et al.*, 2008;). These appear to be two separate categories of mass movement because the
1808 avalanches are rarely associated with mobilized blocks and spectral evidence suggests they could
1809 simply be mobilizing the surface seasonal frost deposits (*Pommerol et al.*, 2013). Avalanches
1810 observable at the time of day of HiRISE observations occur exclusively in early spring (*Russell*
1811 *et al.*, 2014). Some scarps appear to be more active than the others, hinting at the importance of

1812 some type of localized conditions such as near-surface winds or sun exposure (*Russell et al.*,
1813 2014). However, it is still an open question regarding whether the origin of these avalanches is
1814 caused by the thermal stresses in the scarp, sublimation of the seasonal CO₂ deposits, the wind,
1815 or a yet-identified process (*Becerra et al.*, 2020; *Byrne et al.*, 2017). Conversely, the fallen
1816 blocks of ice are thought to be detached by thermal stresses on these exposed locations and were
1817 thought to potentially balance the deformation of the scarps via viscous deformation (*Sori et al.*,
1818 2016). However, the fallen blocks at one well-studied north polar site account for a minimum
1819 average scarp retreat rate of ~0.2 m/kyr, which does not balance the published 0.01–1 m/yr
1820 viscous flow rates, suggesting that either viscous flow rates are lower than modeled or that
1821 additional processes act to maintain the scarps' steepness (*Fanara et al.*, 2020a). The activity of
1822 both the blocks and avalanches are important to understand because they give us insight into the
1823 mass balance of the polar cap and the climate record exposed at these steep scarps.
1824



1825 Figure 19: (a) Polar avalanche in enhanced-color HiRISE image ESP_016228_2650. (b)
1826 “Before” HiRISE image ESP_027750_2640 and (c) “after” HiRISE image ESP_036888_2640
1827 showing a blockfall with insets showing detail of the blocks and other changes between the
1828 images. The scalebar and north arrow apply to both (b) and (c) panels.
1829
1830

1831 5.3 Open questions for these mass-wasting aided landforms

1832 In general, with these mass-wasting landforms, we do not yet definitively understand the
1833 suite of processes involved and thus cannot interpret the observed landforms and activity as

1834 markers of specific environmental conditions. Volatiles, thermal cycling, aeolian processes,
1835 and/or seismicity are often invoked as drivers for initiation of the downslope transport of
1836 materials, and determining specifically (and preferably, quantitatively) what causes the activity
1837 would be useful because then these features can be used as a proxy indicator of their initiation
1838 mechanism. Additionally, understanding the role of volatiles in rock breakdown and
1839 mobilization is important for constraining long-term erosion rates on Mars and interpreting the
1840 degradation state of landforms (e.g., relative dating of fan surfaces in gullies).

1841 In particular, RSL represent the latest in a series of surface features interpreted as evidence for
1842 flowing water on Mars today, given the clear preference for warmer slopes and the temporal
1843 behavior mimicking that of seasonal seeps of water on Earth. Although further observations and
1844 analyses have led to difficulties with every proposed water-driven model, given the planetary
1845 protection significance of potential water on Mars today, there is large interest in further
1846 measurements to conclusively determine the formation mechanism for these features (*ICE-SAG*,
1847 2019; *McEwen*, 2018; *NEX-SAG*, 2015). At present, RSL sites have been classified as potential
1848 sites where terrestrial microbes might flourish (denoted “unknown special regions”: *Rummel et*
1849 *al.*, 2014; *Kminek et al.*, 2017) and thus areas that spacecraft must avoid unless they can achieve
1850 very high levels of sterilization; for example, the presence of RSL was used to rule out candidate
1851 landing sites for the Mars 2020 rover (*Grant et al.*, 2018). If RSL are dry or only transiently wet
1852 at very cold temperatures, then this restriction on future Mars exploration could be lifted
1853 (*McEwen*, 2018), but recent work suggests that putative deliquescent RSL sites could be
1854 habitable (*Maus et al.*, 2020).

1855

1856 **6 Summary of the measurements needed to answer remaining** 1857 **questions**

1858 The general aim of geomorphic studies is to connect quantitatively the observed landforms to
1859 their formative environmental drivers, via models of the active process(es). For the landforms
1860 and surface activity we have described, advances generally require additional information about
1861 the specific environmental drivers for formation and subsequent modification and/or evolution.
1862 For example, additional information about environmental drivers is needed to progress our
1863 knowledge of araneiform activity (§3). Both surface properties in araneiform-forming regions as
1864 well as time-resolved global atmospheric conditions and dynamics (including winds, clouds, and
1865 dust content) are needed to determine how and where CO₂ ice accumulates and evolves

1866 seasonally, which is essential information for constraining models of CO₂ basal sublimation and
1867 thus the scale of eruptive vents and basal erosion in araneiform terrain. Such information,
1868 combined with observations of the growth of the seasonal ice cap, would also allow for tests of
1869 predictions of where CO₂ ice is of sufficient thickness and strength for the formation and growth
1870 of araneiforms—in the present climate or during a recent past climate.

1871 Information needed to address the open questions outlined in previous sections (§2.3, 2.4,
1872 3.4, 4.5, 5.3) can be gathered through a few complementary study types:

1873 With observational data:

- 1874 1) Mapping where the landforms exist and/or are active, and where they are not
- 1875 2) Geomorphological measurement of the landform and its activity
- 1876 3) Characterization of the timing of activity (e.g., in season, in time of day, in event duration,
1877 and identification of interannual variation)
- 1878 4) Characterization of the surface (and potentially subsurface) and atmospheric environment
1879 where and when the activity occurs

1880 With laboratory, terrestrial field analog, and physics modeling studies:

- 1881 5) Identification of possible environmental drivers and investigation of scaling relationships,
1882 temporal evolution rates, and interactions between materials

1883 Table 3 summarizes which of these areas are most needed for studies of the martian surface
1884 activities discussed above.

1885 To acquire the observational data related to mapping and timing, continued high-resolution
1886 orbital imagery is key. The advent of HiRISE-type imaging demonstrated that the martian
1887 surface is active in the present climate, yielding a paradigm shift from the view that most of the
1888 interesting martian geologic activity occurred in the ancient past (i.e., during the Noachian and
1889 Hesperian). Continued repeat imaging of the surface with similar sub-meter resolution and
1890 illumination will enable identification of yet more surface changes, including those with slower
1891 activity rates, and potentially tie activity timing to specific seasons. Additionally, increased
1892 spatial coverage will enhance mapping studies; HiRISE has so far imaged only ~2% of Mars'
1893 surface. To aid image comparison and identification of geomorphic changes, MRO's current
1894 orbit is sun-synchronous (i.e., observations recur at specific local solar times of 3 a.m. and 3
1895 p.m.). The ability to observe the surface at different times of day is also critical because some
1896 active processes on Mars may only occur during a specific time-of-day. Spacecraft in other orbits

1897 can view different times of day, but with other constraints such as the changing viewing
1898 conditions making change detection analysis more difficult. For example, a spacecraft in a
1899 circular orbit with inclination of 75° would drift through all times of day, $\sim 3x$ per season (*NEX-*
1900 *SAG*, 2015). Currently, MEx and TGO are both in elliptical orbits and can view the surface
1901 during different times of day, albeit with visible imagery at lower resolution than HiRISE.
1902 Alternatively, in situ observations can provide high-resolution and high-frequency observations
1903 throughout a Mars day, at the location of the sensors. Correlation of observations acquired by
1904 different spacecraft enables a powerful confluence of high temporal and spatial resolution
1905 information within regional/global coverage, as well as imagery over a range of wavelengths.

1906 An additional benefit to continuation of global imaging is that interannual variations in
1907 surface activity can be tracked, yielding another way to constrain environmental drivers. In
1908 particular, observations of activity before and after the 2018 PEDE have shown that the
1909 redistribution of dust and related atmospheric effects have increased the frequency of some
1910 surface changes, such as RSL formation (*McEwen et al.*, 2021), suggesting that these activities
1911 may involve more dust than was originally hypothesized. The extensive dust activity also altered
1912 the seasonal frost cap formation/sublimation cycle and related landform activity (e.g., *Calvin and*
1913 *Seelos*, 2019; *Hansen et al.*, 2020).

1914 To connect the landforms to environmental controls, we also need measurements of the
1915 environment where these landforms and activity are found. Coupling surface and subsurface
1916 compositional, thermophysical, and structural measurements with meteorological conditions over
1917 sites where a specific landform and/or activity is observed allows for a holistic analysis of the
1918 full system. From orbit, globally distributed (if not with global coverage) compositional and
1919 thermophysical information has been gleaned from spectral images through the near-infrared to
1920 thermal wavelengths. However, these datasets are limited to spatial resolutions much coarser
1921 than the scale of the activity: many are 100 m/pixel or coarser, the best is CRISM with ~ 20
1922 m/pixel (*Murchie et al.*, 2007). Furthermore, many spectral datasets are only sensitive to surface
1923 exposures, so a thin layer of dust is enough to obscure the surface materials. In such areas,
1924 geologic unit mapping can provide some constraints, based on extrapolation from visible
1925 outcrops, topography, and radar analysis. In situ compositional data, as collected by the Mars
1926 rovers and landers, allow for much more detailed measurement of surface and near-subsurface

1927 properties. Coupling the in situ data with the global perspective provided through orbital
 1928 observations has been key to constraining some of the interpolative analysis.

1929 Such analysis will also be important for studies of meteorological conditions, with orbital
 1930 data providing a look at global circulation and atmospheric features such as clouds. However,
 1931 existing in situ aeolian and other meteorological data are insufficient to robustly answer surface-
 1932 atmosphere interaction questions because no dedicated sediment sensors were included in past
 1933 missions and the meteorological instruments flown were not well accommodated and were not
 1934 designed to be part of a comprehensive aeolian/meteorological experiment (*ICE-SAG*, 2019;
 1935 *MEPAG*, 2020). In situ monitoring of surface atmosphere exchanges would provide key new
 1936 information for constraining volatile and sediment flux models under Mars conditions (Table 4).

1937
 1938 Table 3. A high-level summary of the types of data currently thought to be needed to advance
 1939 studies of these features. As hypotheses evolve, definition of the next-needed data would likely
 1940 change; in all cases more or new data could prompt unexpected new questions or analyses. The
 1941 numbers/headers for the columns are discussed at the start of this section. Note that columns #1-
 1942 4 are more focused on spacecraft-acquired observational data, and #5 is more focused on
 1943 laboratory, terrestrial field analog, and physics modeling studies. Color coding: (Green)
 1944 Extensive analysis exists or future analysis of existing data types and coverage would be
 1945 sufficient to assess the broad questions; (Blue) The existing data type(s) are sufficient but
 1946 increased spatial and/or temporal coverage is needed to address the broad questions, (Purple)
 1947 New types of data/investigations are needed to address the broad questions.

	1: mapping	2: geomorphology	3: timing	4: environment	5: drivers/ interactions
Decimeter-scale ripples	B	G	B	P	B
Meter-scale ripples	G	B	B	P	P
Decameter-scale ripples	B	B	B	P	P
Dunes	B	G	B	P	B
Gullies	G	G	G	P	P
Dune alcoves	B	G	B	B	P
Linear gullies	B	G	G	B	B
Araneiforms	B	G	G	P	B
SPRC	G	B	B	B	B
H ₂ O ice layers within the MCID	G	G	G	B	P
MCID	P	G	P	P	P
Northern cap	G	G	G	P	P

Sublimation thermokarst	G	G	P	P	B
Ice Scarps	G	G	B	P	B
Patterned Ground	G	G	P	B	G
RSL	G	P	B	P	P
Avalanches from rocky slopes	B	B	P	P	B
Avalanches from icy slopes	G	G	B	B	B
Fallen blocks from icy slopes	G	G	G	B	B

1948
1949
1950
1951
1952

Table 4. Some of the Mars in situ aeolian and meteorological concurrently-collected information needed to fill critical gaps in surface-atmosphere interaction and landform formation models (compiled from recent Mars community discussions and reports such as *ICE-SAG*, 2019; *MEPAG*, 2020).

Science Investigation		In situ Measurements
Responses Measure the surface-atmosphere fluxes of sand, dust, volatiles, heat, and momentum.	Volatiles	Absolute concentration in the atmosphere
	Dust	Local surface dust erosion and deposition rates
		Lofted dust flux and grain sizes
	Sand	Surface sand erosion and deposition rates
		Saltation profile: Number, sizes, and velocities of grains in motion, as a function of height
		Reptation flux rates and grain sizes involved
		Creep flux rates and grain sizes involved
	Heat	Temperature profile
		Net downwelling and upwelling radiation
	Momentum	Horizontal wind measurements from at least <u>three</u> heights – to derive surface shear stress; of frequency to determine “average” velocities and the gust velocity distribution (or 3D wind measurements)
Drivers Determine the controls on mechanisms that lead to sediment, volatiles, and heat being moved from the surface	Meteorological Controls (+ winds, above)	Atmospheric temperature and pressure – to derive atmospheric density
		Atmospheric composition (including trace gases/humidity)
		Surface pressure and temperature
		Turbulence (i.e., high-frequency 3D wind measurements)
		Vortices/dust devils: number/frequency, surface shear stress, and amount of dust carried
		Overhead clouds, coverage, characteristics, and altitude
		Atmospheric electric field and electric conductivity
	Grain size distribution on the nearby surface	

into the atmosphere and transported.	Surface Controls	Surface grain properties (e.g., angularity, composition, electrostatics)
		Local surface topography, geologic-type (e.g., bedrock exposure, dust cover), and surface roughness elements
		Local surface mechanical and thermoconductive properties (e.g., cohesion, thermal inertia)

1953

1954 **7 Mars as a “natural laboratory” for comparative planetology studies**

1955 As discussed above, Mars is the only body outside of the Earth-Moon system where we have
 1956 acquired sufficient data (in time/space/type) to observe present-day activity and to investigate
 1957 processes within a measured environmental and geological “system.” In particular, repeat high-
 1958 resolution observations have yielded many examples of present-day surface activity and these
 1959 changes have or could be studied in enough detail to suggest the driving process(es) and/or
 1960 influential environmental conditions. Furthermore, decades of previous work have yielded ample
 1961 geologic and atmospheric contextual information and models that will greatly enhance
 1962 incorporation of the broader geologic and atmospheric/climatological context within process-
 1963 focused investigations. Timely acquisition of new data needed to fully constrain and calibrate a
 1964 process model (§6) may also be possible because commercial and international interest in
 1965 sending spacecraft (and humans) to Mars, along with Mars’ relatively close proximity to Earth,
 1966 suggest that access opportunities should exist for sending new spacecraft and instruments to
 1967 Mars over the next decade. This may be especially true for small spacecraft that do not need a
 1968 dedicated launch vehicle—which may be sufficient for targeted environmental monitoring
 1969 studies.

1970 Furthermore, Mars’ atmospheric, surface, and planetary conditions are different enough from
 1971 Earth’s to test and stretch terrestrial study-based models, but similar enough that the terrestrial
 1972 models are a reasonable starting point. As will be described, Mars’ conditions often have values
 1973 between those on Earth and other planetary bodies, such as Kuiper Belt Objects (KBOs) or the
 1974 Moon. Mars’ surface activity in modern times and through the last few billions of years can,
 1975 thus, serve as a valuable and unique comparative planetology experiment for both (1) processes
 1976 active on Earth, but under very different conditions (e.g., aeolian processes within a low density
 1977 atmosphere or with much higher obliquity), and (2) processes not active on Earth but that are
 1978 active on other planetary bodies (e.g., sublimation-dominated frost dynamics; or records of

1979 active processes without complications from recent extensive fluvial or biological activity) (also
1980 discussed in *Lapôtre et al.*, 2020).

1981 In the following sections, we describe how Mars serves as a great (perhaps the current best)
1982 comparative planetology basis for studies of (1) aeolian surface processes and meteorological
1983 dynamics, (2) sublimation-driven geomorphic dynamics, and (3) planetary bodies with variable-
1984 density atmospheres. Although not covered in this review, we note that, at Mars, one can also
1985 study both the above individual phenomena and interactions between them. There are also many
1986 additional study areas where Mars serves well as a non-Earth comparison point or extraterrestrial
1987 “laboratory” for testing and refining models, such as impact cratering rates and processes,
1988 habitability/life evolution, atmospheric dynamics, and polar/ice climate records (e.g., *Lapôtre et*
1989 *al.*, 2020; *I.B. Smith et al.*, 2020).

1990

1991 **7.1 Aeolian surface processes and meteorological dynamics**

1992 Aeolian sand and dust are known to significantly influence landscape evolution and climate
1993 across the Solar System. In addition to the aeolian landforms and dynamics studied on Earth and
1994 Mars (§2):

- 1995 • A few dune fields (*Greeley et al.*, 1995; *Weitz et al.*, 1994; Figure 20e), many wind streaks,
1996 and a few potential yardangs (*Greeley et al.*, 1995) have been identified on Venus, under an
1997 atmosphere 9× thicker than Earth’s.
- 1998 • On Saturn’s moon Titan, sand produced from photochemical organic aerosols and water ice
1999 has formed vast dunes and sand seas (*Barnes et al.*, 2015; *Lorenz et al.*, 2006; *Radebaugh*
2000 *et al.*, 2008; Figure 20c); dust storms may also occur during equinox (*Jackson et al.*, 2020),
2001 similar to those observed on Mars (*P. Thomas and Gierasch*, 1985).
- 2002 • Even on comets (*N. Thomas et al.*, 2015; Figure 20i) and icy worlds, such as Pluto (*Telfer et*
2003 *al.*, 2018; Figure 20a), aeolian processes within a transient, rarified atmosphere appear to
2004 have formed bedforms.

2005 Interpretations of these landforms and processes have generally relied upon models of sediment
2006 fluxes and transport dynamics (i.e., saltation and reptation rates and profiles) derived primarily
2007 from terrestrial field and laboratory experiments, with scaling applied based on specific planetary
2008 conditions. This has led to new tests of bedform evolution models (e.g., *Claudin and Andreotti*,
2009 2006; *Duran Vinent et al.*, 2019; *Kok*, 2010; *Kok et al.*, 2012; *Parteli and Herrmann*, 2007;

2010 *Sullivan and Kok, 2017; Sullivan et al., 2020; Vaz et al., 2017*) and proposal of a new scaling
2011 relationship to predict ripple equilibrium wavelength (e.g., *Lapôtre et al., 2016; 2017; 2018;*
2012 *2021*) after Earth conditions-based model predictions were found to be inconsistent with
2013 bedforms observed on another planet.

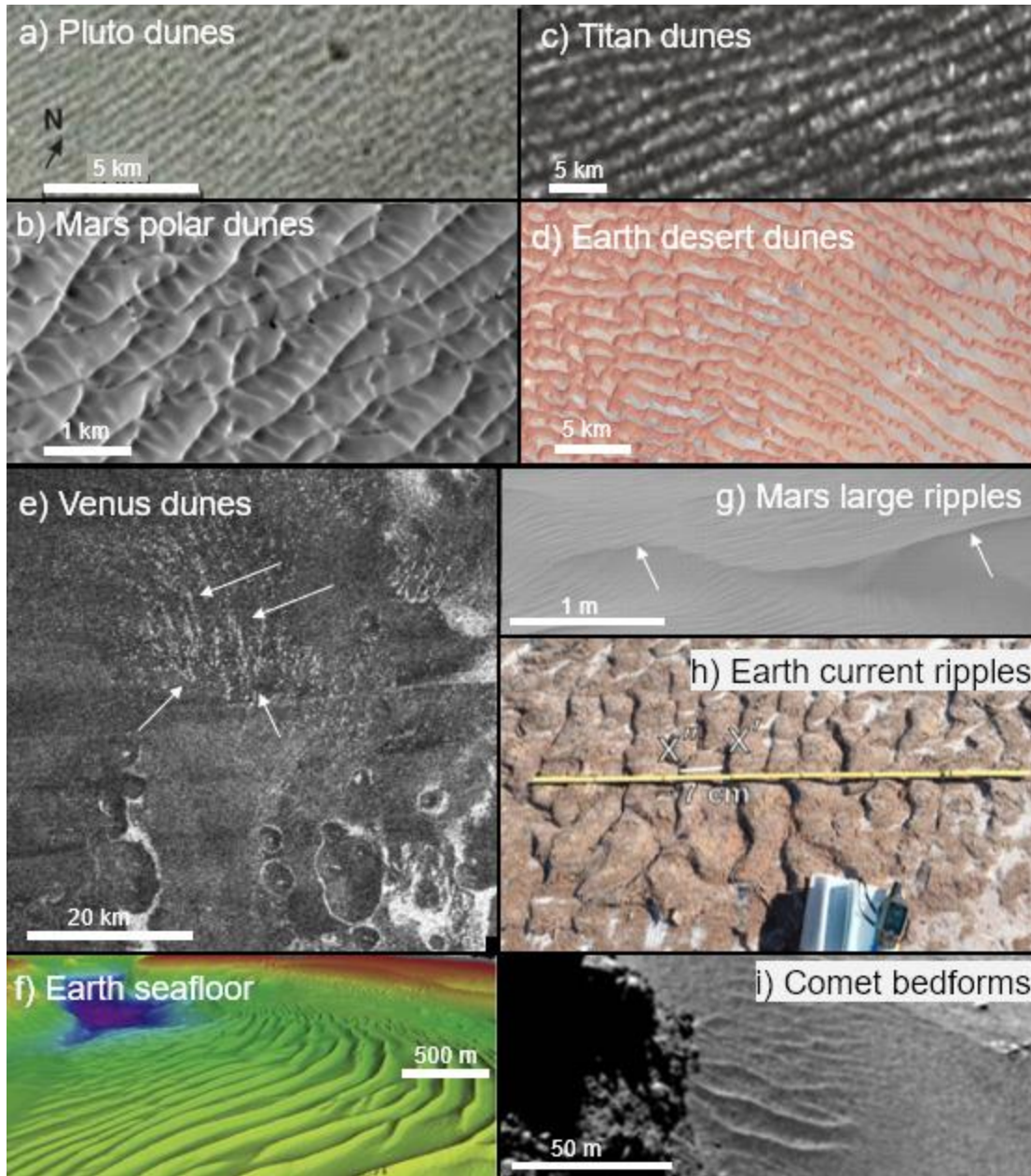
2014 Further study of martian aeolian and other meteorological systems, and how conditions drive
2015 surface activity, will enable more detailed testing and refinement of surface-atmosphere
2016 interaction process models. In particular, in situ “field” measurements of martian atmospheric
2017 boundary layer dynamics driving sand/dust and volatile transport would provide novel
2018 calibration data for models and wind-tunnel experiments within an environment with a
2019 substantially lower impact threshold than fluid threshold (*Kok, 2010*). Such “ground truth” is
2020 needed to advance a cross-planet model to describe sand and dust lofting and transport, including
2021 helping to discriminate between models such as fluid-dominated (e.g., *Bagnold, 1941; Shao and*
2022 *Lu, 2000*) or impact-dominated (e.g., *Kok and Renno, 2009; Sullivan and Kok, 2017*) transport or
2023 coarse grain motion via direct-drag or impact-driven creep (e.g., *Baker et al., 2018a, Silvestro et*
2024 *al., 2020*).

2025 Another model presently untested under extraterrestrial conditions is the one used to estimate
2026 turbulent eddy fluxes (which result in the exchange of energy, momentum, and quantities like
2027 dust, water, and other chemical species between the surface and atmosphere). On Earth, turbulent
2028 fluxes can be directly calculated from correlated, high frequency measurements of the 3D wind
2029 components and the quantity of interest; such fluxes are also related to large-scale (and more
2030 easily measured) quantities such as the vertical gradient of temperature and of the horizontal
2031 wind (i.e., the wind shear) (*Businger and Yaglom, 1971; Businger et al., 1967; Monin and*
2032 *Obukhov, 1954*), with ample testing and calibration of the physical model through terrestrial field
2033 and laboratory studies. These relationships are assumed in planetary studies but have never been
2034 shown to extend to those environments despite generally being far outside of terrestrial
2035 conditions (e.g., Mars has an extremely stable nocturnal inversion and unstable afternoon
2036 convective layer). New in situ martian meteorological measurements would enable validation
2037 and calibration of this theory within a wider range of atmospheric conditions.

2038 Mars is already used as the comparative planetology basis for some studies, due to its low
2039 atmospheric density. For example, the threshold curve under low-density gas conditions derived
2040 for Mars analog conditions in the MARSWIT (*Greeley and Iversen, 1985*) has also been used to

2041 model aeolian-type transport resulting from jetting on comets (*Cheng et al.*, 2013). Dune-like
2042 patterns on the surface of comet 67P/Churyumov-Gerasimenko (*N. Thomas et al.*, 2015) have
2043 been suggested to result from thermal winds, although the process involves outgassing from
2044 cometary jets feeding a rarefied atmosphere rather than from atmospherically driven winds as on
2045 the surfaces of Mars and Titan (*Jia et al.*, 2017). In imaging data from the New Horizons
2046 mission, Pluto was shown to have 0.4–1 km-wavelength bedform-like morphologies (*Stern et al.*,
2047 2015). Proposed to be aeolian dunes (*Telfer et al.*, 2018), a minimum wind shear required for
2048 saltation was estimated based on work performed in the MARSWIT that separated Reynolds
2049 number and interparticle cohesion effects (*Iversen and White*, 1982). The important point of
2050 analogy here is the substantially lower impact threshold than fluid threshold, as discussed in
2051 §2.2.1.

2052



2053
 2054 Figure 20. Examples of bedforms on different planetary bodies: (a-d) Planetary features with
 2055 remarkable geomorphic similarities, leading to hypotheses of aeolian dune fields. (e-j) Examples
 2056 from the diverse suite of bedforms found on other bodies, which may be more analogous to
 2057 terrestrial subaqueous bedforms than subaerial ones (proposed terrestrial analogs are shown in (f
 2058 and h), for Venus and Mars/comet, respectively). Rough scale bars are included, but distances
 2059 are not exact because images are generally not orthorectified. Images were selected/adapted
 2060 based on: (a) *Telfer et al.*, 2018: New Horizons color-composite MVIC images, (b) *Diniega et*
 2061 *al.*, 2017: HiRISE image PSP_007115_2600, (c) *Radebaugh et al.*, 2010: Cassini synthetic
 2062 aperture radar (SAR) image, (d) Landsat image of Rub' al Khali in the Arabian peninsula
 2063 (<https://earthobservatory.nasa.gov/blogs/earthmatters/2012/11/02/dune-gallery/>), (e) *Diniega et*
 2064 *al.*, 2017: Magellan SAR image of Menat Undae dune field/NASA Photojournal PIA00483, (f)
 2065 *Neakrase et al.*, 2017: sand waves in San Francisco Bight (from Fig. 6), (g, h) *Lapôtre et al.*,

2066 2018: MSL Mastcam image acquired in Sol 1221, image of current ripples from dry riverbed in
2067 Death Valley, CA (from Fig. 2), (i) *Thomas et al.*, 2015: Rosetta image NAC_2014-09-
2068 18T00.33.01.377Z_ID10_1397549800_F22.
2069

2070 **7.2 Sublimation-driven geomorphic dynamics**

2071 As discussed above, each martian fall/winter CO₂ frost and ice are deposited in a thick
2072 seasonal layer and in the winter/spring hemisphere this layer sublimates. Mars has lower gravity
2073 and a lower pressure and temperature environment than Earth, causing sublimation processes to
2074 differ from terrestrial analogs, including laboratory analogs. Mars' atmosphere is in vapor
2075 equilibrium with surface CO₂ frost/ice (*Leighton and Murray*, 1966), thus Mars has an
2076 environment closer to those of Triton, Pluto, and possibly other Kuiper Belt Objects (*Ingersoll*,
2077 1990; *Owen et al.*, 1993), rather than terrestrial and laboratory analogs. For example, no large-
2078 scale sublimation dynamics naturally occur on Earth, and within laboratory studies we cannot
2079 replicate low gravity over timescales relevant for sublimation.

2080 Sublimation is thought to be the main-driver forming a range of depressions or pits on Mars,
2081 including SPRC pitting (§4.1.1), icy scarps (§4.3.1), and scalloped depressions (§4.3).
2082 Sublimation has also been linked to the formation of other (non-active) depressions which have
2083 not been discussed above, including pitted terrain in and around impact craters (*Boyce et al.*,
2084 2012; *Tornabene et al.*, 2012), crenulated and labyrinthine pitted surfaces of martian glaciers
2085 (e.g. *Levy et al.*, 2009a; *Mangold*, 2003), and dissected latitude dependent mantle (*Milliken et al.*,
2086 2003; *Mustard et al.*, 2001; *Soare et al.*, 2017). These different features are proposed to form due
2087 to sublimation from volatile reservoirs of different sizes/forms/ages, and vastly different
2088 sublimation rates. Thus, studies of these features on Mars enable discrimination between
2089 different proposed models and identification of key geomorphological or environmental
2090 signatures for separating features that likely formed through slightly different processes, within
2091 different environments, and/or over very different timescales.

2092 *Mangold* (2011) provides a detailed review of sublimation landforms in the Solar System,
2093 and here we add new results with the additional perspective of using Mars as an analog. Some
2094 sublimation-generated depressions on Mars that have already been compared to depressions on
2095 the surfaces of other bodies in the Solar System include the following:

- 2096 • Hollows on Mercury (e.g., *Blewett et al.*, 2011; *R.J. Thomas et al.*, 2014) (Figure 21b)
2097 which are thought to be due to volatile-loss or sublimation of sulfur-related compounds,

2098 likely sulfides (e.g., *Bennett et al.*, 2016) and analogies have been drawn to martian swiss
2099 cheese terrain (§4.1.1; Figure 21a).

2100 • Pitted surfaces have been discovered on asteroids, notably pitted crater floors on Vesta
2101 (*Denevi et al.*, 2012) and Ceres (*Sizemore et al.*, 2017; 2019) which are remarkably similar
2102 to pitted terrain found in craters on Mars (*Boyce et al.*, 2012; *Tornabene et al.*, 2012).

2103 Additionally, pitted areas and scarps on outer Solar System moons have been grouped with
2104 Mars polar features as evidence of sublimation degradation (*Moore et al.*, 1996).

2105 • Pitted terrains on Pluto (Figure 21c) that are thought to represent erosion from sublimation-
2106 driven winds of the surface of nitrogen ice and possibly methane ice (*Buhler and Ingersoll*,
2107 2018; *Moore et al.*, 2017). Similar terrains are thought to exist on other Kuiper Belt
2108 Objects, and the origins of flat-floored pits on Arrokoth remain mysterious (*Schenk et al.*,
2109 2020). Bladed terrains on Pluto are also thought to derive from sublimation (*Moore et al.*,
2110 2017).

2111 • Pitted surfaces found on comets (e.g., *Sunshine et al.*, 2016). Recent exploration of 67P
2112 Churyumov–Gerasimenko by Rosetta maintains that these pits, which span a range of sizes,
2113 grow primarily via sublimation (e.g., tens to hundreds of meters-wide pits: *Vincent et al.*
2114 (2015), meters-wide pits: *Birch et al.* (2017)).

2115 On Mars, sublimation is thought to have an important role to play in initiating and/or
2116 enhancing mass wasting over sandy slopes (§3.2.1-2, 3.3.1, 5.2) and rocky slopes (§3.2.1, 5.2)
2117 (Figure 21d). Martian mass-wasting features have been proposed to form useful analogies for:

2118 • Gully-like landforms identified on Mercury (*Malliband et al.*, 2019) and Vesta (*Krohn et al.*
2119 *et al.*, 2014; *Scully et al.*, 2015) (Figure 21e,f), potentially related to sublimation of sulfur-
2120 compounds and water, respectively.

2121 • Downslope features that have been observed on Helene, one of Saturn's Trojan moons,
2122 whose formation has been ascribed to sublimation (*Umurhan et al.*, 2016) (Figure 21g).

2123 Furthermore, it is likely that closer inspection of other planetary bodies will reveal further
2124 examples of sublimation-driven mass-wasting processes.

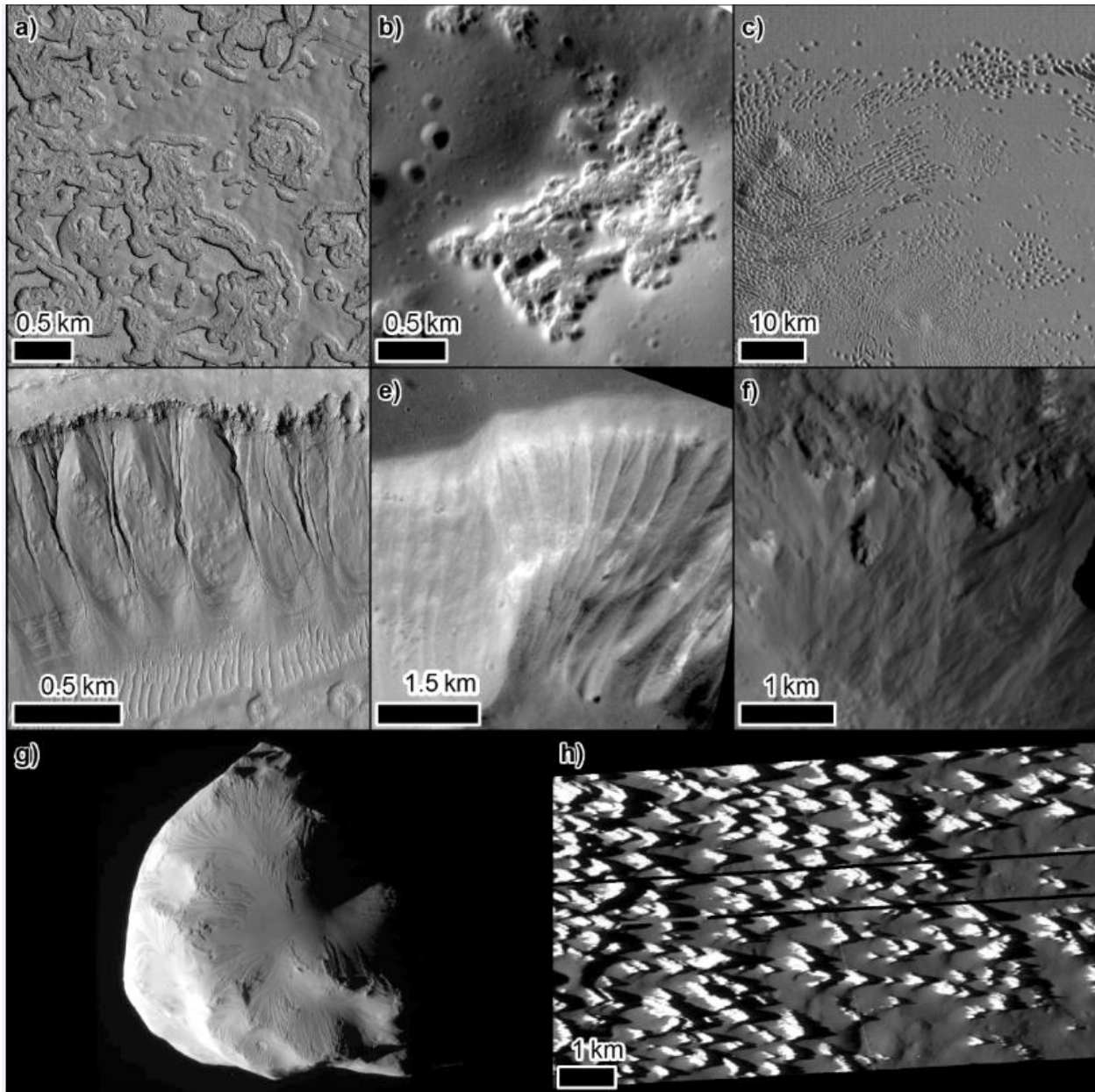
2125 In general, sublimation and related processes drive dust and other contaminants up to the
2126 atmosphere or, in the case of comets, into their coma. Escaping pressurized gas from sublimation
2127 at the base of the CO₂ seasonal ice cap on Mars erodes araneiforms (*Hansen et al.*, 2010; *Kieffer*,
2128 2007; *Piqueux et al.*, 2003; *Portyankina et al.*, 2017), radially organized and /or dendritic

2129 channels (*Mc Keown et al.*, 2017) initially dubbed “spiders,” and deposits material across the
2130 surface (*N. Thomas et al.*, 2010). These jets of gas, whose origin is via basal sublimation and the
2131 solid state greenhouse effect (§3.1; *Kieffer*, 2007), and the patterns/rates of material they spew
2132 out could be useful analogues for the following:

- 2133 • Sublimation processes proposed to cause to global-scale contrasting albedo regions on
2134 Iapetus and Ganymede (*Giese et al.*, 2008; *Prockter et al.*, 1998; *Spencer and Denk*, 2010).
- 2135 • CO₂ ice signatures found on the trailing hemispheres of the Uranian satellites (*Cartwright*
2136 *et al.*, 2015; *Grundy*, 2003; *Grundy et al.*, 2006), notably visible as a bright deposit inside
2137 Wunda Crater on Umbriel (*Sori et al.*, 2017). Severe sublimation of CO₂-ices is thought to
2138 explain the pinnacle terrain on Callisto (*Howard et al.*, 2008; *White et al.*, 2016) (Figure
2139 21h).
- 2140 • Solar-driven jets of materials found on other bodies. The solar-driven theory was actually
2141 proposed to explain plumes on Triton (*Soderblom et al.*, 1990) before it was applied to
2142 Mars’ geysers (*Kieffer et al.*, 2006), although later Triton observations suggested a
2143 cryovolcanic origin might instead be responsible (*Waite et al.*, 2017).

2144 Additionally, interactions between wind and sublimation dynamics can be explored on Mars. For
2145 example, a “sublimation wave” model of dynamics at the interface between an icy substrate and
2146 a turbulent boundary layer flow may explain certain icy landform periodicities on Mars and
2147 Earth (*Bordiec et al.*, 2020). Bodies such as Pluto, Ceres, and Jovian and Saturnian icy moons
2148 are also hypothesized to have surface sublimation and winds, so similar dynamics could be
2149 expected there (*Bordiec et al.*, 2020).

2150

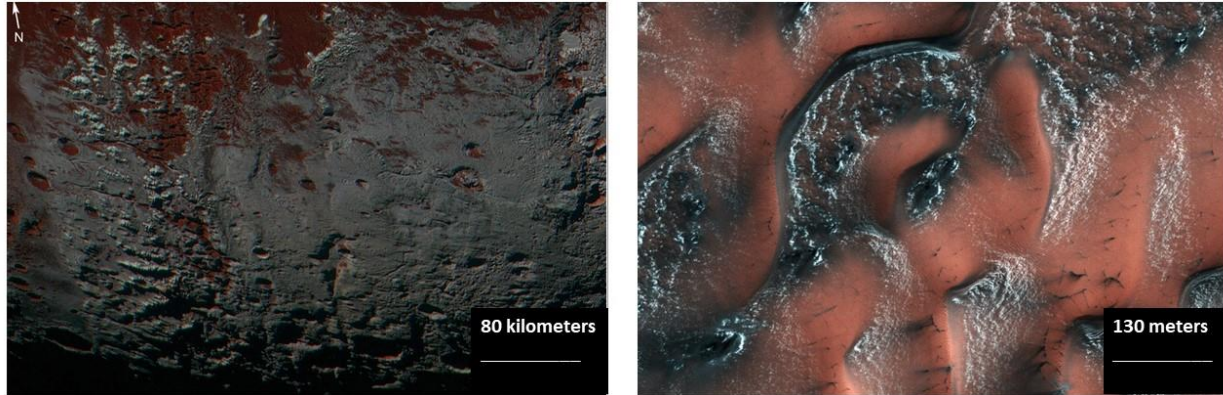


2151
 2152 Figure 21. Geomorphic features on multiple planetary bodies, thought to be formed through
 2153 surface frost sublimation and potentially analogous to features on Mars. (a) Swiss cheese terrain
 2154 on Mars HiRISE image ESP_057828_0930. (b) Hollows on Mercury in Scarlatti impact basin,
 2155 MDIS NAC image EN1051805374M. (c) Pits on Pluto, New Horizons LORRI image
 2156 0299179742. (d) Gullies on Mars, HiRISE image. (e) Mass wasting gullies on Mercury in
 2157 Nathair Facula, MDIS NAC image EN1059620367M. (f) Mass wasting gullies on Vesta in
 2158 Cornelia Crater, DAWN Framing Camera image FC21B0025747. (g) Image of Saturn's Moon
 2159 Helene taken by Cassini-Huygens ISS NA camera. Lit terrain is on the leading hemisphere of
 2160 Helene measuring ~33 km across and North is down. (h) Pinnacle terrain on Callisto, Galileo
 2161 image PICNO (Picture number) 30C0003. Image processing for MDIS and Galileo was
 2162 performed using ISIS3 via the U.S. Geological Survey PILOT and POW systems.
 2163

2164 In addition to sublimation, studies of the present-day accumulation and evolution of frost and
2165 ice on Mars may provide analog information about the types and interactions of frost and ice on
2166 other bodies. For example, one model of methane snow on Pluto (*Witzke, 2015*;
2167 <https://www.nasa.gov/feature/methane-snow-on-pluto-s-peaks>; Figure 22) indicates that it
2168 forms due to a circulation-induced high-altitude enrichment of gaseous methane, a process
2169 different from those forming high-altitude snowpacks on Earth (*Bertrand et al., 2020*).
2170 Comparisons with H₂O and CO₂ snow on Mars may provide a better comparative planetology
2171 starting point to understand precipitation and volatile transport on planets and dwarf planets with
2172 tenuous atmospheres. The surface pressure of the martian atmosphere is 2–3 orders of magnitude
2173 less than that of the Earth, and Pluto’s atmosphere is another ~3 orders of magnitude lower,
2174 providing a large physical range for future modeling that applies to a full suite of planetary
2175 atmospheres in the Solar System and elsewhere. Laboratory studies of H₂O and CO₂ ice (e.g.,
2176 *Chinnery et al., 2018; Kaufmann and Hagermann, 2017; Pommerol et al., 2019; Portyankina et*
2177 *al., 2019; Yoldi et al., 2021*), as well as how evolution of such materials is altered through
2178 interaction between the ices and dust, coupled with Mars ice and environment observations
2179 provides the current best route for formulating and calibrating models of these strange ices under
2180 extraterrestrial conditions. Even if not providing a direct analog, study of martian ices may also
2181 help ground truth models and demonstrate how to interpret spacecraft observations and connect
2182 them with terrestrial experiments involving exotic ices.

2183 Finally, while not directly related to present-day frost accumulation/sublimation or
2184 observable activity, the creep of martian glaciers also likely presents a useful analog for studies
2185 of outer Solar System bodies. The balance between sublimation/ablation, deposition, and flow
2186 rates is thought to be significantly different in martian vs. terrestrial glaciers. For example, due to
2187 an overall lower surface temperature, water-ice glaciers on Mars exhibit different dynamics from
2188 most terrestrial glaciers, i.e., without basal melting or basal sliding (*Head and Marchant, 2003*;
2189 *Marchant et al., 1993*); there may be evidence of past CO₂ glaciers (*Kreslavsky and Head,*
2190 *2011*). Both valley and piedmont glaciers on Pluto have been identified in the region of Sputnik
2191 Planitia (*Moore et al., 2016*). Some show evidence of bulk flow, with basement material or
2192 nunatoks protruding above the mobile material (*Stern et al., 2015*).

2193



2194
2195 Figure 22. Snow on Pluto and Mars. The image on the left from the Multispectral Visible
2196 Imaging Camera on the New Horizons spacecraft shows possible methane snow on mountains in
2197 the southern hemisphere of Pluto. The image on the right is a false color image from the High
2198 Resolution Imaging Science Experiment (HiRISE) camera on NASA's Mars Reconnaissance
2199 Orbiter shows CO₂ frost on martian dunes at a northern latitude of 76° (north is down). Picture
2200 credits left: NASA/JHU APL/SwRI (discussed in NASA press-release 03-03-2016,
2201 <https://www.nasa.gov/feature/methane-snow-on-pluto-s-peaks>). Right: NASA/JPL/UA, HiRISE
2202 ESP_050703_2560.
2203

2204 7.3 Planetary bodies with variable-density atmospheres

2205 Although in this study we primarily focused on known or hypothesized present-day surface
2206 activity and related landforms, as discussed above, studies of the present-day Mars provides a
2207 key to interpret the archive of past Mars' surface processes and climate conditions. In particular,
2208 both aeolian processes and sublimation dynamics will be influenced by atmospheric density,
2209 which has varied on Mars over seasonal to much longer timescales. Studies of observable surface
2210 activities in the present (including variations in activity rates correlated to seasonal or interannual
2211 environmental variations) enables testing of models that then are extrapolated back to past
2212 martian climates, or to other bodies that may experience analogous cyclic variations and/or
2213 atmospheric collapse.

2214 As discussed in §3.1, the CO₂ atmosphere of Mars is in vapor pressure equilibrium with
2215 surface ice; seasonally CO₂ sublimates and condenses, changing the atmospheric density by >25%
2216 in the present climate (e.g., *Forget et al.*, 1998; 1999; *Hartogh et al.*, 2005; *Leighton and*
2217 *Murray*, 1966; *Pollack et al.*, 1990; 1993). The dynamics of this process modulate the global
2218 circulation and drive local sublimation winds, such as katabatic winds that are thought to play an
2219 important role in the formation of polar troughs (*Spiga and Smith*, 2018). Similar surface-
2220 atmosphere processes act on other planetary bodies where the atmosphere is in vapor pressure
2221 equilibrium with surface ice, such as on Triton, Pluto, and KBOs (*Bertrand et al.*, 2020; *Hansen*

2222 *et al.*, 2018; *Zalucha and Michaels*, 2013). Thus, Mars' processes and climate cycles may
2223 present a good analog for interpreting the integrative geomorphological result of atmosphere-
2224 surface processes on these bodies, including sublimation-driven formation of surface features
2225 and aeolian-driven processes (*Moore et al.*, 2017; *Young*, 2012).

2226 Due to cycles in various orbital parameters (such as obliquity), the Mars atmospheric density
2227 may cycle through a range of 1–12 mbar over thousands to millions of years timescales (*Buhler*
2228 *et al.*, 2020; *Manning et al.*, 2019). Derivation of present-day martian surface activity models
2229 that quantitatively connect landform morphologies to driving environmental conditions will
2230 enable improved interpretation of relict features and reduce uncertainty when extrapolating
2231 activity models through past Mars climates. Such developments will also provide a testable basis
2232 for generation of similar models on other bodies that also experience large, cyclic changes in
2233 atmospheric density, such as on Pluto (*Betrand et al.*, 2018; *Forget et al.*, 2017; *Hansen and*
2234 *Paige*, 1996) and Triton (*Hansen and Paige*, 1992; *Trafton*, 1984; *Yelle et al.*, 1995). As Earth's
2235 atmosphere has not gone through comparable large swings in atmospheric density during the
2236 portion of Earth's history when most of the Earth's observable rock record was formed, Mars
2237 provides important "ground truth" for this type of extrapolative analysis and integration of
2238 predicted geologic records through different atmospheric pressures.

2239 For example, on Mars, both ancient surface and stratigraphic features and modern active
2240 processes can be directly observed and measured. This enables models of sedimentary processes
2241 to be investigated through different climate conditions. In particular, the morphologies of large
2242 martian ripples have been proposed to provide a way to constrain atmospheric density changes
2243 within Mars' climate history (*Lapôtre et al.*, 2016). As previously discussed (§2.1.3), the
2244 wavelength of large martian ripples appears to be a function of atmospheric density (*Lapôtre et*
2245 *al.*, 2016; *Lorenz et al.*, 2014). The wavelength of old ripples can be read in inactive ripple fields,
2246 but also within the cross-stratification left behind by bedforms (e.g., *Rubin*, 1987; *Rubin and*
2247 *Carter*, 2006). Thus, provided that bedform dimensions can be extrapolated from the martian
2248 aeolian record (e.g., *Banham et al.*, 2018; *Grotzinger et al.*, 2005; *Lapôtre et al.*, 2016) and with
2249 a mechanistic understanding of how atmospheric density controls bedform size (e.g., through
2250 kinematic viscosity, specific sediment density, and possibly wind shear velocity; *Lapôtre et al.*,
2251 2016; 2017), one should be able to reconstruct the history of atmospheric density from the
2252 aeolian rock record. Such results, especially coupled with terrestrial-based sedimentary process

2253 models, could advance studies of analogous sedimentary deposits on other planetary bodies and
2254 enable even more climatological and geologic history to be interpreted from limited
2255 observations.

2256 Another example is about how erosive potential of basal sublimation from CO₂ ice slabs is
2257 affected by the thickness of the seasonal ice layer or insolation conditions, leading to the
2258 formation of araneiforms. As discussed in §3.3.2, some studies of these features suggested that
2259 araneiforms may be active at very slow rates (*Piqueux and Christensen, 2008*), but repeat high-
2260 resolution imaging of these features has not yielded any discernible changes in topography over
2261 the last decade. Based on lab experiments of the CO₂ ice sublimation activity over granular
2262 materials, it has instead been proposed that some of the araneiforms (especially the largest and
2263 those displaying a non-radial network) may be relicts of a past climate when the frost depth or
2264 insolation amount was different, leading to more energetic sublimation (*Mc Keown et al., 2021*).
2265 Determination of the environmental controls on the basal sublimation rates and resultant erosion
2266 potential of the escaping gas would enable improved interpretation of the ice layer
2267 thickness/strength needed to form these features. Should the needed ice layer be more than those
2268 forming in the present climate, then the araneiforms could be interpreted as direct records of past
2269 wintertime conditions. Such results provide constraints on models of the pressures attained via
2270 basal sublimation—a distinctively non-terrestrial process that would be applicable towards
2271 studies of jets and substrate erosion on other bodies.

2272 In parallel, but out of phase with variable density atmospheres, the surface deposition of
2273 meteoric ice will result in layered and likely stratified volatile deposits with impurities. On Mars,
2274 impurities likely include dust, lithic fragments from volcanic eruptions or ejecta, fine salt grains,
2275 trapped gasses, and isotopologues (*ICE-SAG, 2019; I.B. Smith et al., 2020*). Mars is not the only
2276 planetary body to experience partial atmospheric collapse (*Soto et al., 2015*). Pluto (*Bertrand et*
2277 *al., 2018; 2019; Hansen and Paige, 1996; Olkin et al., 2015*) and Titan (*Lorenz et al., 1997*)
2278 likewise have strong seasonal atmospheric cycles (lasting hundreds of Earth years) and orbital
2279 variations that could cause similar ice layering as is found on Mars, and atmospheric collapse has
2280 been proposed for tidally locked planets around TRAPPIST-1 (*Turbot et al., 2018*). Earth, with
2281 anthropomorphic influences, abundant biology, and liquid phases, does not provide a good
2282 analog for such layered ice deposits or climate models.

2283

2284 **8 Lessons learned from planetary geomorphological studies**

2285 Based on recurrent challenges and some of the key science advancements within studies of
2286 martian present-day activity, we identify pitfalls and strategies that may benefit future planetary
2287 and terrestrial geomorphological studies. First, a key lesson is that geomorphological similarity
2288 to terrestrial landforms may present a good starting point for a hypothesis of similar formation
2289 process and driving environmental conditions, but geomorphological similarity alone is not
2290 sufficient to conclude parallel evolution. One needs to consider other observations and datasets
2291 to determine if there is “system”-level consistency with processes or environmental conditions
2292 similar to those on the Earth (e.g., the timing of activity, geologic context, compositional
2293 constraints, and contemporaneous environmental characterization). This applies both to
2294 comparisons between features on the same planet (e.g., martian gullies (§3.2.1) versus dune
2295 alcoves (§3.2.2)) and to comparisons between features on different planets (e.g., gullies (§3.2.1)
2296 on Mars, Mercury, and Vesta (§7.2)).

2297 A second key lesson is that many interactions and controls are nonlinear, so there are often
2298 complications both in scaling an analog process or landform under new environmental conditions
2299 and in trying to separate out the influences of multiple processes on a planetary surface. For the
2300 first, laboratory/field experiments and modeling studies are crucial for testing proposed
2301 relationships and even seeing what the process looks like under exotic conditions; for example,
2302 due to the low surface pressure, liquid water would flow and boil on the present-day martian
2303 surface, creating small “flow” morphologies different from those observed on Earth (*Herny et*
2304 *al.*, 2019; *Massé et al.*, 2016; *Raack et al.*, 2017); until these experiments were run, levitating
2305 sand pellets were not expected or taken into account in theories. For the second, looking at a
2306 range of activity and landform types across a planetary surface, as well as mapping where a
2307 process seems to be active and where it appears to not be active (e.g., Figure 2), can help
2308 detangle processes and driving environmental conditions.

2309 A third key lesson is that long-term observation of change is needed to fully characterize a
2310 process and its expression and rate(s), as moderated by changes in driving environmental
2311 conditions. Activity levels can vary dramatically from year to year (e.g., as is currently being
2312 investigated with the 2018 Mars PEDE).

2313 Finally, to increase the science value of new observations and enable a holistic look at Mars
2314 present-day phenomena, the international space agencies and Mars exploration programs along

2315 with an active and connected Mars science community have been instrumental in enabling
2316 strategic linkages between observations, especially between orbital and in situ assets. Having
2317 such community communication/coordination and data accessibility is clearly key for the
2318 “system” science generally involved in investigations of geomorphological processes. Related, a
2319 research and analysis program that supports both data analysis and fundamental research studies
2320 helps scientists collaborate and combine different types of study (e.g., Mars’ “natural laboratory”
2321 observations, laboratory/wind tunnel experiments, field analog studies, and physical/numerical
2322 models) to robustly test and calibrate models describing the observed activity, and then
2323 extrapolate from observed conditions to past or more exotic environments. As such work is
2324 inherently cross-disciplinary, cross-target, and diverse in scope, it is critical also that the
2325 community foster an interdisciplinary, diverse, equitable, inclusive, and accessible environment
2326 so that a wide range of people and perspectives can interact, communicate, and then contribute
2327 towards understanding the active surface processes and improve science advancement.

2328

2329 **9 Acknowledgements**

2330 We thank our reviewers, Clémence Herny and Mackenzie Day, for their very thorough reads and
2331 thoughtful critiques and suggestions. The work by JPL authors (SD, BB, SP) was carried out at
2332 the Jet Propulsion Laboratory, California Institute of Technology, under a contract with the
2333 National Aeronautics and Space Administration (80NM0018D0004). MC wishes to thank NASA
2334 Mars Data Analysis Program grant 80NSSC20K1066. ML wishes to thank NASA Solar System
2335 Workings Program grant 80NSSC20K0145. SJC is grateful to the French Space Agency CNES
2336 for funding her HiRISE and CaSSIS related work. Some manuscript content was derived based
2337 on personal communications with terrestrial and planetary aeolian community members and we
2338 appreciate the insights and information; in particular, Scot Rafkin (SwRI) assisted with the
2339 description of important untested models of meteorologic dynamics. Finally, we thank the many
2340 space/Earth/physical sciences agencies’ staff, planetary mission and instrument teams, and
2341 researchers who have enabled the observations, analysis, and community collaborations that
2342 contribute towards studies of Mars as an active and connected system. This includes, but is not
2343 limited to, the spacecraft and instrument engineering teams for the successful completion and
2344 operation of MRO and TGO/CaSSIS. CaSSIS is a project of the University of Bern funded
2345 through the Swiss Space Office via ESA's PRODEX programme; the CaSSIS instrument
2346 hardware development was also supported by the Italian Space Agency (ASI) (ASI-INAF

2347 agreement no. I/018/12/0), INAF/ Astronomical Observatory of Padova, and the Space Research
2348 Center (CBK) in Warsaw.

2349

2350 **10 References**

2351 Abotalib, A.Z., Heggy, E., 2019. A deep groundwater origin for recurring slope lineae on Mars.
2352 *Nature Geoscience*, **12**, 235–241, doi:10.1038/s41561-019-0327-5.

2353 Achilles, C., Downs, R.T., Ming, D.W., Rampe, E.B., Morris, R.V., Treiman, A.H., Morrison,
2354 S.M., Blake, D.F., Vaniman, D.T., Ewing, R.C., Chipera, S.J., 2017. Mineralogy of an active
2355 eolian sediment from the Namib Dune, Gale Crater, Mars. *Journal of Geophysical Research:*
2356 *Planets*, **122**, 2344–2361, doi:10.1002/2017JE005262.

2357 Anderson, D., Gatto, L.W., Ugolini, F., 1973. An examination of Mariner 6 and 7 imagery for
2358 evidence of permafrost terrain on Mars. In: Sanger, F.G. (Ed.), *Permafrost: Second*
2359 *International Conference*, 499–508.

2360 Andreotti, B., Claudin, P., Douady, S., 2002. Selection of dune shapes and velocities Part 1:
2361 Dynamics of sand, wind and barchans. *Eur. Phys. J.*, **B28**, 321–339.

2362 Andreotti, B., Claudin, P., Pouliquen, O. 2006. Aeolian sand ripples: Experimental study of fully
2363 developed states. *Physical Review Letters*, **96**, 028001, doi:10.1103/PhysRevLett.96.028001

2364 Appéré, T., Schmitt, B., Langevin, Y., Douté, S., Pommerol, A., Forget, F., Spiga, A., Gondet,
2365 B., Bibring, J.-P., 2011. Winter and spring evolution of northern seasonal deposits on Mars
2366 from OMEGA on Mars Express. *Journal of Geophysical Research: Planets*, **116**(E5),
2367 E05001, doi:10.1029/2010JE003762.

2368 Arvidson, R.E., Iagnemma, K.D., Maimone, M., Fraeman, A.A., Zhou, F., Heverly, M.C.,
2369 Bellutta, P., Rubin, D., Stein, N.T., Grotzinger, J.P., Vasavada, A.R., 2017. Mars Science
2370 Laboratory Curiosity rover megaripple crossings up to sol 710 in Gale crater. *Journal of*
2371 *Field Robotics*, **34**(3), 495–518, doi:10.1002/rob.21647.

2372 Atwood-Stone, C., McEwen, A.S., 2013. Avalanche slope angles in low-gravity environments
2373 from active martian sand dunes. *Geophysical Research Letters*, **40**, 2929–2934,
2374 doi:10.1002/grl.50586.

2375 Ayoub, F., Avouac, J.-P., Newman, C., Richardson, M., Lucas, A., Leprince, S., Bridges, N.,
2376 2014. Threshold for sand mobility on Mars calibrated from seasonal variations of sand flux.
2377 *Nature Communications*, **5**, 5096, doi:10.1038/ncomms6096.

2378 Bagnold, R.A., 1936. The movement of desert sand. *Proceedings of the Royal Society of London.*
2379 *Series A-Mathematical and Physical Sciences*, **157**(892), 594–620.

2380 Bagnold, R.A., 1937. The transport of sand by wind. *The Geographical Journal*, **89**(5), 409–438.

2381 Bagnold, R.A., 1941. *The Physics of Blown Sand and Desert Dunes*. Methuen: London

2382 Baker, M.M., Newman, C.E., Lapôtre, M.G.A., Sullivan, R., Bridges, N.T., Lewis, K.W., 2018a.
2383 Coarse sediment transport in the modern martian environment. *Journal of Geophysical*
2384 *Research: Planets*, **123**(6), 1380–1394, doi:10.1002/2017JE005513.

2385 Baker, M.M., Lapôtre, M.G., Minitti, M.E., Newman, C.E., Sullivan, R., Weitz, C.M., Rubin,
2386 D.M., Vasavada, A.R., Bridges, N.T., Lewis, K.W., 2018b. The Bagnold dunes in southern

- 2387 summer: Active sediment transport on Mars observed by the Curiosity rover. *Geophysical*
2388 *Research Letters*, **45**(17), 8853–8863, doi:10.1029/2018GL079040.
- 2389 Balme, M., Greeley, R., 2006. Dust devils on Earth and Mars. *Review of Geophysics*, **44**(3),
2390 RG3003, doi:10.1029/2005RG000188.
- 2391 Balme, M., Berman, D.C., Bourke, M.C., Zimbelman, J.R., 2008. Transverse aeolian ridges
2392 (TARs) on Mars. *Geomorphology*, **101**, 703–720, doi:10.1016/j.geomorph.2008.03.011.
- 2393 Balme, M.R., Gallagher, C.J., Page, D.P., Murray, J.B., 2009. Sorted stone circles in Elysium
2394 Planitia, Mars: Implications for recent martian climate. *Icarus*, **200**, 30–38,
2395 doi:10.1016/j.icarus.2008.11.010.
- 2396 Banfield, D., Spiga, A., Newman, C., 2020. The atmosphere of Mars as observed by InSight.
2397 *Nature Geoscience*, **13**, 190–198, doi:10.1038/s41561-020-0534-0.
- 2398 Banham, S.G., Gupta, S., Rubin, D.M., Watkins, J.A., Sumner, D.Y., Edgett, K.S., Grotzinger,
2399 J.P., Lewis, K.W., Edgar, L.A., Stack-Morgan, K.M., Barnes, R., 2018. Ancient martian
2400 aeolian processes and palaeomorphology reconstructed from the Stimson formation on the
2401 lower slope of Aeolis Mons, Gale crater, Mars. *Sedimentology*, **65** (4), 993–1042,
2402 doi:10.1111/sed.12469.
- 2403 Banks, M.E., Byrne, S., Galla, K., McEwen, A.S., Bray, V.J., Dundas, C.M., Fishbaugh, K.E.,
2404 Herkenhoff, K.E., Murray, B.C., 2010. Crater population and resurfacing of the Martian
2405 north polar layered deposits. *Journal of Geophysical Research*, 115, E08006,
2406 doi:10.1029/2009JE003523.
- 2407 Banks, M.E., Geissler, P.E., Bridges, N.T., Russell, P., Silvestro, S., Chojnacki, M., Zimbelman,
2408 J.R., Delamere, W.A., 2015. Emerging global trends in aeolian bedform mobility on Mars.
2409 Presented at *Fourth Int. Planetary Dunes Workshop*, Ab. #8036.
- 2410 Banks, M.E., Fenton, L.K., Bridges, N.T., Geissler, P.E., Chojnacki, M., Runyon, K.D.,
2411 Silvestro, S., Zimbelman, J.R., 2018. Patterns in mobility and modification of middle- and
2412 high-latitude southern hemisphere dunes on Mars. *Journal of Geophysical Research: Planets*,
2413 doi:10.1029/2018JE005747.
- 2414 Baratoux, D., Mangold, N., Arnalds, O., Bardintzeff, J.M., Platevoet, B., Grégoire, M. Pinet, P.,
2415 2011. Volcanic sands of Iceland-Diverse origins of aeolian sand deposits revealed at
2416 Dyngjusandur and Lambahraun. *Earth Surface Processes and Landforms*, **36**(13), 1789–
2417 1808, doi:10.1002/esp.2201.
- 2418 Barnes, J.W., Lorenz, R.D., Radebaugh, J., Hayes, A.G., Arnold, K., Chandler, C., 2015.
2419 Production and global transport of Titan’s sand particles. *Planetary Science*, **4** (1), 1–19,
2420 doi:10.1186/s13535-015-0004-y.
- 2421 Barrett, A.M., Balme, M.R., Patel, M.R., Hagermann, A., 2017. Clastic patterned ground in
2422 Lomonosov crater, Mars: Examining fracture controlled formation mechanisms. *Icarus*, **295**,
2423 125–139, doi:10.1016/j.icarus.2017.06.008.
- 2424 Bauer, B.O., Davidson-Arnott, R.G.D., Hesp, P.A., Namikas, S.L., Ollerhead, J., Walker, I.J.,
2425 2009. Aeolian sediment transport on a beach: Surface moisture, wind fetch, and mean
2426 transport. *Geomorphology*, **105**(1-2), 106–116, doi:10.1016/j.geomorph.2008.02.016.

- 2427 Becerra, P., Byrne, S., Brown, A.J., 2015. Transient bright “halos” on the south polar residual
2428 cap of Mars: implications for mass-balance. *Icarus*, **251**, 211–225,
2429 doi:10.1016/j.icarus.2014.04.050.
- 2430 Becerra, P., Conway, S., Thomas, N., The HiRISE team, 2020. Avalanches of the martian north
2431 polar cap. Presented at *EGU General Assembly 2020*, 22331.
- 2432 Bennett, C.J., McLain, J.L., Sarantos, M., Gann, R.D., DeSimone, A., Orlando, T.M., 2016.
2433 Investigating potential sources of Mercury’s exospheric Calcium: Photon–stimulated
2434 desorption of Calcium Sulfide: PSD OF CAS. *Journal of Geophysical Research: Planets*,
2435 **121**, 137–146, doi:10.1002/2015JE004966.
- 2436 Benson, J. L., Kass, D. M., Kleinböhl, A. 2011. Mars’ north polar hood as observed by the Mars
2437 Climate Sounder. *Journal of Geophysical Research*, **116**, E03008,
2438 doi:10.1029/2010JE003693.
- 2439 Berger, J.A., Schmidt, M.E., Gellert, R., Campbell, J.L., Boyd, N.I., Elliott, B.E., Fisk, M.R.,
2440 King, P.L., Ming, D.W., Perrett, G.M., Thompson, L.M., 2015. Germanium enrichments in
2441 sedimentary rocks in Gale Crater, Mars: Constraining the timing of alteration and character
2442 of the protolith. Presented at the *46th Lunar and Planetary Science Conference*, Ab. 1564.
- 2443 Berman D.C., Balme M.R., Rafkin S.C.R., Zimbelman J.R., 2011. Transverse aeolian ridges
2444 (TARs) on Mars II: Distributions, orientations, and ages. *Icarus*, **213**, 116–130,
2445 doi:10.1016/j.icarus.2011.02.014.
- 2446 Berman, D.C., Balme, M.R., Michalski, J.R., Clark, S.C., Joseph, E.S.C., 2018. High-resolution
2447 investigations of transverse aeolian ridges on Mars. *Icarus*, **312**, 247–266,
2448 doi:10.1016/j.icarus.2018.05.003.
- 2449 Bertrand, T., Forget, F., Umurhan, O.M., Grundy, W.M., Schmitt, B., Protopapa, S., Zangari,
2450 A.M., White, O.L., Schenk, P.M., Singer, K.N., Stern, A., 2018. The nitrogen cycles on Pluto
2451 over seasonal and astronomical timescales. *Icarus*, **309**, 277–296,
2452 doi:10.1016/j.icarus.2018.03.012.
- 2453 Bertrand, T., Forget, F., Umurhan, O.M., Moore, J.M., Young, L.A., Protopapa, S., Grundy,
2454 W.M., Schmitt, B., Dhingra, R.D., Binzel, R.P., Earle, A.M., 2019. The CH₄ cycles on Pluto
2455 over seasonal and astronomical timescales. *Icarus*, **329**, 148–165,
2456 doi:10.1016/j.icarus.2019.02.007.
- 2457 Bertrand, T., Forget, F., White, O., Schmitt, B., Stern, S.A., Weaver, H.A., Young, L.A., Ennico,
2458 K., Olkin, C.B., New Horizons Science Team, 2020. Pluto’s beating heart regulates the
2459 atmospheric circulation: Results from high-resolution and multiyear numerical climate
2460 simulations. *Journal of Geophysical Research: Planets*, **125**(2), e2019JE006120,
2461 doi:10.1029/2019JE006120.
- 2462 Bibring, J.-P., Langevin, Y., Poulet, F., Gendrin, A., Gondet, B., Berthé, M., Soufflot, A., Drossart,
2463 P., Combes, M., Bellucci, G., Moroz, V., 2004. Perennial water ice identified in the south polar
2464 cap of Mars. *Nature*, **428**(6983), 627–630.
- 2465 Bierson, C.J., Phillips, R.J., Smith, I.B., Wood, S.E., Putzig, N.E., Nunes, D., Byrne, S., 2016.
2466 Stratigraphy and evolution of the buried CO₂ deposit in the martian south polar cap.
2467 *Geophysical Research Letters*, **43**(9), 4172–4179.

2468 Birch, S.P.D., Tang, Y., Hayes, A.G., Kirk, R.L., Bodewits, D., Campins, H., Fernandez, Y., de
2469 Freitas Bart, R., Kutsop, N.W., Sierks, H., Soderblom, J.M., Squyres, S.W., Vincent, J.-B.,
2470 2017. Geomorphology of comet 67P/Churyumov–Gerasimenko. *Monthly Notices of the*
2471 *Royal Astronomical Society* **469**, S50–S67, doi:10.1093/mnras/stx1096.

2472 Bishop, J.L., Yeşilbaş, M., Hinman, N.W., Burton, Z.F.M., Englert, P.A.J., Toner, J.D.,
2473 McEwen, A.S., Gulick, V.C., Gibson, E.K., Koeberl, C., 2020. Martian subsurface cryosalt
2474 expansion and collapse as trigger for landslides. *Science Advances*, in press.

2475 and Blewett, D.T., Chabot, N.L., Denevi, B.W., Ernst, C.M., Head, J.W., Izenberg, N.R.,
2476 Murchie, S.L., Solomon, S.C., Nittler, L.R., McCoy, T.J., Xiao, Z., Baker, D.M.H., Fassett,
2477 C.I., Braden, S.E., Oberst, J., Scholten, F., Preusker, F., Hurwitz, D.M., 2011. Hollows on
2478 Mercury: MESSENGER evidence for geologically recent volatile-related activity. *Science*,
2479 **333**, 1856–1859, doi:10.1126/science.1211681.

2480 Bordiec, M., Carpy, S., Bourgeois, O., Hery, C., Massé, M., Perret, L., Claudin, P., Pochat, S.,
2481 Douté, S., 2020. Sublimation waves: Geomorphic markers of interactions between icy
2482 planetary surfaces and winds. *Earth-Science Reviews*, **211**, 103350,
2483 doi:10.1016/j.earscirev.2020.103350.

2484 Bourke, M.C., Cranford, A., 2011. Seasonal furrow formation on Mars polar dunes. Presented at
2485 *Fifth International Conference on Mars Polar Science and Exploration*, Ab. #6059.

2486 Bourke, M., Wilson, S.A., Zimelman, J.R., 2003. The variability of transverse aeolian ridges in
2487 troughs on Mars. Presented at the *34th Lunar and Planetary Science Conference*, Ab. 2090.

2488 Bourke, M.C., Bullard, J.E., Barnouin-Jha, O.S., 2004. Aeolian sediment transport pathways and
2489 aerodynamics at troughs on Mars. *Journal of Geophysical Research: Planets*, **109**, E07005,
2490 doi:10.1029/2003JE002155.

2491 Bourke, M., Edgett, K., Cantor, B., 2008. Recent aeolian dune change on Mars. *Geomorphology*,
2492 **94**, 247–255, doi: 10.1016/j.geomorph.2007.05.012.

2493 Bourke, M.C., Ewing, R.C., Finnegan, D., McGowan, H.A., 2009. Sand dune movement in the
2494 Victoria Valley, Antarctica. *Geomorphology*, **109**, 148–160,
2495 doi:10.1016/j.geomorph.2009.02.028.

2496 Bourke, M.C., Nield, J.M., Diniega, S., Hansen, C.J., McElwain, J.N., Titus, T.N., 2016a. The
2497 geomorphic effect of sublimating CO₂ blocks on dune lee slopes at Grand Falls, Arizona.
2498 Presented at the *47th Lunar and Planetary Science Conference*, Ab. 2407.

2499 Bourke, M., Nield, J., Diniega, S., Hansen, C., McElwaine, J., 2016b. A field study of the
2500 geomorphic effects of sublimating CO₂ blocks on dune slopes at Coral Pink Dunes, Utah.
2501 Presented at the *European Planetary Science Conference*, Ab. EPSC2016-10450.

2502 Boyce, J.M., Wilson, L., Mougini-Mark, P.J., Hamilton, C.W., Tornabene, L.L., 2012. Origin of
2503 small pits in martian impact craters. *Icarus*, **221**, 262–275, doi:10.1016/j.icarus.2012.07.027.

2504 Boynton, W., Feldman, W.C., Squyres, S.W., Prettyman, T.H., Brückner, J., Evans, L.G., Reedy,
2505 R.C., Starr, R., Arnold, J.R., Drake, D.M., Englert, P.A.J., 2002. Distribution of hydrogen in
2506 the near surface of Mars: Evidence for subsurface ice deposits. *Science*, 297(5578), 81–85,
2507 doi:10.1126/science.1073722.

- 2508 Bramson, A.M., Byrne, S., Putzig, N.E., Sutton, S., Plaut, J.J., Brothers, T.C., Holt, J.W., 2015.
2509 Widespread excess ice in Arcadia Planitia, Mars. *Geophysical Research Letters*, **42**(16),
2510 6566–6574, doi:10.1002/2015GL064844.
- 2511 Bramson, A.M., Byrne, S., Bapst, J., 2017. Preservation of mid-latitude ice sheets on Mars.
2512 *Journal of Geophysical Research*, **122**, 2250–2266, doi:10.1002/2017JE005357.
- 2513 Bramson, A.M., Byrne, S., Bapst, J., Smith, I.B., McClintock, T., 2019. A migration model for
2514 the polar spiral troughs of Mars. *JGR Planets*, **124**(4), 1020–1043,
2515 doi:10.1029/2018JE005806.
- 2516 Bridges, N.T., Ehlmann, B.L., 2018. The Mars Science Laboratory (MSL) Bagnold dunes
2517 campaign, Phase I: Overview and introduction to the special issue. *Journal of Geophysical*
2518 *Research: Planets*, **123**(1), 3–19, doi:10.1002/2017JE005401.
- 2519 Bridges, N.T., Herkenhoff, K.E., Titus, T.N., Kieffer, H.H., 2001. Ephemeral dark spots
2520 associated with martian gullies. Presented at *32nd Lunar and Planetary Science Conference*,
2521 Ab. #2126.
- 2522 Bridges, N.T., Geissler, P.E., McEwen, A.S., Thomson, B.J., Chuang, F.C., Herkenhoff, K.E.,
2523 Keszthelyi, L.P., Martínez-Alonso, S., 2007. Windy Mars: A dynamic planet as seen by the
2524 HiRISE camera. *Geophysical Research Letters*, **34**(23), L23205,
2525 doi:10.1029/2007GL031445.
- 2526 Bridges, N.T., Bourke, M.C., Geissler, P.E., Banks, M.E., Colon, C., Diniega, S., Golombek,
2527 M.P., Hansen, C.J., Mattson, S., McEwen, A.S., Mellon, M.T., 2012a. Planet-wide sand
2528 motion on Mars. *Geology*, **40**(1), 31–34, doi:10.1130/G32373.1.
- 2529 Bridges, N.T., Ayoub, F., Avouac, J.-P., Leprince, S., Lucas, A., Mattson, S., 2012b. Earth-like
2530 sand fluxes on Mars. *Nature*, **485**, 339–342, doi:10.1038/nature11022.
- 2531 Bridges, N.T., Geissler, P., Silvestro, S., Banks, M., 2013. Bedform migration on Mars: Current
2532 results and future plans. *Aeolian Research*, **9**, 133–151, doi:10.1016/j.aeolia.2013.02.004.
- 2533 Bridges, N.T., Sullivan, R., Newman, C.E., Navarro, S., van Beek, J., Ewing, R.C., Ayoub, F.,
2534 Silvestro, S., Gasnault, O., Le Mouélic, S., Lapôtre, M. G. A., Rapin, W., 2017. martian
2535 aeolian activity at the Bagnold Dunes, Gale Crater: The view from the surface and orbit.
2536 *Journal of Geophysical Research: Planets*, **112**, 2077–2100, doi:10.1002/2017JE005263.
- 2537 Brothers S.C., Kocurek G., 2018. The transitional depositional environment and sequence
2538 stratigraphy of Chasma Boreale. *Icarus*, **308**, 27–41, doi:10.1016/j.icarus.2017.08.038.
- 2539 Brown, J.R., Roberts, G.P., 2019. Possible evidence for variation in magnitude for marsquakes
2540 from fallen boulder populations, Grjota Valles, Mars. *Journal of Geophysical Research:*
2541 *Planets*, **124**, 801–822, doi:10.1029/2018JE005622.
- 2542 Brown, A.J., Calvin, W.M., Becerra, P., Byrne, S., 2016. Martian north polar cap summer water
2543 cycle. *Icarus*, **277**, 401–415, doi:10.1016/j.icarus.2016.05.007.
- 2544 Buhler, P.B., Ingersoll, A.P., 2018. Sublimation pit distribution indicates convection cell surface
2545 velocities of ~ 10 cm per year in Sputnik Planitia, Pluto. *Icarus*, **300**, 327–340,
2546 doi:10.1016/j.icarus.2017.09.018.
- 2547 Buhler, P.B., Ingersoll, A.P., Ehlmann, B.L., Fassett, C.I., Head, J.W., 2017. How the martian
2548 residual south polar cap develops quasi-circular and heart-shaped pits, troughs, and moats.
2549 *Icarus*, **286**, 69–93, doi:10.1016/j.icarus.2017.01.012.

- 2550 Buhler, P.B., Dickson, J., Ehlmann, B.L., Ingersoll, A.P., Byrne, S., Tao, Y., Muller, J.P., 2018.
2551 Prospects for measuring vertical change on the martian residual south polar cap using HiRISE
2552 digital elevation models. Presented at the 49th Lunar and Planetary Science Conference, Ab.
2553 2908.
- 2554 Buhler, P.B., Ingersoll, A.P., Piqueux, S., Ehlmann, B.L., Hayne, P.O., 2020. Coevolution of Mars'
2555 atmosphere and massive south polar CO₂ ice deposit. *Nature Astronomy*, **4**, 364–371,
2556 doi:10.1038/s41550-019-0976-8.
- 2557 Businger, J.A., Yaglom, A.M., 1971. Introduction to Obukhov's paper on 'turbulence in an
2558 atmosphere with a non-uniform temperature'. *Boundary-Layer Meteorology*, **2**(1), 3–6.
- 2559 Byrne, S., Ingersoll, A.P., 2003a. Martian climatic events on timescales of centuries: Evidence
2560 from feature morphology in the residual south polar ice cap. *Geophysical Research Letters*,
2561 **30**(13), 1696, doi:10.1029/2003GL017597.
- 2562 Byrne, S., Ingersoll, A.P., 2003b. A sublimation model for martian south polar ice features.
2563 *Science*, **299**(5609), 1051–1053, doi:10.1126/science.1080148.
- 2564 Byrne, S., Murray, B.C. 2002. North polar stratigraphy and the paleo-erg of Mars. *Journal of*
2565 *Geophysical Research*, **107**, 1–12.
- 2566 Byrne, S., Dundas, C.M., Kennedy, M.R., Mellon, M.T., McEwen, A.S., Cull, S.C., Daubar, I.J.,
2567 Shean, D.E., Seelos, K.D., Murchie, S.L., Cantor, B.A., 2009. Distribution of mid-latitude
2568 ground ice on Mars from new impact craters. *Science*, **325**(5948), 1674–1676,
2569 doi:10.1126/science.1175307.
- 2570 Byrne, S., Hayne, P.O., Becerra, P., the HiRISE Team, 2015. Evolution and stability of the residual
2571 CO₂ ice cap. Presented at the 46th Lunar and Planetary Science Conference, Ab. 1657.
- 2572 Byrne, S., Sori, M.M., Russell, P., Pathare, A.V., Becerra, P., Molaro, J.L., Sutton, S., Mellon,
2573 M.T., the HiRISE Team, 2017. Mars polar cliffs: stressed out and falling apart. Presented at
2574 the *European Planetary Science Congress 2017*, Ab. 333.
- 2575 Calvin, W.M., Seelos, K.D., 2019. Evolution within the Martian Southern Seasonal Cryptic
2576 Terrain from CTX and CRISM. Presented at the *AGU Fall Meeting*, 2019, Ab. P33F-3501.
- 2577 Calvin, W.M., James, P.B., Cantor, B.A., Dixon, E.M., 2015. Interannual and seasonal changes
2578 in the north polar ice deposits of Mars: Observations from MY 29–31 using MARCI. *Icarus*,
2579 **251**, 181-190, doi:10.1016/j.icarus.2014.08.026.
- 2580 Cardinale, M., Pozzobon, R., Tangari, A.C., Runyon, K., Di Primio, M., Marinangeli, L., 2020.
2581 Reconstruction of the sand transport pathways and provenance in Moreux crater, Mars.
2582 *Planetary and Space Science*, **181**, 104788, doi:10.1016/j.pss.2019.104788.
- 2583 Cartwright, R.J., Emery, J.P., Rivkin, A.S., Trilling, D.E., Pinilla-Alonso, N., 2015. Distribution
2584 of CO₂ ice on the large moons of Uranus and evidence for compositional stratification of
2585 their near-surfaces. *Icarus*, **257**, 428–456, doi:10.1016/j.icarus.2015.05.020.
- 2586 Cedillo-Flores, Y., Treiman, A. H., Lasue, J., Clifford, S. M., 2011. CO₂ gas fluidization in the
2587 initiation and formation of martian polar gullies. *Geophysical Research Letters*, **38**, L21202,
2588 doi:10.1029/2011GL049403.
- 2589 Chamberlain, M.A., Boynton, W.V., 2007. Response of martian ground ice to orbit-induced
2590 climate change. *Journal of Geophysical Research*, **112**, E06009.
2591 <https://doi.org/10.1029/2006JE002801>.

- 2592 Cheng, A.F., Lisse, C.M., A'Hearn, M., 2013. Surface geomorphology of Jupiter Family
2593 Comets: A geologic process perspective. *Icarus*, **222**(2), 808–817,
2594 doi:10.1016/j.icarus.2012.10.004.
- 2595 Chevrier, V.F., Rivera-Valentin, E.G., 2012. Formation of recurring slope lineae by liquid brines
2596 on present-day Mars. *Geophysical Research Letters*, **39**, doi:10.1029/2012GL054119.
- 2597 Chinnery, H.E., Hagermann, A., Kaufmann, E., Lewis, S.R., 2018. The penetration of solar
2598 radiation into carbon dioxide ice. *Journal of Geophysical Research: Planets*, **123**(4), 864–
2599 871, doi:10.1002/2018JE005539.
- 2600 Chojnacki, M., Moersch, J., Burr, D., 2010. Climbing and falling dunes in Valles Marineris,
2601 Mars. *Geophysical Research Letters*, **37**(8), L08201, doi:10.1029/2009GL042263.
- 2602 Chojnacki, M., Burr, D.M., Moersch, J.E., 2014a. Valles Marineris dune fields as compared with
2603 other martian populations: Diversity of dune compositions, morphologies, and
2604 thermophysical properties. *Icarus (Third Planetary Dunes Systems)*, **230**, 96–142,
2605 doi:10.1016/j.icarus.2013.08.018.
- 2606 Chojnacki, M., Burr, D.M., Moersch, J.E., Wray J. J., 2014b. Valles Marineris dune sediment
2607 provenance and pathways. *Icarus*, **232**, 187–219, doi:10.1016/j.icarus.2014.01.011.
- 2608 Chojnacki, M., Johnson, J.R., Moersch, J.E., Fenton, L.K., Michaels, T.I., Bell III, J.F., 2015.
2609 Persistent aeolian activity at Endeavour crater, Meridiani Planum, Mars: new observations
2610 from orbit and the surface. *Icarus*, **251**, 275–290, doi:10.1016/j.icarus.2014.04.044.
- 2611 Chojnacki, M., McEwen, A., Dundas, C., Ojha, L., Urso, A., Sutton, S., 2016. Geologic context
2612 of Recurring Slope Lineae in Melas and Coprates Chasmata, Mars. *Journal of Geophysical
2613 Research*, **121**(2), 1204–1231, doi:10.1002/2015JE004991.
- 2614 Chojnacki, M., Urso, A.C., Fenton, L.K., Michaels, T.I., 2017. Aeolian dune sediment flux
2615 heterogeneity in Meridiani Planum, Mars. *Aeolian Research*, **26**, 73–88,
2616 doi:10.1016/j.aeolia.2016.07.004.
- 2617 Chojnacki, M., Banks, M., Urso, A., 2018. Wind-driven erosion and exposure potential at Mars
2618 2020 rover candidate-landing sites. *Journal of Geophysical Research: Planets*, **123**, 468–488,
2619 doi:10.1002/2017JE005460.
- 2620 Chojnacki, M., Banks, M.E., Fenton, L.K., Urso, A.C., 2019. Boundary condition controls on the
2621 high-sand-flux regions of Mars. *Geology*, **47**(5), 427–430, doi: 10.1130/G45793.1.
- 2622 Chojnacki, M., Fenton, L.K., Weintraub, A.R., Edgar, L.A., Jodhpurkar, M.J., Edwards, C.S.
2623 2020. Ancient martian aeolian sand dune deposits recorded in the stratigraphy of Valles
2624 Marineris and implications for past climates. *Journal of Geophysical Research: Planets*, **125**,
2625 e2020JE006510, doi:10.1029/2020JE006510.
- 2626 Chuang, F.C., Beyer, R.A., McEwen, A.S., Thomson, B.J., 2007. HiRISE observations of slope
2627 streaks on Mars. *Geophysical Research Letters*, **34**(20), L20204,
2628 doi:10.1029/2007GL031111.
- 2629 Claudin, P., Andreotti, B., 2006. A scaling law for aeolian dunes on Mars, Venus, Earth, and for
2630 subaqueous ripples. *Earth and Planetary Science Letters*, **252**, 30–44,
2631 doi:10.1016/j.epsl.2006.09.004.

- 2632 Colaprete, A., Barnes, J.R., Haberle, R.M., Hollingsworth, J.L., Kieffer, H.H., Titus, T.N., 2005.
2633 Albedo of the south pole on Mars determined by topographic forcing of atmosphere dynamics.
2634 *Nature*, **435**, 184–188, doi:10.1038/nature03561.
- 2635 Costard, F.M., Kargel, J.S., 1995. Outwash plains and thermokarst on Mars. *Icarus*, **114**, 93–112.
- 2636 Courrech du Pont, S., Narteau, C., Gao, X. 2014. Two modes for dune orientation. *Geology*,
2637 **42**(9), 743–746, doi: 10.1130/G35657.1.
- 2638 Cross, A.J., Goldsby, D.L., Hager, T.F., Smith, I.B., 2020. The rheological behavior of CO₂ ice:
2639 Application to glacial flow on Mars. *Geophysical Research Letters*, **47**(22), GL090431,
2640 doi:10.1029/2020GL090431.
- 2641 Daubar, I.J., McEwen, A.S., Byrne, S., Kennedy, M.R., Ivanov, B., 2013. The current martian
2642 cratering rate. *Icarus*, **225**, 506–516, doi:10.1016/j.icarus.2013.04.009.
- 2643 Daubar, I.J., Banks, M.E., Schmerr, N.C., Golombek, M.P., 2019. Recently formed crater
2644 clusters on Mars. *Journal of Geophysical Research: Planets*, **124**(4), 958–969,
2645 doi:10.1029/2018JE005857.
- 2646 Davis, J.M., Banham, S.G., Grindrod, P.M., Boazman, S.J., Balme, M.R., Bristow, C.S., 2020.
2647 Morphology, development, and sediment dynamics of elongating linear dunes on Mars.
2648 *Geophysical Research Letters*, **47**, e2020GL088456, doi:10.1029/2020GL088456.
- 2649 Day, M., Kocurek, G. 2016. Observations of an aeolian landscape: From surface to orbit in Gale
2650 crater. *Icarus*, **280**, 37–71, doi: 10.1016/j.icarus.2015.09.042
- 2651 Day, M., Edgett, K. S., Stumbaugh, D., 2019. Ancient stratigraphy preserving a wet-to-dry,
2652 fluvio-lacustrine to aeolian transition near Barth crater, Arabia Terra, Mars. *Journal of*
2653 *Geophysical Research: Planets*, **124**(12), 3402–3421, doi:10.1029/2019JE006226.
- 2654 de Haas, T., McArdell, B.W., Conway, S.J., McElwaine, J.N., Kleinhans, M.G., Salese, F.,
2655 Grindrod, P.M., 2019. Initiation and flow conditions of contemporary flows in Martian
2656 gullies. *J. Geophys Res. Planets*, **124**, 2246–2271, doi:10.1029/2018JE005899.
- 2657 Denevi, B.W., Blewett, D.T., Buczkowski, D.L., Capaccioni, F., Capria, M.T., De Sanctis, M.C.,
2658 Garry, W.B., Gaskell, R.W., Le Corre, L., Li, J.-Y., Marchi, S., McCoy, T.J., Nathues, A.,
2659 O'Brien, D.P., Petro, N.E., Pieters, C.M., Preusker, F., Raymond, C.A., Reddy, V., Russell,
2660 C.T., Schenk, P., Scully, J.E.C., Sunshine, J.M., Tosi, F., Williams, D.A., Wyrick, D., 2012.
2661 Pitted terrain on Vesta and implications for the presence of volatiles. *Science*, **338**, 246–249,
2662 doi:10.1126/science.1225374.
- 2663 Dickson, J.L., Head, J.W., Levy, J.S., Marchant, D.R., 2013. Don Juan Pond, Antarctica: near-
2664 surface CaCl₂-brine feeding Earth's most saline lake and implications for Mars. *Scientific*
2665 *Reports*, **3**, 1166, doi:10.1038/srep01166.
- 2666 Dickson, J.L., Kerber, L.A., Fassett, C.I., Ehlmann, B.L., 2018. A global, blended CTX mosaic
2667 of Mars with vectorized seam mapping: a new mosaicking pipeline using principles of non-
2668 destructive image editing. Presented at the 49th Lunar and Planetary Science Conference, Ab.
2669 2480.
- 2670 Diniega, S., Smith, I.B., 2020. High-priority science questions identified at the Mars Workshop
2671 on Amazonian and Present-day Climate. *Planetary and Space Science*, **182**, 104813,
2672 doi:10.1016/j.pss.2019.104813.

- 2673 Diniega, S., Byrne, S., Bridges, N.T., Dundas, C.M., McEwen, A.S., 2010. Seasonality of
2674 present-day martian dune-gully activity. *Geology*, **38**, 1047–1050, doi:10.1130/G31287.1.
- 2675 Diniega, S., Hansen, C.J., McElwaine, J.N., Hugenholtz, C.H., Dundas, C.M., McEwen, A.S.,
2676 Bourke, M.C., 2013. A new dry hypothesis for the formation of martian linear gullies. *Icarus*,
2677 **225**(1), 526–537, doi:10.1016/j.icarus.2013.04.006.
- 2678 Diniega, S., Kreslavsky, M., Radebaugh, J., Silvestro, S., Telfer, M., Tirsch, D., 2017. Our
2679 evolving understanding of aeolian bedforms, based on observation of dunes on different
2680 worlds. *Aeolian Research*, **26**, 5–27, doi:10.1016/j.aeolia.2016.10.001.
- 2681 Diniega, S., Hansen, C.J., Allen, A., Grigsby, N., Li, Z., Perez, T., Chojnacki, M., 2019a. Dune-
2682 slope activity due to frost and wind throughout the north polar erg, Mars. *Geological Society,*
2683 *London, Special Publications*, **467**, 95–114, doi:10.1144/SP467.6
- 2684 Diniega, S., Widmer, J.M., Gary-Bicas, C., Fraeman, A.A., Hayne, P.O., Piqueux, S., 2019b.
2685 Correlating present-day surface and subsurface frost conditions with geomorphologic activity
2686 on Mars. Presented at the 50th Lunar and Planetary Science Conference, Ab. 2165.
- 2687 Dorn, T., Day, M. 2020. Intracrater sediment trapping and transport in Arabia Terra, Mars.
2688 *Journal of Geophysical Research: Planets*, **125**(9), e2020JE006581,
2689 doi:10.1029/2020JE006581.
- 2690 Dundas, C.M., 2017. Effects of varying obliquity on Martian sublimation thermokarst landforms.
2691 *Icarus*, **281**, 115–120, doi:10.1016/j.icarus.2016.08.031.
- 2692 Dundas, C.M., 2020a. An aeolian grainflow model for martian Recurring Slope Lineae, *Icarus*,
2693 **343**, 113681, doi:10.1016/j.icarus.2020.113681.
- 2694 Dundas, C.M., 2020b. Geomorphological evidence for a dry dust avalanche origin of slope
2695 streaks on Mars. *Nature Geoscience*, **13**, 473–476, doi:10.1038/s41561-020-0598-x.
- 2696 Dundas, C.M., Byrne, S., 2010. Modeling sublimation of ice exposed by new impacts in the
2697 martian mid-latitudes. *Icarus*, **206**, 716–728. <https://doi.org/10.1016/j.icarus.2009.09.007>.
- 2698 Dundas, C.M., Diniega, S., Hansen, C.J., Byrne, S. McEwen, A.S., 2012. Seasonal activity and
2699 morphological changes in Martian gullies. *Icarus*, **220**(1), 124–143,
2700 doi:10.1016/j.icarus.2012.04.005.
- 2701 Dundas, C.M., Byrne, S., McEwen, A.S., Mellon, M.T., Kennedy, M.R., Daubar, I.J., Saper, L.,
2702 2014. HiRISE observations of new impact craters exposing martian ground ice. *Journal of*
2703 *Geophysical Research*, **119**, 109–127, doi:10.1002/2013JE004482.
- 2704 Dundas, C.M., Diniega, S., McEwen, A.S., 2015a. Long-term monitoring of martian gully
2705 formation and evolution with MRO/HiRISE. *Icarus*, **251**, 244–263,
2706 doi:10.1016/j.icarus.2014.05.013.
- 2707 Dundas, C.M., Byrne, S., McEwen, A., 2015b. Modeling the development of martian
2708 sublimation thermokarst landforms. *Icarus*, **262**, 154–169, doi:10.1016/j.icarus.2015.07.033.
- 2709 Dundas, C.M., McEwen, A.S., Chojnacki, M., Milazzo, M.P., Byrne, S., McElwaine, J.N., Urso,
2710 A., 2017. Granular flows at recurring slope lineae on Mars indicate a limited role for liquid
2711 water. *Nature Geoscience*, **10**(12), 903–907.

- 2712 Dundas, C.M., Bramson, A.M., Ojha, L., Wray, J.J., Mellon, M.T., Byrne, S., McEwen, A.S.,
2713 Putzig, N.E., Viola, D., Sutton, S., Clark, E., 2018. Exposed subsurface ice sheets in the
2714 martian mid-latitudes. *Science*, **359**, 199–201, doi:10.1126/science.aao1619.
- 2715 Dundas, C.M., McEwen, A.S., Diniega, S., Hansen, C. J., Byrne, S., McElwaine, J.N., 2019a.
2716 The formation of gullies on Mars today. *Geological Society, London, Special Publications*,
2717 **467**, 67–94, doi:10.1144/SP467.5.
- 2718 Dundas, C.M., Mellon, M.T., Conway, S.J., Gastineau, R., 2019b. Active boulder movement at
2719 high martian latitudes. *Geophysical Research Letters*, **46**(10), 2019GL082293,
2720 doi:10.1029/2019GL082293.
- 2721 Duran Vinent, O., Andreotti, B., Claudin, P., Winter, C., 2019. A unified model of ripples and
2722 dunes in water and planetary environments. *Nature Geoscience*, **12**, 345–350,
2723 doi:10.1038/s41561-019-0336-4.
- 2724 Edgett, K., Christensen, P., 1991. The particle size of martian aeolian dunes. *Journal of*
2725 *Geophysical Research*, **96**(E5), 22,765–22,776.
- 2726 Edgett, K.S., Lancaster, N., 1993. Volcaniclastic aeolian dunes: terrestrial examples and
2727 application to martian sands. *Journal of Arid Environments*, **25**(3), 271–297,
2728 doi:10.1006/jare.1993.1061.
- 2729 Edgett, K.S., Malin, M.C., 2000. New views of Mars eolian activity, materials, and surface
2730 properties: Three vignettes from the Mars Global Surveyor Mars Orbiter Camera. *Journal of*
2731 *Geophysical Research*, **105**, 1623–1650, doi:10.1029/1999JE001152.
- 2732 Edwards, C.S., Piqueux, S., 2016. The water content of recurring slope lineae on Mars.
2733 *Geophysical Research Letters*, **43**, doi:10.1002/2016GL070179.
- 2734 Edwards, C.S., Piqueux, S., Hamilton, V.E., Fergason, R.L., Herkenhoff, K.E., Vasavada, A.R.,
2735 Bennett, K.A., Sacks, L., Lewis, K., Smith, M.D., 2018. The thermophysical properties of the
2736 Bagnold Dunes, Mars: Ground-truthing orbital data. *Journal of Geophysical Research:*
2737 *Planets*, **123**, 1307–1326, doi:10.1029/2017JE005501.
- 2738 Ehlmann, B.L., Edgett, K.S., Sutter, B., Achilles, C.N., Litvak, M.L., Lapôtre, M.G.A., Sullivan,
2739 R., Fraeman, A.A., Arvidson, R.E., Blake, D.F., Bridges, N.T., 2017. Chemistry, mineralogy,
2740 and grain properties at Namib and High dunes, Bagnold dune field, Gale crater, Mars: A
2741 synthesis of Curiosity rover observations. *Journal of Geophysical Research: Planets*, **122**,
2742 2510–2543, doi:10.1002/2017JE005267.
- 2743 Ewing R.C., Kocurek G., 2010. Aeolian dune-field pattern boundary conditions.
2744 *Geomorphology*, **114**, 175–187, doi:10.1016/j.geomorph.2009.06.015.
- 2745 Ewing, R.C., Lapôtre, M.G.A., Lewis, K.W., Day, M., Stein, N., Rubin, D.M., Sullivan, R.,
2746 Banham, S., Lamb, M.P., Bridges, N.T., Gupta, S., 2017. Sedimentary processes of the
2747 Bagnold Dunes: Implications for the eolian rock record of Mars. *Journal of Geophysical*
2748 *Research: Planets*, **122**, 2544–2573, doi:10.1002/2017JE005324.
- 2749 Fanale, F.P., Salvail, J.R., Zent, A.P., Postawko, S.E., 1986. Global distribution and migration of
2750 subsurface ice on Mars. *Icarus*, **67**(1), 1–18, doi:10.1016/0019-1035(86)90170-3.
- 2751 Fanara, L., Gwinner, K., Hauber, E., Oberst, J., 2020a. Present-day erosion rate of north polar
2752 scarps on Mars due to active mass wasting. *Icarus*, **342**, 113434,
2753 doi:10.1016/j.icarus.2019.113434.

- 2754 Fanara, L., Gwinner, K., Hauber, E., Oberst, J., 2020b. Automated detection of block falls in the
2755 north polar region of Mars. *Planetary and Space Science*, **180**, 104733,
2756 doi:10.1016/j.pss.2019.104733.
- 2757 Farley, K.A., Malespin, C., Mahaffy, P., Grotzinger, J.P., Vasconcelos, P.M., Milliken, R.E.,
2758 Malin, M., Edgett, K.S., Pavlov, A.A., Hurowitz, J.A., Grant, J.A., 2014. In situ radiometric
2759 and exposure age dating of the Martian surface. *Science*, **343**(6169), 1247166,
2760 doi:10.1126/science.1247166.
- 2761 Fedo, C.M., McGlynn, I.O., McSween Jr, H.Y., 2015. Grain size and hydrodynamic sorting
2762 controls on the composition of basaltic sediments: Implications for interpreting martian soils.
2763 *Earth and Planetary Science Letters*, **423**, 67–77, doi:10.1016/j.epsl.2015.03.052.
- 2764 Fenton, L.K., 2005. Potential sand sources for the dune fields in Noachis Terra, Mars. *Journal of*
2765 *Geophysical Research*, **110**, E11004, doi:10.1029/2005JE002436.
- 2766 Fenton, L.K., 2020. Updating the global inventory of dune fields on mars and identification of
2767 many small dune fields. *Icarus*, **352**, 114018, doi:10.1016/j.icarus.2020.114018.
- 2768 Fenton, L.K., Hayward R.K.. 2010. Southern high latitude dune fields on Mars: Morphology,
2769 aeolian inactivity, and climate change. *Geomorphology*, **121**, 98–121,
2770 doi:10.1016/j.geomorph.2009.11.006.
- 2771 Fenton, L.K., Michaels, T.I., 2010. Characterizing the sensitivity of daytime turbulent activity on
2772 Mars with the MRAMS LES: Early results. *Mars*, **5**, 159–171, doi:10.1555/mars.2010.0007.
- 2773 Fenton, L.K., Ewing, R.C., Bridges, N.T., Lorenz, R., 2013. 11.15 Extraterrestrial Aeolian
2774 Landscapes. In *Treatise on Geomorphology*. Elsevier, 287–312.
- 2775 Fenton, L.K., Gullikson, A.L., Hayward, R.K., Charles, H., Titus, T.N., 2019. The Mars Global
2776 Digital Dune Database (MGD3): global patterns of mineral composition and bedform
2777 stability. *Icarus*, **330**, 189–203, doi:10.1016/j.icarus.2019.04.025.
- 2778 Fischer, E., Martínez, G.M., Rennó, N.O., Tamppari, L.K., Zent, A.P., 2019. Relative humidity
2779 on Mars: new results from the Phoenix TECP sensor. *Journal of Geophysical Research:*
2780 *Planets*, **124**(11), 2780–2792, doi:10.1029/2019JE006080.
- 2781 Forget, F., Hourdin, F., Talagrand, O., 1998. CO₂ snowfall on Mars: Simulation with a general
2782 circulation model. *Icarus*, **131**(2), 302–316, doi:10.1006/icar.1997.5874.
- 2783 Forget, F., Hourdin, F., Fournier, R., Hourdin, C., Talagrand, O., Collins, M., Lewis, S. R., Read,
2784 P. L., Huot, J.-P., 1999. Improved general circulation models of the Martian atmosphere from
2785 the surface to above 80 km. *Journal of Geophysical Research*, **104**, 24,155-24,176,
2786 doi:10.1029/1999JE001025.
- 2787 Forget, F., Bertrand, T., Vangvichith, M., Leconte, J., Millour, E., Lellouch, E., 2017. A post-
2788 new horizons global climate model of Pluto including the N₂, CH₄ and CO cycles. *Icarus*,
2789 **287**, 54–71, doi:10.1016/j.icarus.2016.11.038.
- 2790 Foroutan, M., Steinmetz, G., Zimbelman, J.R., Duguay, C.R.. 2019. Megaripples at Wau-an-
2791 Namus, Libya: A new analog for similar features on Mars. *Icarus*, **319**, 840–851,
2792 doi:10.1016/j.icarus.2018.10.021.
- 2793 Foroutan, M., Zimbelman, J.R.. 2016. Mega-ripples in Iran: A new analog for transverse aeolian
2794 ridges on Mars. *Icarus*, **274**, 99–105, doi:10.1016/j.icarus.2016.03.025.

- 2795 French, H., 2007. *The Periglacial Environment*, Third Edition. Wiley, Chichester.
- 2796 Gallagher, C.J., Balme, M.R., 2011. Landforms indicative of ground-ice thaw in the northern
2797 high latitudes of Mars. *Geological Society, London, Special Publications*, **356**(1), 87–110,
2798 doi:10.1144/SP356.6.
- 2799 Gallagher, C., Balme, M.R., Conway, S.J., Grindrod, P.M., 2011. Sorted clastic stripes, lobes and
2800 associated gullies in high-latitude craters on Mars: Landforms indicative of very recent,
2801 polycyclic ground-ice thaw and liquid flows. *Icarus*, **211**(1), 458–471,
2802 doi:10.1016/j.icarus.2010.09.010.
- 2803 Gao, X., Narteau, C., Rozier, O., du Pont, S.C., 2015. Phase diagrams of dune shape and
2804 orientation depending on sand availability. *Scientific Reports*, **5**, 14677.
2805 doi:10.1038/srep14677.
- 2806 Gardin, E., Allemand, P., Quantin, C., Thollot, P., 2010. Defrosting, dark flow features, and dune
2807 activity on Mars: example in Russell crater. *Journal of Geophysical Research: Planets*,
2808 **115**(E6), E06016, doi:10.1029/2009JE003515.
- 2809 Gary-Bicas, C.E., Hayne, P.O., Horvath, T., Heavens, N.G., Kass, D.M., Kleinböhl, A., Piqueux,
2810 S., Shirley, J.H., Schofield, J.T., McCleese, D.J., 2020. Asymmetries in snowfall, emissivity,
2811 and albedo of Mars' seasonal polar caps: Mars Climate Sounder observations. *Journal of*
2812 *Geophysical Research: Planets*, **125**(5), e2019JE006150, doi:10.1029/2019JE006150.
- 2813 Giese, B., Denk, T., Neukum, G., Roatsch, T., Helfenstein, P., Thomas, P.C., Turtle, E.P.,
2814 McEwen, A., Porco, C.C., 2008. The topography of Iapetus' leading side. *Icarus*, **193**(2),
2815 359–371, doi:10.1016/j.icarus.2007.06.005.
- 2816 Geissler, P.E., 2014. The birth and death of transverse aeolian ridges on Mars. *Journal of*
2817 *Geophysical Research: Planets*, **119**(12), 2583–2599, doi:10.1002/2014JE004633.
- 2818 Geissler, P.E., Wilgus, J.T., 2017. The morphology of transverse aeolian ridges on Mars. *Aeolian*
2819 *Research*, **26**, 63–71, doi:10.1016/j.aeolia.2016.08.008.
- 2820 Geissler, P. E., Banks, M. E., Bridges, N. T., Silvestro, S., the HiRISE Team, 2012. HiRISE
2821 observations of sand dune motion on Mars: Emerging global trends. Presented at 3rd
2822 *International Planetary Dunes Workshop*, Ab. #7053.
- 2823 Gendrin, A., Mangold, N., Bibring, J.-P., Langevin, Y., Gondet, B., Poulet, F., Bonello, G.,
2824 Quantin, C., Mustard, J., Arvidson, R., LeMouélic, S., 2005. Sulfates in martian layered
2825 terrains: the OMEGA/Mars Express view. *Science*, **307**(5715), 1587–1591,
2826 doi:10.1126/science.1109087.
- 2827 Golombek, M.P., Grant, J.A., Crumpler, L.S., Greeley, R., Arvidson, R.E., Bell, J.F., Weitz,
2828 C.M., Sullivan, R., Christensen, P.R., Soderblom, L.A., Squyres, S.W., 2006. Erosion rates at
2829 the Mars Exploration Rover landing sites and long-term climate change on Mars. *Journal of*
2830 *Geophysical Research: Planets*, **111**(E12), E12S10, doi:10.1029/2006JE002754.
- 2831 Golombek, M.P., Warner, N.H., Ganti, V., Lamb, M.P., Parker, T.J., Ferguson, R.L., Sullivan,
2832 R., 2014. Small crater modification on Meridiani Planum and implications for erosion rates
2833 and climate change on Mars: Small crater modification on Mars. *Journal of Geophysical*
2834 *Research: Planets*, **119**, 2522–2547, doi:10.1002/2014JE004658.
- 2835 Golombek, M.P., Charalambous, C., Pike, W.T., Sullivan, R., 2018. The origin of sand on Mars.
2836 Presented at the 49th *Lunar and Planetary Science Conference*, Ab. 2319.

- 2837 Gomez-Elvira, J., Armiens, C., Carrasco, I., Genzer, M., Gomez, F., Haberle, R., Hamilton, V.E.,
2838 Harri, A.M., Kahanpaa, J., Kempainen, O., Lepinette, A. 2014. Curiosity's rover
2839 environmental monitoring station: Overview of the first 100 sols. *Journal of Geophysical*
2840 *Research: Planets*, **11**, 1680–1688, doi: 10.1002/2013JE004576
- 2841 Goudie, A.S., Watson, A., 1981. The shape of desert sand dune grains. *Journal of Arid*
2842 *Environments*, **4**(3), 185–190, doi:10.1016/S0140-1963(18)31559-3.
- 2843 Gough, R. V., Nuding, D. L., Toigo, A., Guzewich, S., Tolbert, M. A., 2019a. An Examination
2844 of Atmospheric Water Vapor as a Source for Recurring Slope Lineae on Mars. Presented at
2845 the *Ninth International Conference on Mars*, Ab. 6327.
- 2846 Gough, R.V., Primm, K.M., Rivera-Valentín, E.G., Martínez, G.M., Tolbert, M.A., 2019b. Solid-
2847 solid hydration and dehydration of Mars-relevant chlorine salts: Implications for Gale Crater
2848 and RSL locations. *Icarus*, **321**, 1–13, doi:10.1016/j.icarus.2018.10.034.
- 2849 Grant, J.A., Golombek, M.P., Wilson, S.A., Farley, K.A., Williford, K.H., Chen, A., 2018. The
2850 science process for selecting the landing site for the 2020 Mars rover. *Planetary and Space*
2851 *Science*, **164**, 106–126, doi:10.1016/j.pss.2018.07.001.
- 2852 Greeley, R., Iversen, J.D., 1985. *Wind as a geological process on Earth, Mars, Venus and Titan*.
2853 Greeley R (ed). Cambridge Univ. Press: New York
- 2854 Greeley, R., White, B., Leach, R., Iversen, J., Pollack, J., 1976. Mars: Wind friction speeds for
2855 particle movement. *Geophysical Research Letters*, **3**(8), 417–420.
- 2856 Greeley, R., Leach, R., White, B., Iversen, J., Pollack, J., 1980. Threshold windspeeds for sand
2857 on Mars: Wind tunnel simulations. *Geophysical Research Letters*, **7**(2), 121-124.
- 2858 Greeley, R., Leach, R.N., Williams, S.H., White, B.R., Pollack, J.B., Krinsley, D.H., Marshall,
2859 J.R., 1982. Rate of wind abrasion on Mars. *Journal of Geophysical Research*, **87**, 10009–
2860 10024, doi:10.1029/JB087iB12p10009.
- 2861 Greeley, R., Lancaster, N., Lee, S., Thomas, P., 1992. Martian aeolian processes, sediments, and
2862 features. In *Mars*, pp.730–766.
- 2863 Greeley, R., Bender, K., Thomas, P.E., 1995. Wind-related features and processes on Venus:
2864 Summary of Magellan results. *Icarus*, **115**, 399–420.
- 2865 Greeley, R., Arvidson, R.E., Barlett, P.W., Blaney, D., Cabrol, N.A., Christensen, P.R.,
2866 Ferguson, R.L., Golombek, M.P., Landis, G.A., Lemmon, M.T., McLennan, S.M., 2006.
2867 Gusev Crater: Wind-related features and processes observed by the Mars Exploration Rover
2868 Spirit. *Journal of Geophysical Research*, **111**, E02S09, doi:10.1029/2005JE002491
- 2869 Gigsby, N., Diniega, S., 2008. Slope and volume analysis of alcove-channel-apron avalanche
2870 morphologies within the north polar region of Mars. Presented at the *49th Lunar and*
2871 *Planetary Science Conference*, Ab. 1122.
- 2872 Grimm, R.E., Harrison, K.P., Stillman, D.E., 2014. Water budgets of martian recurring slope
2873 lineae. *Icarus*, **233**, 316–327, doi:10.1016/j.icarus.2013.11.013.
- 2874 Grotzinger, J.P., Milliken, R.E., 2012. The sedimentary rock record of Mars: Distribution,
2875 origins, and global stratigraphy. *SEPM Special Publication: Sedimentary Geology of Mars*,
2876 **102**, 1–48, doi:10.2110/pec.12.102.0001.

2877 Grotzinger, J.P., Arvidson, R.E., Bell Iii, J.F., Calvin, W., Clark, B.C., Fike, D.A., Golombek,
2878 M., Greeley, R., Haldemann, A., Herkenhoff, K.E., Jolliff, B.L., 2005. Stratigraphy and
2879 sedimentology of a dry to wet eolian depositional system, Burns Formation, Meridiani
2880 Planum, Mars. *Earth and Planetary Science Letters*, **240**, 11–72.

2881 Grundy, W., 2003. Discovery of CO₂ ice and leading–trailing spectral asymmetry on the uranian
2882 satellite Ariel. *Icarus*, **162**, 222–229, doi:10.1016/S0019-1035(02)00075-1.

2883 Grundy, W., Young, L., Spencer, J., Johnson, R., Young, E., Buie, M., 2006. Distributions of
2884 H₂O and CO₂ ices on Ariel, Umbriel, Titania, and Oberon from IRTF/SpEX observations.
2885 *Icarus*, **184**, 543–555, doi:10.1016/j.icarus.2006.04.016.

2886 Gwinner, K., Bostelmann, J., Dumke, A., Michael, G., Annibaldi, S., Stark, A., Kersten, E., Walter,
2887 S., Roatsch, T., Jaumann, R., 2019. Characteristics of the HRSC Mars Chart (HMC-30) and its
2888 quality of co-registration with the MOLA reference. Presented at the *European Planetary
2889 Science Conference*, Ab. EPSC-DPS2019-2006-1.

2890 Haberle, R. M., Gómez–Elvira, J., de la Torre Juárez, M., Harri, A.-M., Hollingsworth, J.L.,
2891 Kahanpaa, H., Kahre, M.A., Lemmon, M., Martín-Torres, F.J., Mischna, M., Moores, J.E.,
2892 Newman, C., Rafkin, S.C.R., Rennó, N., Richardson, M.I., Rodríguez–Manfredi, J.A.,
2893 Vasavada, A.R., Zorzano-Mier, M.-P., 2014. Preliminary interpretation of the REMS pressure
2894 data from the first 100 sols of the MSL mission. *Journal of Geophysical Research: Planets*,
2895 **19(3)**, 440–453.

2896 Hallet, B., 2013. Stone circles: form and soil kinematics. *Proc. R. Soc. A*, **371**(2004), 20120357–
2897 17, doi:10.1098/rsta.2012.0357.

2898 Hansen, C.J., Paige, D.A., 1992. A thermal model for the seasonal nitrogen cycle on Triton.
2899 *Icarus*, **99**(2), 273–288.

2900 Hansen, C.J., Paige, D.A., 1996. Seasonal Nitrogen Cycles on Pluto. *Icarus*, **120**, 247–265.

2901 Hansen, C. J., Thomas, N., Portyankina, G., McEwen, A.S., Becker, T., Byrne, S., Herkenhoff,
2902 K., Kieffer, H., Mellon, M., 2010. HiRISE observations of gas sublimation-driven activity in
2903 Mars’ southern polar regions: I. Erosion of the surface. *Icarus*, **205**, 283–295,
2904 doi:10.1016/j.icarus.2009.07.021.

2905 Hansen, C.J., Bourke, M., Bridges, N.T., Byrne, S., Colon, C., Diniega, S., Dundas, C.,
2906 Herkenhoff, K., McEwen, A., Mellon, M., Portyankina, G., Thomas, N., 2011. Seasonal
2907 erosion and restoration of Mars’ northern polar dunes. *Science*, **331**, 575–578,
2908 doi:10.1126/science.1197636.

2909 Hansen, C.J., Diniega, S. Bridges, N., Byrne, S., Dundas, C., McEwen, A., Portyankina, G.,
2910 2015. Agents of change on Mars’ northern dunes: CO₂ ice and wind. *Icarus* **251**, 264–274,
2911 doi:10.1016/j.icarus.2014.11.015.

2912 Hansen, C.J., Diniega, S., Hayne, P.O., 2018. Mars' Snowfall and Sand Avalanches. Presented at
2913 the *49th Lunar and Planetary Science Conference*, Ab. 2175.

2914 Hansen, C.J., Aye, K.M., Diniega, S., Hayne, P., McEwen, A., Portyankina, G., Schwamb, M.E.,
2915 2020. Dynamic Seasons on Mars—Polar Images and Investigations. Presented at the *7th
2916 International Conference on Mars Polar Science and Exploration*, Ab. 6019.

- 2917 Hao, J., Michael, G. G., Adeli, S., Jaumann, R., Portyankina, G., Hauber, E., Millot, C.,
2918 Zuschneid, W., 2020. Variability of spider spatial configuration at the Martian south pole.
2919 *Planet. Space Sci.*, **185**, 104848, doi:10.1016/j.pss.2020.104848.
- 2920 Harrison, T., Malin, M.C., Edgett, K.S., 2009. Present-day activity, monitoring, and
2921 documentation of gullies with the Mars Reconnaissance Orbiter (MRO) Context Camera
2922 (CTX). Presented at *Geological Society of America Meeting*, Ab. 97-12.
- 2923 Harri, A.M., Genzer, M., Kempainen, O., Kahanpää, H., Gomez-Elvira, J., Rodriguez-Manfredi,
2924 J.A., Haberle, R., Polkko, J., Schmidt, W., Savijärvi, H., Kauhanen, J., 2014. Pressure
2925 observations by the Curiosity rover: Initial results. *Journal of Geophysical Research:*
2926 *Planets*, **119**(1), 82–92, doi:10.1002/2013JE004423.
- 2927 Hart, H.M., Jakosky, B.M., 1986. Composition and stability of the condensate observed at the
2928 Viking Lander 2 site on Mars. *Icarus*, **66**(1), 134–142, doi:10.1016/0019-1035(86)90013-8.
- 2929 Hartogh, P., Medvedev, A. S., Kuroda, T., Saito, R., Villanueva, G., Feofilov, A. G., Kutepov,
2930 A. A., Berger, U., 2005. Description and climatology of a new general circulation model of
2931 the Martian atmosphere. *Journal of Geophysical Research*, **110**, doi:10.1029/2005JE002498.
- 2932 Hayne, P.O., Paige, D.A., Schofield, J.T., Kass, D.M., Kleinböhl, A., Heavens, N.G., McCleese,
2933 D.J., 2012. Carbon dioxide snow clouds on Mars: southern polar winter observations by the
2934 Mars Climate Sounder. *Journal of Geophysical Research*, **117**, E8, E08014,
2935 doi:10.1029/2011JE004040.
- 2936 Hayne, P.O., Paige, D.A., Heavens, N.G., 2014. The role of snowfall in forming the seasonal ice
2937 caps of Mars: Models and constraints from the Mars Climate Sounder. *Icarus*, **231**, 122–130,
2938 doi:10.1016/j.icarus.2013.10.020.
- 2939 Hayne, P. O., Hansen, C. J., Byrne, S., Kass, D. M., Kleinböhl, A., Piqueux, S., McCleese, D. J.,
2940 Diniega, S., Portyankina, G., 2016. Snowfall variability and surface changes in the polar
2941 regions of Mars. Presented at *6th International Conference on Mars Polar Science and*
2942 *Exploration*, Ab. #6012.
- 2943 Hayward, R., Mullins, K., Fenton, L., Hare, T., Titus, T., Bourke, M., Colaprete, A., Christensen,
2944 P., 2007. Mars global digital dune database: MC2-MC20 Rep. 2331-1258, U.S. Geological
2945 Survey.
- 2946 Hayward, R., Fenton, L., Tanaka, K., Titus, T., Colaprete, A., Christensen, P., 2010. Mars global
2947 digital dune database: MC-1 Rep. 2010-1170, U.S. Geological Survey.
- 2948 Hayward, R., Fenton, L., Titus, T., Colaprete, A., Christensen, P., 2012. Mars global digital dune
2949 database: MC-30 Rep. 2331-1258, U.S. Geological Survey.
- 2950 Hayward, R.K., Fenton, L.K., Titus, T.N., 2014. Mars Global Digital Dune Database (MGD3):
2951 Global dune distribution and wind pattern observations. *Icarus*, **230**, 38–46,
2952 doi:10.1016/j.icarus.2013.04.011.
- 2953 Head, J.W., Marchant, D.R., 2003. Cold-based mountain glaciers on Mars: Western Arsia Mons.
2954 *Geology*, **31**, 641–644.
- 2955 Head, J.W., Mustard, J.F., Kreslavsky, M.A., Milliken, R.E., Marchant, D.R., 2003. Recent ice
2956 ages on Mars. *Nature*, **426**(6968), 797–802, doi:10.1038/nature02114.

- 2957 Heinz, J., Schulze-Makuch, D., Kounaves, S. P., 2016. Deliquescence-induced wetting and RSL-
2958 like darkening of a Mars analogue soil containing various perchlorate and chloride salts.
2959 *Geophysical Research Letters*, **43**, 4880–4884, doi:10.1002/2016GL068919.
- 2960 Herkenhoff, K.E., Byrne, S., Russell, P.S., Fishbaugh, K.E., McEwen, A.S., 2007. Meter-scale
2961 morphology of the north polar region of Mars. *Science*, **317**, 1711–1715,
2962 doi:10.1126/science.1143544.
- 2963 Herny, C., Masse, M., Bourgeois, O., Carpy, S., Le Mouelic, S., Appere, T., Smith, I.B., Spiga,
2964 A., Rodriguez, S., 2014. Sedimentation waves on the martian north polar cap: Analogy with
2965 megadunes in Antarctica. *Earth and Planetary Science Letters*, **403**, 56–66,
2966 doi:10.1016/j.epsl.2014.06.033.
- 2967 Herny, C., Conway, S. J., Raack, J., Carpy, S., Colleu-Banse, T., Patel, M. R., 2019. Downslope
2968 sediment transport by boiling liquid water under Mars-like conditions: experiments and
2969 potential implications for martian gullies. *Geological Society, London, Special Publications*,
2970 **467**, 373–410, doi:10.1144/SP467.10.
- 2971 Hess, S.L., Henry, R.M., Leovy, C.B., Ryan, J.A., Tillman, J.E., Chamberlain, T.E., Cole, H.L.,
2972 Dutton, R.G., Greene, G.C., Simon, W.E., Mitchell, J.L., 1976. Preliminary meteorological
2973 results on Mars from the Viking 1 lander. *Science*, **193**(4255), 788–791,
2974 doi:10.1126/science.193.4255.788.
- 2975 Hoffman, N., 2002. Active polar gullies on Mars and the role of carbon dioxide. *Astrobiology*, **2**,
2976 313–323, doi:10.1089/153110702762027899.
- 2977 Horgan, B.H.N., Bell III, J. F., 2012. Seasonally active slipface avalanches in the north polar
2978 sand sea of Mars: Evidence for a wind-related origin. *Geophysical Research Letters*, **39**,
2979 L09201, doi:10.1029/2012GL051329.
- 2980 Houben, H., 1997. Stability of Ground Ice on Mars. Presented at *DPS Meeting*, Ab. 06-06.
- 2981 Houben, H., Haberle, R.M., Young, R.E., Zent, A.P., 1997a. Modeling the Martian seasonal
2982 water cycle. *Journal of Geophysical Research: Planets*, **102**(E4), 9069–9083.
- 2983 Howard, A.D., 2000. The role of eolian processes in forming surface features of the martian
2984 polar layered deposits. *Icarus*, **144**, 267–288, doi:10.1006/icar.1999.6305.
- 2985 Howard, A. D., Moore, J. M., 2008. Sublimation-driven erosion on Callisto: A landform
2986 simulation model test. *Geophysical Research Letters*, **35**(3), L03203,
2987 doi:10.1029/2007GL032618.
- 2988 Huber, C., Ojha, L., Lark, L., Head, J.W., 2020. Physical models and predictions for recurring
2989 slope lineae formed by wet and dry processes. *Icarus*, **335**, 113385.
- 2990 Hudson, T.L., Aharonson, O., Schorghofer, N., Farmer, C.B., Hecht, M.H., Bridges, N.T., 2007.
2991 Water vapor diffusion in Mars subsurface environments. *Journal of Geophysical Research:*
2992 *Planets*, **112**(E5), E05016, doi:10.1029/2006JE002815.
- 2993 Hugenholtz, C.H., 2008. Frosted granular flow: A new hypothesis for mass wasting in martian
2994 gullies. *Icarus*, **197**, 65–72, doi:10.1016/j.icarus.2008.04.010.
- 2995 Hugenholtz, C.H., Barchyn, T.E., Boulding, A., 2017. Morphology of transverse aeolian ridges
2996 (TARs) on Mars from a large sample: Further evidence of a megaripple origin? *Icarus*, **286**,
2997 193–201, doi:10.1016/j.icarus.2016.10.015.

- 2998 ICE-SAG, 2019. Report from the Ice and Climate Evolution Science Analysis group (ICE-SAG).
2999 Chaired by S. Diniega and N. E. Putzig, 157 pages posted 08 July 2019, by the Mars
3000 Exploration Program Analysis Group (MEPAG) at <http://mepag.nasa.gov/reports.cfm>.
- 3001 ICE-WG, 2015. ISRU and Civil Engineering needs for future human Mars missions. Chaired by
3002 S. Hoffman, posted at
3003 <https://mepag.jpl.nasa.gov/reports/HLS2%20briefing%2027Oct15%20ICEWG%20v2.pdf>
- 3004 Ingersoll, A.P., 1970. Mars: Occurrence of liquid water. *Science*, **168**(3934), 972–973.
- 3005 Ingersoll, A. P., 1990. Dynamics of Triton’s Atmosphere. *Nature*, **344**, 315–317.
- 3006 Ishii, T., Sasaki, S., 2004. Formation of recent Martian gullies by avalanches of CO₂ Frost.
3007 Presented at 35th Lunar and Planetary Science Conference, Ab. #1556.
- 3008 Iversen, J.D., White, B.R., 1982. Saltation threshold on Earth, Mars and Venus. *Sedimentology*,
3009 **29**(1), 111-119.
- 3010 Jackson, B., Lorenz, R.D., Barnes, J.W., Szurgot, M., 2020. Dust devils on Titan. *Journal of*
3011 *Geophysical Research: Planets*, **125**, e2019JE006238, doi:10.1029/2019JE006238.
- 3012 Jakosky, B.M., Haberle, R.M., 1990. Year-to-year instability of the Mars south polar cap.
3013 *Journal of Geophysical Research*, **95**(B2), 1359–1365, doi:10.1029/JB095iB02p01359.
- 3014 Jakosky, B.M., Mellon, M.T., Varnes, E.S., Feldman, W.C., Boynton, W.V., Haberle, R.M.,
3015 2005. Mars low-latitude neutron distribution: Possible remnant near-surface water ice and a
3016 mechanism for its recent emplacement. *Icarus*, **175**(1), 58–67,
3017 doi:10.1016/j.icarus.2004.11.014.
- 3018 James, P.B., Kieffer, H.H., Paige, D.A., 1992. The seasonal cycle of carbon dioxide on Mars.
3019 *Mars*, 934–968.
- 3020 Jerolmack, D.J., Mohrig, D., Grotzinger, J.P., Fike, D.A., Watters, W.A., 2006. Spatial grain
3021 size sorting in eolian ripples and estimation of wind conditions on planetary surfaces:
3022 Application to Meridiani Planum, Mars. *Journal of Geophysical Research*, **111**, E12S02,
3023 doi:10.1029/2005JE002544.
- 3024 Jia, P., Andreotti, B., Claudin, P., 2017. Giant ripples on comet 67P/Churyumov–Gerasimenko
3025 sculpted by sunset thermal wind. *Proceedings of the National Academy of Science of U.S.A.*,
3026 **114**(10), 2509–2514, doi:10.1073/pnas.1612176114.
- 3027 Johnson, F.S., 1965. Atmosphere of Mars. *Science*, **150**(3702), 1445–1448,
3028 doi:10.1126/science.150.3702.1445
- 3029 Johnson, J.R., Achilles, C., Bell III, J.F., Bender, S., Cloutis, E., Ehlmann, B., Fraeman, A.,
3030 Gasnault, O., Hamilton, V.E., Le Mouélic, S., Maurice, S., 2017. Visible/near-infrared
3031 spectral diversity from in situ observations of the Bagnold dune field sands in Gale crater,
3032 Mars. *Journal of Geophysical Research: Planets*, **122**, 2655–2684,
3033 doi:10.1002/2016JE005187.
- 3034 Johnson, J.R., Bell III, J.F., Bender, S., Cloutis, E., Ehlmann, B., Fraeman, A., Gasnault, O.,
3035 Maurice, S., Pinet, P., Thompson, L., Wellington, D., 2018. Bagnold Dunes campaign Phase
3036 2: Visible/near-infrared reflectance spectroscopy of longitudinal ripple sands. *Geophysical*
3037 *Research Letters*, **45**(18), 9480–948, doi:10.1029/2018GL079025.

3038 Jouannic, G., Gargani, J., Costard, F., Ori, G.G., Marmo, C., Schmidt, F., Lucas, A., 2012.
3039 Morphological and mechanical characterization of gullies in a periglacial environment: The
3040 case of the Russell crater dune (Mars). *Planetary and Space Science*, **71**(1), 38–54,
3041 doi:10.1016/j.pss.2012.07.005.

3042 Jouannic, G., Conway, S.J., Gargani, J., Costard, F., Massé, M., Bourgois, O., Carter, J.,
3043 Schmidt, F., Marmo, C., Ori, G.G., Nachon, M., Pasquon, K., 2019. Morphological
3044 characterization of landforms produced by springtime seasonal activity on Russell crater
3045 megadune, Mars. *Geol. Soc. London Spec. Pub.*, **467**, 115–144, doi:10.1144/SP467.16.

3046 Lämmel, M., Meiwald, A., Yizhaq, H., Tsoar, H., Katra, I., Kroy, K., 2018. Aeolian sand sorting
3047 and megaripple formation. *Nature Physics*, **14**, 759–765, doi:10.1038/s41567-018-0106-z.

3048 Kaufmann, E., Hagermann, A., 2017. Experimental investigation of insolation-driven dust ejection
3049 from Mars' CO₂ ice caps. *Icarus*, **282**, 118–126, doi:10.1016/j.icarus.2016.09.039.

3050 Kessler, M.A., Werner, B.T., 2003. Self-organization of sorted patterned ground. *Science*,
3051 **299**(5605), 380–383, doi:10.1126/science.1077309.

3052 Kieffer, H.H., 2007. Cold jets in the martian polar caps. *Journal of Geophysical Research:*
3053 *Planets*, **112**, E08005, doi:10.1029/2006JE002816.

3054 Kieffer, H.H., Christensen, P.R., Titus, T.N., 2006. CO₂ jets formed by sublimation beneath
3055 translucent slab ice in Mars' seasonal south polar ice cap. *Nature*, **442**, 793–796,
3056 doi:10.1038/nature04945.

3057 Kite, E.S., Mayer, D.P., 2017. Mars sedimentary rock erosion rates constrained using crater
3058 counts, with applications to organic-matter preservation and to the global dust cycle. *Icarus*,
3059 **286**, 212–222, doi:10.1016/j.icarus.2016.10.010.

3060 Kminek, G., Conley, C., Hipkin, V., Yano, H., 2017. COSPAR's planetary protection policy.
3061 *Space Research Today*, **200**, 12–25, doi:10.1016/j.srt.2017.11.010.

3062 Kocurek, G., Lancaster, N., 1999. Aeolian system sediment state: theory and Mojave Desert
3063 Kelso dune field example. *Sedimentology*, **46**(3), 505–515.

3064 Kok, J.F., 2010. An improved parameterization of wind-blown sand flux on Mars that includes
3065 the effect of hysteresis. *Geophysical Research Letters*, **37**, L12202,
3066 doi:10.1029/2010GL043646.

3067 Kok, J.F., Renno, N.O., 2006. Enhancement of the emission of mineral dust aerosols by electric
3068 forces. *Geophysical Research Letters*, **33**, L19S10, doi:10.1029/2006GL026284.

3069 Kok, J.F., Renno, N.O., 2009. A comprehensive numerical model of steady state saltation
3070 (COMSALT). *Journal of Geophysical Research*, **114**, D17204, doi:10.1029/2009JD011702.

3071 Kok, J.F., Parteli, E.J.R., Michaels, T.I., Bou Karam, D., 2012. The physics of windblown sand
3072 and dust. *Rep. Prog. Phys.*, **75**, 106901, doi:10.1088/0034-4885/75/10/106901.

3073 Kolb, K.J., Pelletier, J.D., McEwen, A.S., 2010. Modeling the formation of bright slope deposits
3074 associated with gullies in Hale crater, Mars: Implications for recent liquid water. *Icarus*, **205**,
3075 113–137, doi:10.1016/j.icarus.2009.09.009.

3076 Kreslavsky M.A., Head, J.W., 2011. Carbon dioxide glaciers on Mars: Products of recent low
3077 obliquity epochs (?). *Icarus*, **216**, 111–115, doi:10.1016/j.icarus.2011.08.020.

- 3078 Kreslavsky, M.A., Head, J.W., Marchant, D.R., 2008. Periods of active permafrost layer formation
3079 during the geological history of Mars: Implications for circum-polar and mid-latitude surface
3080 processes. *Planetary and Space Science*, **56**(2), 289–302, doi:10.1016/j.pss.2006.02.010.
- 3081 Krinsley, D.H., Smalley, I.J., 1972. Sand: The study of quartz sand in sediments provides much
3082 information about ancient geological environments. *American Scientist*, **60**(3), 286-291.
- 3083 Krohn, K., Jaumann, R., Otto, K., Hoogenboom, T., Wagner, R., Buczkowski, D.L., Garry, B.,
3084 Williams, D.A., Yingst, R.A., Scully, J., De Sanctis, M.C., Kneissl, T., Schmedemann, N.,
3085 Kersten, E., Stephan, K., Matz, K.-D., Pieters, C.M., Preusker, F., Roatsch, T., Schenk, P.,
3086 Russell, C.T., Raymond, C.A., 2014. Mass movement on Vesta at steep scarps and crater
3087 rims. *Icarus*, **244**, 120–132, doi:10.1016/j.icarus.2014.03.013.
- 3088 Laity, J.E., Bridges, N.T., 2009. Ventifacts on Earth and Mars: Analytical, field, and laboratory
3089 studies supporting sand abrasion and windward feature development. *Geomorphology*,
3090 **105**(3–4), 202–217, doi:10.1016/j.geomorph.2008.09.014.
- 3091 Lancaster, N., Greeley, R., 1990. Sediment volume in the north polar sand seas of Mars. *Journal*
3092 *of Geophysical Research*, **95**, 10921–10927, doi:10.1029/JB095iB07p10921.
- 3093 Langevin, Y., Poulet, F., Bibring, J.-P., Schmitt, B., Douté, S., Gondet, B., 2005. Summer
3094 evolution of the north polar cap of Mars as observed by OMEGA/Mars express. *Science*,
3095 **307**(5715), 1581–1584.
- 3096 Langevin, Y., Bibring, J.-P., Montmessin, F., Forget, F., Vincendon, M., Douté, S., Poulet, F.
3097 and Gondet, B., 2007. Observations of the south seasonal cap of Mars during recession in
3098 2004–2006 by the OMEGA visible/near-infrared imaging spectrometer on board Mars
3099 Express. *Journal of Geophysical Research: Planets*, **112**, E08S12,
3100 doi:10.1029/2006JE002841.
- 3101 Landis, G.A., 2007. Observation of frost at the equator of Mars by the Opportunity rover.
3102 Presented at *38th Lunar and Planetary Science Conference*, Ab. 2423.
- 3103 Landis, M.E., Byrne, S., Daubar, I.J., Herkenhoff, K.E., Dundas, C.M., 2016. A revised surface
3104 age for the north polar layered deposits of Mars. *Geophysical Research Letters*, **43**(7), 3060–
3105 3068, doi:10.1002/2016GL068434.
- 3106 Lane, M.D., Christensen, P.R., 2013. Determining olivine composition of basaltic dunes in Gale
3107 crater, Mars, from orbit: Awaiting ground truth from Curiosity. *Geophysical Research*
3108 *Letters*, **40**(14), 3517–3521, doi:10.1002/grl.50621.
- 3109 Lapôtre, M.G.A., Lamb, M., McElroy, B., 2017. What sets the size of current ripples? *Geology*,
3110 **45**(3), 243–246, doi:10.1130/G38598.1.
- 3111 Lapôtre, M.G.A., Rampe, E., 2018. Curiosity’s investigation of the Bagnold Dunes, Gale crater:
3112 Overview of the two-phase scientific campaign and introduction to the special collection.
3113 *Geophysical Research Letters*, **45**, 10200–10210, doi:10.1029/2018GL079032.
- 3114 Lapôtre, M.G.A., Ewing, R.C., Lamb, M.P., Fischer, W.W., Grotzinger, J.P., Rubin, D.M.,
3115 Lewis, K.W., Ballard, M.J., Day, M., Gupta, S., Banham, S.G., Bridges, N.T., Des Marais,
3116 D.J., Fraeman, A.A., Grant, J.A., Herkenhoff, K.E., Ming, D.W., Mischna, M.A., Rice, M.S.,
3117 Sumner, D.Y., Vasavada, A.R., Yingst, R.A., 2016. Large wind ripples on Mars: A record of
3118 atmospheric evolution. *Science*, **353**, 6294, 55–58.

- 3119 Lapôtre, M.G.A., Ehlmann, B.L., Minson, S.E., Arvidson, R.E., Ayoub, F., Fraeman, A.A.,
3120 Ewing, R.C., Bridges, N.T., 2017. Compositional variations in sands of the Bagnold dunes,
3121 Gale crater, Mars, from visible-shortwave infrared spectroscopy and comparison with ground
3122 truth from the Curiosity rover. *Journal of Geophysical Research: Planets*, **122**, 2489–2509,
3123 doi:10.1002/2016JE005133.
- 3124 Lapôtre, M.G.A., Ewing, R. C., Weitz, C. M., Lewis, K.W., Lamb, M.P., Ehlmann, B.L., Rubin,
3125 D.M., 2018. Morphologic diversity of martian ripples: Implications for large-ripple
3126 formation. *Geophysical Research Letters*, **45**(19), 10,229–10,239,
3127 doi:10.1029/2018GL079029.
- 3128 Lapôtre, M.G.A., O'Rourke, J.G., Schaefer, L.K., Siebach, K.L., Spalding, C., Tikoo, S.M.,
3129 Wordsworth, R.D., 2020. Probing space to understand Earth. *Nature Reviews Earth and*
3130 *Environment*, **1**, 170–181, doi:10.1038/s43017-020-0029-y.
- 3131 Lapôtre, M.G.A., Ewing, R. C., Lamb, M.P., 2021. An evolving understanding of enigmatic
3132 large ripples on Mars. *Journal of Geophysical Research: Planets*, in press.
- 3133 Laskar, J., Correia, A.C.M., Gastineau, M., Joutel, F., Levrard, B., Robutel, P., 2004. Long term
3134 evolution and chaotic diffusion of the insolation quantities of Mars. *Icarus*, **170**(2), 343–364,
3135 doi:10.1016/j.icarus.2004.04.005.
- 3136 Lasue, J., Cousin, A., Meslin, P.Y., Mangold, N., Wiens, R.C., Berger, G., Dehouck, E., Forni,
3137 O., Goetz, W., Gasnault, O., Rapin, W., 2018. Martian eolian dust probed by ChemCam.
3138 *Geophysical Research Letters*, **45**(20), 10,968–10,977, doi:10.1029/2018GL079210.
- 3139 Leask, E.K., Ehlmann, B.L., Dundas, M.M., Murchie, S.L., Seelos, F.P., 2018. Challenges in the
3140 search for perchlorate and other hydrated minerals with 2.1- μm absorptions on Mars.
3141 *Geophysical Research Letters*, **45**, 12,180–12,189, doi:10.1029/2018GL080077.
- 3142 Lefort, A., Russell, P.S., Thomas, N., McEwen, A.S., Dundas, C.M., Kirk, R.L., 2009.
3143 Observations of periglacial landforms in Utopia Planitia with the High Resolution Imaging
3144 Science Experiment (HiRISE). *Journal of Geophysical Research*, **114**, E04005,
3145 doi:10.1029/2008JE003264.
- 3146 Lefort, A., Russell, P.S., Thomas, N., 2010. Scalloped terrains in the Peneus and Amphitrites
3147 Paterae region of Mars as observed by HiRISE. *Icarus*, **205**, 259–268,
3148 doi:10.1016/j.icarus.2009.06.005.
- 3149 Leighton, R.B., Murray, B.C., 1966. Behavior of carbon dioxide and other volatiles on Mars.
3150 *Science*, **153**, 136–144, doi:10.1126/science.153.3732.136.
- 3151 Leprince, S., Barbot, S., Ayoub, F., Avouac, J.-P., 2007. Automatic and precise
3152 orthorectification, coregistration, and subpixel correlation of satellite images, application to
3153 ground deformation measurements. *IEEE Transactions on Geoscience and Remote Sensing*,
3154 **45**, 1529–1558, doi:10.1109/TGRS.2006.888937.
- 3155 Levrard, B., Forget, F., Montmessin, F., Laskar, J., 2007. Recent formation and evolution of
3156 northern martian polar layered deposits as inferred from a global climate model. *Journal of*
3157 *Geophysical Research*, **112**, E06012. doi:10.1029/2006JE002772.
- 3158 Levy, J., 2012. Hydrological characteristics of recurrent slope lineae on Mars: Evidence for
3159 liquid flow through regolith and comparisons with Antarctic terrestrial analogs. *Icarus*, **219**,
3160 1–4, doi:10.1016/j.icarus.2012.02.016.

- 3161 Levy, J.S., Marchant, D.R., Head, J.W., 2006. Distribution and origin of patterned ground on
3162 Mullins Valley debris-covered glacier, Antarctica: The roles of ice flow and sublimation.
3163 *Antarctic Science*, **18**(3), 385.
- 3164 Levy, J.S., Head, J.W., Marchant, D.R., 2009a. Concentric crater fill in Utopia Planitia: History
3165 and interaction between glacial “brain terrain” and periglacial mantle processes. *Icarus*, **202**,
3166 462–476, doi:10.1016/j.icarus.2009.02.018.
- 3167 Levy, J., Head, J., Marchant, D., 2009b. Thermal contraction crack polygons on Mars:
3168 Classification, distribution, and climate implications from HiRISE observations. *Journal of*
3169 *Geophysical Research: Planets*, **114**(E1), E01007, doi:10.1029/2008JE003273.
- 3170 Levy, J.S., Marchant, D.R., Head, J.W., 2010. Thermal contraction crack polygons on Mars: A
3171 synthesis from HiRISE, Phoenix, and terrestrial analog studies. *Icarus*, **206**(1), 229–252,
3172 doi:10.1016/j.icarus.2009.09.005.
- 3173 Levy, J.S., Fassett, C.I., Rader, L.X., King, I.R., Chaffey, P.M., Wagoner, C.M., Hanlon, A.E.,
3174 Watters, J.L., Kreslavsky, M.A., Holt, J.W., Russell, A.T., 2018. Distribution and
3175 characteristics of boulder halos at high latitudes on Mars: Ground ice and surface processes
3176 drive surface reworking. *Journal of Geophysical Research: Planets*, **123**(2), 322–334,
3177 doi:10.1002/2017JE005470.
- 3178 Liu, J., Di, K., Gou, S., Yue, Z, Liu, B., Xiao, J., Liu, Z., 2020. Mapping and spatial statistical
3179 analysis of Mars yardangs. *Planetary and Space Science*, **192**, 105035,
3180 doi:10.1016/j.pss.2020.105035.
- 3181 Lorenz, R.D., 1996. Martian surface wind speeds described by the Weibull distribution. *Journal*
3182 *of Spacecraft and Rockets*, **33**, 754–756.
- 3183 Lorenz, R.D., McKay, C.P., Lunine, J.I., 1997. Photochemically driven collapse of Titan’s
3184 atmosphere. *Science*, **275**, 642–644.
- 3185 Lorenz, R.D., Wall, S., Radebaugh, J., Boubin, G., Reffet, E., Janssen, M., Stofan, E., Lopes, R.,
3186 Kirk, R., Elachi, C., Lunine, J., 2006. The sand seas of Titan: Cassini RADAR observations
3187 of longitudinal dunes. *Science*, **312**, 724–727, doi:10.1126/science.1123257.
- 3188 Lorenz, R.D., Bridges, N.T., Rosenthal, A.A., Donkor, E., 2014. Elevation dependence of
3189 bedform wavelength on Tharsis Montes, Mars: Atmospheric density as a controlling
3190 parameter. *Icarus*, **230**, 77–80.
- 3191 Lowell, 1895. [https://en.wikisource.org/wiki/Mars_\(Lowell\)](https://en.wikisource.org/wiki/Mars_(Lowell)): Mars (Lowell). (2012, October 5).
3192 In *Wikisource* . Retrieved 06:58, July 3, 2020,
3193 from [https://en.wikisource.org/w/index.php?title=Mars_\(Lowell\)&oldid=4087387](https://en.wikisource.org/w/index.php?title=Mars_(Lowell)&oldid=4087387)
- 3194 Malin, M.C., Edgett, K.S., 2000. Evidence for recent groundwater seepage and surface runoff on
3195 Mars. *Science*, **288**(5475), 2330–2335, doi:10.1126/science.288.5475.2330.
- 3196 Malin, M.C., Edgett, K.S., 2001. Mars Global Surveyor Mars Orbiter Camera: Interplanetary
3197 cruise through primary mission. *Journal of Geophysical Research*, **106**, 23,429–23,570,
3198 doi:10.1029/2000JE001455.
- 3199 Malin, M.C., Danielson, G.E., Ingersoll, A.P., Masursky, H., Veverka, J., Ravine, M.A.,
3200 Soulanille, T.A., 1992. Mars Observer Camera. *Journal of Geophysical Research*, **97**, 7699,
3201 doi:10.1029/92JE00340.

- 3202 Malin, M.C., Caplinger, M.A., Davis, S.D., 2001. Observational evidence for an active surface
3203 reservoir of solid carbon dioxide on Mars. *Science*, **294**(5549), 2146–2148.
- 3204 Malin, M.C., Edgett, K.S., Posiolova, L.V., McColley, S.M., Noe Dobrea, E.Z., 2006. Present-
3205 day impact cratering rate and contemporary gully activity on Mars. *Science*, **314**, 1573-1577,
3206 doi:10.1126/science.1135156.
- 3207 Malin, M.C., Bell, J.F., Cantor, B.A., Caplinger, M.A., Calvin, W.M., Clancy, R.T., Edgett, K.S.,
3208 Edwards, L., Haberle, R.M., James, P.B., Lee, S.W., 2007. Context camera investigation on
3209 board the Mars Reconnaissance Orbiter. *Journal of Geophysical Research*, **112**, E05S04,
3210 doi:10.1029/2006JE002808.
- 3211 Malin, M.C., Edgett, K.S., Cantor, B.A., Caplinger, M.A., Danielson, G.E., Jensen, E.H., Ravine,
3212 M.A., Sandoval, J.L., Supulver, K.D., 2010. An overview of the 1985–2006 Mars Orbiter
3213 Camera science investigation. *Mars*, **5**, 1–60.
- 3214 Malliband, C.C., Conway, S.J., Rothery, D.A., Balme, M.R., 2019. Potential identification of
3215 downslope mass movements on Mercury driven by volatile-loss. Presented at the *50th Lunar*
3216 *and Planetary Science Conference*, Ab. 1804.
- 3217 Mangold, N., 2003. Geomorphic analysis of lobate debris aprons on Mars at Mars Orbiter Camera
3218 scale: Evidence for ice sublimation initiated by fractures. *Journal of Geophysical Research*,
3219 108(E4), 8021 doi:10.1029/2002JE001885.
- 3220 Mangold, N., 2005. High latitude patterned grounds on Mars: Classification, distribution and
3221 climatic control. *Icarus*, **174**(2), 336–359, doi:10.1016/j.icarus.2004.07.030.
- 3222 Mangold, N., 2011. Ice sublimation as a geomorphic process: A planetary perspective.
3223 *Geomorphology*, 126, 1–17, doi:10.1016/j.geomorph.2010.11.009.
- 3224 Mangold, N., Costard, F., Forget, F., 2003. Debris flows over sand dunes on Mars: Evidence for
3225 liquid water. *Journal of Geophysical Research*, 108, doi:10.1029/2002JE001958.
- 3226 Mangold, N., Mangeney, A., Migeon, V., Ansan, V., Lucas, A., Baratoux, D., Bouchut, F., 2010.
3227 Sinuous gullies on Mars: Frequency, distribution, and implications for flow properties. *Journal*
3228 *of Geophysical Research: Planets*, **115**, E11001, doi:10.1029/2009JE003540.
- 3229 Manning, C.V., Bierson, C., Putzig, N.E. McKay, C.P., 2019. The formation and stability of buried
3230 polar CO₂ deposits on Mars. *Icarus*, **317**, 509–517, doi:10.1016/j.icarus.2018.07.021.
- 3231 Marchant, D.R., Denton, G.H., Sugden, D.E., Swisher, C.C., 1993. Miocene glacial stratigraphy
3232 and landscape evolution of the western Asgard Range, Antarctica. *Geografiska Annaler* **75A**,
3233 303–330.
- 3234 Marchant, D.R., Lewis, A.R., Phillips, W.M., Moore, E.J., Souchez, R.A., Denton, G.H., Sugden,
3235 D.E., Potter, N., Landis, G.P., 2002. Formation of patterned ground and sublimation till over
3236 Miocene glacier ice in Beacon Valley, southern Victoria Land, Antarctica. *Geological Society*
3237 *of America Bulletin*, 114(6), 718–730.
- 3238 Martínez, G.M., Newman, C.N., De Vicente-Retortillo, A., Fischer, E., Renno, N.O.,
3239 Richardson, M.I., Fairén, A.G., Genzer, M., Guzewich, S.D., Haberle, R.M., Harri, A.M.,
3240 2017. The modern near-surface martian climate: A review of in-situ meteorological data
3241 from Viking to Curiosity. *Space Science Reviews*, **212**(1-2), 295–338, doi:10.1007/s11214-
3242 017-0360-x.

- 3243 Masursky, H., 1973. An overview of geological results from Mariner 9. *Journal of Geophysical*
3244 *Research*, **78**(20), 4009–4030, doi:10.1029/JB078i020p04009.
- 3245 Massé, M., Bourgeois, O., Lemouélic, S., Verpoorter, C., Spiga, A., Le Deit, L. 2012. Wide
3246 distribution and glacial origin of polar gypsum on Mars. *Earth and Planetary Science*
3247 *Letters*, **317–318**, 44–55, doi:10.1016/j.epsl.2011.11.035.
- 3248 Massé, M., Conway, S.J., Gargani, J., Patel, M.R., Pasquon, K., McEwen, A., Carpy, S.,
3249 Chevrier, V., Balme, M.R., Ojha, L., Vincendon, M., 2016. Transport processes induced by
3250 metastable boiling water under martian surface conditions. *Nature Geoscience*, **9**(6), 425–
3251 428, doi:10.1038/ngeo2706.
- 3252 Matson, D.L., Brown, R.H., 1989. Solid-state greenhouse and their implications for icy satellites.
3253 *Icarus*, **77**(1), 67–81, doi:10.1016/0019-1035(89)90007-9.
- 3254 Matsuo, K., Heki, K., 2009. Seasonal and inter-annual changes of volume density of martian
3255 CO₂ snow from time-variable elevation and gravity. *Icarus*, **202**, 90–94,
3256 doi:10.1016/j.icarus.2009.02.023.
- 3257 Maus, D., Heinz, J., Schirmack, J., Airo, A., Kounaves, S. P., Wagner, D., Schulze-Makuch, D.,
3258 2020. Methanogenic Archaea can produce methane in deliquescence-driven Mars analog
3259 environments. *Scientific Reports*, **10**, 6, doi:10.1038/s41598-019-56267-4.
- 3260 McEwen, A.S., 2018. Are recurring slope lineae habitable? In *From Habitability to Life on*
3261 *Mars*, N.A. Cabrol and E.A. Grin, Editors, Chapter 10, Elsevier Inc., 249–274,
3262 doi:10.1016/B978-0-12-809935-3.00008-6.
- 3263 McEwen, A.S., Eliason, E.M., Bergstrom, J.W., Bridges, N.T., Hansen, C.J., Delamere, W.A.,
3264 Grant, J.A., Gulick, V.C., Herkenhoff, K.E., Keszthelyi, L., Kirk, R.L., 2007. Mars
3265 Reconnaissance Orbiter’s High Resolution Imaging Science Experiment (HiRISE). *Journal*
3266 *of Geophysical Research*, **112**, E05S02, doi:10.1029/2005JE002605.
- 3267 McEwen, A.S., Ojha, L., Dundas, C.M., Mattson, S.S., Byrne, S., Wray, J.J., Cull, S.C.,
3268 Murchie, S.L., Thomas, N., Gulick, V.C., 2011. Seasonal flows on warm martian slopes.
3269 *Science*, 333, 740–743, doi:10.1126/science.1204816.
- 3270 McEwen, A.S., Dundas, C.M., Mattson, S.S., Toigo, A.D., Ojha, L., Wray, J.J., Chojnacki, M.,
3271 Byrne, S., Murchie, S.L., Thomas, N., 2014. Recurring slope lineae in equatorial regions of
3272 Mars. *Nature Geoscience*, **7**, 53–58, doi:10.1038/ngeo2014.
- 3273 McEwen, A.S., Schaefer, E., Sutton, S., Chojnacki, M., 2019. Remarkably widespread RSL
3274 activity following the great martian dust storm of 2018. Presented at *EPSC-DPS Joint*
3275 *Meeting 2019*, Ab. EPSC-DPS2019-557.
- 3276 McEwen, A.S., Schafer, E.I., Dundas, C.M., Sutton, S. S., Tamppiri, L. K., Chojnacki, M., 2021.
3277 Mars: Abundant recurring slope lineae (RSL) following the planet-encircling dust event
3278 (PEDE) of 2018. *Journal of Geophysical Research: Planets*, JGRE_21573, doi:
3279 10.1029/2020JE006575.
- 3280 McGlynn, I.O., Fedo, C.M., McSween Jr., H.Y., 2011. Origin of basaltic soils at Gusev crater,
3281 Mars, by aeolian modification of impact-generated sediment. *Journal of Geophysical*
3282 *Research: Planets*, **116**(E7), E00F22, doi:10.1029/2010JE003712.
- 3283 McKee, E.D., 1979. Introduction to a study of global sand seas. In *A Study of Global Sand Seas*.
3284 U.S. Geol. Surv. Prof. Pap. **1052**: 3–17.

- 3285 Mc Keown, L.E., Bourke, M.C., McElwaine, J.N., 2017. Experiments on sublimating carbon
3286 dioxide ice and implications for contemporary surface processes on Mars. *Scientific Reports*,
3287 **7**, 14181, doi:10.1038/s41598-017-14132-2.
- 3288 Mc Keown, L.E., Bourke, M.C., McElwaine, J.N., Sylvest, M.E., Patel, M.R., 2021. The
3289 formation of araneiforms by carbon dioxide venting and vigorous sublimation dynamics
3290 under martian conditions. *Scientific Reports*, in press,
3291 <https://www.essoar.org/doi/10.1002/essoar.10501015.1>
- 3292 McLennan, S.M., Grotzinger, J.P., Hurowitz, J.A., Tosca, N.J., 2019. The sedimentary cycle on
3293 Early Mars. *Annual Review of Earth and Planetary Sciences*, **47**, 91–118,
3294 doi:10.1146/annurev-earth-053018-060332.
- 3295 McSween, H.Y., Arvidson, R.E., Bell, J.F., Blaney, D., Cabrol, N.A., Christensen, P.R., Clark,
3296 B.C., Crisp, J.A., Crumpler, L.S., Des Marais, D.J., Farmer, J.D., 2004. Basaltic rocks
3297 Aanalyzed by the Spirit rover in Gusev crater. *Science*, **305**, 842–845,
3298 doi:10.1126/science.3050842.
- 3299 Mellon, M.T., 1997. Small-scale polygonal features on Mars: Seasonal thermal contraction cracks
3300 in permafrost. *Journal of Geophysical Research*, 102(E11), 25617–25628.
- 3301 Mellon, M.T., Jakosky, B.M., 1993. Geographic variations in the thermal and diffusive stability
3302 of ground ice on Mars. *Journal of Geophysical Research*, 98, 3,345–3,364.
- 3303 Mellon, M.T., Jakosky, B.M., 1995. The distribution and behavior of martian ground ice during
3304 past and present epochs. *Journal of Geophysical Research*, 100, 11,781–11,799.
- 3305 Mellon, M. T., Jakosky, B.M., Postawko, S.E., 1997. The persistence of equatorial ground ice on
3306 Mars. *Journal of Geophysical Research*, 102, 19,357–19,369.
- 3307 Mellon, M.T., Feldman, W.C., Prettyman, T.H., 2004. The presence and stability of ground ice
3308 in the southern hemisphere of Mars. *Icarus*, **169**, 324–340, doi:10.1016/j.icarus.2003.10.022.
- 3309 Mellon, M.T., Arvidson, R.E., Marlow, J.J., Phillips, R.J., Asphaug, E., 2008. Periglacial
3310 landforms at the Phoenix landing site and the northern plains of Mars. *Journal of Geophysical
3311 Research*, **113**, E00A23, doi:10.1029/2007JE003039.
- 3312 MEPAG, 2020. Mars Scientific Goals, Objectives, Investigations, and Priorities: 2020. D.
3313 Banfield, ed., 89 p. white paper posted March, 2020 by the Mars Exploration Program Analysis
3314 Group (MEPAG) at <https://mepag.jpl.nasa.gov/reports.cfm>.
- 3315 Milkovich, S.M., Byrne, S., Russell, P.S., 2012. Variations in surface texture of the north polar
3316 residual cap of Mars. Presented at the 43rd Lunar and Planetary Science Conference, Ab. 2226.
- 3317 Milliken, R.E., Mustard, J.F., Goldsby, D.L., 2003. Viscous flow features on the surface of Mars:
3318 Observations from high-resolution Mars Orbiter Camera (MOC) images. *Journal of
3319 Geophysical Research: Planets*, **108**, 5057, doi:10.1029/2002JE002005.
- 3320 Milliken, R.E., Ewing, R.C., Fischer, W.W., Hurowitz, J., 2014. Wind-blown sandstones
3321 cemented by sulfate and clay minerals in Gale Crater, Mars. *Geophysical Research Letters*,
3322 **41**, 2013GL059097, doi:10.1002/2013GL059097.
- 3323 Ming, D.W., Gellert, R., Morris, R.V., Arvidson, R.E., Brueckner, J., Clark, B.C., Cohen, B.A.,
3324 d'Uston, C., Economou, T., Fleischer, I., Klingelhofer, G., 2008. Geochemical properties of
3325 rocks and soils in Gusev crater, Mars: Results of the Alpha-Particle X-Ray Spectrometer

- 3326 from Cumberland Ridge to Home Plate. *Journal of Geophysical Research*, 113, E12S39,
3327 doi:10.1029/2008JE003195.
- 3328 Minitti, M.E., Kah, L.C., Yingst, R.A., Edgett, K.S., Anderson, R.C., Beegle, L.W., Carsten,
3329 J.L., Deen, R.G., Goetz, W., Hardgrove, C., Harker, D.E., 2013. MAHLI at the Rocknest
3330 sand shadow: Science and science-enabling activities. *Journal of Geophysical Research:*
3331 *Planets*, **118**(11), 2338–2360, doi:10.1002/2013JE004426.
- 3332 Miyamoto, H., Dohm, J.M., Baker, V.R., Beyer, R.A., Bourke, M., 2004. Dynamics of unusual
3333 debris flows on martian sand dunes. *Geophysical Research Letters*, **31**, L13701,
3334 doi:10.1029/2004GL020313.
- 3335 Möhlmann, D.T.F., Thomsen, K., 2011. Properties of cryobrines on Mars. *Icarus*, 212, 123–130.
- 3336 Monin, A.S., Obukhov, A.M., 1954. Basic laws of turbulent mixing in the surface layer of the
3337 atmosphere. *Contrib. Geophys. Inst. Acad. Sci. USSR*, **151**(163), e187.
- 3338 Moore, H.J., Bickler, D.B., Crisp, J.A., Eisen, H.J., Gensler, J.A., Haldemann, A.F.C., Matijevic,
3339 J.R., Reid, L.K., Pavlics, F., 1999. Soil-like deposits observed by Sojourner, the Pathfinder
3340 rover. *Journal of Geophysical Research*, **104**, 8729, doi:10.1029/1998JE900005.
- 3341 Moore, J.M., Mellon, M.T., Zent, A.P., 1996. Mass wasting and ground collapse in terrains of
3342 volatile-rich deposits as a solar system-wide geological process: The pre-Galileo view.
3343 *Icarus*, **122** (1), 63–78, doi:10.1006/icar.1996.0109.
- 3344 Moore, J.M., McKinnon, W.B., Spencer, J.R., Howard, A.D., Schenk, P.M., Beyer, R.A.,
3345 Nimmo, F., Singer, K.N., Umurhan, O.M., White, O.L., Stern, S.A., 2016. The geology of
3346 Pluto and Charon through the eyes of New Horizons. *Science*, **352**, 1284–1293.
- 3347 Moore, J.M., Howard, A.D., Umurhan, O.M., White, O.L., Schenk, P.M., Beyer, R.A.,
3348 McKinnon, W.B., Spencer, J.R., Grundy, W.M., Lauer, T.R., Nimmo, F., Young, L.A., Stern,
3349 S.A., Weaver, H.A., Olkin, C.B., Ennico, K., 2017. Sublimation as a landform-shaping
3350 process on Pluto. *Icarus*, **287**, 320–333, doi:10.1016/j.icarus.2016.08.025.
- 3351 Moores, J.E., Smith, C.L., Toigo, A.D., Guzewich, S.D., 2017. Penitentes as the origin of the
3352 bladed terrain of Tartarus Dorsa on Pluto. *Nature*, **541**(7636), 188–190,
3353 doi:10.1038/nature20779.
- 3354 Morgenstern, A., Hauber, E., Reiss, D., van Gasselt, S., Grosse, G., Schirrmeyer, L., 2007.
3355 Deposition and degradation of a volatile-rich layer in Utopia Planitia and implications for
3356 climate history on Mars. *Journal of Geophysical Research*, **112**, E06010.
- 3357 Morris, R.V., Klingelhofer, G., Schröder, C., Rodionov, D.S., Yen, A., Ming, D.W., De Souza,
3358 P.A., Fleischer, I., Wdowiak, T., Gellert, R., Bernhardt, B., 2006. Mössbauer mineralogy of
3359 rock, soil, and dust at Gusev Crater, Mars: Spirit's journey through weakly altered olivine
3360 basalt on the plains and pervasively altered basalt in the Columbia Hills. *Journal of*
3361 *Geophysical Research*, **111**, E02S13, doi:10.1029/2005JE002584.
- 3362 Murchie, S., Arvidson, R., Bedini, P., Beisser, K., Bibring, J.-P., Bishop, J., Boldt, J., Cavender,
3363 P., Choo, T., Clancy, R.T., Darlington, E.H., 2007. Compact reconnaissance imaging
3364 spectrometer for Mars (CRISM) on Mars reconnaissance orbiter (MRO). *Journal of*
3365 *Geophysical Research: Planets*, **112**, E05S03, doi:10.1029/2006JE002682.
- 3366 Munaretto, G., Pajola, M., Cremonese, G., Re, C., Lucchetti, A., Simioni, E., McEwen, A. S.,
3367 Pommerol, A., Becerra, P., Conway, S. J., Thomas, N., Massironi, M., 2020. Implications for

- 3368 the origin and evolution of martian Recurring Slope Lineae at Hale crater from CaSSIS
3369 observations. *Planetary and Space Science*, **187**, 104947.
- 3370 Mustard, J.F., Cooper, C.D., Rifkin, M.K., 2001. Evidence for recent climate change on Mars
3371 from the identification of youthful near-surface ground ice. *Nature*, **412**, 411–414,
3372 doi:10.1038/35086515.
- 3373 Neakrase, L.D.V., Klose, M., Titus, T.N., 2017. Terrestrial subaqueous seafloor dunes: Possible
3374 analogs for Venus. *Aeolian Research*, **26**, 47–56, doi:10.1016/j.aeolia.2017.03.002.
- 3375 Neukum, G., Jaumann, R., the HRSC Co-Investigator Team, 2004a. HRSC: The High Resolution
3376 Stereo Camera of Mars Express. European Space Agency SP-1240, 17–36.
- 3377 Neukum, G., Jaumann, R., Hoffmann, H., Hauber, E., Head, J.W., Basilevsky, A.T., Ivanov, B.A.,
3378 Werner, S.C., Van Gasselt, S., Murray, J.B., McCord, T., 2004b. Recent and episodic volcanic
3379 and glacial activity on Mars revealed by the High Resolution Stereo Camera. *Nature*,
3380 **432**(7020), 971–979, doi:10.1038/nature03231.
- 3381 NEX-SAG, 2015. Report from the Next Orbiter Science Analysis Group (NEX-SAG), chaired by
3382 B. Campbell and R. Zurek. 77 pages posted December, 2015 by the Mars Exploration Program
3383 Analysis Group (MEPAG) at <http://mepag.nasa.gov/reports.cfm>.
- 3384 Newman, C.E., Gomez-Elvira, J., Marin, M., Navarro, S., Torres, J., Richarson, M.I., Battalio,
3385 J.M., Guzewich, S.D., Sullivan, R., de la Torre, M., Vasavada, A.R., Bridges, N.T. 2017.
3386 Winds measured by the Rover Environmental Monitoring Station (REMS) during the Mars
3387 Science Laboratory (MSL) rover's Bagnold dunes campaign and comparison with numerical
3388 modeling using MarsWRF. *Icarus*, **291**, 203–231, doi: 10.1016/j.icarus.2016.12.016
- 3389 Nguyen, T.G., Radebaugh, J., Innanen, A., Moores, J.E., 2020. A survey of small-scale (<50 m)
3390 surface features on the martian north polar cap using HiRISE. *Planetary and Space Science*,
3391 **182**, 104809, doi:10.1016/j.pss.2019.104809.
- 3392 O'Connell-Cooper, C.D., Spray, J.G., Thompson, L.M., Gellert, R., Berger, J.A., Boyd, N.I.,
3393 Desouza, E.D., Perrett, G.M., Schmidt, M., VanBommel, S.J., 2017. APXS-derived
3394 chemistry of the Bagnold dune sands: Comparisons with Gale crater soils and the global
3395 martian average. *Journal of Geophysical Research: Planets*, **122**, 2623–2643,
3396 doi:10.1002/2017JE005268.
- 3397 O'Connell-Cooper, C.D., Thompson, L.M., Spray, J.G., Berger, J.A., VanBommel, S.J., Gellert,
3398 R., Boyd, N.I., DeSouza, E., 2018. Chemical diversity of sands within the linear and barchan
3399 dunes of the Bagnold dunes, Gale crater, as revealed by APXS onboard Curiosity.
3400 *Geophysical Research Letters*, **45**(18), 9460–9470, doi:10.1029/2018GL079026.
- 3401 Ojha, L., Wray, J.J., Murchie, S.L., McEwen, A.S., Wolff, M.J., Karunatillake, S., 2013. Spectral
3402 constraints on the formation mechanism of recurring slope lineae. *Geophysical Research*
3403 *Letters*, **40**(1), 5621–5626, doi:10.1002/2013GL057893.
- 3404 Ojha, L., McEwen, A., Dundas, C., Byrne, S., Mattson, S., Wray, J., Massé, M., Schaefer, E.,
3405 2014. HiRISE observations of recurring slope lineae (RSL) during southern summer on
3406 Mars. *Icarus*, **231**, 365–376, doi:10.1016/j.icarus.2013.12.021.
- 3407 Ojha, L., Wilhelm, M. B., Murchie, S. L., McEwen, A. S., Wray, J. J., Hanley, J., Massé, M.,
3408 Chojnacki, M., 2015. Spectral evidence for hydrated salts in recurring slope lineae on Mars.
3409 *Nature Geoscience*, **8**, 829–833, doi:10.1038/ngeo2546.

- 3410 Ojha, L., Nerozzi, S., Lewis, K., 2019. Compositional constraints on the north polar cap of Mars
3411 from gravity and topography. *Geophysical Research Letters*, **46**, 8671-8679,
3412 doi:10.1029/2019GL082294.
- 3413 Olkin, C.B., Young, L.A., Borncamp, D., Pickles, A., Sicardy, B., Assafin, M., Bianco, F.B.,
3414 Buie, M.W., de Oliveira, A.D., Gillon, M., French, R.G., 2015. Evidence that Pluto's
3415 atmosphere does not collapse from occultations including the 2013 May 04 event. *Icarus*,
3416 **246**, 220–225.
- 3417 Orgel, C., Hauber, E., van Gasselt, S., Reiss, D., Johnsson, A., Ramsdale, J.D., Smith, I., Swirad,
3418 Z.M., Séjourné, A., Wilson, J.T., Balme, M.R., 2019. Grid mapping the northern plains of
3419 Mars: A new overview of recent water-and ice-related landforms in Acidalia Planitia. *Journal*
3420 *of Geophysical Research: Planets*, **124**(2), 454–482, doi:10.1029/2018JE005664.
- 3421 Orloff, T., Kreslavsky, M., Asphaug, E., Korteniemi, J., 2011. Boulder movement at high northern
3422 latitudes of Mars. *Journal of Geophysical Research*, **116**, E11006,
3423 doi:10.1029/2011JE003811.
- 3424 Ould Ahmedou, D., Ould Mahfoudh, A., Dupont, P., Ould El Moctar, A., Valance, A.,
3425 Rasmussen, K.R., 2007. Barchan dune mobility in Mauritania related to dune and interdune
3426 sand fluxes. *Journal of Geophysical Research: Earth Surface*, **112**, F02016,
3427 doi:10.1029/2006JF000500.
- 3428 Owen, T.C., Roush, T.L., Cruikshank, D.P., Elliot, J.L., Young, L.A., deBergh, C., Schmitt, B.,
3429 Geballe, T.R., Brown, R.H., Bartholomew, M.J., 1993. Surface ices and the atmospheric
3430 composition of Pluto. *Science*, **261**, 745-748.
- 3431 Pahtz, T., Clark, A.H., Valyrakis, M., Duran, O. 2020. The physics of sediment transport
3432 initiation, cessation, and entrainment across aeolian and fluvial environments. *Reviews of*
3433 *Geophysics*, **58**(1), e2019RG000679, doi:10.1029/2019RG000679.
- 3434 Pan, C., Rogers, A.D., 2017. Occurrence and scale of compositional heterogeneity in martian
3435 dune fields: Toward understanding the effects of aeolian sorting on martian sediment
3436 compositions. *Icarus*, **282**, 56–69, doi:10.1016/j.icarus.2016.09.021.
- 3437 Parra, S.A., Milkovich, S.M., Byrne, S., Russell, P.S., 2017. Variations in texture of the north polar
3438 residual cap of Mars. Presented at the 48th Lunar and Planetary Science Conference, Ab. 1719.
- 3439 Parteli, E.J., Herrmann, H.J., 2007. Dune formation on the present Mars. *Physical Review E*,
3440 **76**(4), 041307, doi:10.1103/PhysRevE.76.041307.
- 3441 Pasquon, K., Gargani, J., Massé, M., Conway, S.J., 2016. Present-day formation and seasonal
3442 evolution of linear dune gullies on Mars. *Icarus*, **274**, 195–210,
3443 doi:10.1016/j.icarus.2016.03.024.
- 3444 Pasquon, K., Gargani, J., Nachon, M., Conway, S.J., Massé, M., Jouannic, G., Balme, M.R.,
3445 Costard, F., Vincendon, M., 2019a. Are different martian gully morphologies due to different
3446 processes on the Kaiser dune field? *Geological Society, London, Special Publications*, **467**.
3447 [doi:10.1144/SP467.13](https://doi.org/10.1144/SP467.13)
- 3448 Pasquon, K., Gargani, J., Massé, M., Vincendon, M., Conway, S.J., Séjourné, A., Jomelli, V.,
3449 Balme, M.R., Lopez, S., Guimpier, A., 2019b. Present-day development of gully-channel
3450 sinuosity by carbon dioxide gas supported flows on Mars. *Icarus*, **329**, 296–313.
3451 [doi:10.1016/j.icarus.2019.03.034](https://doi.org/10.1016/j.icarus.2019.03.034)

- 3452 Pathare, A.V., Feldman, W.C., Prettyman, T.H., Maurice, S., 2018. Driven by excess? Climatic
3453 implications of new global mapping of near-surface water-equivalent hydrogen on Mars.
3454 *Icarus*, **301**, 97–116, doi:10.1016/j.icarus.2017.09.031.
- 3455 Pelkey, S., Jakosky, B., 2002. Surficial geologic surveys of Gale crater and Melas Chasma,
3456 Mars: Integration of remote-sensing data. *Icarus*, **160**(2), 228–257,
3457 doi:10.1006/icar.2002.6978.
- 3458 Pelletier, J.D., Kolb, K.J., Kirk, R.L., 2008. Recent bright gully deposits on Mars: Wet or dry
3459 flow? *Geology*, **36**, 211–214, doi:10.1130/G24346A.1.
- 3460 Petersen, E.I., Holt, J.W., Levy, J.S., 2018. High ice purity of martian lobate debris aprons at the
3461 regional scale: evidence from an orbital radar sounding survey in Deuteronilus and Protonilus
3462 Mensae. *Geophysical Research Letters*, **45**(21), 11–595, doi:10.1029/2018GL079759.
- 3463 Phillips, R.J., Davis, B.J., Tanaka, K.L., Byrne, S., Mellon, M.T., Putzig, N.E., Haberle, R.M.,
3464 Kahre, M.A., Campbell, B.A., Carter, L.M., Smith, I.B., 2011. Massive CO₂ ice deposits
3465 sequestered in the south polar layered deposits of Mars. *Science*, **332**(6031), 838–841,
3466 doi:10.1126/science.1203091.
- 3467 Pilorget, C., Forget, F., 2016. Formation of gullies on Mars by debris flows triggered by CO₂
3468 sublimation. *Nature Geoscience*, **9**(1), 65–69, doi:10.1038/ngeo2619.
- 3469 Pilorget, C., Forget, F., Millour, E., Vincendon, M., Madeleine, J.B., 2011. Dark spots and cold
3470 jets in the polar regions of Mars: New clues from a thermal model of surface CO₂ ice. *Icarus*,
3471 **213**(1), 131–149, doi:10.1016/j.icarus.2011.01.031.
- 3472 Pilorget, C., Edwards, C.S., Ehlmann, B.L., Forget, F., Millour, E., 2013. Material ejection by
3473 the cold jets and temperature evolution of the south seasonal polar cap of Mars from
3474 THEMIS/CRISM observations and implications for surface properties. *Journal of*
3475 *Geophysical Research: Planets*, **118**(12), 2520–2536, doi:10.1002/2013JE004513.
- 3476 Piqueux, S., Christensen, P.R., 2008. North and south subice gas flow and venting of the
3477 seasonal caps of Mars: A major geomorphological agent. *Journal of Geophysical Research:*
3478 *Planets*, **113**, E06005, doi:10.1029/2007JE003009.
- 3479 Piqueux S., Byrne S., Richardson M. I., 2003. Sublimation of Mars' southern seasonal CO₂ ice
3480 cap and the formation of spiders. *Journal of Geophysical Research*, **108**, 5084,
3481 doi:10.1029/2002JE002007.
- 3482 Piqueux, S., Byrne, S., Kieffer, H.H., Titus, T.N., Hansen, C.J., 2015a. Enumeration of Mars
3483 years and seasons since the beginning of telescopic exploration. *Icarus*, **251**, 332–338,
3484 doi:10.1016/j.icarus.2014.12.014.
- 3485 Piqueux, S., Kleinböhl, A., Hayne, P.O., Kass, D.M., Schofield, J.T., McCleese, D.J., 2015b.
3486 Variability of the martian seasonal CO₂ cap extent over eight Mars years. *Icarus*, **251**, 164–
3487 180, doi:10.1016/j.icarus.2014.10.045.
- 3488 Piqueux, S., Kleinböhl, A., Hayne, P.O., Heavens, N.G., Kass, D.M., McCleese, D.J., Schofield,
3489 J.T., Shirley, J.H., 2016. Discovery of a widespread low-latitude diurnal CO₂ frost cycle on
3490 Mars. *Journal of Geophysical Research: Planets*, **121**(7), 1174–1189,
3491 doi:10.1002/2016JE005034.

- 3492 Piqueux, S., Buz, J., Edwards, C.S., Bandfield, J.L., Kleinböhl, A., Kass, D.M., Hayne, P.O., the
3493 MCS and THEMIS Teams, 2019. Widespread shallow water ice on Mars at high latitudes
3494 and midlatitudes. *Geophysical Research Letters*, **46**(24), 14290–14298.
- 3495 Pollack, J.B., Haberle, R.M., Schaeffer, J., Lee, H., 1990. Simulations of the general circulation
3496 of the Martian atmosphere. 1. Polar processes. *Journal of Geophysical Research*, **95**, 1447–
3497 1473, doi:10.1029/JB095iB02p01447.
- 3498 Pollack, J.B., Haberle, R.M., Murphy, J.R., Schaeffer, J., Lee, H., 1993. Simulations of the
3499 general circulation of the Martian atmosphere. 2. Seasonal pressure variations. *Journal of*
3500 *Geophysical Research*, **98**, 3149–3181, doi:10.1029/92JE02947.
- 3501 Pommerol, A., Appéré, T., Portyankina, G., Aye, K.-M., Thomas, N., Hansen, C.J., 2013.
3502 Observations of the northern seasonal polar cap on Mars III: CRISM/HiRISE observations of
3503 spring sublimation. *Icarus*, **225**, 911–922, doi:10.1016/j.icarus.2012.08.039.
- 3504 Pommerol, A., Jost, B., Poch, O., Yoldi, Z., Brouet, Y., Gracia-Berná, A., Cerubini, R., Galli, A.,
3505 Wurz, P., Gundlach, B., Blum, J., Carrasco, N., Szopa, C., Thomas, N., 2019. Experimenting
3506 with mixtures of water ice and dust as analogues for icy planetary material. *Space Science*
3507 *Reviews*, **215**, 37, doi:10.1007/s11214-019-0603-0.
- 3508 Portyankina, G., Markiewicz, W.J., Thomas, N., Hansen, C.J., Milazzo, M., 2010. HiRISE
3509 observations of gas sublimation-driven activity in Mars' southern polar regions: III. Models
3510 of processes involving translucent ice. *Icarus*, **205**, 311–320,
3511 doi:10.1016/j.icarus.2009.08.029.
- 3512 Portyankina, G., Pommerol, A., Aye, K.-M., Hansen, C.J., Thomas, N., 2012. Polygonal cracks
3513 in the seasonal semi-translucent CO₂ ice layer in martian polar areas. *Journal of Geophysical*
3514 *Research: Planets*, **117**, E02006, doi:10.1029/2011JE003917.
- 3515 Portyankina, G., Hansen, C.J., Aye, K.-M., 2017. Present-day erosion of Martian polar terrain by
3516 the seasonal CO₂ jets. *Icarus*, **282**, 93–103, doi:[10.1016/j.icarus.2016.09.007](https://doi.org/10.1016/j.icarus.2016.09.007).
- 3517 Portyankina, G., Merrison, J., Iversen, J.J., Yoldi, Z., Hansen, C.J., Aye, K.-M., Pommerol, A.,
3518 Thomas, N., 2019. Laboratory investigations of the physical state of CO₂ ice in a simulated
3519 Martian environment. *Icarus*, **322**, 210–220, doi:10.1016/j.icarus.2018.04.021.
- 3520 Preston, S., Chojnacki, M., 2019. Aeolian ripple rate variability in response to different boundary
3521 conditions. Presented at the *50th Lunar and Planetary Science Conference*, Ab. 2142.
- 3522 Prockter, L.M., Head, J.W., Pappalardo, R.T., Senske, D.A., Neukum, G., Wagner, R., Wolf, U.,
3523 Oberst, J.O., Giese, B., Moore, J.M., Chapman, C.R., 1998. Dark terrain on Ganymede:
3524 Geological mapping and interpretation of Galileo Regio at high resolution. *Icarus*, **135**(1),
3525 317–344.
- 3526 Putzig, N.E., Mellon, M.T., 2007. Apparent thermal inertia and the surface heterogeneity of Mars.
3527 *Icarus*, **191**(1), 68–94, doi:10.1016/j.icarus.2007.05.013.
- 3528 Putzig, N.E., Smith, I.B., Perry, M.R., Foss II, F.J., Campbell, B.A., Phillips, R.J., Seu, R., 2018.
3529 Three-dimensional radar imaging of structures and craters in the martian polar caps. *Icarus*,
3530 **308**, pp.138–147.
- 3531 Raack, J., Reiss, D., Appéré, T., Vincendon, M., Ruesch, O., Hiesinger, H., 2015. Present-day
3532 seasonal gully activity in a south polar pit (Sisyphi Cavi) on Mars. *Icarus*, **251**, 226–243,
3533 doi:10.1016/j.icarus.2014.03.040.

- 3534 Raack, J., Conway, S.J., Herny, C., Balme, M.R., Carpy, S., Patel, M.R., 2017. Water induced
3535 sediment levitation enhances downslope transport on Mars. *Nature Communications*, **8**(1),
3536 1511, doi:10.1038/s41467-017-01213-z.
- 3537 Raack, J., Conway, S.J., Heyer, T., Bickel, V.T., Philippe, M., Hiesinger, H., Johnsson, A.,
3538 Massé, M., 2020. Present-day gully activity in Sisyphi Cavi, Mars - Flow-like features and
3539 block movements. *Icarus*, **350**, 113899, doi:10.1016/j.icarus.2020.113899
- 3540 Radebaugh, J., Lorenz, R.D., Lunine, J.I., Wall, S.D., Boubin, G., Reffet, E., Kirk, R.L., Lopes,
3541 R.M., Stofan, E.R., Soderblom, L., Allison, M., 2008. Dunes on Titan observed by Cassini
3542 RADAR. *Icarus*, **194**(2), 690–703, doi:10.1016/j.icarus.2007.10.015
- 3543 Radebaugh, J., Lorenz, R., Farr, T., Paillou, P., Savage, C., Spencer, C., 2010. Linear dunes on
3544 Titan and Earth: Initial remote sensing comparisons. *Geomorphology*, **121**(1–2), 122–132,
3545 doi:10.1016/j.geomorph.2009.02.022.
- 3546 Rampe, E.B., Lapôtre, M.G.A., Bristow, T.F., Arvidson, R.E., Morris, R.V., Achilles, C.N.,
3547 Weitz, C., Blake, D.F., Ming, D.W., Morrison, S.M., Vaniman, D.T., 2018. Sand mineralogy
3548 within the Bagnold dunes, Gale crater, as observed in situ and from orbit. *Geophysical*
3549 *Research Letters*, **45**(18), 9488–9497, doi:10.1029/2018GL079073.
- 3550 Ramsdale, J.D., Balme, M.R., Gallagher, C., Conway, S.J., Smith, I.B., Hauber, E., Orgel, C.,
3551 Séjourné, A., Costard, F., Eke, V.R., van Gasselt, S.A., 2019. Grid mapping the northern
3552 plains of Mars: Geomorphological, radar, and water-equivalent hydrogen results from
3553 Arcadia Plantia. *Journal of Geophysical Research: Planets*, **124**(2), 504–527,
3554 doi:10.1029/2018JE005663.
- 3555 Reiss, D., Erkeling, G., Bauch, K.E., Hiesinger, H., 2010. Evidence for present day gully activity
3556 on the Russell crater dune field, Mars. *Geophysical Research Letters*, **37**(6), L06203,
3557 doi:10.1029/2009GL042192.
- 3558 Roback, K.P., Runyon, K.D., Avouac, J.-P., Newman, C.E., Ayoub, F., 2019. Understanding
3559 ripple and whole-dune motion at active martian dune fields. Presented at the *50th Lunar and*
3560 *Planetary Science Conference*, Ab. 3169.
- 3561 Roback, K.P., Runyon, K.D., Avouac, J.-P. 2020. Craters as sand traps: Dynamics, history, and
3562 morphology of modern sand transport in an active dune field. *Icarus*, **342**, 113642,
3563 doi:10.1016/j.icarus.2020.113642
- 3564 Roberts, G.P., Matthews, B., Bristow, C., Guerrieri, L., Vetterlein, J., 2012. Possible evidence of
3565 paleomarsquakes from fallen boulder populations, Cerberus Fossae, Mars. *Journal of*
3566 *Geophysical Research: Planets*, **117**, E02009, doi:10.1029/2011JE003816.
- 3567 Rogers, A.D., Aharonson, O., 2008. Mineralogical composition of sands in Meridiani Planum
3568 determined from Mars Exploration Rover data and comparison to orbital measurements.
3569 *Journal of Geophysical Research*, **113**, E06S14, doi:10.1029/2007JE002995.
- 3570 Rubin, D.M., 1987. Cross-bedding, bedforms and paleocurrents. In *Concepts in Sedimentology*
3571 *and Palaeontology*, Editor D.M. Rubin, SEPM, 1, 187 pp.
- 3572 Rubin, D. M., 2012. A unifying model for planform straightness of ripples and dunes in air and
3573 water. *Earth Science Review*, **113**, 176–185, doi:10.1016/j.earscirev.2012.03.010.
- 3574 Rubin, D.M., Carter, C.L., 2006. Bedforms and Cross-Bedding in Animation. SEPM, Atlas
3575 Series, 2, DVD.

- 3576 Rubin, D.M., Hunter, R.E. (1987). Bedform alignment in directionally varying flows. *Science*,
3577 **237**(4812), 276–278, doi:10.1126/science.237.4812.276.
- 3578 Rummel, J.D., Beaty, D.W., Jones, M.A., Bakermans, C., Barlow, N.G., Boston, P.J., Chevrier,
3579 V.F., Clark, B.C., de Vera, J.-P.P., Gough, R.V., Hallsworth, J.E., Head, J.W., Hipkin, V.J.,
3580 Kieft, T.L., McEwen, A.S., Mellon, M.T., Mikucki, J.A., Nicholson, W.L., Omelon, C.R.,
3581 Peterson, R., Roden, E.E., Sherwood Lollar, B., Tanaka, K.L., Viola, D., Wray, J.J., 2014. A
3582 new analysis of Mars "special regions": findings of the second MEPAG special regions
3583 science analysis group (SR-SAG2). *Astrobiology*, 14 (11), 887–968,
3584 doi:10.1089/ast.2014.1227.
- 3585 Runyon, K.D., Bridges, N.T., Ayoub, F., Newman, C.E., Quade, J.J., 2017. An integrated model
3586 for dune morphology and sand fluxes on Mars. *Earth and Planetary Science Letters*, **457**,
3587 204-212, doi:10.1016/j.epsl.2016.09.054.
- 3588 Russell, P., Thomas, N., Byrne, S., Herkenhoff, K., Fishbaugh, K., Bridges, N., Okubo, C.,
3589 Milazzo, M., Daubar, I., Hansen, C., McEwen, A., 2008. Seasonally active frost-dust
3590 avalanches on a north polar scarp of Mars captured by HiRISE. *Geophysical Research*
3591 *Letters*, **35**, L23204, doi:10.1029/2008GL035790.
- 3592 Russell, P.S., Byrne, S., Dawson, L.C., 2014. Active powder avalanches on the steep north polar
3593 scarps of Mars: 4 years of HiRISE observation. Presented at the 45th Lunar and Planetary
3594 *Science Conference*, Ab. 2688.
- 3595 Russell, P.S., Parra, S.A., Milkovich, S.M., Becerra, P., Byrne, S., 2019. Visible and topographic
3596 texture of the north polar residual cap of Mars. Presented at the 50th Lunar and Planetary
3597 *Science Conference*, Ab. 3048.
- 3598 Sagan, C., Veverka, J., Fox, P., Dubisch, R., Lederberg, J., Levinthal, E., Quam, L., Tucker, R.,
3599 Pollack, J.B., Smith, B.A., 1972. Variable features on Mars: Preliminary Mariner 9 television
3600 results. *Icarus*, **17**(2), 346–372, doi:10.1016/0019-1035(72)90005-X.
- 3601 Sagan, C., Toon, O.B., Gierasch, P.J., 1973. Climatic change on Mars. *Science*, **181**(4104),
3602 1045–1049.
- 3603 Schaefer, E.I., McEwen, A.S., Sutton, S.S., 2019. A case study of recurring slope lineae (RSL) at
3604 Tivat crater: Implications for RSL origins. *Icarus*, **317**, 621-648,
3605 doi:10.1016/j.icarus.2018.07.014.
- 3606 Schenk, P., Singer, K., Beyer, R., Beddingfield, C., Robbins, S.J., McKinnon, W.B., Lauer, T.R.,
3607 Verbiscer, A.J., Keane, James. T., Dhingra, R.D., Moore, J., Parker, J.W., Olkin, C., Spencer,
3608 J., Weaver, H., Stern, S.A., 2020. Origins of pits and troughs and degradation on a small
3609 primitive planetesimal in the Kuiper Belt: high-resolution topography of (486958) Arrokoth
3610 (aka 2014 MU69) from New Horizons. *Icarus*, 113834, doi:10.1016/j.icarus.2020.113834.
- 3611 Schmidt, F., Andrieu, F., Costard, F., Kocifaj, M., Meresescu, A., 2017. Formation of recurring
3612 slope lineae on Mars by rarefied gas-triggered granular flows. *Nature Geoscience*, **10**, 270–
3613 273, doi:10.1038/ngeo2917.
- 3614 Schorghofer, N., Aharonson, O., 2005. Stability and exchange of subsurface ice on Mars.
3615 *Journal of Geophysical Research*, **110**, E05003, doi:10.1029/2004JE002350.
- 3616 Schorghofer, N., Edgett, K.S., 2006. Seasonal surface frost at low latitudes on Mars. *Icarus*, **180**,
3617 321–334, doi:10.1016/j.icarus.2005.08.022.

- 3618 Schorghofer, N., Forget, F., 2012. History and anatomy of subsurface ice on Mars. *Icarus*, **220**,
3619 1112–1120, doi:10.1016/j.icarus.2012.07.003.
- 3620 Schorghofer, N., Aharonson, O., Khatiwala, S., 2002. Slope streaks on Mars: Correlations with
3621 surface properties and the potential role of water. *Geophysical Research Letters*, **29**, 41-1–
3622 41-4, doi:10.1029/2002GL015889.
- 3623 Schorghofer, N., Levy, J.S., Goudge, T.A., 2019. High-resolution thermal environment of
3624 Recurring Slope Lineae in Palikir Crater, Mars, and its implications for volatiles. *Journal of*
3625 *Geophysical Research Planets*, **124**(11), 2852–2862.
- 3626 Schwamb, M.E., Aye, K.-M., Portyankina, G., Hansen, C.J., Allen, C., Allen, S., Calef, F.J.,
3627 Duca, S., McMaster, A., Miller, G.R.M., 2018. Planet Four: Terrains – Discovery of
3628 araneiforms outside of the south polar layered deposits. *Icarus*, **308**, 148–187,
3629 doi:10.1016/j.icarus.2017.06.017.
- 3630 Scully, J.E.C., Russell, C.T., Yin, A., Jaumann, R., Carey, E., Castillo-Rogez, J., McSween,
3631 H.Y., Raymond, C.A., Reddy, V., Le Corre, L., 2015. Geomorphological evidence for
3632 transient water flow on Vesta. *Earth and Planetary Science Letters*, **411**, 151–163,
3633 doi:10.1016/j.epsl.2014.12.004.
- 3634 Seelos, K.D., Seelos, F.P., Viviano-Beck, C.E., Murchie, S.L., Arvidson, R.E., Ehlmann, B.L.,
3635 Fraeman, A.A., 2014. Mineralogy of the MSL Curiosity landing site in Gale crater as
3636 observed by MRO/CRISM. *Geophysical Research Letters*, **41**, 4880–4887, doi:10.1002/
3637 2014GL060310.
- 3638 Séjourné, A., Costard, F., Gargani, J., Soare, R.J., Fedorov, A., Marmo, C., 2011. Scalloped
3639 depressions and small-sized polygons in western Utopia Planitia, Mars: A new formation
3640 hypothesis. *Planetary and Space Science*, **59**, 412–422.
- 3641 Séjourné, A., Costard, F., Gargani, J., Soare, R.J., Marmo, C., 2012. Evidence of an eolian ice-
3642 rich and stratified permafrost in Utopia Planitia, Mars. *Planetary and Space Science*, **60**,
3643 248–254.
- 3644 Séjourné, A., Costard, F., Swirad, Z.M., Łosiak, A., Bouley, S., Smith, I., Balme, M.R., Orgel,
3645 C., Ramsdale, J.D., Hauber, E., Conway, S.J., 2019. Grid mapping the northern plains of
3646 Mars: Using morphotype and distribution of ice-related landforms to understand multiple ice-
3647 rich deposits in Utopia Planitia. *Journal of Geophysical Research: Planets*, **124**(2), 483–503,
3648 doi:10.1029/2018JE005665.
- 3649 Senthil Kumar, P., Krishna, N., Prasanna Lakshmi, K.J., Raghukanth, S.T.G., Dhabu, A., Platz,
3650 T., 2019. Recent seismicity in Valles Marineris, Mars: Insights from young faults, landslides,
3651 boulder falls and possible mud volcanoes. *Earth and Planetary Science Letters*, **505**, 51–64,
3652 doi:10.1016/j.epsl.2018.10.008.
- 3653 Shao, Y., Lu, H., 2000. A simple expression for wind erosion threshold friction velocity. *Journal*
3654 *of Geophysical Research: Atmospheres*, **105**(D17), 22437–22443,
3655 doi:10.1029/2000JD900304.
- 3656 Sharp, R.P., 1963. Wind ripples. *Journal of Geology*, **71**(5), 617–636.
- 3657 Sharp, R.P., 1973. Mars: Fretted and chaotic terrains. *Journal of Geophysical Research*, **78**,
3658 4073–4083.

- 3659 Silvestro, S., Fenton, L.K., Vaz, D.A., Bridges, N.T., Ori, G.G., 2010. Ripple migration and dune
3660 activity on Mars: Evidence for dynamic wind processes. *Geophysical Research Letters*, **37**,
3661 L20203.
- 3662 Silvestro, S., Fenton, L.K., Michaels, T.I., Valdez, A., Ori, G.G., 2012. Interpretation of the
3663 complex dune morphology on Mars: dune activity, modelling and a terrestrial analogue.
3664 *Earth Surface Processes and Landforms*, **37** (13), 1424–1436.
- 3665 Silvestro, S., Vaz, D.A., Ewing, R.C., Rossi, A.P., Fenton, L.K., Michaels, T.I., Flahaut, J.,
3666 Geissler, P.E., 2013. Pervasive aeolian activity along rover Curiosity's traverse in Gale
3667 crater, Mars. *Geology*, **41**, 483–486, doi:10.1130/G34162.1.
- 3668 Silvestro, S., Chojnacki, M., Vaz, D.A., Cardinale, M., Yizhaq, H., Esposito, F., 2020.
3669 Megaripple migration on Mars. *Journal of Geophysical Research: Planets*, **125**,
3670 e2020JE006446, doi:10.1029/2020JE006446.
- 3671 Sizemore, H.G., Platz, T., Schorghofer, N., Prettyman, T.H., De Sanctis, M.C., Crown, D.A.,
3672 Schmedemann, N., Neesemann, A., Kneissl, T., Marchi, S., Schenk, P.M., Bland, M.T.,
3673 Schmidt, B.E., Hughson, K.H.G., Tosi, F., Zambon, F., Mest, S.C., Yingst, R.A., Williams,
3674 D.A., Russell, C.T., Raymond, C.A., 2017. Pitted terrains on (1) Ceres and implications for
3675 shallow subsurface volatile distribution. *Geophysical Research Letters*, **44**, 6570–6578,
3676 doi:10.1002/2017GL073970.
- 3677 Sizemore, H.G., Schmidt, B.E., Buczkowski, D.A., Sori, M.M., Castillo-Rogez, J.C., Berman,
3678 D.C., Ahrens, C., Chilton, H.T., Hughson, K.H.G., Duarte, K., Otto, K.A., Bland, M.T.,
3679 Neesemann, A., Scully, J.E.C., Crown, D.A., Mest, S.C., Williams, D.A., Platz, T., Schenk,
3680 P., Landis, M.E., Marchi, S., Schorghofer, N., Quick, L.C., Prettyman, T.H., De Sanctis,
3681 M.C., Nass, A., Thangjam, G., Nathues, A., Russell, C.T., Raymond, C.A., 2019. A global
3682 inventory of ice-related morphological features on dwarf planet Ceres: Implications for the
3683 evolution and current state of the cryosphere. *Journal of Geophysical Research: Planets*,
3684 **124**, 1650–1689, doi:10.1029/2018JE005699.
- 3685 Sletten, R.S., Hallet, B., Fletcher, R.C., 2003. Resurfacing time of terrestrial surfaces by the
3686 formation and maturation of polygonal patterned ground. *Journal of Geophysical Research:*
3687 *Planets*, **108**(E4), 8044, doi:10.1029-2002JE001914.
- 3688 Smith, D.E., Zuber, M.T., Neumann, G.A., 2001. Seasonal variations of snow depth on Mars.
3689 *Science*, **294**(5549), 2141–2146.
- 3690 Smith, I.B., Putzig, N.E., Holt, J.W., Phillips, R.J., 2016. An ice age recorded in the polar
3691 deposits of Mars. *Science*, **352**, 1075–1079, doi:10.1126/science.aad6968.
- 3692 Smith, I.B., Hayne, P.O., Byrne, S., Becerra, P., Kahre, M., Calvin, W., Hvidberg, C., Milkovich,
3693 S., Buhler, P., Landis, M., Horgan, B., 2020. The Holy Grail: A road map for unlocking the
3694 climate record stored within Mars' polar layered deposits. *Planetary and Space Science*, **184**,
3695 104841, doi:10.1016/j.pss.2020.104841.
- 3696 Smith, M.D., 2002. The annual cycle of water vapor on Mars as observed by the Thermal
3697 Emission Spectrometer. *Journal of Geophysical Research: Planets*, **107**(E11), 25-1–25-19,
3698 doi:10.1029/2001JE001522.
- 3699 Smith, M.D., 2008. Spacecraft observations of the martian atmosphere. *Annual Review Earth*
3700 *and Planetary Science*, **36**, 191–219.

- 3701 Smith, I.B., Holt, J.W., 2010. Onset and migration of spiral troughs on Mars revealed by orbital
3702 radar. *Nature*, **465**(7297), 450–453, doi:10.1038/nature09049
- 3703 Smith, P.H., Tamppari, L.K., Arvidson, R.E., Bass, D., Blaney, D., Boynton, W.V., Carswell, A.,
3704 Catling, D.C., Clark, B.C., Duck, T., DeJong, E., 2009. H₂O at the Phoenix landing site.
3705 *Science*, **325**(5936), 58–61.
- 3706 Smoluchowski, R., 1968. Mars: Retention of ice. *Science*, **159**(3821), 1348–1350.
- 3707 Soare, R.J., Kargel, J.S., Osinski, G.R., Costard, F., 2007. Thermokarst processes and the origin
3708 of crater-rim gullies in Utopia and western Elysium Planitia. *Icarus*, **191**, 95–112.
- 3709 Soare, R.J., Osinski, G.R., Roehm, C.L., 2008. Thermokarst lakes and ponds on Mars in the very
3710 recent (late Amazonian) past. *Earth and Planetary Science Letters*, **272**, 382–393.
- 3711 Soare, R.J., Séjourné, A., Pearce, G., Costard, F., Osinski, G.R., 2011. The Tuktoyaktuk
3712 Coastlands of northern Canada: A possible “wet” periglacial analog of Utopia Planitia, Mars.
3713 *Geological Society of American, Special Paper*, **483**, 203–218.
- 3714 Soare, R.J., Conway, S.J., Dohm, J.M., 2014. Possible ice-wedge polygons and recent landscape
3715 modification by “wet” periglacial processes in and around the Argyre impact basin, Mars.
3716 *Icarus*, **233**, 214–228.
- 3717 Soare, R.J., Conway, S.J., Gallagher, C., Dohm, J.M., 2016. Sorted (clastic) polygons in the
3718 Argyre region, Mars, and possible evidence of pre- and post-glacial periglaciation in the Late
3719 Amazonian Epoch. *Icarus*, **264**, 184–197.
- 3720 Soare, R.J., Conway, S.J., Gallagher, C., Dohm, J.M., 2017. Ice-rich (periglacial) vs icy (glacial)
3721 depressions in the Argyre region, Mars: a proposed cold-climate dichotomy of landforms.
3722 *Icarus*, **282**, 70–83, doi:10.1016/j.icarus.2016.09.009.
- 3723 Soare, R.J., Conway, S.J., Gallagher, C.J., Williams, J.P., Osinski, G.R., 2018. Paleo-periglacial
3724 and “ice-rich” complexes in Utopia Planitia. In *Dynamic Mars*, pp. 209–237, Elsevier.
- 3725 Soare, R.J., Conway, S.J., Williams, J.P., Gallagher, C., Mc Keown, L.E., 2019. Possible (closed
3726 system) pingo and ice-wedge/thermokarst complexes at the mid latitudes of Utopia Planitia,
3727 Mars. *Icarus*, **342**, 113233, doi:10.1016/j.icarus.2019.03.010.
- 3728 Soderblom, L.A., Kieffer, S.W., Becker, T.L., Brown, R.H., Cook, A.F., Hansen, C.J., Johnson,
3729 T.V., Kirk, R.L., Shoemaker, E.M., 1990. Triton's geysir-like plumes: Discovery and basic
3730 characterization. *Science*, **250**(4979), 410–415.
- 3731 Sori, M.M., Byrne, S., Hamilton, C.W., Landis, M.E., 2016. Viscous flow rates of icy
3732 topography on the north polar layered deposits of Mars. *Geophysical Research Letters*, **43**,
3733 541–549, doi:10.1002/2015GL067298.
- 3734 Sori, M.M., Bapst, J., Bramson, A.M., Byrne, S., Landis, M.E., 2017. A Wunda-full world?
3735 Carbon dioxide ice deposits on Umbriel and other Uranian moons. *Icarus*, **290**, 1–13,
3736 doi:10.1016/j.icarus.2017.02.029.
- 3737 Soto, A., Mischna, M., Schneider, T., Lee, C., Richardson, M., 2015. Martian atmospheric
3738 collapse: Idealized GCM studies. *Icarus*, **250**, 553–569, doi:10.1016/j.icarus.2014.11.028.
- 3739 Spencer, J., Denk, T., 2010. Formation of Iapetus' extreme albedo dichotomy by exogenically
3740 triggered thermal ice migration. *Science*, **327**, 432–435.

- 3741 Spiga, A., Smith, I., 2018. Katabatic jumps in the martian northern polar regions. *Icarus*, **308**,
3742 197–208, doi: 10.1016/j.icarus.2017.10.021.
- 3743 Steele, L.J., Balme, M.R., Lewis, S.R., 2017. Regolith-atmosphere exchange of water in Mars’
3744 recent past. *Icarus*, **284**, 233–248, doi:10.1016/j.icarus.2016.11.023.
- 3745 Stern, S.A., Bagenal, F., Ennico, K., Gladstone, G.R., Grundy, W.M., McKinnon, W.B., Moore,
3746 J.M., Olkin, C.B., Spencer, J.R., Weaver, H.A., Young, L.A., 2015. The Pluto system: Initial
3747 results from its exploration by New Horizons. *Science*, **350**(6258), aad1815,
3748 doi:10.1126/science.aad1815.
- 3749 Stillman, D.E., 2018. Unraveling the mysteries of recurring slope lineae. In *Dynamic Mars:
3750 Recent and Current Landscape Evolution of the Red Planet*, Editors R.J. Soare, S.J. Conway,
3751 S.M. Clifford, Elsevier, 474 pages, doi:10.1016/C2016-0-04489-3.
- 3752 Stillman, D.E., Grimm, R.E., 2018. Two pulses of seasonal activity in martian southern mid-
3753 latitude recurring slope lineae (RSL). *Icarus*, **302**, 126–133,
3754 doi:10.1016/j.icarus.2017.10.026.
- 3755 Stillman, D.E., Michaels, T.I., Grimm, R.E., Harrison, K.P., 2014. New observations of martian
3756 southern mid-latitude recurring slope lineae (RSL) imply formation by freshwater subsurface
3757 flows. *Icarus*, **233**, 328–341, doi:10.1016/j.icarus.2014.01.017.
- 3758 Stillman, D.E., Michaels, T.I., Grimm, R.E., Hanley, J., 2016. Observations and modeling of
3759 northern mid-latitude recurring slope lineae (RSL) suggest recharge by a present-day martian
3760 briny aquifer. *Icarus*, **265**, 125–138, doi:10.1016/j.icarus.2015.10.007.
- 3761 Stillman, D.E., Michaels, T.I., Grimm, R.E., 2017. Characteristics of the numerous and
3762 widespread recurring slope lineae (RSL) in Valles Marineris, Mars. *Icarus*, **285**, 195–210,
3763 doi:10.1016/j.icarus.2016.10.025.
- 3764 Stillman, D.E., Bue, B.D., Wagstaff, K.L., Primm, K.M., Michaels, T.I., Grimm, R.E., 2020.
3765 Evaluation of wet and dry recurring slope lineae (RSL) formation mechanisms based on
3766 quantitative mapping of RSL in Garni crater, Valles Marineris, Mars. *Icarus*, **335**, 113420.
- 3767 Stockstill-Cahill, K.R., Anderson, F.S., Hamilton, V.E., 2008. A study of low-albedo deposits
3768 within Amazonis Planitia craters: Evidence for locally derived ultramafic to mafic materials.
3769 *Journal of Geophysical Research*, **113**, doi:10.1029/2007JE003036.
- 3770 Sullivan, R., Kok, J., 2017. Aeolian saltation on Mars at low wind speeds. *Journal of
3771 Geophysical Research: Planets*, **122**, 2111–2143, doi:10.1002/2017JE005275.
- 3772 Sullivan, R., Banfield, D., Bell, J.F., Calvin, W., Fike, D., Golombek, M., Greeley, R.,
3773 Grotzinger, J., Herkenhoff, K., Jerolmack, D., Malin, M., 2005. Aeolian processes at the
3774 Mars exploration rover Meridiani Planum landing site. *Nature*, **436**(7047), 58–61,
3775 doi:10.1038/nature03641.
- 3776 Sullivan, R., Arvidson, R., Bell III, J.F., Gellert, R., Golombek, M., Greeley, R., Herkenhoff, K.,
3777 Johnson, J., Thompson, S., Whelley, P., Wray, J., 2008. Wind-driven particle mobility on
3778 Mars: Insights from Mars Exploration Rover observations at “El Dorado” and surroundings
3779 at Gusev Crater. *Journal of Geophysical Research*, **113**, E06S07,
3780 doi:10.1029/2008JE003101.

3781 Sullivan, R., Kok, J.F., Katra, I., Yizhaq, H. 2020. A broad continuum of aeolian impact ripple
3782 morphologies on Mars is enabled by low wind dynamic pressures. *Journal of Geophysical*
3783 *Research: Planets*, **125**(10), e2020JE006485, doi: 10.1029/2020JE006485

3784 Sunshine, J.M., Thomas, N., El-Maarry, M.R., Farnham, T.L., 2016. Evidence for geologic
3785 processes on comets. *Journal of Geophysical Research: Planets*, **121**, 2194–2210,
3786 doi:10.1002/2016JE005119.

3787 Swann, C., Sherman, D.J., Ewing, R.C., 2020. Experimentally derived thresholds for windblown
3788 sand on Mars. *Geophysical Research Letters*, **47**, e2019GL084484,
3789 doi:10.1029/2019GL084484.

3790 Sweeney, J., Warner, N.H., Ganti, V., Golombek, M.P., Lamb, M.P., Ferguson, R., Kirk, R.,
3791 2018. Degradation of 100 m-scale rocky ejecta craters at the InSight landing site on Mars and
3792 implications for surface processes and erosion rates in the Hesperian and Amazonian.
3793 *Journal of Geophysical Research*, **123**, 2732–2759, doi:10.1029/2018JE005618.

3794 Svitek, T., Murray, B.C., 1990. Winter frost at Viking Lander 2 site. *Journal of Geophysical*
3795 *Research*, **95**, 1495-1510.

3796 Sylvest, M.E., Conway, S.J., Patel, M.R., Dixon, J.C., Barnes, A., 2016. Mass wasting triggered
3797 by seasonal CO₂ sublimation under Martian atmospheric conditions: Laboratory experiments.
3798 *Geophysical Research Letters*, **43**(24), 12–363, doi:10.1002/2016GL071022.

3799 Sylvest, M.E., Dixon, J.C., Conway, S.J., Patel, M.R., McElwaine, J.N., Hagermann, A., Barnes,
3800 A., 2019. CO₂ sublimation in martian gullies: Laboratory experiments at varied slope angle
3801 and regolith grain sizes. *Geological Society, London, Special Publications*, 467(1), 343–371,
3802 doi:10.1144/SP467.11.

3803 Tamppari, L.K., Lemmon, M.T., 2020. Near-surface atmospheric water vapor enhancement at
3804 the Mars Phoenix lander site. *Icarus*, **343**, 113624, doi:10.1016/j.icarus.2020.113624.

3805 Tamppari, L.K., Bass, D., Cantor, B., Daubar, I., Dickinson, C., Fisher, D., Fujii, K.,
3806 Gunnlauggson, H.P., Hudson, T.L., Kass, D., Kleinböhl, A., 2010. Phoenix and MRO
3807 coordinated atmospheric measurements. *Journal of Geophysical Research: Planets*, **115**,
3808 E00E17, doi:10.1029/2009JE003415.

3809 Tanaka, K.L., 2005. Geology and insolation-driven climatic history of Amazonian north polar
3810 materials on Mars. *Nature*, **437**(7061), 991–994, doi:10.1038/nature04065.
3811

3812 Taylor, P.A., Kahanpää, H., Weng, W., Akingunola, A., Cook, C., Daly, M., Dickinson, C.,
3813 Harri, A.M., Hill, D., Hipkin, V., Polkko, J., 2010. On pressure measurement and seasonal
3814 pressure variations during the Phoenix mission. *Journal of Geophysical Research: Planets*,
3815 **115**(E3), E00E15, doi:10.1029/2009JE003422.

3816 Tebalt, M., Levy, J., Goudge, T., Schorghofer, N., 2020. Slope, elevation, and thermal inertia
3817 trends of recurring slope lineae initiation and termination points: Multiple possible processes
3818 occurring on coarse, sandy slopes. *Icarus*, **338**, 113536, doi:10.1016/j.icarus.2019.113536.

3819 Telfer, M.W., Parteli, E.J., Radebaugh, J., Beyer, R.A., Bertrand, T., Forget, F., Nimmo, F.,
3820 Grundy, W.M., Moore, J.M., Stern, S.A., Spencer, J., 2018. Dunes on Pluto. *Science*, **360**
3821 (6392), 992–997, doi:10.1126/science.aao2975.

- 3822 Tesson, P.-A., Conway, S.J., Mangold, N., Ciazela, J., Lewis, S.R., Mège, D., 2020. Evidence for
3823 thermal–stress–induced rockfalls on Mars impact crater slopes. *Icarus*, **342**, 113503,
3824 doi:10.1016/j.icarus.2019.113503.
- 3825 Thomas, M.F., McEwen, A.S., Dundas, C.M., 2020. Present-day mass wasting in sulfate-rich
3826 sediments in the equatorial regions of Mars. *Icarus*, **342**, 113566,
3827 doi:10.1016/j.icarus.2019.113566.
- 3828 Thomas, N., Hansen, C.J., Portyankina, G., Russell, P.S., 2010. HiRISE observations of gas
3829 sublimation-driven activity in Mars' southern polar regions: II. Surficial deposits and their
3830 origins. *Icarus*, **205** (1), 296–310, doi:10.1016/j.icarus.2009.05.030.
- 3831 Thomas, N., Sierks, H., Barbieri, C., Lamy, P.L., Rodrigo, R., Rickman, H., Koschny, D., Keller,
3832 H.U., Agarwal, J., A'Hearn, M.F., Angrilli, F., 2015. The morphological diversity of comet
3833 67P/Churyumov–Gerasimenko. *Science*, **347** (6220), aaa0440, doi:10.1126/science.aaa0440.
- 3834 Thomas, N., Cremonese, G., Ziethe, R., Gerber, M., Brändli, M., Bruno, G., Erismann, M.,
3835 Gambicorti, L., Gerber, T., Ghose, K., Gruber, M., 2017. The colour and stereo surface
3836 imaging system (CaSSIS) for the ExoMars trace gas orbiter. *Space science reviews*, 212(3–
3837 4), 1897–1944, doi10.1007/s11214-017-0421-1.
- 3838 Thomas, P., Gierasch, P., 1985. Dust devils on Mars. *Science*, **230**(4722), 175–177,
3839 doi:10.1126/science.230.4722.175.
- 3840 Thomas, P.C., Malin, M.C., Edgett, K.S., Carr, M.H., Hartmann, W.K., Ingersoll, A.P., James,
3841 P.B., Soderblom, L.A., Veverka, J., Sullivan, R., 2000. North-south geological differences
3842 between the residual polar caps on Mars. *Nature*, **404**(6774), 161–164.
- 3843 Thomas, P.C., Malin, M.C., James, P.B., Cantor, B.A., Williams, R.M.E. Gierasch, P., 2005. South
3844 polar residual cap of Mars: Features, stratigraphy, and changes. *Icarus*, **174**(2), 535–559.
- 3845 Thomas, P.C., James, P.B., Calvin, W.M., Haberle, R., Malin, M.C., 2009. Residual south polar
3846 cap of Mars: Stratigraphy, history, and implications of recent changes. *Icarus*, **203**(2), 352–
3847 375, doi:10.1016/j.icarus.2009.05.014.
- 3848 Thomas, P.C., Calvin, W.M., Gierasch, P., Haberle, R., James, P.B., Sholes, S., 2013. Time scales
3849 of erosion and deposition recorded in the residual south polar cap of Mars. *Icarus*, **225**(2), 923–
3850 932, doi:10.1016/j.icarus.2012.08.038.
- 3851 Thomas, P.C., Calvin, W., Cantor, B., Haberle, R., James, P.B. and Lee, S.W., 2016. Mass balance
3852 of Mars' residual south polar cap from CTX images and other data. *Icarus*, **268**, 118–130,
3853 doi:10.1016/j.icarus.2015.12.038.
- 3854 Thomas, P.C., Calvin, W.M. James, P.B., 2020. Debris accumulations of CO₂ ice in the south polar
3855 residual cap of mars: Longevity and processes. *Icarus*, 113625.
- 3856 Thomas, R.J., Rothery, D.A., Conway, S.J., Anand, M., 2014. Hollows on Mercury: Materials
3857 and mechanisms involved in their formation. *Icarus*, **229**, 221–235,
3858 doi:10.1016/j.icarus.2013.11.018.
- 3859 Tirsch, D., Jaumann, R., Pacifici, A., Poulet, F., 2011. Dark aeolian sediments in martian craters:
3860 composition and sources. *Journal of Geophysical Research*, **116**, E03002,
3861 doi:10.1029/2009JE003562.
- 3862 Titus, T.N., Kieffer, H.H., Christensen, P.R., 2003. Exposed water ice discovered near the south
3863 pole of Mars. *Science*, **299**(5609), 1048–1051.

- 3864 Titus, T.N., Williams, K.E., Cushing, G.E., 2020. Conceptual model for the removal of cold-
3865 trapped H₂O ice on the Mars northern seasonal springtime polar cap. *Geophysical Research*
3866 *Letters*, **47**(15), e2020GL087387, doi:10.1029/2020GL087387.
- 3867 Tornabene, L.L., Osinski, G.R., McEwen, A.S., Boyce, J.M., Bray, V.J., Caudill, C.M., Grant,
3868 J.A., Hamilton, C.W., Mattson, S., Mouginis-Mark, P.J., 2012. Widespread crater-related
3869 pitted materials on Mars: Further evidence for the role of target volatiles during the impact
3870 process. *Icarus*, **220**, 348–368, doi:10.1016/j.icarus.2012.05.022.
- 3871 Trafton, L., 1984. Large seasonal variations in Triton's atmosphere. *Icarus*, **58**(1), 312–324.
- 3872 Tsoar, H., Greeley, R., Peterfreund, A.R., 1979. Mars: The north polar sand sea and related wind
3873 patterns. *Journal of Geophysical Research*, **84**, 8167–8180.
- 3874 Turbet, M., Bolmont, E., Leconte, J., Forget, F., Selsis, F., Tobie, G., Caldas, A., Naar, J., Gillon,
3875 M., 2018. Modeling climate diversity, tidal dynamics and the fate of volatiles on TRAPPIST-
3876 1 planets. *Astronomy and Astrophysics*, **612**, A86, doi:10.1051/0004-6361/201731620.
- 3877 Ulrich, M., Morgenstern, A., Günther, F., Reiss, D., Bauch, K.E., Hauber, E., Rössler, S.,
3878 Schirrmeister, L., 2010. Thermokarst in Siberian ice-rich permafrost: Comparison to
3879 asymmetric scalloped depressions on Mars. *Journal of Geophysical Research*, **115**, E10009.
- 3880 Umurhan, O.M., White, O.L., Moore, J.M., Howard, A.D., Schenk, P., 2016. Modeling surface
3881 processes occurring on moons of the outer Solar System. Presented at the *AGU Fall Meeting*,
3882 Ab. EP43D-08.
- 3883 Vaz, D.A., Silvestro, S., Sarmiento, P.T., Cardinale, M., 2017. Migrating meter-scale bedforms
3884 on martian dark dunes: Are terrestrial aeolian ripples good analogues? *Aeolian Research*, **26**,
3885 101–116, doi:10.1016/j.aeolia.2016.08.003.
- 3886 Vermeesch, P., Drake, N., 2008. Remotely sensed dune celerity and sand flux measurements of
3887 the world's fastest barchans (Bodélé, Chad). *Geophysical Research Letters*, **35**, L24404,
3888 doi:10.1029/2008GL035921.
- 3889 Vincendon, M., Mustard, J., Forget, F., Kreslavsky, M., Spiga, A., Murchie, S., Bibring, J.-P.,
3890 2010a. Near-tropical subsurface ice on Mars. *Geophysical Research Letters*, **37**, L01202,
3891 doi:10.1029/2009GL041426.
- 3892 Vincendon, M., Forget, F., Mustard, J., 2010b. Water ice at low to midlatitudes on Mars. *Journal*
3893 *of Geophysical Research: Planets*, **115**, E10001, doi:10.1029/2010JE003584.
- 3894 Vincendon, M., Pilonget, C., Carter, J., Stcherbinine, A., 2019. Observational evidence for a dry
3895 dust–wind origin of Mars seasonal dark flows. *Icarus*, **325**, 115–127,
3896 doi:10.1016/j.icarus.2019.02.024.
- 3897 Vincent, J.-B., Bodewits, D., Besse, S., Sierks, H., Barbieri, C., Lamy, P., Rodrigo, R., Koschny,
3898 D., Rickman, H., Keller, H.U., Agarwal, J., A'Hearn, M.F., Auger, A.-T., Barucci, M.A.,
3899 Bertaux, J.-L., Bertini, I., Capanna, C., Cremonese, G., Da Deppo, V., Davidsson, B., Debei,
3900 S., De Cecco, M., El-Maarry, M.R., Ferri, F., Fornasier, S., Fulle, M., Gaskell, R.,
3901 Giacomini, L., Groussin, O., Guilbert–Lepoutre, A., Gutierrez–Marques, P., Gutierrez, P.J.,
3902 Guttler, C., Hoekzema, N., Hofner, S., Hviid, S.F., Ip, W.-H., Jorda, L., Knollenberg, J.,
3903 Kovacs, G., Kramm, R., Kuhrt, E., Koppers, M., La Forgia, F., Lara, L.M., Lazzarin, M.,
3904 Lee, V., Leyrat, C., Lin, Z.-Y., Lopez Moreno, J.J., Lowry, S., Magrin, S., Maquet, L.,
3905 Marchi, S., Marzari, F., Massironi, M., Michalik, H., Moissl, R., Mottola, S., Naletto, G.,

- 3906 Oklay, N., Pajola, M., Preusker, F., Scholten, F., Thomas, N., Toth, I., Tubiana, C., 2015.
3907 Large heterogeneities in comet 67P as revealed by active pits from sinkhole collapse. *Nature*,
3908 **523**, 63–66, doi:10.1038/nature14564.
- 3909 Viola, D., McEwen, A.S., Dundas, C.M., Byrne, S., 2015. Expanded secondary craters in the
3910 Arcadia Planitia region, Mars: Evidence for tens of Myr-old shallow subsurface ice. *Icarus*,
3911 **248**, 190–204.
- 3912 Viola, D., McEwen, A., 2018. Geomorphological evidence for shallow ice in the southern
3913 hemisphere of Mars. *Journal of Geophysical Research: Planets*, **123**, 262–277.
- 3914 Wagstaff, K.L., Titus, T.N., Ivanov, A.B., Castaño, R., Bandfield, J.L., 2008. Observations of the
3915 north polar water ice annulus on Mars using THEMIS and TES. *Planetary and Space*
3916 *Science*, **56**(2), 256-265.
- 3917 Wall, S.D., 1981. Analysis of condensates formed at the Viking 2 Lander site: The first winter.
3918 *Icarus*, **47**(2), 173–183.
- 3919 Waite, J.H., Glein, C.R., Perryman, R.S., Teolis, B.D., Magee, B.A., Miller, G., Grimes, J.,
3920 Perry, M.E., Miller, K.E., Bouquet, A., Lunine, J.I., 2017. Cassini finds molecular hydrogen
3921 in the Enceladus plume: evidence for hydrothermal processes. *Science*, **356**(6334), 155–159,
3922 doi:10.1126/science.aai8703.
- 3923 Wang, A., Ling, Z., Yan, Y., McEwen, A.S., Mellon, M.T., Smith, M.D., Jolliff, B.L., Head, J.,
3924 2019. Subsurface Cl-bearing salts as potential contributors to recurring slope lineae (RSL) on
3925 Mars. *Icarus*, **333**, 464–480.
- 3926 Ward, A.W., 1979. Yardangs on Mars: Evidence of recent wind erosion. *JGR Solid Earth*,
3927 **84**(B14), 8147–8166, doi:10.1016/j.pss.2020.105035.
- 3928 Weitz, C.M., Plaut, J.J., Greeley, R., Saunders, R.S., 1994. Dunes and microdunes on Venus:
3929 Why were so few found in the Magellan data. *Icarus*, **112**, 282–295.
- 3930 Weitz, C., Sullivan, R., Lapôtre, M., Rowland, S., Grant, J., Baker, M., Yingst, R.A., 2018. Sand
3931 grain sizes and shapes in eolian bedforms at Gale crater, Mars. *Geophysical Research*
3932 *Letters*, **45**(18), 9471–9479, doi:10.1029/2018GL078972.
- 3933 Weitz, C.M., Sullivan, R.J., Lapôtre, M.G.A., Rowland, S.K., Grant, J.A., Baker, M.M., Yingst,
3934 R.A., 2020. Physical Properties of Sand Grains in the Bagnold Dunes at Gale Crater, Mars.
3935 Presented at the 6th *International Planetary Dunes Workshop*, Ab. 3004.
- 3936 Werner, B., Haff, P., Livi, R., Anderson, R., 1986. Measurement of eolian sand ripple cross-
3937 sectional shapes. *Geology*, **14**, 743, doi:10.1130/0091-
3938 7613(1986)14<743:MOESRC>2.0.CO;2.
- 3939 White, O.L., Umurhan, O.M., Moore, J.M., Howard, A.D., 2016. Modeling of ice pinnacle
3940 formation on Callisto. *Journal of Geophysical Research: Planets*, **121**(1), 21–45,
3941 doi:10.1002/2015JE004846.
- 3942 Widmer, J.M., Diniega, S., Hayne, P.O., Alsaeed, N., Gary-Bicas, C.E., 2020. Martian seasonal
3943 frost and snowfall in the northern mid-latitudes—growing the seasonal frost cap and
3944 contributing environmental factors. Presented at the *2020 AGU Fall Meeting*, P033-0010.
- 3945 Wilcoski, A.X., Hayne, P.O., 2020. Surface roughness evolution and implications for the age of
3946 the north polar residual cap of Mars. *Journal of Geophysical Research: Planets*, **125**(12),
3947 E006570, doi:10.1029/2020JE006570.

- 3948 Wilson, I.G. (1972). Aeolian bedforms—their development and origins. *Sedimentology*, **19**(3–
3949 4), 173–210.
- 3950 Wilson, L., Head, J.W., 1994. Mars: review and analysis of volcanic eruption theory and
3951 relationships to observed landforms. *Rev. Geophys.*, **32** (3), 221–263.
- 3952 Wilson, S.A., Zimbelman, J.R., 2004. Latitude-dependent nature and physical characteristics of
3953 transverse aeolian ridges on Mars. *Journal of Geophysical Research*, **109**, E10003,
3954 doi:10.1029/2004JE002247.
- 3955 Withers, P., Smith, M.D., 2006. Atmospheric entry profiles from the Mars Exploration Rovers
3956 Spirit and Opportunity. *Icarus*, **185**(1), 133–142, doi:10.1016/j.icarus.2006.06.013.
- 3957 Witzke, A., 2015. Pluto snow forecast poses atmospheric conundrum. *Nature*, **525**, 13–14,
3958 doi:0.1038/525013a.
- 3959 Yelle, R.V., Lunine, J.I., Pollack, J.B., Brown, R.H., 1995. Lower atmospheric structure and
3960 surface–atmosphere interactions on Triton'. In *Neptune and Triton*, Editor D.P. Cruikshank,,
3961 Univ. of Arizona Press, Tucson, 1021 pages.
- 3962 Yen, A.S., Gellert, R., Schröder, C., Morris, R.V., Bell, J.F., Knudson, A.T., Clark, B.C., Ming,
3963 D.W., Crisp, J.A., Arvidson, R.E., Blaney, D., 2005. An integrated view of the chemistry and
3964 mineralogy of martian soils. *Nature*, **436**, 49–54, doi:10.1038/nature03637.
- 3965 Yizhaq, H., Kok, J. F., Kutra, I., 2014. Basaltic sand ripples at Eagle crater as indirect evidence
3966 for the hysteresis effect in martian saltation. *Icarus*, **230**, 143–150,
3967 doi:10.1016/j.icarus.2013.08.006.
- 3968 Yoldi, Z., Pommerol, A., Poch, O., Thomas, N., 2021. Reflectance study of ice and Mars soil
3969 simulant associations – I. H₂O ice. *Icarus*, 114169, doi:10.1016/j.icarus.2020.114169.
- 3970 Young, L.A., 2012. Volatile Transport on Inhomogeneous Surfaces: I Analytic Expressions, with
3971 Application to Pluto's Day. *Icarus*, **221**, 80–88, doi:10.1016/j.icarus.2012.06.032.
- 3972 Zalucha, A.M., Michaels, T.I., 2013. A 3D general circulation model for Pluto and Triton with
3973 fixed volatile abundance and simplified surface forcing. *Icarus*, **223**(2), 819–83,
3974 doi:10.1016/j.icarus.2013.01.026.
- 3975 Zanetti, M., Hiesinger, H., Reiss, D., Hauber, E., Neukum, G., 2010. Distribution and evolution
3976 of scalloped terrain in the southern hemisphere, Mars. *Icarus*, **206**, 691–706,
3977 doi:10.1016/j.icarus.2009.09.010.
- 3978 Zimbelman, J.R., 2010. Transverse aeolian ridges on Mars: First results from HiRISE images.
3979 *Geomorphology*, **121**, 22–29, doi:10.1016/j.geomorph.2009.05.012.
- 3980 Zimbelman, J.R., 2019. The transition between sand ripples and megaripples on Mars. *Icarus*,
3981 **333**, 127–129, doi:10.1016/j.icarus.2019.05.017.
- 3982 Zimbelman, J.R., Foroutan, M. (2020). Dingo Gap: Curiosity went up a small transverse aeolian
3983 ridge and came down a megaripple. *Journal of Geophysical Research: Planets*, **125**(12),
3984 e2020JE006489, doi: 10.1029/2020JE006489.